Universitat Autònoma de Barcelona

Cross section measurement of the muon neutrino charged current single positive pion interaction on hydrocarbon using the T2K near detector with 4∏ solid angle acceptance

Danaisis Vargas Oliva

IFAE

Institut de Física
d'Altes Energies

Danaisis Vargas Oliva

Cross section measurement of the muon neutrino charged current single positive pion interaction on hydrocarbon using the T2K near detector with 4π solid angle acceptance

A thesis dissertation supervised by

Dr. Thorsten LUX and Dr. Federico SÁNCHEZ NIETO

UAB

Universitat Autònoma
de Barcelona

Universitat Autònoma
de Barcelona

Cross section measurement of the muon neutrino charged current single positive pion interaction on hydrocarbon using the T2K near detector with 4π solid angle acceptance

Danaisis Vargas Oliva

Thesis presented to qualify for the degree of

PhD IN PHYSICS

Supervised by:

Dr. Thorsten Lux (Director)

Dr. Federico Sánchez Nieto (Director)

Dr. Jose Maria Crespo Vicente (Tutor)

and assessed by:

Dr. Juan Nives _________ (President)

Dr. Pilar Casado _________ (Secretary)

Dr. Claudio Giganti _________ (Vocal)

Cerdanyola (Barcelona), January 21st, 2022

Universitat Autònoma
de Barcelona

Medición de la sección eficaz de interacción de corriente cargada de neutrino muónico con producción de un pion positivo en hydrocarbon en el detector cercano de T2K con aceptación de 4π ángulo sólido

Danaisis Vargas Oliva

Tesis presentada para obtener el grado de

DOCTOR EN FÍSICA

Supervisada por:

Dr. Thorsten Lux (Director)

Dr. Federico Sánchez Nieto (Director)

Dr. Jose Maria Crespo Vicente (Tutor)

y evaluada por:

Dr. Juan Nives _________ (President)

Dr. Pilar Casado _________ (Secretary)

Dr. Claudio Giganti _________ (Vocal)

Cerdanyola (Barcelona), 21 de Enero del 2022

Declaration of authorship

I, *Danaisis Vargas Oliva*, declare that this thesis titled, *"Cross section measurement of the muon neutrino charged current single positive pion interaction on hydrocarbon using the T2K near detector with 4π solid angle acceptance"* and the work presented in it are my own. I confirm that:

- This work was done wholly or mainly while in candidature for a research degree at this University.
- Where any part of this thesis has previously been submitted for a degree or any other qualification at this University or any other institution, this has been clearly stated.
- Where I have consulted the published work of others, this is always clearly attributed.
- Where I have quoted from the work of others, the source is always given. With the exception of such quotations, this thesis is entirely my own work.
- I have acknowledged all main sources of help.
- Where the thesis is based on work done by myself jointly with others. I have made clear exactly what was done by others and what I have contributed myself.

Signed:

Date:

Acknowledgments

Firstly, I would like to express my gratitude to my supervisors, Ph.D. Prof. Thorsten Lux and Ph.D. Prof. Federico Sánchez Nieto for the continuous support of my PhD study and related research, for their patience, motivation, and immense knowledge. Their doors were always open whenever I ran into a troubled spot. They consistently steered me in the right direction whenever they thought I needed it. There is no better duo to guide you at the beginning of your research career. They helped me during the research for this thesis and the writing after. I could not have imagined having better supervisors and mentors for my Ph.D. studies.

I would like to acknowledge the support received from the Ministerio de Ciencia e Innovation under grants FPA2014-59855-P, TEC2012-39150-C02-02, and Centro de Excelencia Severo Ochoa SEV-2012-0234, some of which include ERDF funds from the European Union. I would also like to thank the T2K collaboration, J-PARC, and CERN for providing valuable particle production data and opportunities for experimental work.

Thank you very much to Ph.D. Juan M. Nieves, Ph.D. Pilar Casado, Ph.D. Claudio Giganti, Ph.D. Imma Riu and Ph.D. Juan A. Caballero, for agreeing to be part of the jury for my doctoral defense.

I have a special thanks to Ph.D. Caspar M. Schloesser, you have been my rock; thanks for keeping me sane and for all your work that made mine easier. To Kevin Fusshoeller and Stephanie Bron, only we know all the ups and downs when developing the selection. Still, during this time, it was good to discuss everything with you. Thanks to Ph.D. Stephen Dolan and Ph.D. Ciro Riccio, for being there every time that I needed them, regardless of the hour or how busy they were. Thank you, César Jesús-Valls, for the physics discussions and the endless days we worked together. Thanks for all the fun we have had in the last four years and the Game Nights.

Last but not least, I would like to thank my parents, brothers and friends for supporting me spiritually throughout writing this thesis and my life in general. Without them, this accomplishment would not have been possible.

Thank you.
Danaisis Vargas Oliva

Abstract

Cross section measurement of the muon neutrino charged current single positive pion interaction on hydrocarbon using the T2K near detector with 4π solid angle acceptance

Danaisis Vargas Oliva

Institute of High Energy Physics
Autonomous University of Barcelona
Barcelona, Spain
2022

T2K is a long-baseline neutrino experiment located in Japan that aims to measure neutrino oscillations. An accelerator produces neutrinos, which are detected in a near detector complex and a far detector (Super-Kamiokande). The neutrino beamline is designed so that the neutrino energy spectrum can be tuned making T2K the first experiment to use off-axis. The muon neutrino charged current interactions in the near detector (ND280) are used to predict the event rate at the far detector and better constrain the cross section parameters, which is dominant in the oscillation analysis, together with the flux uncertainty.

We present the study of charged current interactions on carbon with a single positively charged pion in the final state at the T2K off-axis near detector. This signal, defined as one negatively charged muon (with 4π solid angle acceptance), one positive charged pion (that can be observed in the TPC, as an isolated track in the FGD or via Michel electron tagging), no additional mesons, and any number of nucleons as the final state particles. This signal constitutes the main background for the muon neutrino disappearance measurement when the charged pion is not observed, and its precise knowledge is relevant for all current and planned neutrino oscillation experiments. Single pion production is sensitive mainly to resonant processes, with some non-resonant and coherent pion production contributions. Additionally, final-state interactions in the nuclear target have to be considered.

The CC$1\pi^+$ signal measurement builds on a previous result, with significant changes to the kinematic particle ranges considered, solid angle acceptance, an increase in statistics, and a new treatment for the evaluation and propagation of systematic uncertainties. This thesis has produced a set of flux integrated muon neutrino CC$1\pi^+$ cross sections on hydrocarbon using the T2K off-axis near detector data. These cross section measurements are used to reduce model-related systematics, which will be particularly important for next generation oscillation experiments.

Adler Angles are observable carrying information about the polarization of the Delta resonance and the interference with the non-resonant single pion production. They were measured with limited statistics in bubble chamber experiments, but it is possible to measure the Adler angles for single charged pion production in neutrino interactions with heavy nuclei as the target.

Key Words: Neutrino Physics, Cross section, Oscillation, Adler angles

Contents

Outline

This thesis details the study of ν_μ interactions via charged current with one positive charged pion in the final state with a 4π solid angle acceptance. We aim to characterize such interaction using the T2K near detector. Ten Chapters and six Appendices form this thesis.

The thesis starts with the basics that are divided into three chapters: Chapter 1 where a short historical introduction to the discovery of the neutrino is presented. Some essential elements of the theoretical foundation will be described, such as the Standard Model, the different neutrino sources, and the concept of neutrino flavor oscillation. Then, Chapter 2 that summarizes the current knowledge about the neutrino, their interactions, and cross section are presented. General discussions of the neutrino cross section and the neutrino/antineutrino interactions with nucleon and nucleus are provided. The third one is Chapter 3, where a description of the T2K experiment is provided. It starts with the main sites J-PARK, near detector complex, and Far detector. A brief description of the different detectors and components is presented.

The thesis continues with the core of the main analysis, tools and methods are explained. Chapter 4 describes the motivation for the analysis, the analysis strategy, and the methods used to unfold the data, validate the fitter, and extract a differential cross section in kinematic variables. Chapter 5 present the framework used and goes on to explain the development of the selection used for the analysis and the different steps and signal that can be studied. Then a description of the signals and their performance is presented. Using the selection developed and presented is selected and study the signal of interest for this analysis ($CC1\pi^+$) and the reconstructed variables computed with that signal and this is presented in Chapter 6. The characterization and evaluation of systematic uncertainties are presented in Chapter 7. The different sources of systematic uncertainties (detector, flux, and model) accounted for in this analysis are briefly explained.

To Finish, this is followed by Chapter 8 where several fit framework validation studies to ensure the extracted cross sections are not biased are presented. In Chapter 9 are presented the best fit results for the real data and the extraction of the final results of the cross section. A summary of several prospects and an interpretation of the results is presented in Chapter 10.

Chapter 1

Neutrino physics

In 1914, Chadwick demonstrated that the β-spectrum was continuous. In order to maintain the concept of energy, momentum, and angular momentum (spin) conservation in β-decay Wolfgang Pauli proposed, in an open letter to a physics conference at Tubingen on 4 December 1930, addressed to "Dear Radioactive Ladies and Gentlemen", that the existence of a neutral weakly interacting fermion emitted in β-decay could solve the problems [59]. He called this neutral fermion "neutron", with a mass of the order of the electron.

In 1932 Enrico Fermi renamed the Pauli particle to neutrino because of the experimental detection of the real neutron as we know it today. Fermi and Perrin independently concluded in 1933 that neutrinos could be massless! W. Pauli was afraid that this neutral, massless particle (as conceived initially) would never be detected. However, in 1956 (26 years later), Clyde Cowan and Frederick Reines experimentally detected the neutrino from a reactor source in the United States of America [63].

Nowadays, there are several neutrino experiments worldwide, and the study of neutrinos extends to a large variety of fields such as Astrophysics, Nuclear Physics, and Particle Physics. In this chapter, some fundamental elements of the theoretical foundation will be described, like the Standard Model, the different neutrino sources, and the concept of neutrino flavor oscillation.

1.1 Standard Model (SM)

The Standard Model of elementary particle physics describes the strong, electromagnetic, and weak interactions in quantum field theory. It is a gauge theory based on the local symmetry group $SU(3)_C \times SU(2)_L \times U(1)_Y$, where the subscripts C, L and Y denote color, left-handed chirality, and weak hypercharge, respectively. The SM has predicted various properties of weak neutral currents and the W and Z bosons with great accuracy.

The SM includes members of several families of particles like fermions and bosons (which are the force-carrying gauge particles). They are divided into two categories, quarks, and leptons, according to the scheme Figure 1.1. They are three generations of fermions with identical properties but with different masses. In each generation, leptons are lighter than the quarks, which are constituents of the baryons.

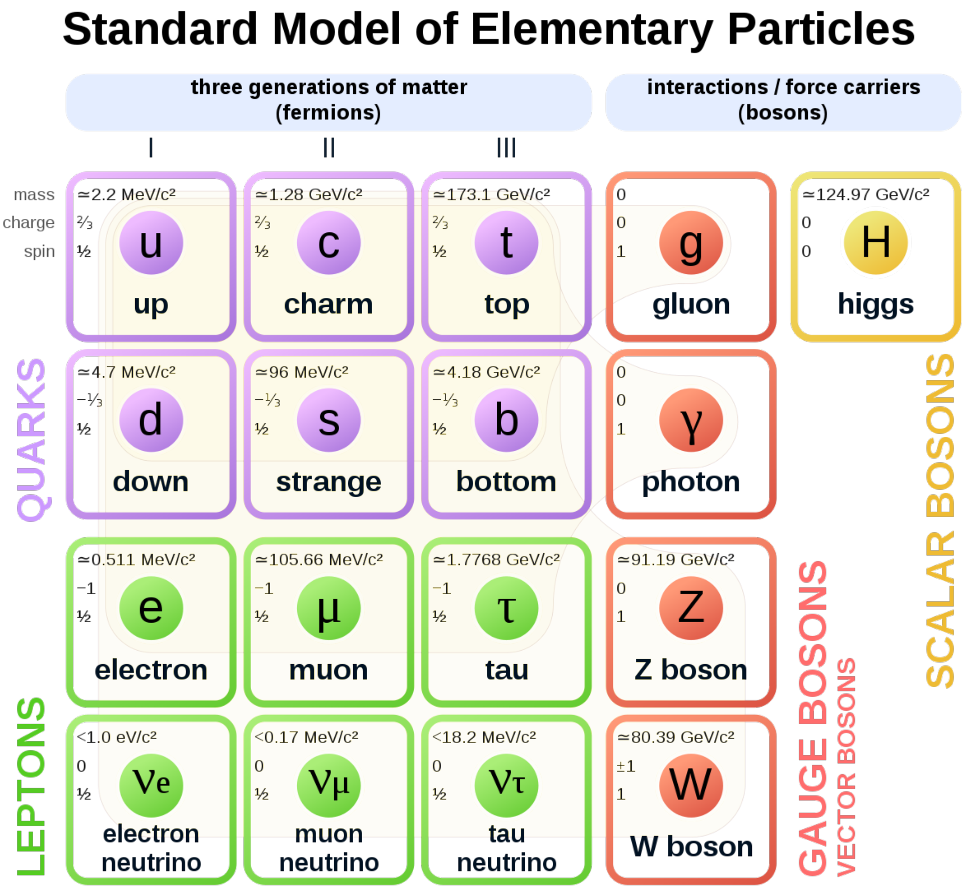

FIGURE 1.1: Electroweak Standard Model of elementary particles scheme after symmetry breaking [2]

1.1.1 Electroweak theory

The electroweak part of the SM is based on the symmetry group $SU(2)_L \times U(1)_Y$, which determines the interactions of neutrinos (neutrinos only interact via this force). In the SM, electroweak interactions can be studied separately from strong interactions because the symmetry under the color group $SU(3)_C$ is unbroken, and there is no mixing between the $SU(3)_C$ and $SU(2)_L \times U(1)_Y$ sectors. Due to mixing between the neutral gauge bosons of $SU(2)_L$ and $U(1)_Y$, the electromagnetic and weak interactions must be treated together [47].

Lagrangian of the electroweak interaction

The interaction part of the Lagrangian after the spontaneous symmetry breaking via the Higgs mechanism:

$$\mathcal{L}_{int} = -\frac{g}{2\sqrt{2}}(\mathcal{J}_\alpha^{CC} W^{\alpha\dagger} + h.c.) - \frac{g}{2cos\theta_W}\mathcal{J}_\alpha^{NC} Z^\alpha - e\mathcal{J}_\alpha^{EM} A^\alpha \tag{1.1}$$

The weak charged current (CC) $\mathcal{J}_\alpha^{CC}$, the weak neutral current (NC) $\mathcal{J}_\alpha^{NC}$ and the electromagnetic current (EM) $\mathcal{J}_\alpha^{EM}$ couple to the charged W-boson field W^α, the neutral Z-boson field Z^α and the photon field A^α, respectively. The currents can be separated into a leptonic part (j_α) and a hadronic part (J_α):

$$\mathcal{J}_{\alpha}^{CC} = j_{\alpha} + J_{\alpha} \tag{1.2}$$

Since parity is maximal violated in weak interactions, the weak currents have to have a vector-axial vector ($V - A$) structure.

Leptonic currents

The charged current couples to a charged $W^{\pm}$ boson. It does not change the flavor but turns a charged lepton into a neutrino or vice versa (more in the next chapter 2). The coupling involves only left-handed fields leading to a vector-axial vector structure in the current. Neutral currents couples mediated a neutral Z^0 bosons. Those interactions also cannot change the flavor and even keep the identity of the lepton. For neutrinos, only coupling to left-handed fields is possible; for charged leptons, both left, and right-handed fields are involved but with different couplings with the weak mixing angle (Weinberg angle) $sin\theta_W$. The electromagnetic current couples to photons.

Each of the contributions are given by:

$$j_{\alpha}^{CC} = \sum_{l=e,\mu,\tau} \bar{\nu}_l \gamma_{\alpha}(1-\gamma_5)l \tag{1.3}$$

$$j_{\alpha}^{NC} = \sum_{l=e,\mu,\tau} \frac{1}{2}\bar{\nu}_l\gamma_{\alpha}(1-\gamma_5)\nu_l - \frac{1}{2}(1-2sin^2\theta_W)\bar{l}\gamma_{\alpha}(1-\gamma_5)l + sin^2\theta_W\bar{l}\gamma_{\alpha}(1+\gamma_5)l \tag{1.4}$$

$$j_{\alpha}^{EM} = \sum_{l=e,\mu,\tau} \bar{l}\gamma_{\alpha}l \tag{1.5}$$

1.1.2 Neutrino in the Standard Model

The β-decay process would imply the emission of electrons and neutrinos that would gather the energy loss in the process. The β-decay process was defined as: $n \to p + e^- + \bar{\nu}$.

Neutrino flavors and masses

During the following decades after the postulation of the neutrino, new particles were discovered, specifically, the muon and pions. Pions decay into a muon, which emerges with an almost perpendicular track to the pion, ensuring the existence of an extremely light particle in the process. Looking at the muon decay, unlike the process $\mu \to e + \nu + \bar{\nu}$, the reaction $\mu \to e + \gamma$ was not observed (its experimental limits were many orders of magnitude smaller than predicted). Consequently, it was proposed the existence of two different kinds of neutrinos, one related to the electron and another one to the muon [70].

In 1962 Leon Max Lederman, Melvin Schwartz, and Jack Steinberger showed that more than one type of neutrino existed when the ν_{μ} was first detected at Brookhaven National Laboratory (BNL) after the experimental proof of the muon decay into an electron led to the conclusion that two neutrinos must accompany the latter. Finally, in 2000 it was announced that the first direct evidence of ν_{τ} was discovered by the DONUT (Direct Observation of the Nu Tau) collaboration [53] after a series of experiments between 1974 and 1977 by Martin Lewis Perl.

$$\begin{aligned} \pi^+ &\to \mu^+ + \nu_\mu, \\ \pi^- &\to \mu^- + \bar{\nu}_\mu, \\ \mu^+ &\to e^+ + \nu_e + \bar{\nu}_\mu, \\ \mu^- &\to e^- + \nu_\mu + \bar{\nu}_e. \end{aligned}$$

Neutrinos are leptons, there are three neutrino flavors: electron neutrino (ν_e), muon neutrino (ν_μ) and tau neutrino (ν_τ) (Table 1.1). Each neutrino/antineutrino forms a doublet with the corresponding charged lepton (Figure 1.2).

TABLE 1.1: The family of leptons. Data taken from [3].

	Charge leptons			Neutrinos		
	Symbol	Charge	Mass	Symbol	Charge	Mass
1^{st} generation	e^- e^+	-1 +1	0.511 MeV	ν_e $\bar{\nu}_e$	0 0	< 3 eV
2^{nd} generation	μ^- μ^+	-1 +1	105.658 MeV	ν_μ $\bar{\nu}_\mu$	0 0	< 0.19 MeV
3^{rt} generation	τ^- τ^+	-1 +1	1777.03 GeV	ν_τ $\bar{\nu}_\tau$	0 0	< 18.2 MeV

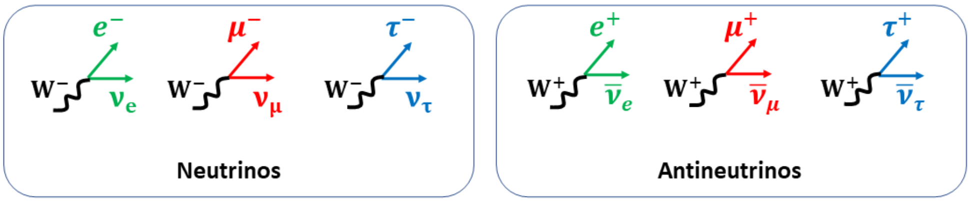

FIGURE 1.2: Doublet form for each neutrino and antineutrino [47].

The Z^0 decay width can determine the number of neutrinos participating in the electroweak interaction, confirming that there are three light neutrinos. In the 1990s, the LSND experiment claimed that three neutrinos were not enough to explain their results and introduced a "sterile" [24]. The sterile neutrinos do not participate in weak interactions (and strong and electromagnetic interactions, as all neutrino fields); their only interaction is gravitational. The search for sterile neutrinos is an active area of particle physics, and it is expected that future neutrino oscillation facilities could shed more light on this issue.

Neutrino mass is considered the first manifestation of physics beyond the standard model and one of the major interrogates of neutrino physics. It is the topic of intense experimental and theoretical investigation. Pauli proposed the neutrino mass to be of the order of the electron mass and even massless. Finally, we know now that neutrinos have mass, although only two small values of squared-mass differences are known (this can be better understood looking at neutrino oscillations 1.2). Neutrino mass and mixing are new physics, and there are several models (like leptogenesis [34]) that accommodate but do not explain the results. Moreover, we can only argue what is the most possible.

Helicity

In the late 1950s was shown that parity is violated in weak interactions. Goldhaber observed that neutrinos have an antiparallel spin at their moment (*left-handed*) and antineutrinos have a parallel spin at their moment (*right-handed*) (Figure 1.3). Neutrinos and antineutrinos can be right-handed or left-handed, but all the neutrinos that we have ever seen are, in fact, left-handed, symmetrically, all of the antineutrinos right-handed. So in the SM, only left-handed neutrinos and right-handed antineutrinos interact. The property that characterizes left-handed or right-handed here is called "helicity". The helicity of a particle is defined as the z-component of spin divided by the magnitude of the spin. The helicity is +1 for a right-handed antineutrino, and -1 for a left-handed neutrino since the neutrinos in the SM are considered massless [47].

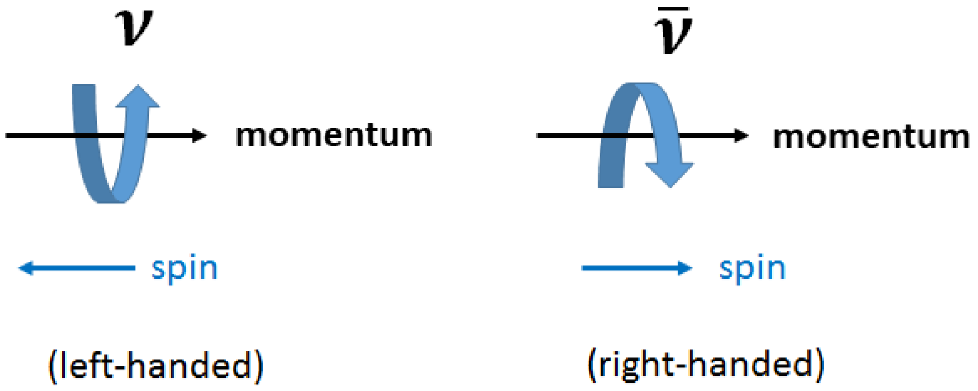

FIGURE 1.3: Neutrino and antineutrino helicity.

1.2 Neutrino oscillations

Physicists considered the neutrino non-massive for a long time. Today we know that this picture is outdated. The experimental evidence of solar [16], atmospheric [42], reactor [38] and accelerator [18] neutrino oscillation led to the conclusion that neutrinos are not massless. Those experiments have obtained non-zero differences of squared neutrino masses and have proven that neutrinos have masses. The mass of the neutrinos constitutes the first experimental evidence of physics beyond the Standard Model. There are alternative models to generate neutrino masses and to extend the Standard Model. There are two groups of models: Some imply the existence of right-handed neutrinos (Dirac mass models), other than the leptonic number non-conservation (Majorana mass models) and some even both, as the most popular explanation of why neutrinos are massive but so light, the so-called see-saw mechanism [58].

A flavor auto-state ($|\nu_l\rangle$) is a quantum superposition of three mass auto-states ($|\nu_\alpha\rangle$) [66, 47]. A neutrino with a specific mass has no specific flavor; a neutrino with a specific flavor has no specific mass.

$$|\nu_l\rangle = \sum_{\alpha=1}^{3} U_{l\alpha} |\nu_\alpha\rangle , \tag{1.6}$$

where $l = e, \mu, \tau$, $\alpha = 1, 2, 3$, $U_{l\alpha}$ is the leptonic mixture matrix, known as the matrix of Pontecorvo-Maki-Nakagawa-Sakata (PMNS) mixture, and is analogous to the Cabibbo-Kobayashi-Maskawa (CKM) matrix which mixes the weak and strong quarks [66, 47].

$$U_{l\alpha} = \begin{pmatrix} U_{e1} & U_{e2} & U_{e3} \\ U_{\mu 1} & U_{\mu 2} & U_{\mu 3} \\ U_{\tau 1} & U_{\tau 2} & U_{\tau 3} \end{pmatrix} . \tag{1.7}$$

The physical parameters of the $N \times N$ leptonic mix matrix can be divided into $[N(N-1)]/2$ mixing angles and $[(N-1)(N-2)]/2$ physical phases. In the case of two-generation mixing ($N = 2$), the mixing matrix only depends on the Cabibbo angle. In the case of three generations ($N = 3$), it depends on three mixing angles (θ_{12}, θ_{23} and θ_{13}) and a physical phase (δ_{CP}) which is called the CP (Charge Parity) transformation violation phase. Experimentally, the violation of the CP transformation was observed in the K^0 and B^0 meson systems. The experimental data is compatible with the hypothesis that the violation of the CP transformation is generated by the physical phase of the mixture matrix [66, 47].

The three-generation leptonic mix matrix describes a rotation of the shape of Figure 1.4. Rewriting each term according to the mixing angles and the physical phase we have:

$$U_{l\alpha} = \begin{pmatrix} c_{12}c_{13} & s_{12}c_{13} & s_{13}e^{-i\delta_{CP}} \\ -s_{12}c_{23} - c_{12}s_{23}s_{13}e^{i\delta_{CP}} & c_{12}c_{23} - s_{12}s_{23}s_{13}e^{i\delta_{CP}} & s_{23}c_{13} \\ s_{12}s_{23} - c_{12}c_{23}s_{13}e^{i\delta_{CP}} & -c_{12}s_{23} - s_{12}c_{23}s_{13}e^{i\delta_{CP}} & c_{23}c_{13} \end{pmatrix} , \tag{1.8}$$

being $c_{ab} \equiv cos\, \theta_{ab}$ and $s_{ab} \equiv sin\, \theta_{ab}$, where $0 \leq \theta_{ab} \leq \pi/2$ and $0 \leq \delta_{CP} \leq 2\pi$ [66, 47].

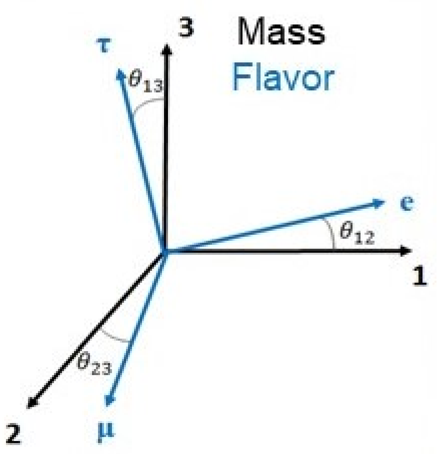

FIGURE 1.4: Rotation of the mass and flavor axes.

Currently, the absolute values of the masses of the neutrinos are still unknown, but the upper limits were measured (Table 1.1). These upper mass limits can and will be constrained even more with the next generation of neutrinos experiments. A maximum limit for the sum of the masses can be obtained by combining data from the cosmic microwave background, the baryonic acoustic oscillations, and the survey of galaxies [66], such small masses are indicative of a new fundamental mass scale, which is not easily explained in the Standard Model [66].

$$m_{tot} = \sum_{\alpha=1}^{3} m_\alpha, \tag{1.9}$$

This m_{tot} is a sum of the neutrino masses. This sum is defined from the effectively stable neutrinos, those with mean lifetimes on cosmological scales. While an upper limit to the matter density of $\Omega_m h^2 < 0.12$ would constrain $m_{tot} < 11eV$, much stronger constraints are obtained from a combination of observations of the Cosmic Microwave Background (CMB) [3].

The discovery of the mass of the neutrino and the leptonic mixture comes from the observation of the fluctuation of the neutrino's flavor (was predicted by Bruno Pontecorvo [60]). Neutrinos can be detected indirectly by identifying the charged particles produced in the weak charged current interactions. The flavor of the neutrino destroyed in a weak charged current interaction corresponds, by definition, to the flavor of the associated charged lepton.

The flavor fluctuation takes place as the neutrino propagates in space-time, with the transition probability determined by the elements of the leptonic mixture matrix, relating the auto-states of flavor, mass, and a sinusoidal dependence in L/E (distance L traveled by the neutrino divided by its energy E) with frequencies established by the differences in eigenvalues of mass [66]. The probability of transition from a ν_l neutrino to a ν_x neutrino can be written as (where $\Delta m^2_{\alpha j} = m^2_\alpha - m^2_j$):

$$\begin{aligned} P(\nu_l \to \nu_x) = \delta_{lx} - 4\sum_{\alpha>j} Re(U^*_{l\alpha}U_{x\alpha}U_{lj}U^*_{xj}) sin^2\left(\frac{\Delta m^2_{\alpha j}L}{4E}\right) \\ + 2\sum_{\alpha>j} Im(U^*_{l\alpha}U_{x\alpha}U_{lj}U^*_{xj}) sin\left(\frac{\Delta m^2_{\alpha j}L}{2E}\right) \end{aligned} \tag{1.10}$$

For the effects of the oscillation to be observable, the phase ($\Delta m^2 \frac{L}{E}$) must be of the order of 1; this means that the characteristic oscillation length ($L_{osc} \sim \frac{E}{\Delta m^2}$) should be similar to the distance between the source and the L detector.

- If $L << L_{osc}$, oscillations do not have time to develop.
- If $L >> L_{osc}$, only the average effect on probability is detectable.

If neutrinos are massless, all $\Delta m^2 = 0$, e $P(\nu_l \to \nu_x) = \delta_{lx}$. Thus, the observation of neutrino oscillations implies that at least one neutrino flavor has a mass different from zero [66]. For just two flavors of neutrinos, the probability of oscillation is simplified:

$$P(\nu_l \to \nu_x) = sin^2 2\theta_{ab}\, sin^2\left(\frac{\Delta m^2 L}{4E}\right) \to sin^2 2\theta_{ab}\, sin^2\left(\frac{\Delta m^2 c^3 L}{4\hbar E}\right), \tag{1.11}$$

with the Planck constant $\hbar$ and the speed of light c inserted in the last expression. When Δm^2 is measured in eV, L in kilometers and E in GeV, the expression becomes:

$$P(\nu_l \rightarrow \nu_x) = sin^2 2\theta_{ab}\, sin^2\left(1,27\,\frac{\Delta m^2 L}{4E}\right). \tag{1.12}$$

One of the main problems is that experiments studying neutrino oscillation can determine the differences of squared neutrino masses but not their values.

$$\Delta m^2{}_{32} = \Delta m^2{}_{atmospheric} \sim 2.4 \times 10^{-3} eV^2, \tag{1.13}$$

$$\Delta m^2{}_{21} = \Delta m^2{}_{solar} \sim 7.6 \times 10^{-5} eV^2, \tag{1.14}$$

Two observed squared neutrino masses differences are determined from atmospheric/accelerator and solar/reactor neutrino experiments, respectively.

We know that there is a large and a small Δm^2 and that m_2 is heavier than m_1 (from matter effects) [57]. We don't know if m_3 is heavier or lighter than m_1 and m_2 or the absolute mass scale. The latter question is known as the "neutrino mass hierarchy problem" (Figure 1.5). The absolute mass values (m_1, m_2, and m_3), and the question of whether the mass hierarchy is normal or inverted, remain unknown. Normal hierarchy is said to be when $m_1 < m_2 < m_3$ and inverted when $m_3 < m_1 < m_2$. Current data results can reject the wrong hierarchy for more than 20% of all possible values of yet unknown CP-violating phase δ_{CP} [57]. This effect has deep connections to efforts to determine whether or not the neutrino is its own antiparticle and provides essential information about the number and types of isotopes produced in supernovae and the particle/antiparticle asymmetry problem.

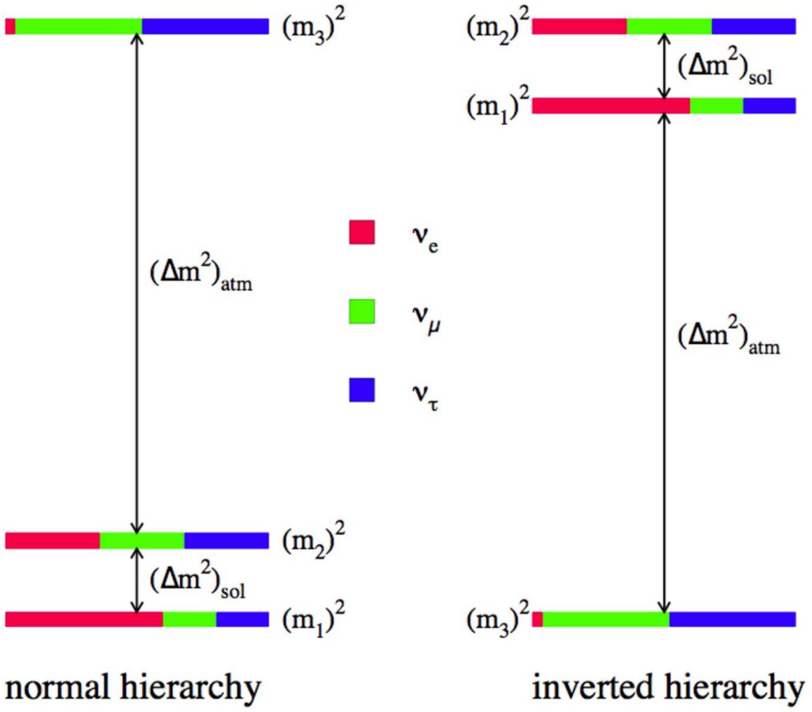

FIGURE 1.5: Neutrino mass hierarchy. Though the value of the individual masses m_1, m_2 and m_3 are unknown, there are two possible orderings [4].

There are two methods to determine neutrino oscillations:

- **Appearance mode:** These experiments are focused on the search for a new neutrino flavor, absent in the original beam, or an enhancement of neutrinos of a given flavor in the initial beam.
- **Disappearance mode:** It is based on the reduction of the expected number of a particular neutrino flavor at the detector. This method requires an accurate understanding of the neutrino beam at the source.

In the presence of matter, this vacuum oscillation scheme becomes more complicated [65]. Under certain conditions, an almost complete flavor inversion is possible, known as the Mikheyev-Smirnov-Wolfenstein effect (MSW effect). Those matter effects can be crucial.

The equations for the probability of ν_e ($\bar{\nu}_e$) appearance and the probability of ν_μ, $\bar{\nu}_\mu$ disappearance in matter:

$$\begin{aligned} P(\nu_\mu \to \nu_e) \approx\ & \frac{1}{(A_{32}-1)^2}\, sin^2 2\theta_{13}\, sin^2\theta_{23}\, sin^2[(A_{32}-1)\hat{\Delta}_{32}] \\ & \mp \frac{\alpha}{A_{32}\,(1-A_{32})}\, cos\theta_{13}\, sin2\theta_{12}\, sin2\theta_{23}\, sin2\theta_{13} \\ & \times sin\delta_{CP}\, sin\hat{\Delta}_{32}\, sinA_{32}\hat{\Delta}_{32}\, sin[(1-A_{32})\hat{\Delta}_{32}] \\ & + \frac{\alpha}{A_{32}\,(1-A_{32})}\, cos\theta_{13}\, sin2\theta_{12}\, sin2\theta_{23}\, sin2\theta_{13} \\ & \times cos\delta_{CP}\, cos\hat{\Delta}_{32}\, sinA_{32}\hat{\Delta}_{32}\, sin[(1-A_{32})\hat{\Delta}_{32}] \\ & + \frac{\alpha^2}{{A_{32}}^2}\, cos^2\theta_{23}\, sin^2 2\theta_{12}\, sin^2 A_{32}\hat{\Delta}_{32} \end{aligned} \tag{1.15}$$

$$P(\nu_\mu \to \nu_\mu) \approx 1 - (cos^4 2\theta_{13}\, sin^2 2\theta_{23} + sin^2 2\theta_{13}\, sin^2\theta_{23})\, sin^2\hat{\Delta}_{31}, \tag{1.16}$$

$$\alpha = \frac{\Delta {m^2}_{21}}{\Delta {m^2}_{32}} << 1, \tag{1.17}$$

$$\hat{\Delta}_{ji} = \frac{\Delta {m^2}_{ji}\, L}{4\, E_\nu}, \tag{1.18}$$

$$A_{ji} = 2\sqrt{2}\, G_F\, n_e\, \frac{E_\nu}{\Delta {m^2}_{ji}}, \tag{1.19}$$

were $G_F = 1.16637 \times 10^{-5}\, GeV^{-2}$ is the Fermi coupling constant and n_e is the electron density of the matter [41]. Neutrino sources employed in oscillation experiments are diverse, going from nuclear reactors ($\bar{\nu}_e$), atmospheric ($\nu_e, \bar{\nu}_e, \nu_\mu, \bar{\nu}_\mu$), solar ($\nu_e$) and accelerators ($\nu_e, \bar{\nu}_e, \nu_\mu, \bar{\nu}_\mu$).

Using the ν_e ($\bar{\nu}_e$) appearance we can measure the δ_{CP}. Recently was published a measurement using this long-baseline neutrino and antineutrino oscillations observed by the T2K experiment were they reported a large increase in the neutrino oscillation probability, excluding values of δ_{CP} that result in a large increase in the observed antineutrino oscillation probability. These results indicate CP violation in leptons, and future measurements with larger data sets will test whether leptonic CP violation is larger than the CP violation in quarks [12].

1.3 Neutrino sources

There are different sources of neutrinos (Figure 1.6). They can be generated on Earth or come from space. Most neutrinos that reach the Earth are produced by the Sun (solar neutrinos). They are the product of the decay of other particles, as those neutrinos generated by reactions of the subatomic particles in the outer layers of the atmosphere. Neutrinos are also created in large numbers in supernovae (supernova neutrinos), and others come directly from the Big Bang (relic neutrinos). We also have neutrinos from reactors and accelerators.

The phenomenon of neutrino oscillation provides us with a revolutionary and straightforward solution to the so-called ”atmospheric neutrinos anomaly” and ”solar neutrinos anomaly” however, this idea required experimental confirmation. The group of atmospheric neutrinos was led by Takaaki Kajita in the Super-Kamiokande experiment, which in 1998 announced its result, thus confirming the oscillation of atmospheric neutrinos. In this way, the atmospheric and solar neutrinos anomalies were solved [66].

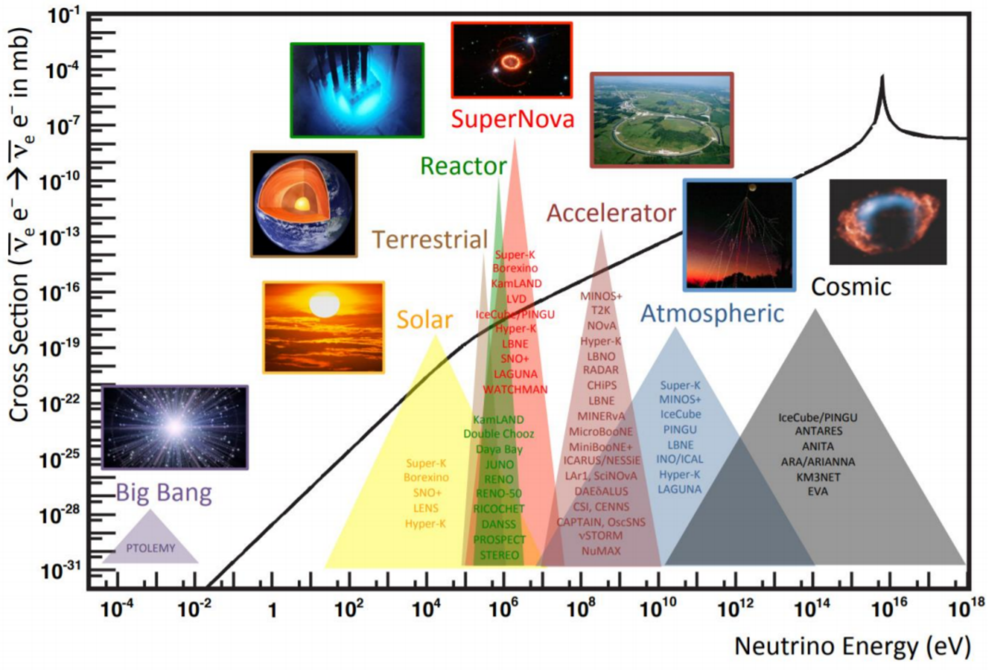

FIGURE 1.6: Various sources of neutrinos depending on the incident neutrino energy. The shock section for electroweak scattering $\bar{\nu}_e + e^- \rightarrow \bar{\nu}_e + e^-$ in free electrons as a function of energy neutrino (for a massless neutrino) is shown for comparison [40].

1.3.1 Solar neutrinos

The Sun is a powerful source of electron neutrinos produced in the thermonuclear fusion reactions in the solar core. The solar neutrino flux on the Earth is about $6 \times 10^{10} cm^{-2} s^{-1}$. The interpretation of the measurements of solar neutrinos requires a substantial understanding of solar physics and nuclear physics, involved in a complex chain of reactions that together are called the Standard Solar Model (SSM). The low energy range for solar neutrinos is from $\sim 10 eV$ to $\sim 15 MeV$.

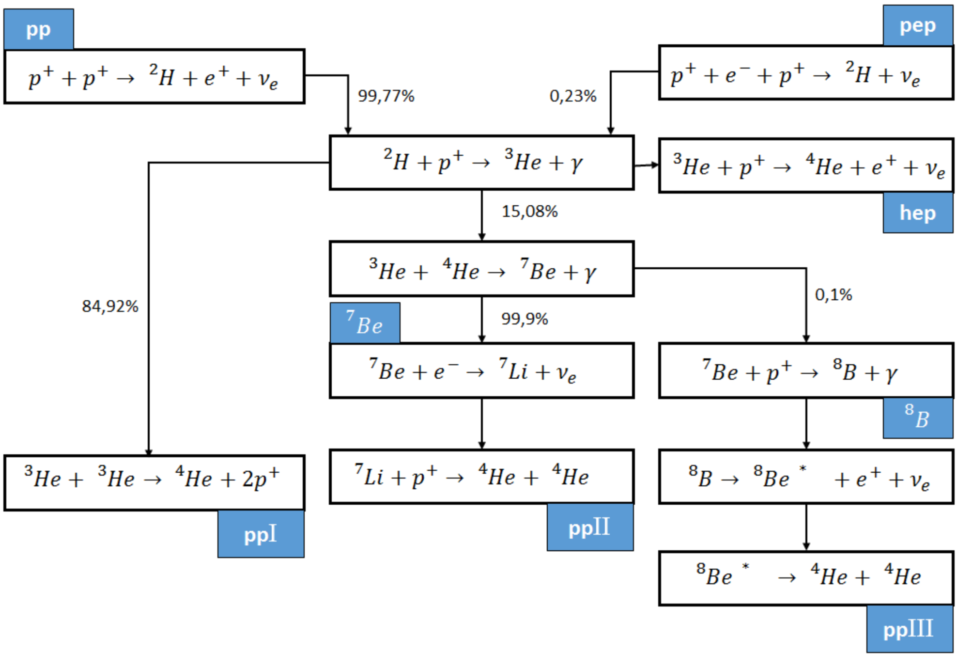

FIGURE 1.7: Solar neutrino reactions chain [69].

In Figure 1.7 we present in schematic form the set of nuclear reactions present in the SMM. The percentage of the probability of the reaction happening and going to the following process is indicated. The flow of solar neutrinos predicted by the SSM as a function of energy is shown in Figure 1.8.

The experiments with solar neutrinos calculate the quotient:

$$R_{solar} = \frac{N_{obs}}{N_{th}}, \tag{1.20}$$

where N_{obs} corresponds to the number of neutrino interactions detected and N_{th} to the number of theoretical neutrino interactions, based on SSM, using the Monte Carlo simulation. Was expected $R_{solar} = 1$.

Solar neutrino anomaly

The solar neutrino problem concerned a large discrepancy between the number of neutrino interactions detected and the expected number of theoretical neutrino interactions. This problem was resolved around 2002. The flow of solar neutrinos is reduced due to fluctuations in flavor. Ray Davis[1] observed a significant deficit of solar neutrinos in 1968, using ^{37}Cl (Chlorine radiochemical experiment) at the Homestake mines in South Dakota, United States of America [22].

---

[1] together with the Brokehaven collaborators

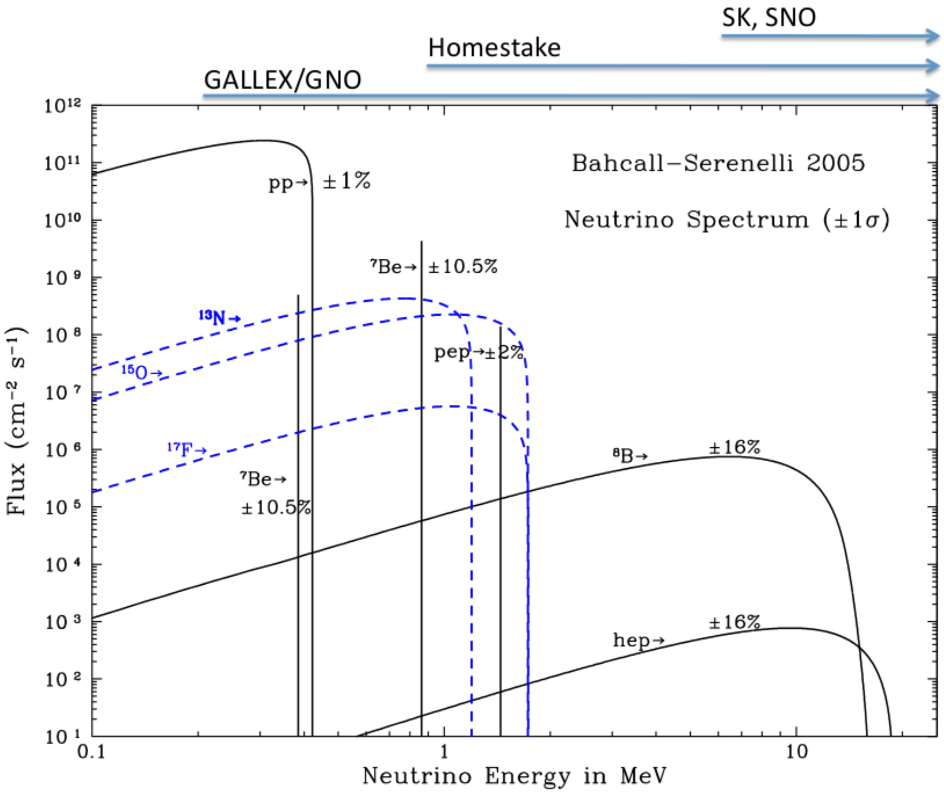

FIGURE 1.8: Energy distributions of the solar neutrino flux predicted by the SSM. The energy ranges associated with the various experiments are indicated at the top of the figure [66].

To see if neutrino oscillation could explain the solar neutrino deficit, Arthur B. McDonald conducted an experiment installed in a deep mine in the Canadian city of Sudbury. This experiment was called SNO (Sudbury Neutrino Observatory) [68]. SNO was designed to detect the three flavors of neutrinos so that the oscillation of solar neutrinos would not affect the result. SNO detected:

- **Charged current interaction:** The neutrino is absorbed in the reaction, and an electron is produced. Only electron neutrinos can participate in this reaction because the solar neutrinos have energies smaller than the mass of muons and tau.

- **Neutral current interaction:** The neutrino break the deuteron into neutron and proton and continues with slightly less energy. All three neutrinos are equally likely to participate in this interaction.

- **Electron elastic scattering:** The neutrino collides with an electron in the atom and transfer some of its energy to the electron. All three neutrinos can interact true this channel through neutral current, and electron neutrinos can also interact through charged current.

Because the Sun only emits electron neutrinos, the detection of muonic or tau neutrinos would confirm the oscillation phenomenon [66]. So it is clear that that one was the first real sign of neutrino oscillation.

1.3.2 Atmospheric neutrinos

The neutrinos generated by interactions of protons (p) of cosmic rays with nucleus (^{A}X) in the top of the Earth's atmosphere (Figure 1.9) are called atmospheric neutrinos. In these reactions we have formation of pions ($\pi^{\pm}$) or kaons ($K^{\pm}$) that will decay into muons ($\mu^{\pm}$) and muonic neutrinos or antineutrinos (ν_{μ} ou $\bar{\nu}_{\mu}$).

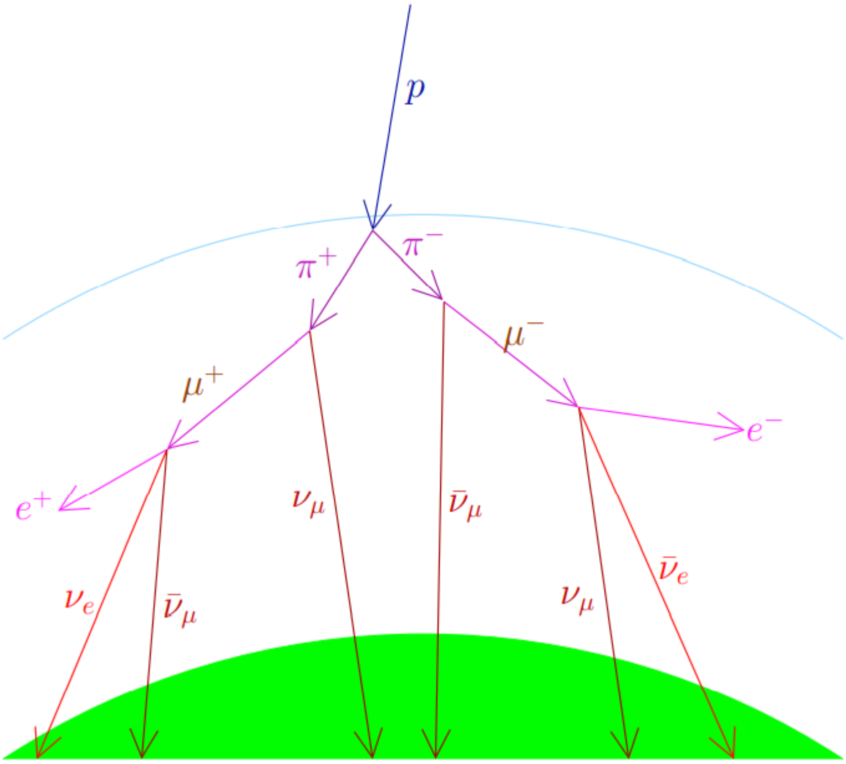

FIGURE 1.9: Schematic view of neutrino production by cosmic-ray proton interactions in the atmosphere, with generation of pions and muons [47].

Where muons can decay into electrons (e^{-}) or positrons (e^{+}) and electron neutrino or antineutrino (ν_{e} or $\bar{\nu}_{e}$) plus antineutrino electrons or muonic neutrino ($\bar{\nu}_{\mu}$ ou ν_{μ}). The energy range for atmospheric neutrinos is from $\sim 10GeV$ to $\sim 100TeV$.

$$\begin{aligned} p +^{A} X \rightarrow \pi^{\pm} + {}^{A}X^{'}, \\ \searrow K^{\pm} + {}^{A}X^{'}, \\ \pi^{\pm} \rightarrow \mu^{\pm} + \nu_{\mu}(\bar{\nu}_{\mu}), \\ K^{\pm} \rightarrow \mu^{\pm} + \nu_{\mu}(\bar{\nu}_{\mu}), \\ \mu^{\pm} \rightarrow e^{\pm} + \nu_{e}(\bar{\nu}_{e}) + \bar{\nu}_{\mu}(\nu_{\mu}). \end{aligned}$$

The experiments to observe atmospheric neutrinos are designed underground to dampen the effects of cosmic rays and other sources of stellar background. They can be detected by directly observing their charged current interaction within the detector.

Atmospheric neutrino anomaly

The atmospheric neutrino anomaly is the discrepancy between the observed and expected number of electron and muon neutrino interactions in underground detectors.

$$R_{atm} = \frac{N_{obs}^{\nu_{e,\mu}}}{N_{th}^{\nu_{e,\mu}}}, \tag{1.21}$$

where $N_{obs}^{\nu_{e,\mu}}$ corresponds to the number of electron and muon neutrino interactions detected and $N_{th}^{\nu_{e,\mu}}$ to the number of theoretical electron and muon neutrino interactions.

1.3.3 Reactor neutrinos

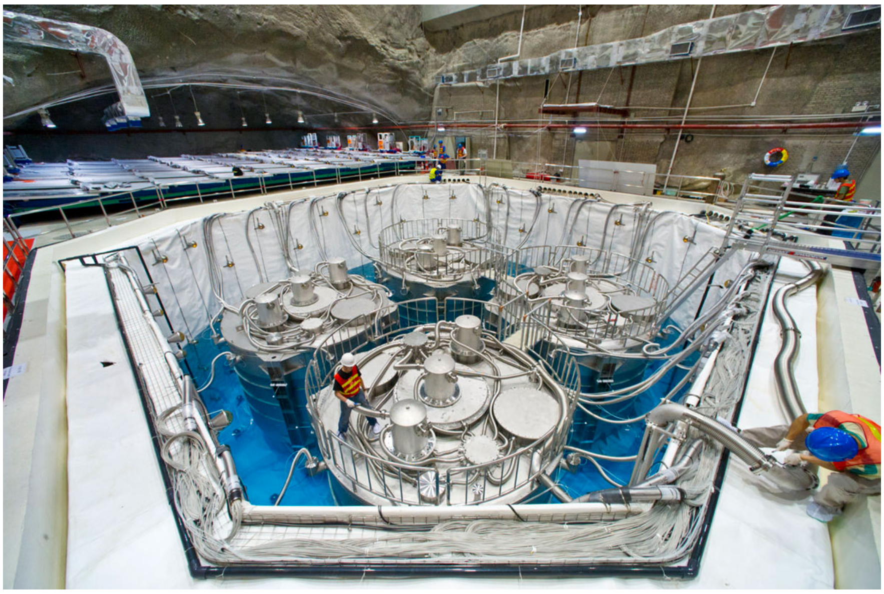

FIGURE 1.10: The Daya Bay Neutrino Experiment added water into the pool holding the four antineutrino detectors in 2012 [5].

Nuclear reactors are very intense sources of neutrinos that have been used all along the neutrino's history, from its discovery up to the most recent oscillation studies. Nuclear reactors isotropically produce $\bar{\nu}_e$ in the β decay of neutron-rich radioactive materials in nuclear power plants. The standard detection process for reactor neutrinos occurs through the reverse β decay (where n is the neutron) $\bar{\nu}_e + p \rightarrow n + e^+$. There are some experiments in nuclear plants like CHOOZ or CHOOZ 2 (Ardennes, France) [37] and San Onofre (in the Bugey reactor) [64]. The energy range for reactor neutrinos is from $\sim 0.1 MeV$ to $\sim 10 MeV$. Figure 1.10 shows the Daya Bay Reactor Neutrino Experiment, located in Daya Bay, China, and designed to measure the mixing angle θ_{13} using antineutrinos produced by reactors.

1.3.4 Accelerator neutrinos

Accelerator neutrinos are produced by artificial sources by scattering particles over a specific target. The energy range for accelerator neutrinos is from $\sim 10 MeV$ to

$\sim 10GeV$. The process for obtaining a neutrino beam from accelerators is as follows (Figure 1.11):

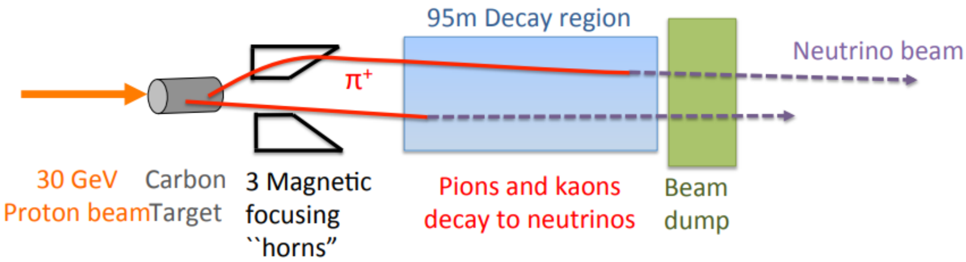

FIGURE 1.11: Accelerator neutrino flux production.

- Incident primary protons extracted from an accelerator complex collide with a light target (such as Beryllium, Carbon, and Aluminum). The incident primary proton energies vary, from $8GeV$ up to $450GeV$ [46].
- The secondary particles (mainly pions) produced by the interactions are focused on by electromagnetic horns. These devices produce a toroidal magnetic field; this results in a checkmark that focuses on π^+ and de-focusing π^-, or vice versa [46].
- The focused secondary particles enter a decay region to produce neutrinos. The main mode of decay when focusing on π^+ is $\pi^+ \to \mu^+ + \nu_\mu$, resulting in a beam mainly composed of ν_μ. However, there are also contributions from the decay of kaons produced on the target ($K_{\mu 2}$, $K_{\mu 3}$, K_{e3}) that give rise to higher energy neutrinos and ν_e in the beam. Muons, (resulting from the decay of the pions) decay in the form of $\mu^+ \to e^+ + \bar{\nu}_\mu + \nu_e$ to give an additional source of ν_e and of $\bar{\nu}_\mu$ along with the $\pi^- \to \mu^- + \bar{\nu}_\mu$ de-focusing π^-, which reach the decay region. A beam mainly composed of $\bar{\nu}_\mu$ can be produced by inverting the polarity of the electromagnets [46].

In the case of the T2K beam, it will be explained in more detail in Chapter 3.

Chapter 2

Neutrino interactions

Some fundamental elements of the theoretical foundation are described in this chapter. We will provide a general discussion of the neutrino cross section and the neutrino/antineutrino interactions with the nucleon and the nucleus. We will be doing emphasis on interactions via Charge Current (CC).

2.1 Notation

Theoretical formalism with the quantities that describe the kinematics of the neutrino interaction is found in Figure 2.1.

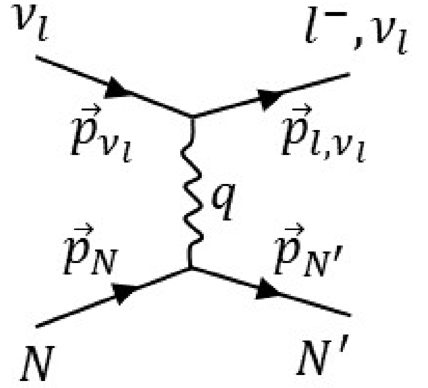

FIGURE 2.1: Diagram of two bodies scattering, between an incident neutrino and a nucleon.

- Incoming neutrino ν_l:
  - 4-moment: $p_\nu = (E_\nu, \vec{p_\nu})$
  - mass: 0
- Incoming nucleon N:
  - 4-moment: $p_N = (E_N, \vec{p_N})$
  - mass: m_N
- Boson exchanged W ou Z:
  - 4-moment: $q = (E_q, \vec{q})$
- Outgoing lepton l ou ν_l:
  - 4-moment: $p_l = (E_l, \vec{p_l})$
  - mass: m_l
- Outgoing hadron N':
  - 4-moment: $p_{N'} = (E_{N'}, \vec{p_{N'}})$
  - mass: $m_{N'}$

Mandelstam variables (Lorentz invariant) for two bodies scattering between an incident neutrino and a nucleon are defined as:

$$s = (p_\nu + p_N)^2 = (p_l + p_{N'})^2, \tag{2.1}$$

$$t = -q^2 = Q^2 = (p_\nu - p_l)^2 = (p_N - p_{N'})^2, \tag{2.2}$$

$$u = (p_\nu - p_{N'})^2 = (p_N - p_l)^2, \tag{2.3}$$

where s is the energy of the center of mass and $Q^2 = -q^2$ is the moment transferred.

2.2 Neutrino-nucleon scattering

Neutrino-nucleon interactions are described, with good precision, by the SM, although the standard model works with massless neutrinos [47].

2.2.1 cross section

The cross section measures the probability that a particular reaction takes place, and can be calculated if the basic interaction between the particles. If F is the flow of particles striking a target (number of incident particles per unit area and unit time), the differential cross section is:

$$\sigma = \frac{d\sigma}{d\Omega}(E, \Omega) = \frac{1}{F}\frac{dN_s}{d\Omega} \tag{2.4}$$

were $\frac{dN_s}{d\Omega}$ is the number of scattered particles in the solid angle $d\Omega$ per unit time. The differential cross section has dimensions of area (geometric section of target intercepted by the beam flux). In general, $d\sigma$ varies with the energy of the beam flux and with the angle of scattering.

In the real situation the target is a large object with many nucleons. In ν experiments, a common configuration assumes the target at rest. If N_t is the target density within a certain volume, and N_s is the number of incoming particles that are scattered, the cross section is:

$$\sigma = \frac{N_s}{\phi N_t}, \tag{2.5}$$

The general expression of the differential cross section for the collision of two particles ($i = 1, 2$) and N outgoing particles ($f = 1, ..., N$) is given as [47]:

$$d\sigma = (2\pi)^4\, \delta^4 \left(\sum_f p'_f \sum_i p_i\right) \frac{1}{4[(p_1 * p_2)^2 - m_1^2\, m_2^2]^{1/2}} \left(\Pi_f \frac{d^3 p'_f}{(2\pi)^3\, 2E'_f}\right) |\mathcal{M}|^2 \tag{2.6}$$

The amplitude $\mathcal{M}$ is the invariant matrix element for the process under consideration. For particles with non-zero spin, unpolarized cross sections are calculated by averaging over initial spin components and summing over final. There is no averaging over initial neutrino helicity for the neutrinos since they occur only left-handed. However, for convenience of calculation, one can formally sum over both helicity states, the factor $(1 - \gamma_5)$ guarantees that right-handed neutrinos do not contribute to the cross section.

The spin averaged matrix element squared is then given by:

$$|\mathcal{M}|^2 = \frac{G_F^2}{2} L_{\alpha\beta} W^{\alpha\beta} \tag{2.7}$$

were G_F^2 is the Fermi coupling constant, $L_{\alpha\beta}$ is the leptonic tensor, and $W^{\alpha\beta}$ is the hadronic tensor. They are

$$L_{\alpha\beta} = L^S_{\alpha\beta} \pm iL^A_{\alpha\beta} \tag{2.8}$$

$$W^{\alpha\beta} = W^{\alpha\beta}_S + iW^{\alpha\beta}_A \tag{2.9}$$

with $W^{\alpha\beta}_{S(A)}$ being real symmetric (antisymmetric) tensor. The cross section follows Eq. 2.6:

$$\frac{d^2\sigma}{d\Omega dE_l} = \frac{d^2\sigma}{d\cos\theta_l \, d\phi \, dE_l} = \frac{G_F^2}{4\pi^2}\frac{|\vec{k}|}{|\vec{k'}|}L_{\alpha\beta}W^{\alpha\beta} \tag{2.10}$$

We also need the differential cross section in terms of the hadronic invariant mass W and the squared momentum transfer $Q2 = -q^2$, which equals the Mandelstam variable t (equations 2.1). The total cross section for a given incident neutrino energy is then given by:

$$\sigma(E_\nu) = \int_{W_{min}}^{W_{max}} dW \int_{Q^2_{min}}^{Q^2_{max}} dQ^2 \, \frac{d\sigma}{dQ^2 dW} \tag{2.11}$$

with $s = m_N^2 + 2m_N E_\nu$, $W_{min} = m_{N'}$, and $W_{max} = \sqrt{s} - m_l$.

$$\begin{aligned} Q^2_{min} &= -m_l^2 + 2E_\nu(E_l - |\vec{k}'|) \\ &= \frac{2m_N E_\nu^2 - m_N m_l - m_l^2 E_\nu - E_\nu\sqrt{(s-m_l^2)^2 - 2(s+m_l^2)m_N^2 + m_N^4}}{2E_\nu + m_N}, \end{aligned} \tag{2.12}$$

$$\begin{aligned} Q^2_{max} &= -m_l^2 + 2E_\nu(E_l - |\vec{k}'|) \\ &= \frac{2m_N E_\nu^2 - m_N m_l + m_l^2 E_\nu + E_\nu\sqrt{(s-m_l^2)^2 - 2(s+m_l^2)m_N^2 + m_N^4}}{2E_\nu + m_N} \end{aligned} \tag{2.13}$$

2.2.2 Decomposition of the cross section

The interactions of neutrinos can be separated into interactions of charged current (CC) and neutral current (NC). The total cross section is written as:

$$\sigma_t = \sigma^{(CC)} + \sigma^{(NC)}, \tag{2.14}$$

being σ_t the total cross section, $\sigma^{(CC)}$ the cross section for CC and $\sigma^{(NC)}$ the cross section for NC. In the charged current, the incident neutrino/antineutrino interacts through a $W^\pm$ boson, changing its identity but not its flavor. Whereas, in the neutral current, the incident neutrino or antineutrino interacts through a boson Z^0, maintaining its identity and without changing its flavor. For each of the currents, we have three associated channels: the quasi-elastic (QE), the production of resonance (RES), the deep inelastic scattering (DIS). Below we detail each of them.

In Figure 2.2 we have the graph of the neutrino and antineutrino cross section - nucleon divided by neutrino energy and plotted as a function of the incident neutrino energy for the charge current interactions. The experimental data are from: NOMAD

[55], MiniBooNE [15], NOMAD [55], ANL(Argonne National Laboratory) [35], ANL [26], GGM [54], BEBC [21], ANL [36], FNAL [52], Baker [25], Serpukov [28], and SKAT [31]. The curves shown were obtained from the NUANCE event generator [33].

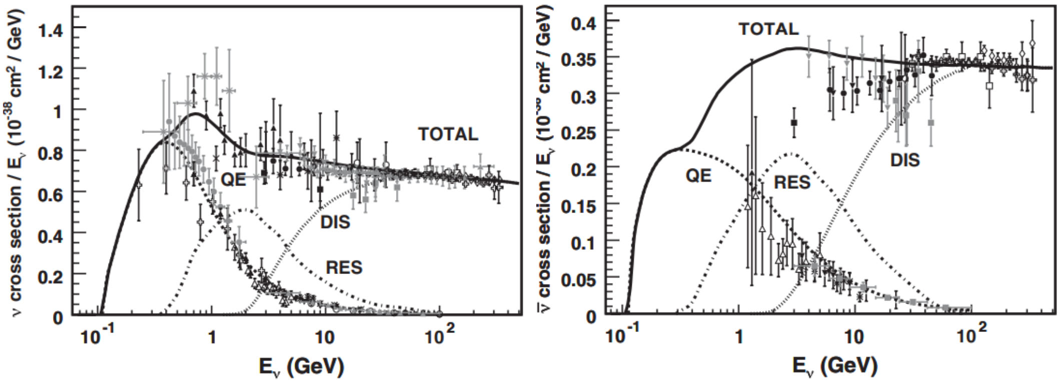

FIGURE 2.2: Neutrino and antineutrino cross section as a function of neutrino and antineutrino energies for Charge Current interactions decomposed into different contributions: QE, RES, DIS.

2.2.3 Elastic and quasi-elastic process

The scattering of a neutrino with a nucleon can be quasi-elastic where the identity changes from the neutrino to the charged lepton (Table 1.1) corresponding (charged current) or elastic where the neutrino identity is maintained (neutral current). For energies of $E_\nu \approx 2\, GeV$ This is the most important reaction (Figure 2.3).

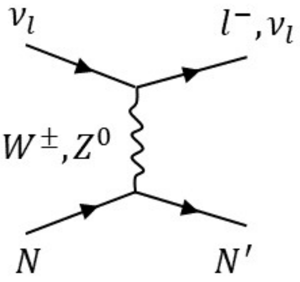

FIGURE 2.3: Feynman diagrams for quasi elastic scattering.

$$\begin{aligned} CCQE: \nu_l + N &\rightarrow l^- + N', \\ \bar{\nu}_l + N &\rightarrow l^+ + N', \\ NCE: \nu_l + N &\rightarrow \nu_l + N, \\ \bar{\nu}_l + N &\rightarrow \bar{\nu}_l + N. \end{aligned}$$

Differential cross section and form factors

The differential cross section for QE is given by:

$$\frac{d^2\sigma}{dQ^2} = \frac{m_N^2 G_F^2 \, cos^2\theta_c}{8\pi E_\nu} \left[A \mp \frac{(s-u)}{m_N^2} B + \frac{(s-u)^2}{m_N^4} C \right] \tag{2.15}$$

and A, B, and C are defined as the following function of various nucleon form factors that are functions of Q^2, the square of the four-momentum transferred from the incoming neutrino to the nucleon:

$$A = \frac{m_l^2 + Q^2}{m_N^2}\Bigg[(1+\tau)F_A^2 - (1-\tau)(F_1^V)^2 + \tau(1-\tau)(F_2^V)^2 + 4\tau F_1^V F_2^V - \frac{m_l^2}{4m_N^2}\left((F_1^V + F_2^V)^2 + (F_A + 2F_P)^2 - (\frac{Q^2}{m_N^2} + 4)F_p^2\right)\Bigg] \tag{2.16}$$

$$B = \frac{Q^2}{m_N^2} F_A(F_1^V + F_2^V) \tag{2.17}$$

$$C = \frac{1}{4}(F_A^2 + (F_1^V)^2 + \tau(F_2^V)^2) \tag{2.18}$$

$$s - u = 4m_N E_\nu - Q^2 - m_l^2 \tag{2.19}$$

$$\tau = \frac{Q^2}{4m_N^2} \tag{2.20}$$

Neutrino and antineutrino scattering differ by the sign in front of the B term. The cross section is valid for all flavors dependent on the lepton mass m_l. Note that F_P is multiplied by m_l^2/m_N^2 so its contribution is negligible for ν_μ and ν_e, but becomes important for ν_τ.

The cross section is given in terms of four unknown form factors F_1^V and F_2^V that are vector form factors, F_A is the axial form factor, and F_P is the pseudoscalar form factors. The vector form factors can be related to electron scattering form factors by assuming Conserved Vector Current Hypothesis (CVC), we get:

$$F_1^V(Q^2) = \frac{(G_E^p(Q^2) - G_E^n(Q^2)) + \frac{Q^2}{4m_N^2}(G_M^p(Q^2) - G_M^n(Q^2))}{1 + \frac{Q^2}{4m_N^2}} \tag{2.21}$$

$$F_2^V(Q^2) = \frac{(G_M^p(Q^2) - G_M^n(Q^2)) - (G_E^p(Q^2) - G_E^n(Q^2))}{1 + \frac{Q^2}{4m_N^2}} \tag{2.22}$$

G_M and G_E are the nucleon's magnetic and electric form factors, respectively. Having related the vector form factors to electron scattering, we shall look at the axial and the pseudoscalar form factors. They can be related by:

$$F_P(Q^2) = \frac{2m_N^2}{Q^2 + m_\pi^2} F_A(Q^2) \tag{2.23}$$

and by applying a dipole form for the axial form factor:

$$F_A(Q^2) = \frac{g_A}{\left(1 + \frac{Q^2}{M_A^2}\right)^2}, \tag{2.24}$$

where g_A is the axial vector constant and M_A is the axial mass.

2.2.4 Resonance pion production

Neutrinos can excite the target nucleon to a state of resonance (R) where the resulting baryonic resonance (Δ, N^*) decays in a variety of possible final states, producing combinations of nucleons and mesons. The resonance production (Figure 2.4) is dominated by the resonance $\Delta(1232)$ [29]. Resonance production is typically described in neutrino interaction simulations using the Rein-Seghal model.

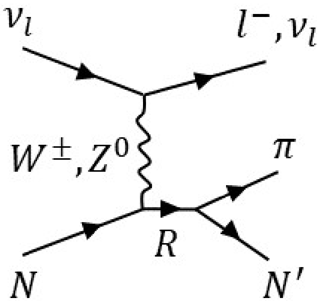

FIGURE 2.4: Feynman diagrams for resonance pion production.

$$\begin{aligned} CCRES: \nu_l + N &\rightarrow l^- + R, \\ \bar{\nu_l} + N &\rightarrow l^+ + R, \\ NCRES: \nu_l + N &\rightarrow \nu_l + R, \\ \bar{\nu_l} + N &\rightarrow \bar{\nu_l} + R. \end{aligned}$$

Differential cross section and form factors

The differential cross section for the CCRES process is calculated to be:

$$\frac{d^2\sigma}{dQ^2 dW} = \frac{G_F^2 \, cos^2\theta_c}{16\pi} \frac{W}{(s - m_N^2)^2} \delta(W^2 - m_\Delta^2) L_{\alpha\beta} W^{\alpha\beta} \tag{2.25}$$

where θ_c is the Cabibbo angle[1] and m_Δ is the mass of the Δ. The Δ width (Γ) is accounted for in the cross section by replacing $\delta(W^2 - m_\Delta^2)$ with:

$$\delta(W^2 - m_\Delta^2) \rightarrow \frac{1}{\pi} W \frac{\Gamma}{(W^2 - m_\Delta^2)^2 + W^2\Gamma^2} \tag{2.26}$$

Up to the present day different authors use different vector and axial-vector transition form factors $C_i^{V,A}$ with $i = 3, \cdots, 6$. The two more common approaches are the parametrization of the neutrino scattering data with phenomenological form factors and calculating those form factors within quark models.

2.2.5 Deep inelastic scattering

Given enough energy, the neutrino can arrange the individual quarks of the nucleon; this is called deep inelastic scattering (DIS) and is manifested in the creation of a hadronic shower. The contribution of DIS (Figure 2.5) is vital for higher energies as it increases in proportion to the energy. Deep inelastic scattering neutrino interactions are typically modeled with the Rein-Seghal coherent model.

---

[1] the Cabibbo angle is related to the relative probability that down and strange quarks decay into up quarks.

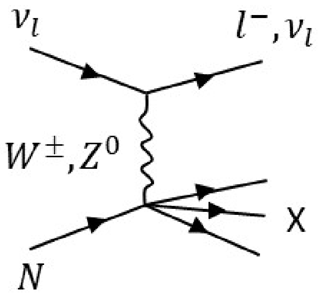

FIGURE 2.5: Feynman diagrams for deep inelastic scattering.

$$\begin{aligned} CCDIS: \nu_l + N &\rightarrow l^- + X, \\ \bar{\nu}_l + N &\rightarrow l^+ + X, \\ NCDIS: \nu_l + N &\rightarrow \nu_l + X, \\ \bar{\nu}_l + N &\rightarrow \bar{\nu}_l + X. \end{aligned}$$

2.3 Neutrino-nucleus scattering

The treatment of the scattering of neutrinos in the nuclear environment is more complex. The neutrino interacts with a single nucleon, and then the intranuclear cascade starts, but the impact area should usually include many nucleons. The processes involve effects of the Fermi momentum, the spectral function (SF), the nuclear structure, and the final state interactions (FSI) (Figure 2.6).

$$\nu_l + {}^{A}X \rightarrow l^- + {}^{A}X', \\ \bar{\nu}_l + {}^{A}X \rightarrow l^+ + {}^{A}X'.$$

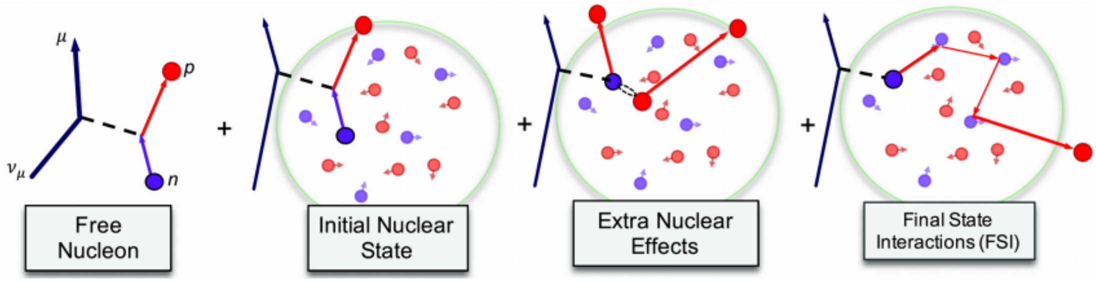

FIGURE 2.6: The processes involve effects of the Fermi momentum, the nuclear structure, and the final state interactions (FSI).

In the experiments, the cross section is calculated on the nucleus, which is divided by the number of nucleons giving a rough approximation of the cross section in the nucleon.

2.3.1 2p2h

The 2p-2h MEC process takes place when a weak or electromagnetic boson from the leptonic current is exchanged by a pair of nucleons (2-body current), leading to the emission of two nucleons from the primary vertex (Figure 2.7). These states, where two nucleons are promoted above the Fermi level leaving two holes inside the Fermi sea, contribute significantly to the so-called "dip region". They correspond to excitation energies between the quasi-elastic (QE) and resonant (RES) excitation peaks.

These contributions are essential for a correct interpretation of current and forthcoming neutrino oscillation experiments. They strongly rely on our understanding of neutrino-nucleus scattering at intermediate energies (from 0.5 to 10 GeV) and the nuclear-structure effects involved. The impacts of 2p-2h are taken into account in the RFG-based descriptions provided by Martini and Nieves [47].

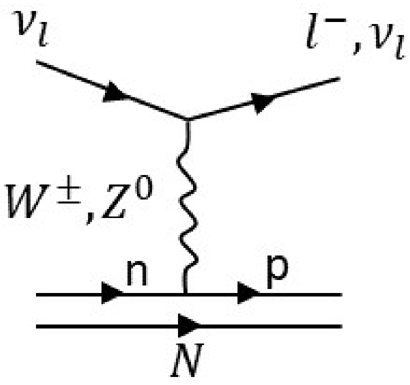

FIGURE 2.7: Feynman diagrams for 2p2h.

2.3.2 Final state interactions (FSI)

The FSI describes the propagation of particles created in a primary neutrino interaction through the nucleus (Figure 2.9). All MC generators (but GIBUU) use the intranuclear cascade model. The primary interaction on the neutrino event generator gives the interaction mode (Figure 2.8 top), once the interaction mode has been chosen, the neutrino event generators code moves on to dynamics (intranuclear cascade).

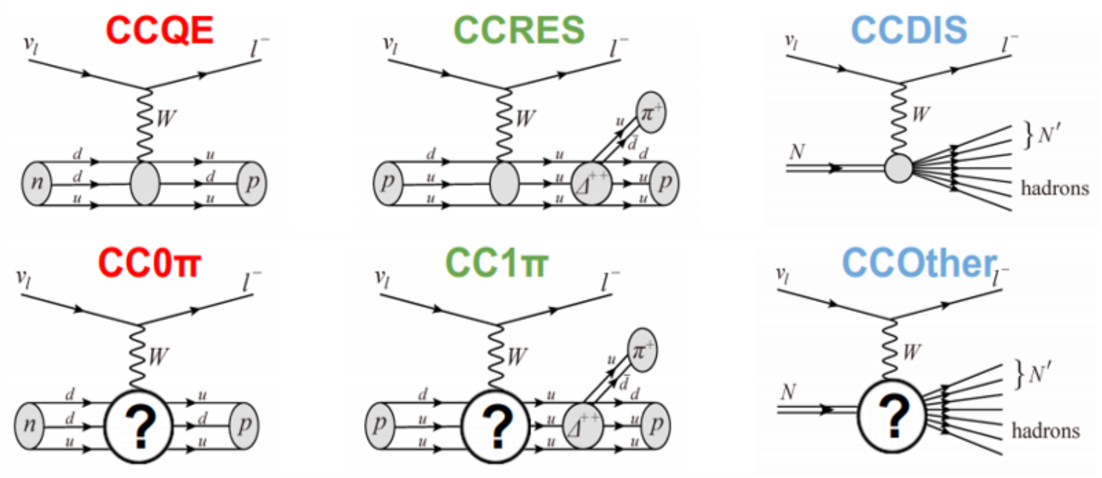

FIGURE 2.8: Interaction modes (top) and interaction topologies (bottom).

After the intranuclear cascade, we obtain the interaction topologies (Figure 2.8 bottom) that are the interaction modes after being affected by the nuclear environment.

Pions or nucleons can re-interact within the nuclear medium before leaving the nucleus changing the outgoing particle content or kinematics in the final state. The interaction topologies are defined based on the multiplicity of outgoing pions.

The FSI of hadrons within the nuclear medium is also simulated using a microscopic cascade model. In the case of final state pions, the considered processes are inelastic scattering, pion absorption, and charge exchange. The simulated nucleon interactions are elastic scattering and single Δ production. FSI interactions alter both the multiplicity of pions in the final state and the kinematics of the pions.

2.3.3 Neutrino event generators

Neutrino event generators are irreplaceable tools in high-energy physics, employed to make preliminary studies successfully, detector design and optimization, data analysis, and systematic error evaluation. Monte Carlo event generators connect experiment and theory. There are several neutrino event generators, and they all differ slightly. Some common event generators used in neutrino community are Geant4, FLUKA (for transport of particles through matter), PYTHIA (for high-energy collisions of elementary particles), GENIE [6], GiBUU [7], NEUT [48], NUANCE, NuWro [8] (for neutrino interactions). Depending on the event generators, the models are different. GENIE, NEUT, and NuWro use the Nieves model, NuWro uses Transverse Enhancement (TE) model by Bodek, and GENIE uses the dytman model. Rein-Sehgal [62] model is commonly used for coherent pion production, but the Berger-Sehgal model replaces RS in NuWro, GENIE.

In a perfect world, MC generators would contain "pure" theoretical models, but in the real world, the theory does not cover everything, so neutrino and non-neutrino data are used to tune generators.

- Elastic and quasi-elastic process:
  - Llewellyn-Smith model is usually used for charged current quasi-elastic scattering
  - Not much difference here between generators (but default parameters)
  - Nucleon structure is parametrized by form factors
- Resonance production:
  - Rein-Sehgal model describes single pion production through baryon resonances below $W = 2GeV$
  - It is used by GENIE and NEUT
  - However, GENIE includes only 16 resonances, and interference between them is neglected
- Deep inelastic scattering:
  - Quark-parton model is used for deep inelastic scattering
  - Bodek-Young modification to the parton distributions at low Q2 is included by most generators

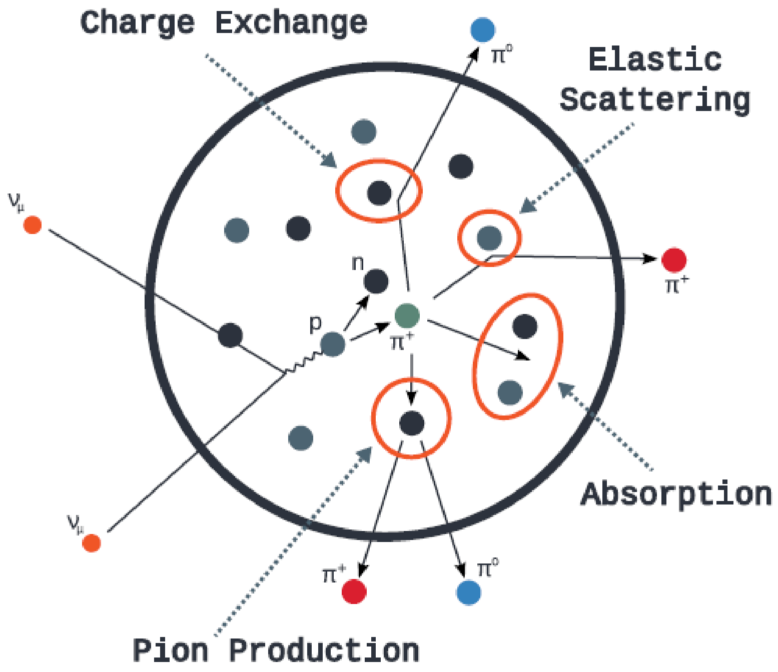

FIGURE 2.9: Schematic of nuclear effects and FSI [9].

2.4 Adler angles

The Adler reference system describes the pπ^+ final state in the pπ^+ reference system. The definition of the Adler angles is shown in Figure 2.10. The Adler angles (ϕ and θ) are sensitive to the transverse and longitudinal polarization of the pπ^+ system for interactions mediated by a Δ^{++}, Δ^+ and for non-resonant contributions.

The two angles are properly defined at the nucleon interaction level, but the FSI and the Fermi momentum of the target nucleon alter them [39].

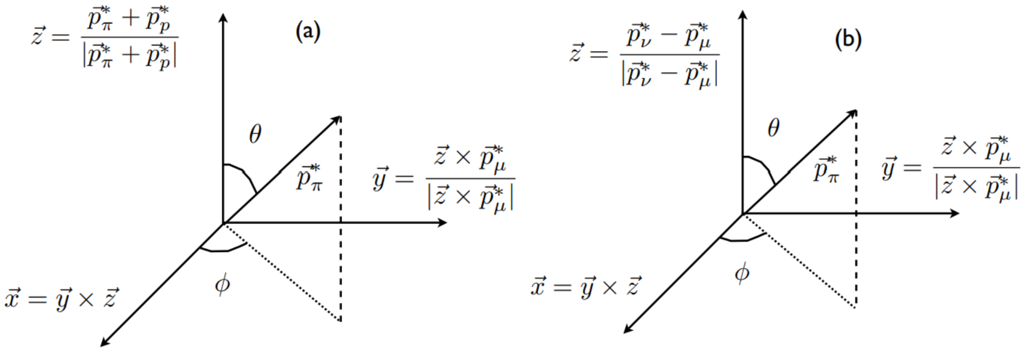

FIGURE 2.10: Definition of the Adler angles at the nucleon (true) level (a) and the nuclear level (b). The momenta of the particles are defined in the $q = \vec{p}_\nu$ - $\vec{p}_\mu$ rest frame [39].

To evaluate the relative contributions to the Adler angles of the Fermi momentum and the FSI, they should be computed under three assumptions:

- True: We should estimate the parameters using the full kinematic information at the nucleon level. These results are experimentally measurable only with a hydrogen target [39],
- Pre-FSI: We should use the true kinematics of the pion at the nucleon level, but we ignore the target nucleon's momentum. In this case, the effect of the Fermi momentum is taken into account, but the FSIs are ignored [39],
- Post-FSI: We should use the information of the pion leaving the nucleus and ignore the kinematic information of the target nucleon. These are the actual experimental observables, and they contain the effect of both the Fermi momentum and of the FSI [39].

2.4.1 Adler angles at the nucleus level

Modern experiments detect neutrino interactions on relatively heavy nuclei (carbon, oxygen, iron, argon) targets. Therefore, the definition of the Adler angles needs to be modified. The first modification is mandated by the fact that usually, the proton is not detected. In this case, the $p\pi^+$ reference system needs to be redefined based on detector observable [39]. They are defined by looking at the μ^- and the π^+ that escape the nucleus, so we already have nuclear effects influencing those measurements.

Chapter 3

The T2K experiment

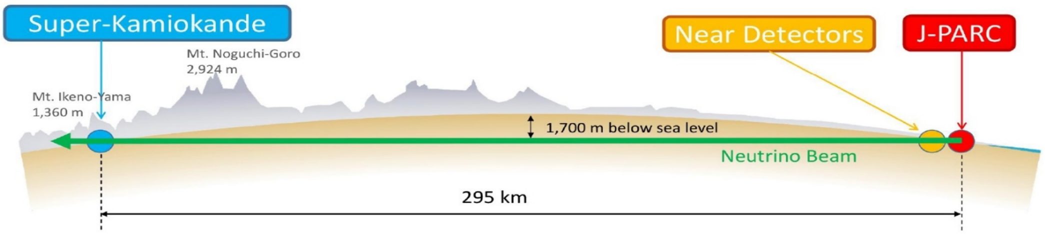

FIGURE 3.1: A schematic of a neutrino's journey from the neutrino beamline at J-PARC (red dot), through the near detectors complex (yellow dot) and then travels $295\ km$ underneath to Super Kamiokande (blue dot) [9].

T2K (Tokai to Kamioka) [14] is a long-baseline neutrino experiment located in Japan (Figure 3.1), which aims to measure neutrino oscillations parameters with precision of $\delta(\Delta m_{23}{}^2) \sim 10^{-4}\ eV^2$ and $\delta(sin^2 2\theta_{23}) \sim 0.01$ via ν_μ disappearance studies and achieving a better sensitivity through the search for $\nu_\mu \rightarrow \nu_e$ appearance ($\frac{1}{2}sin^2 2\theta_{13}$ > 0.004 at 90% CL for CP violating phase $\delta_{CP} = 0$). T2K was designed to probe the mixing of the ν_μ with other species and cast light on the neutrino mass hierarchy. It looks explicitly for the oscillation $\nu_\mu \rightarrow \nu_e$ appearance, thereby measuring θ_{13}. T2K is also now moving to constrain the the value of δ_{CP} by measure muon neutrino to electron neutrino oscillations and the corresponding antineutrino oscillations.

Figure 3.1 shows a schematic layout of the T2K experiment as a whole. The T2k far detector (Super Kamiokande) is used to measure neutrino rates at a distance of $295km$ from the accelerator. The experiment includes a neutrino beamline and a near detectors complex (Figure 3.2) at $280\ m$ (ND280, INGRID, WAGASCI), that are used to characterize the beam just after production. At the near detector site, we have an on-axis detector(INGRID) and two off-axis detectors (ND280, WAGASCI). These measurements are essential to characterize signals and backgrounds observed in the Super Kamiokande far detector.

The T2K collaboration consists of over 500 physicists and technical staff members from 59 institutions in 12 countries (Canada, France, Germany, Italy, Japan, Poland, Russia, South Korea, Spain, Switzerland, the United Kingdom, and the United States) [14]. The construction of the neutrino beamline started in April 2004. The complete chain of accelerator and neutrino beamline was successfully commissioned in 2009, and T2K began accumulating neutrino beam data for physics analysis in January 2010.

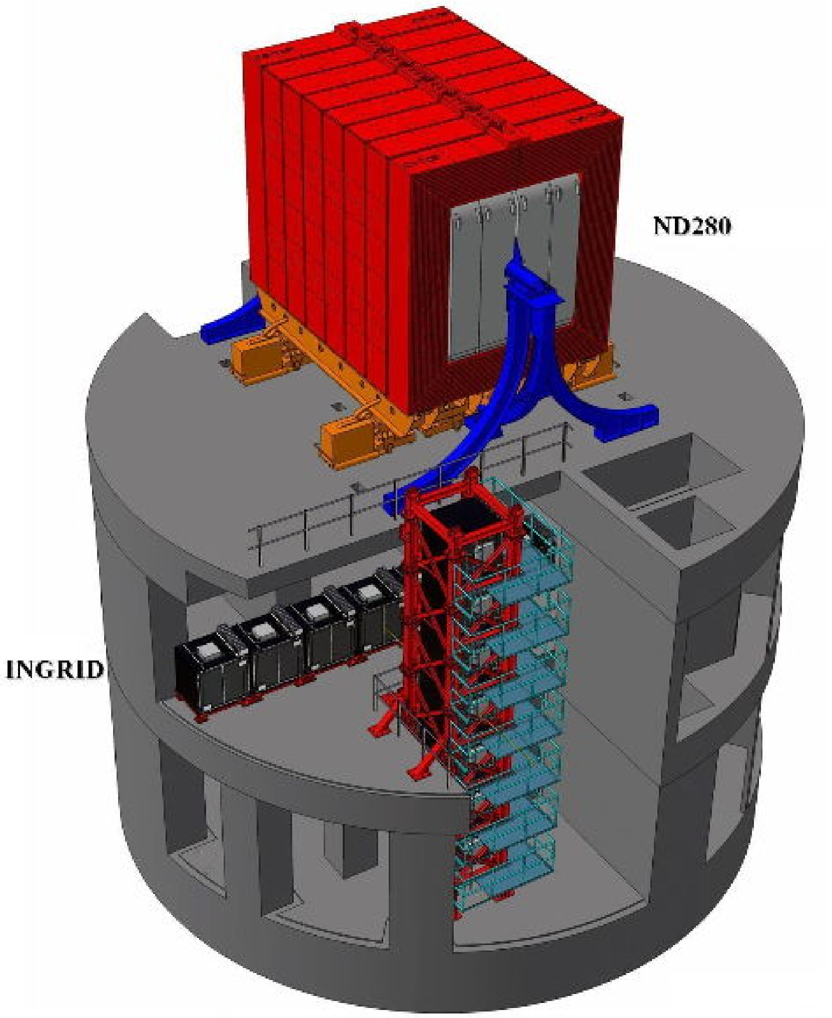

FIGURE 3.2: Near detectors complex. The off-axis detector and the magnet are located on the upper level; horizontal INGRID modules are located on the level below; and the vertical INGRID modules span the bottom two levels [9].

3.1 Accelerator (J-PARC)

The J-PARC accelerator (Figure 3.3) at Tokai, Ibaraki, consists of three accelerators: a linear accelerator (LINAC), a rapid-cycling synchrotron (RCS) and the main ring (MR) synchrotron. An H^- beam is accelerated up to $400\ MeV$ by the LINAC and is converted to an H^+ beam by charge-stripping foils at the RCS injection. The beam is accelerated up to 3 GeV by the RCS with a 25 Hz cycle. The harmonic number of the RCS is two, and there are two bunches in a cycle. About 5% of these bunches are supplied to the MR. The rest of the bunches are provided to the muon and neutron beamline in the Material and Life Science Facility. The proton beam injected into the MR is accelerated up to 30 GeV. The MR has two extraction points: slow extraction for the hadron beamline and fast extraction for the neutrino beamline. The time structure of the extracted proton beam is key to discriminating various backgrounds, including cosmic rays, in the different neutrino detectors [14].

FIGURE 3.3: A schematic of the J-PARC site [10].

3.2 T2K beam

Each proton beam spill consists of eight proton bunches extracted from the MR to the T2K neutrino beamline. The neutrino beamline is composed of two sequential sections: the primary and secondary beamlines. In the primary beamline, the extracted proton beam is transported to point toward Kamioka. In the secondary beamline, the proton beam impinges on a target to produce secondary pions, which are focused by magnetic horns and decay into neutrinos [14].

3.2.1 Primary beamline

The primary beamline can be divided into three sections: the preparation, the arc, and the final focusing. In the preparation section, the extracted proton beam is tuned with four steerings, two dipoles, and five quadrupole magnets. In the arc section, the beam is bent toward the direction of Kamioka using 14 doublets of superconducting combined function magnets (SCFMs). The beam orbit is corrected using three horizontal and vertical superconducting steering magnets. In the final focusing section, four steering, two dipoles, and four quadrupole magnets guide and focus the beam into the target (Figure 3.4).

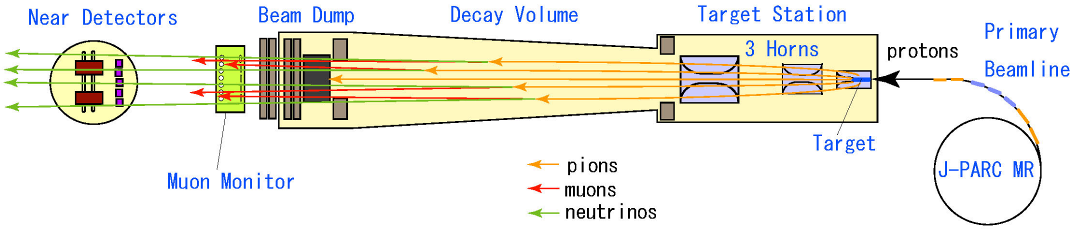

FIGURE 3.4: A schematic of the T2K neutrino beam production [9]

3.2.2 Secondary beamline

The secondary beamline (Figure 3.4) can be divided into three sections: the target station, decay volume, and beam dump. Protons from the primary beamline are directed to the target via the beam window. The proton beam produces mesons in the target station, and three magnetic horns focus on these mesons. These mesons then decay via the following processes:

$$\pi^+ \rightarrow \mu^+ + \nu_\mu \quad and \quad K^+ \rightarrow \mu^+ + \nu_\mu \quad (FHC)$$

$$\pi^- \rightarrow \mu^- + \bar{\nu}_\mu \quad and \quad K^- \rightarrow \mu^- + \bar{\nu}_\mu \quad (RHC)$$

Inside a single volume of $\sim 1500 \ \ m^3$, filled with helium gas to reduce pion absorption. The neutrino or antineutrino beam configurations are called "forward horn current" (FHC) mode or "reverse horn current mode" (RHC) mode, respectively. However, imperfect horn focussing allows some wrong-sign contamination, and some of the subsequent muons also decay, alongside some of the kaons via another mode, to produce a small (anti)electron neutrino component to the beam:

$$\mu^+ \rightarrow e^+ + \nu_e + \bar{\nu}_\mu \quad and \quad K^+ \rightarrow \pi^0 + e^+ + \nu_e \quad (FHC)$$

$$\mu^- \rightarrow e^- + \bar{\nu}_e + \nu_\mu \quad and \quad K^- \rightarrow \pi^0 + e^- + \bar{\nu}_e \quad (RHC)$$

All the hadrons and muons below $\sim 5 \ GeV/c$ are stopped by the beam dump. The neutrinos pass through the beam dump and are used for physics experiments. Any muons above $\sim 5 \ GeV/c$ that pass through the beam dump are monitored to characterize the neutrino beam.

The T2K GPS time synchronization system provides $\mathcal{O}$(50 ns) scale synchronization between neutrino event trigger timestamps at Super-Kamiokande, and beam spill[1] timestamps logged at J-PARC. The system's heart is a custom electronics board called the local time clock (LTC). The LTC module also provides the beam trigger for the beam monitors. At each site, two independent GPS systems run in parallel at all times to eliminate downtime during T2K running [14]

3.2.3 Neutrino flux

To achieve a narrow band neutrino beam, T2K follows the off-axis method (Figure 3.5). The neutrino beam is purposely directed at an angle with respect to the baseline connecting the proton target and the far detector, Super Kamiokande (Figure 3.6).

---

[1] The spill number is the accumulated number of received signals.

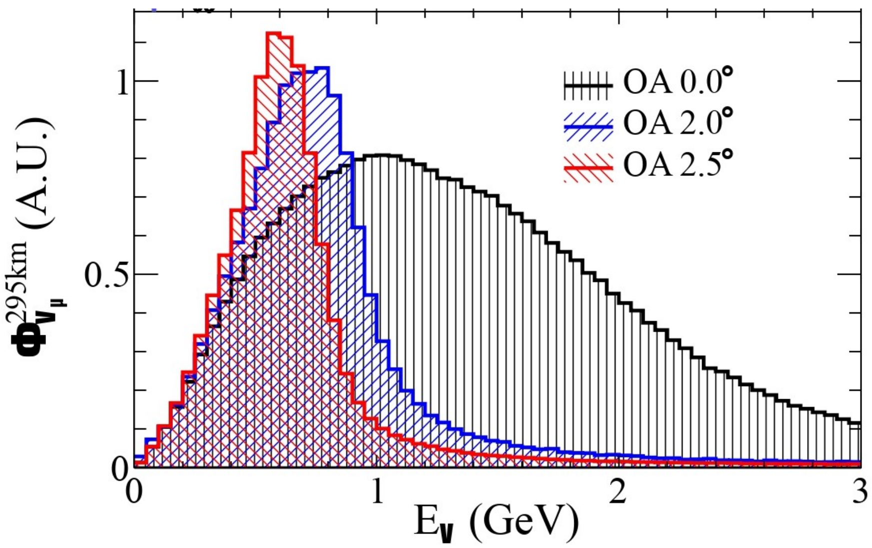

FIGURE 3.5: Neutrino beam T2K in as function of the neutrino energy for three angles configurations [9].

The neutrino beamline is designed so that the neutrino energy spectrum can be tuned by changing the off-axis angle down to a minimum of ~2.0°, from the current maximum angle of $\sim 2.5°$. The narrow-band ν_μ beam generated toward the far detector has a peak energy at $\sim 0.6\ GeV$, which maximizes the effect of the neutrino oscillation at $295\ km$ and minimizes the background to ν_e appearance detection.

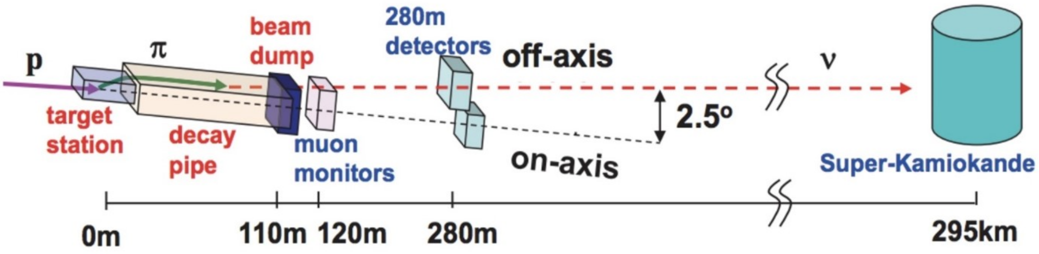

FIGURE 3.6: A schematic of the secondary beamline, near detector complex and SK, showing the configuration for on and off-axis [9].

3.3 T2K on-axis near detector: INGRID

The on-axis near detector, INGRID (Interactive Neutrino GRID), was designed to directly monitor the neutrino beam direction and intensity. The beam center is measured to a precision better than 10 cm by observing the number of neutrino events in each module.

The INGRID detector (Figure 3.7) consists of 14 identical modules arranged as a cross of two identical groups along the horizontal and vertical axis and two additional separate modules located at off-axis directions outside the main cross. The center of the INGRID cross, with two overlapping modules, corresponds to the neutrino beam center, defined as 0° with respect to the direction of the primary proton beamline. The purpose of the two off-axis modules is to check the axial symmetry of the neutrino beam [14].

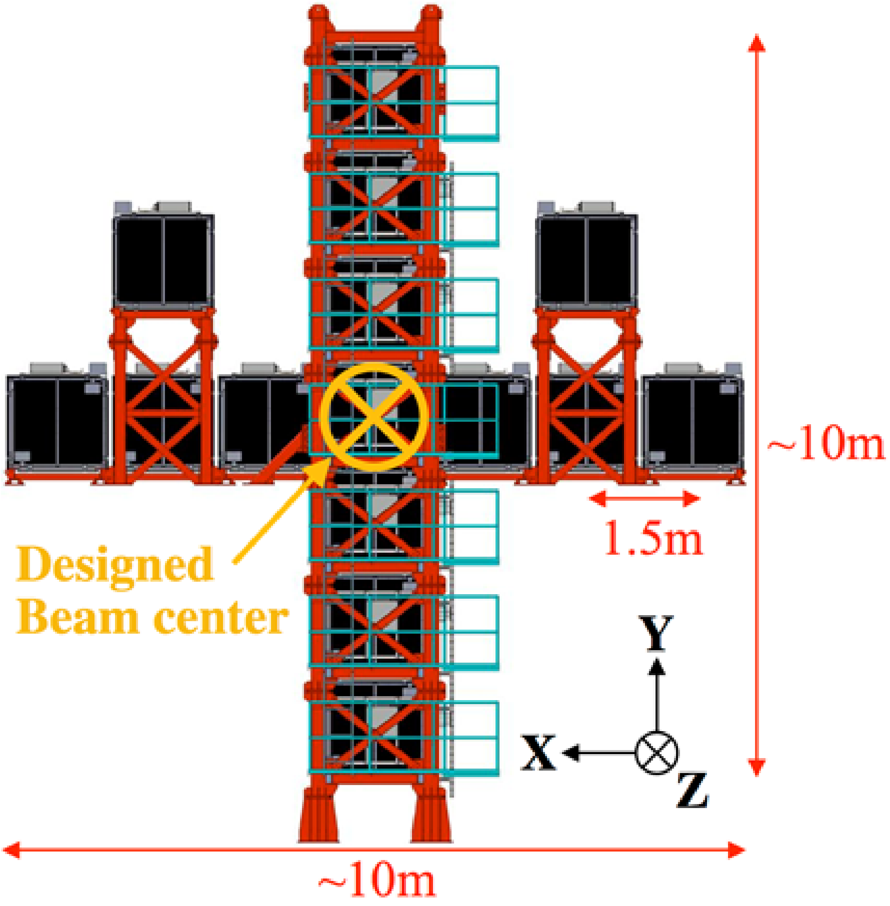

FIGURE 3.7: INGRID on-axis detector [9].

The INGRID modules consist of a sandwich structure of nine iron plates and 11 tracking scintillator planes. Each of the 11 tracking planes consists of 24 scintillator bars in the horizontal direction glued to 24 perpendicular bars in the vertical direction with Cemedine PM200. They are surrounded by veto scintillator planes to reject interactions outside the module. Since adjacent modules can share one veto plane in the boundary region, the modules have either three or four veto planes. Each veto plane consists of 22 scintillator bars segmented in the beam direction [14].

3.4 T2K off-axis near detector: ND280

The ND280 off-axis detector is formed by a water-scintillator detector optimized to identify π^0 (the P∅D), three time projection chambers (TPCs), and two fine-grained detectors (FGDs). An electromagnetic calorimeter (ECal) surrounds the P∅D, TPCs, and FGDs. The whole off-axis detector is placed inside a magnetic field provided by the recycled UA1 magnet and a side muon range detector (SMRD). The detector is simulated using GEANT4. An example of the event display for the GEANT4 Monte Carlo simulation is shown in Figure 3.9.

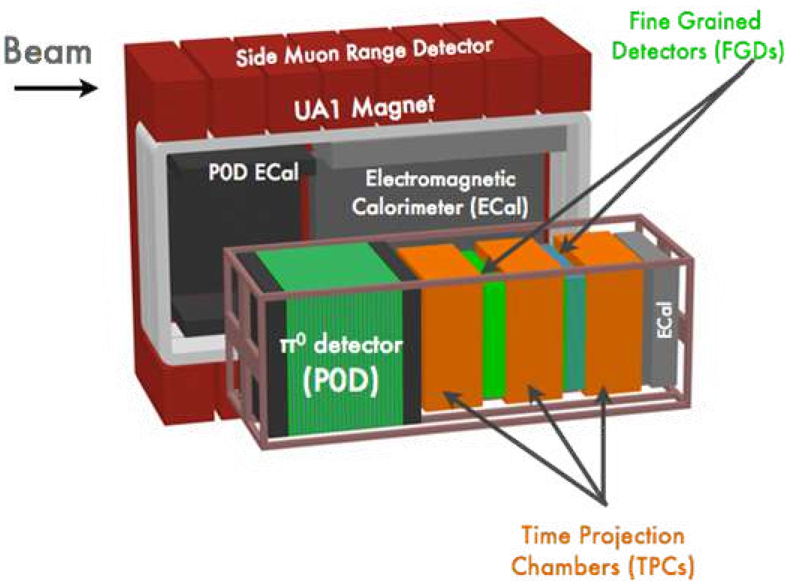

FIGURE 3.8: An exploded view of the ND280 off-axis detector [9].

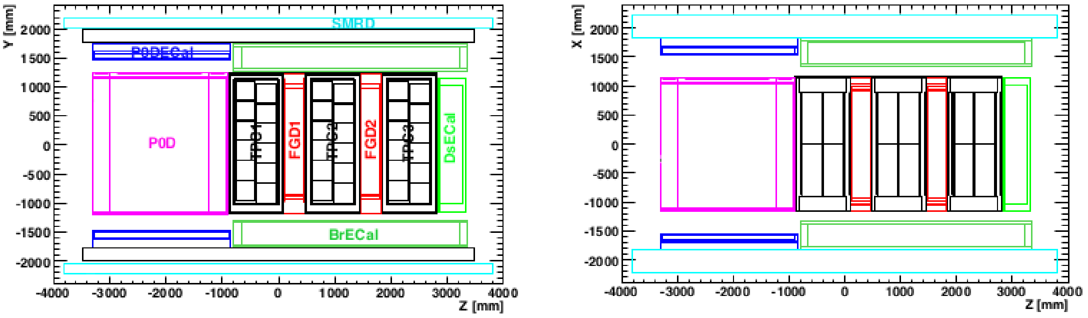

(A) lateral view

(B) top view

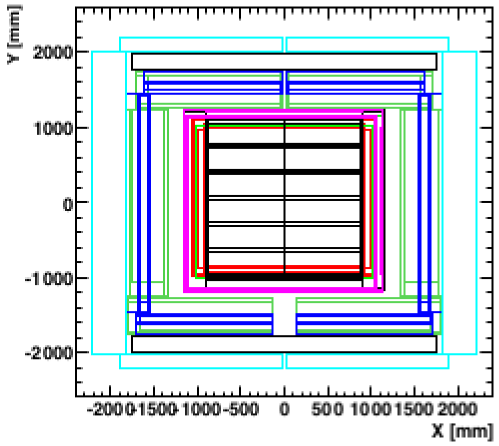

(C) front view

FIGURE 3.9: Event display using GEANT4 Monte Carlo simulation of the ND280 detector, lateral view (a), top view (b), front view (c) [9].

The principal function of ND280 is to measure the neutrino beam's flux, energy spectrum, and flavor composition by observing charged current neutrino interactions. The tracker ($TPCs + FGDs$) is optimized to measure the momenta of charged particles, particularly muons and pions produced by charged current interactions. The ND280 tracker is intended to measure the ν_μ and ν_e fluxes and spectra and various charged current cross sections.

3.4.1 Pi-Zero detector (P∅D)

The P∅D detector is located at the upstream end of the inner volume of the magnet. It consists of tracking planes of scintillating bars alternating with lead foil and water (H^2O) target bags. The primary objective of the P∅D is to measure the neutral current process $\nu_\mu + N \rightarrow \nu_\mu + N + \pi^0 + X$ on a water target. The scintillator bars provide fine segmentation to reconstruct charged particle tracks (muons and pions) and electromagnetic showers. The mass of the detector with water is 16.1 tons.

3.4.2 Fine grained detector (FGD)

The ND280 detector contains two massive fine-grained detectors (FGDs), which provide the target mass for neutrino interactions and track charged particles coming from the interaction vertex. The two FGD modules, placed after the first and second TPCs, consist of layers of finely segmented scintillator bars. The first FGD consists of 5760 scintillator bars, arranged into 30 layers of 192 bars each, with each layer oriented alternatively in the x and y directions perpendicular to the neutrino beam. The second FGD is a water-rich detector consisting of 7 x-y sandwiches of plastic scintillator layers alternating with six $2.5\ cm$ thick layers of water. Both of them contain 1.1 tons of material. Comparing the interaction rates in the two FGDs permits separate determination of cross sections on carbon and water. Direction and ranges of short tracks such as recoil protons produced by CC interactions in the FGDs are measured.

3.4.3 Time projection chamber (TPC)

The ND280 detector contains three time projection chambers (TPCs), which measure the momenta of particles produced by interactions in the detector and it is used to reconstruct the neutrino energy spectrum. The TPC tracking and dE/dx (Figure 3.10) measurements in the TPC will also determine the sign of charged particles and identify muons, pions, and electrons.

From the considerations above, the key measurements for the TPC system are:

- Momentum: here, the goal is to reach a 10% resolution at 1 GeV/c. Given the limited curvature offered by the low magnetic field, this will require good space point resolution. The requirement on the momentum resolution drives the segmentation of the readout plane [14].
- Energy scale: the T2K physics goals require understanding the energy scale at the 2% level. This goal can be met using a combination of magnetic field measurement and mapping, absolute momentum calibration using a physical signal (the invariant mass of K^0 produced in DIS neutrino events and decaying in the TPC volume), excellent control of the electric field distortions [14].

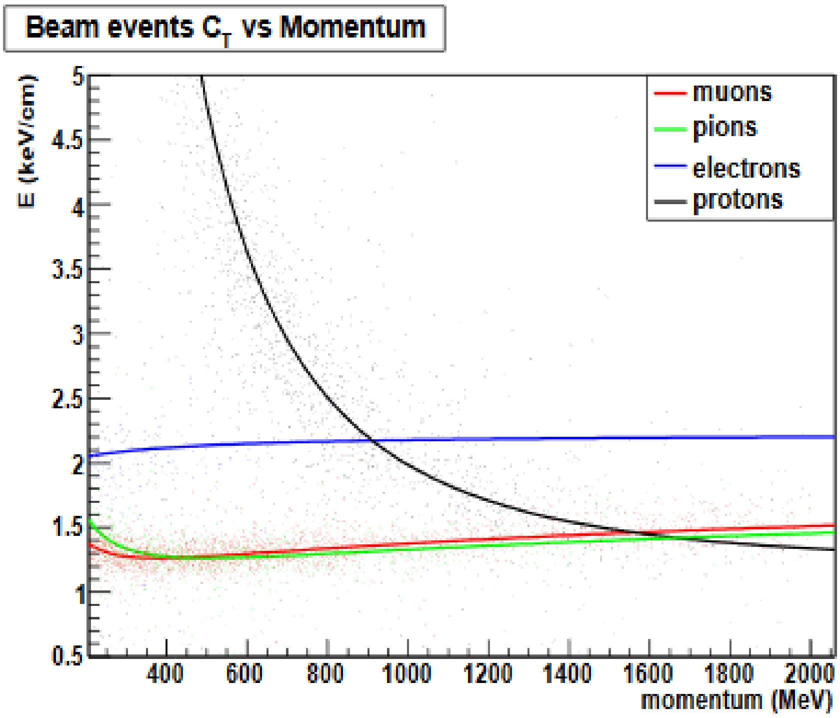

FIGURE 3.10: Energy loss and momentum of positively charged particles produced in neutrino interactions. The expected relationships for muons, positrons, protons, and pions are shown by the curves [32]

- Particle identification through ionization energy loss: here, the purpose is to identify electrons from muons in the $0.5 - 1.0\, GeV/c$ momentum range. The typical separation between the electron and muon dE/dx is 30 to 40%. To achieve a 3 σ separation between the electron and the muon tracks, a dE/dx measurement below 10% is needed. Considering the number of samples, the track length, and the resolution achieved by previous TPCs, this goal can be met. It requires a careful calibration of the detector response both over the readout planes and as a function of time [14].

3.4.4 Electromagnetic calorimeter (ECal)

The ND280 ECal is a sampling electromagnetic calorimeter surrounding the inner detectors (P∅D, TPCs, FGDs). It is made of layers of plastic scintillator bars interleaved with lead foils. The ECal has 13 independent modules of three different types arranged: six Barrel-ECal modules surround the tracker volume on its four sides parallel to the z (beam) axis; one downstream module (Ds-ECal) covers the downstream exit of the tracker volume, and six P∅D-ECal modules surround the P∅D detector volume on its four sides parallel to the z-axis. The main purpose is to measure those $\gamma-$rays produced in ND280 that do not convert in the inner detectors measuring their energy and direction; it is critical for the reconstruction of π^0 decays. It also helps in the detection of charged particles and the extraction of information relevant for their identification (electron-muon-pion separation).

3.4.5 UA1 magnet

ND280 uses the UA1 magnet operated with a magnetic field of $0.2\ T$, perpendicular to the neutrino beam direction, to measure momenta with good resolution and determine the sign of charged particles produced by neutrino interactions. The field is sufficiently uniform in intensity and direction. The magnet consists of water-cooled aluminum coils, which create the horizontally oriented dipole field and a flux return yoke. Each of the two symmetric fractions mirrored about a vertical plane containing the beam axis consisting of 8 C-shaped yokes (Figure 3.11), made of low-carbon steel plates.

FIGURE 3.11: UA1 magnet C-shaped yokes [9].

3.4.6 Side muon range detector (SMRD)

The SMRD consists of three layers of scintillator modules on the top and bottom for all yokes, and it is formed by a total of 440 scintillator modules which are inserted in the $1.7\ cm$ air gaps between $4.8\ cm$ thick steel plates which make up the UA1 magnet flux return yokes. The SMRD records muons escaping with high angles with respect to the beam direction and measures their momentum triggers on cosmic-ray muons that enter or penetrate the ND280 detector and helps identify beam-related event interactions in the surrounding cavity walls and the iron of the magnet.

3.5 T2K off-axis far detector: Super Kamiokande (SK)

Located in the Mozumi mine of the Kamioka Mining and Smelting Company, Japan, is the T2K off-axis far detector, Super Kamiokande. The detector lies $1\ km$ underground (Figure 3.12). It is the world's largest land-based water Cherenkov detector, consisting of a welded stainless-steel tank, $39\ m$ in diameter and $42\ m$ tall, with a total nominal water capacity of 50,000 tons [14]. The detector contains approximately 13,000 photo-multiplier tubes (PMTs) that image neutrino interactions in pure water. Super Kamiokande has been running since 1996 and has produced data for several well-known results that include world leading limits on the proton lifetime [67, 49, 56] and the measurement of flavor oscillations in atmospheric, solar, and accelerator-produced neutrinos [43, 44, 17, 23, 50].

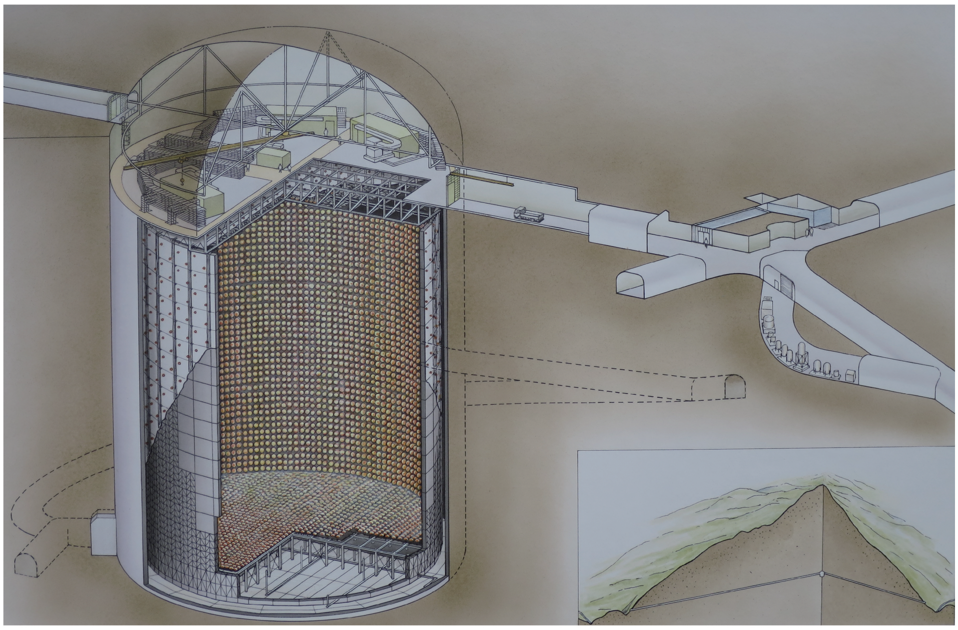

FIGURE 3.12: A schematic of the Super-Kamiokande [11].

The detector is located $295\ km$ west of the beam source, where it is used to sample the beam's flavor composition and look for $\nu_\mu \to \nu_e$ appearance and ν_μ disappearance. The geometry of the Super Kamiokande detector consists of two major volumes, an inner and an outer detector which are separated by a cylindrical stainless steel structure.

- The outer detector (OD) is a cylindrical space about $2\,m$ thick radially and on the axis at both ends. The OD contains along its inner walls 1,885 outward-facing 20 cm diameter PMTs.
- The inner detector (ID) is a cylindrical space $33.8\ m$ in diameter and $36.2\ m$ in height, which currently houses along its inner walls 11,129 inward-facing $50\ cm$ diameter PMTs. The ID is well instrumented, with 40% PMT cathode surface coverage, so that there is sufficient spatial resolution to infer a number of physical quantities from the imaged neutrino interactions.

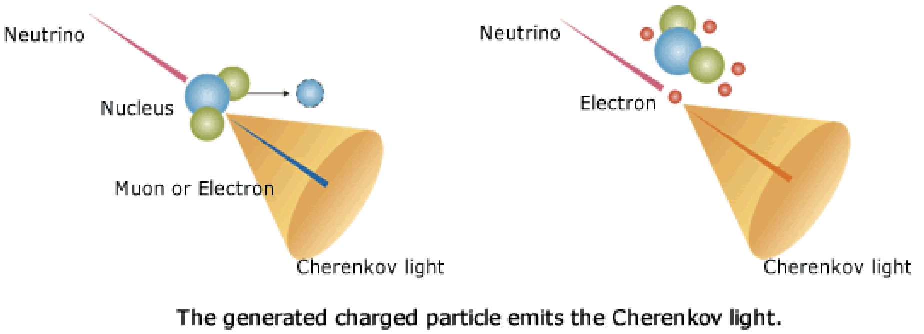

FIGURE 3.13: Cone of Cherenkov light produced by charged particles (from the neutrino interactions) while they traverse the water [11].

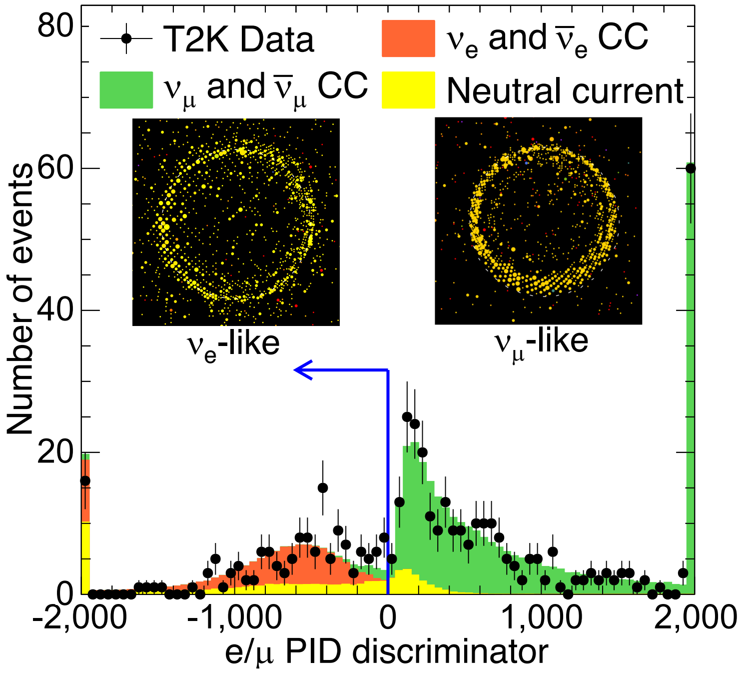

FIGURE 3.14: Particle identification in the SK detector. The particle identification (PID) parameter distribution is used to classify Cherenkov rings as electron-like and muon-like. Events to the left of the blue line are classified as electronlike and those to the right as muon-like. The filled histograms show the expected number of single ring events after neutrino oscillations, with the first and last bins of the distribution containing events with discriminator values above and below the displayed range, respectively. The vertical error bars on the data points are the standard deviation due to statistical uncertainty. The PID algorithm uses the light distribution properties, such as the blurriness of the Cherenkov ring, to classify events. The insets show examples of an electron-like (left) and muon-like (right) Cherenkov ring [12]

Neutrino interactions often produce charged particles that, if above an energy threshold, produce a cone of Cherenkov light as they traverse the water (Figure 3.13). The Cherenkov light is emitted in a cone shape to the direction of a charged particle. The photo-multiplier tubes (PMTs) of the wall of the tank detect this Cherenkov light.

When the photons reach the PMTs on the detector walls, they produce a ring-shaped hit pattern (Figure 3.14) [14]. The PMTs have information on the detected light quantity and the detection timing. The energy, direction, interaction point, and type of the charged particle are decided by the data from the PMTs.

The wall facing into the ID is lined with a black sheet of plastic meant to absorb light and minimize the number of photons that either scatter off of the ID wall back into the ID volume or pass through from the ID to the OD. However, the walls facing the OD are lined with the highly reflective material Tyvek to compensate for the OD's sparse instrumentation. With the Tyvek, photons reflect off of the surface of the OD walls and have a higher chance of finding their way to one of the OD PMTs [14].

The measurement of the oscillation in the Super Kamiokande ID of $\nu_\mu \to \nu_e$ or $\nu_\mu \to \nu_\tau$, is to count CCQE interactions for ν_μ and ν_e. The number of muons measured will give of the ν_μ disappearance while the number of electrons gives of the ν_e appearance. Muons, due to their relatively large mass, that travel through the detector produce a well-defined cone of Cherenkov radiation which leads to a clear, sharp ring of PMT hits seen on the detector wall. Electrons scatter more easily due to their smaller mass and almost always induce electromagnetic showers at the energies relevant to Super Kamiokande. The result of an electron-induced shower is a blurred ring pattern seen by the PMTs, which can be thought of as the sum of many overlapping Cherenkov light cones. These differences are used by the Super Kamiokande event reconstruction software to separate between muon-like or electron-like particles. The OD is an active veto of cosmic ray muons and other backgrounds. The PMT array in the OD is capable of an almost 100% rejection efficiency of cosmic ray muon backgrounds.

3.6 Recent results and future

The main objective of T2K is to measure neutrino oscillations. It looks explicitly for two oscillation channels: $\nu_\mu \to \nu_\mu$ disappearance and $\nu_\mu \to \nu_e$ appearance. Most of the parameters have been measured with $< 10\%$ precision; the θ_{23} mixing angle is known with 15% precision. Due to the ability of the production of $\nu_\mu/\bar{\nu}_\mu$ beam, T2K can provide some information about the remaining unknown parameters (δ_{CP} and mass hierarchy) [14, 45].

Most recently, T2K reported a measurement that favors a large enhancement of the neutrino oscillation probability, excluding values of δ_{CP} which results in a large enhancement of the observed antineutrino oscillation probability at three standard deviations. The data show a preference for values of δ_{CP} which are near maximal CP violation (see Figure 3.15), while both CP conserving points, $\delta_{CP} = 0$ and $\delta_{CP} = \pi$, are ruled out at the 95% confidence level [12]; this is a world leading result and uses the value of θ_{13} from reactor experiments.

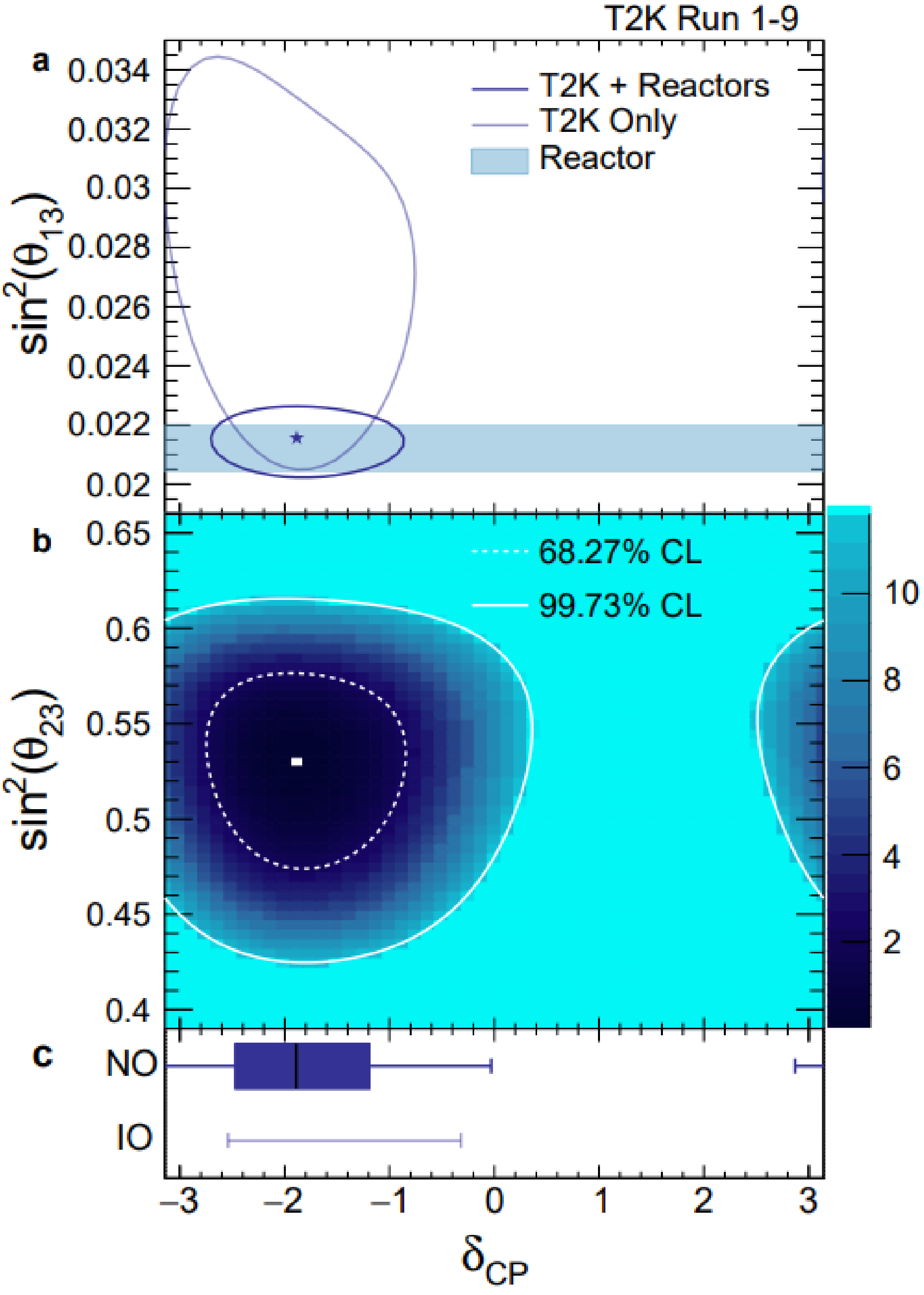

FIGURE 3.15: Constraints on PMNS oscillation parameters. Subfigure a shows 2D confidence intervals at the 68.27% confidence level (CL) for δ_{CP} vs $sin^2\,\theta_{13}$ in the preferred normal ordering. The intervals labeled T2K only indicate the measurement obtained without using the external constraint on $sin^2\,\theta_{13}$, while the T2K + Reactor intervals do use the external constraint. The star shows the best-fit point of the T2K + Reactors fit in the preferred normal mass ordering. Subfigure b shows 2D confidence intervals at the 68.27% and 99.73% confidence level for δ_{CP} vs. $sin^2\,\theta_{23}$ from the T2K + Reactors fit in the normal ordering, with the color scale representing the value of negative two times the logarithm of the likelihood for each parameter value. Subfigure c shows 1D confidence intervals on δ_{CP} from the T2K + Reactors fit in both the normal (NO) and inverted (IO) orderings. The vertical line in the shaded box shows the best-fit value of δ_{CP}, the shaded box itself shows the 68.27% confidence interval, and the error bar shows the 99.73% confidence interval. Notably, there are no values in the inverted ordering inside the 68.27% interval [12].

This measurement relied on the modeling of experimental apparatus to infer the parameters governing the oscillations of neutrinos. The make measurements of neutrino oscillation parameters, precise knowledge of the interaction cross section is required. The main sources of systematic uncertainty in the data analysis are flux, cross section modeling, and the detectors' responses. The different types of uncertainties are shown in Table 3.1. The main three contributions come from nucleon removal energy in the interaction model, electron neutrino and antineutrino interaction model, and neutrino production and interaction model constrained by ND280 data, in that order [12].

Type of Uncertainty	$\nu_e/\bar{\nu}_e$ Candidate Relative Uncertainty (%)
Super-K Detector Model	1.5
Pion Final State Interaction and Re-scattering Model	1.6
Neutrino Production and Interaction Model Constrained by ND280 Data	2.7
Electron Neutrino and Antineutrino Interaction Model	3.0
Nucleon Removal Energy in Interaction Model	3.7
Modeling of Neutral Current Interactions with Single γ Production	1.5
Modeling of Other Neutral Current Interactions	0.2
Total Systematic Uncertainty	6.0

TABLE 3.1: The systematic uncertainty on the predicted relative number of electron neutrino and electron antineutrino candidates in the Super-K samples with no decay electrons [12].

Because of the J-PARC program of upgrades of the beam intensity, the T2K-II proposal requires an increase of the exposure by a factor of ten. The Hyper-K proposal increases by a factor ten of the far detector mass. Facing the potential rise in statistics by two orders of magnitude, it is of great importance to undertake a vigorous program of near detector upgrades, intending to reduce the statistical and systematic uncertainties at the appropriate level of 3-4% or less on the prediction of the $\nu_\mu \to \nu_e$ and $\bar{\nu}_\mu \to \bar{\nu}_e$ appearance signals in the far detector for a given set of oscillation parameters. The ND280 upgrade goals are to use his quasi-3D imaging to improve target tracking, proton detection threshold, and neutron detection capabilities. It will enhance high-angle acceptance by using High-Angle TPC's and reduce the Time of Flight background [19].

T2K ended its data-taking run on February 12, 2020. T2K has accumulated a total of 3.64×10^{21} protons on target (POT) so far.

Chapter 4

Motivation and analysis strategy

This chapter describes the motivation for the analysis, the analysis strategy, and the methods used to unfold the data, validate the fitter, and extract a differential cross section in kinematic variables.

4.1 Motivation

T2K is a long-baseline neutrino experiment located in Japan, aiming to measure neutrino oscillations. An accelerator produces neutrinos, which are then detected in a near detector complex and a far detector (Super-Kamiokande). The main objective of the near detectors in a neutrino oscillation experiment (like T2K) is the reduction of systematic errors in the oscillation analysis. Therefore the events selected at the near detector are used to constrain the flux and cross section parameters. The muon neutrino charged current interactions in the near detector (ND280) are used to predict the event rate at the far detector and better constrain the cross section parameters, which are dominant in the oscillation analysis together with the flux uncertainty.

$$R_{near} = \Phi_{near}(E_\nu) \cdot \sigma_{near}(E_\nu) \cdot N_{t_{near}}, \tag{4.1}$$

$$R_{far} = \Phi_{far}(E_\nu) \cdot \sigma_{far}(E_\nu) \cdot N_{t_{far}} \cdot P_{osc}, \tag{4.2}$$

where P_{osc} is the probability of oscillation, R is the rate of interactions in the detector, Φ is the neutrino flux, σ is the cross section (both Φ and σ depend on the neutrino energy (E_ν)), and N_t is the number of targets, all for both near and far detectors.

The $\nu_l + n \rightarrow l^- + p$ (in the antineutrino case $\bar{\nu_l} + p \rightarrow l^+ + n$), represent the simplest form of neutrino-nucleon (antineutrino-nucleon) interaction, where the charged current (CC) induces a transition from the neutrino (antineutrino) in its corresponding charged lepton l^- (l^+) that results as the signal for an event. The final state interactions (FSI) can produce more than one ejected nucleon and, the production of resonances with the absorption of the emitted pions can also produce more ejected nucleons. These contributions affect the reconstruction of neutrino energy and confuse the classification of the event.

This thesis study the signal, defined as a single negatively charged muon and a single positively charged pion exiting from the target nucleus with 4π detector acceptance, constitutes the main background for the muon neutrino disappearance measurement when the charged pion is not observed, and its precise knowledge is relevant for all current and planned neutrino oscillation experiments. Single pion production is sensitive mainly to resonant processes, with non-resonant and coherent pion production contributions. Additionally, final-state interactions in the nuclear target have to be considered. Adler Angles are observable carrying information about the polarization of the Δ resonance and the interference with the non-resonant single pion production.

They were measured with limited statistics in bubble chamber experiments, but it is possible to measure the Adler angles for single charged pion production in neutrino interactions with heavy nuclei as the target.

The neutrino fluxes, for the experiments, are produced by secondary decays of pions and kaons, usually produced in high proton-nucleon/nucleus collisions. The beam produces a range from hundreds of MeV to several GeV. In this energy range, the dominant contribution to the neutrino-nucleus cross section comes from reactions with CC, from the channels: quasi-elastic scattering, resonance production, and deep-inelastic scattering.

When studying these interactions, there are some challenges, our incomplete understanding of the nuclear effects contributing to the cross section, and inaccuracies in reconstructing the neutrino energy. We have three levels of uncertainties related to neutrino cross section knowledge; cross sections at the nucleon level are not perfectly known, the nuclear medium effects modify the cross sections, and these primary interactions are embedded in the nucleus, where nuclear effects can modify the event topology. Currently, the QE scattering is well studied. We now need to accurately model interactions occurring at higher energies like RES [39].

The use of computational tools is important. The current selections in ND280 [61] are mainly focused on selecting forward-going tracks (Figure 4.1) produced by neutrino interactions inside the FGDs. In contrast, events selected at SK are selected without requiring a forward-going track because of the 4π coverage of the detector. A new selection was developed to select these events with 4π solid angle acceptance.

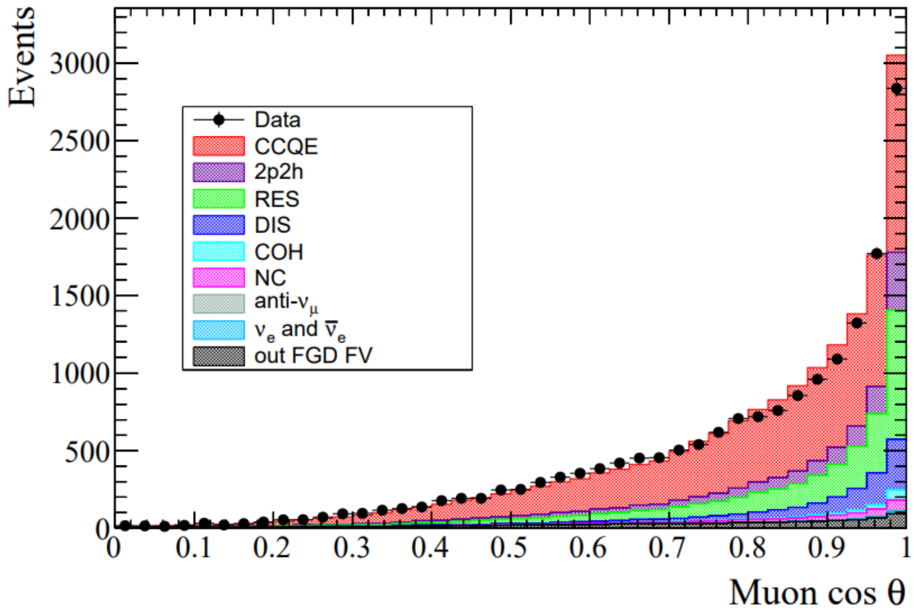

FIGURE 4.1: Distribution of the cosine of the angle between the reconstructed μ direction and the beam direction in the events selected at ND280 for true CC0π interactions by reaction [27]

This thesis describes the performance of the new selection (see Chapter 5) that was developed for the ν_μ charged current multiple pions interactions with and 4π solid angle acceptance; the measurement of the momentum and angular distributions (selecting backward and high angle going tracks) using runs 2, 3, 4 and 8 from production

6T in ND280. This selection has been moved to BANFF (Beam And Nd280 Flux measurement task Force) to be used by the fit to reduce and cross-check the assumptions made to constrain the expected number of events at SK. The selection has the following structure: it first consists of a CC inclusive selection, divided into four samples, depending on the direction of the muon candidate. Each sample is then split into three exclusive samples by either vetoing or requesting the presence of a pion. The CC0π-like samples consist of events without any pions, CC1π^+-like samples contain events with exactly one positive pion, the CCother samples consist of the rest of the events, and with more than one pion or one negative pion.

The different samples of this selection can be used to measure neutrino cross sections with a 4π solid angle coverage to allow a direct comparison of our data in ND280 with SK and other experiments. The sample separation can be used to measure the cross section on the CC1π^+ samples as a function of the muon and positive pion momentum and angle. A measurement of this sample is essential to constraints of both the flux and the cross section parameters.

The 4π acceptance of the SK detector allows for the selection in all directions of leptons produced by neutrino interactions. The expected distributions of cos θ are shown in Figure 4.2 for the ν_e and ν_μ samples.

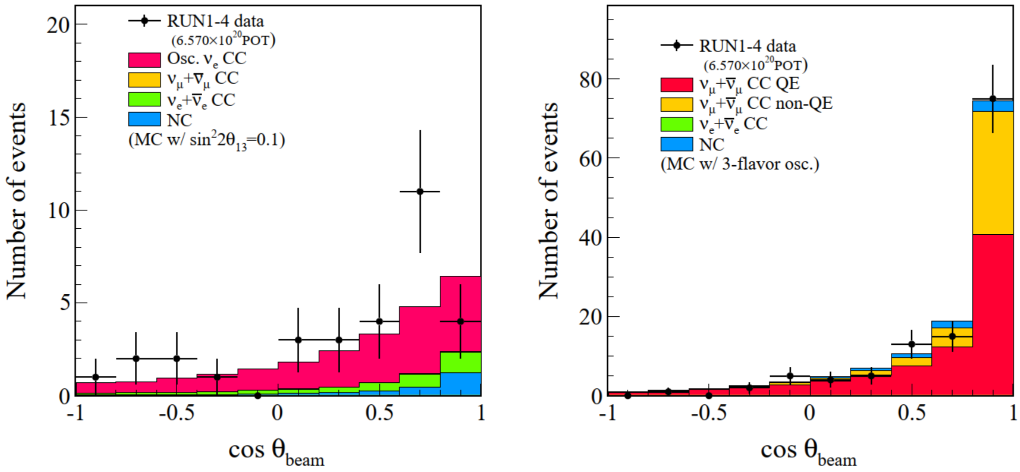

FIGURE 4.2: Distribution of the cosine of the angle between the reconstructed ring direction and the beam direction in the events selected for the ν_e appearance (left) and ν_μ disappearance (right) analysis at SK [27].

In the ν_e appearance channel, 6 of the 28 events have a backward-going electron. The effect is less evident in the ν_μ analysis since there is no cut on the reconstructed energy and the backward events tend to have smaller momenta. Still, even in the ν_μ sample, a non-negligible amount of leptons are produced in the backward direction [45].

4.2 Analysis strategy

The primary aim of this thesis is to provide a better characterization of the physical processes that constitute the main background for the muon neutrino disappearance measurement, particularly the nuclear effects mentioned in chapter 2. To achieve this, a measurement of a flux-integrated, ν_μ $CC1\pi^+$ differential cross section on a hydrocarbon (C_8H_8) target is made as a function of muon and positive pion kinematics.

4.2.1 Signal definition

The signal is defined in terms of the final state particles observed in the detector. The collection of final state particles that define a particular event is denoted as the topology in this thesis. The broad signal definition consists of neutrino interaction events on plastic scintillator (C_8H_8), which contain one negatively charged muon, one positive charged pion, and any number of nucleons as the final state particles where the initial vertex occurred in the fiducial volume of the detector (Figure 4.3). This signal is called CC1π^+ topology, and due to this definition, it removes as much dependence on the interaction modeling[1] as possible.

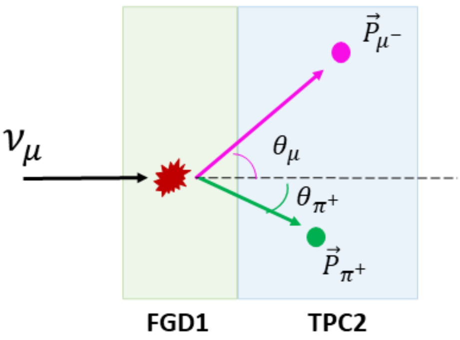

FIGURE 4.3: Schematic of the different signal. TPCs are shown in light blue, FGD1 in light green and ECal in gray.

The event kinematics observable of interest are the measured muon and positive pion momentum (P_μ and P_{π^+}), the cosine of the polar angles between the incident neutrino z-axis[2] and the outgoing muon and positive pion direction ($\cos\theta_\mu$ and $\cos\theta_{\pi^+}$). The neutrino z-axis and the detector z-axis, at ND280, are slightly out of alignment, which is corrected in this analysis. The signal selection has further specific criteria for signal events driven by the detection capabilities of ND280. Since the signal is defined in terms of the final state particles, interactions where a pion was produced in the initial interaction and subsequently absorbed in the nucleus will be lost, but the ones in which a pion was produced in the nuclear medium will be included in the signal definition. Control sample samples are used to assess that the implemented background models can well-describe the data within the freedom afforded to them in their systematic parameters. A summary of the signal and control sample definitions is presented below (more in chapter 6).

- **Signal:** one negatively charged muon, one positive charged pion, and any number of nucleons as the final state particles.
- **Control sample:** one negatively charged muon, one positive charged pion, one other charged pion (charge or neutral), and any number of nucleons as the final state particles.
- **Observables:** Muon momentum and angle (P_μ, $\cos\theta_\mu$) and positive pion momentum and angle (P_{π^+}, $\cos\theta_{\pi^+}$).
- **Flux:** T2K ν_μ flux, version *21bv2*.

---

[1] For example: to correct for pion re-absorption effects

[2] The z-axis is defined to be the direction of the neutrino propagation.

- **Target:** plastic scintillator (C_8H_8) in the FGD1 fiducial volume.
- **Phase space:** Muons with $P_{\mu} \leq 200MeV$ and positive pions with $P_{\pi^+} \leq 160MeV$ (more in chapter 6).

4.2.2 cross section definition

The measurement of the double-differential and quadruple-differential CC1π^+ cross sections on scintillator (C_8H_8) for ND280 is extracted in fit to data as a function of the muon and positive pion kinematics (P_{μ}, cos θ_{μ}, P_{π^+} and cos θ_{π^+}). The cross section is measured as a function of variables directly observable in the detector to reduce the dependence on the nuclear model used in the Monte Carlo (MC) event generator.

The muon and positive pion kinematics variables are directly observable in the detector. In contrast, other reconstructed variables such as the neutrino energy (E_{ν}) or the transferred momentum (Q^2) depend on the underlying model of cross section, and it is important to perform as much as possible a model independent measurement.

A flux-integrated cross section is extracted rather than a flux-averaged or flux-unfolded cross section; this avoids flux corrections that depend on the assumption of neutrino energy. The three standard ways to extract a cross section are flux-unfolded, flux-averaged, and flux-integrated. For the cross section extraction we need: the variable or variables used (x_i), the number of selected signal events in a given bin i (N_i^{signal}), the signal efficiency in each bin ($\epsilon_i^{signal,MC}$), the neutrino flux as a function of the neutrino energy ($\Phi(E_{\nu})$), the integrated flux (Φ), the neutrino energy distribution in each bin ($\mathfrak{w}_i(E_{\nu})$), the number of nucleons in the fiducial volume ($N_{nucleons}^{FV}$), and the bin width (Δx_i).

- **The flux-unfolded cross section (eq 4.3):** In this case we need to know the proper $\mathfrak{w}_i(E_{\nu})$, which makes it strongly dependent on the particular model chosen to apply this correction. Nevertheless, since it has been fully corrected for the flux, it can be used to compare between different experiments directly.

$$\frac{d\sigma}{dx_i} = \frac{N_i^{signal}}{\epsilon_i^{signal,MC} \int_{{E_\nu}_i^{min}}^{{E_\nu}_i^{max}} \mathfrak{w}_i(E_\nu)\, \Phi(E_\nu)\, dE_\nu N_{nucleons}^{FV}} \times \frac{1}{\Delta x_i} \tag{4.3}$$

- **The flux-averaged cross section (eq 4.4):** This case produces experiment-dependent results because it has not been fully unfolded for the particular neutrino flux in each kinematic bin. It is also still model-dependent since an assumption on ${E_\nu}_i^{min}$ and ${E_\nu}_i^{max}$ for each kinematic bin must be made to apply the average flux correction.

$$\frac{d\sigma}{dx_i} = \frac{N_i^{signal}}{\epsilon_i^{signal,MC} \int_{{E_\nu}_i^{min}}^{{E_\nu}_i^{max}} \Phi(E_\nu)\, dE_\nu N_{nucleons}^{FV}} \times \frac{1}{\Delta x_i} \tag{4.4}$$

- **The flux-integrated cross section (eq 4.5):** This case produce experiment-dependent results since no bin-by-bin correction for the flux is applied. It is also completely model-independent since no assumption needs to be made on the particular neutrino energy distribution in each kinematic bin; this is the method used for this analysis.

$$\frac{d\sigma}{dx_i} = \frac{N_i^{signal}}{\epsilon_i^{signal,MC} \Phi N_{nucleons}^{FV}} \times \frac{1}{\Delta x_i} \tag{4.5}$$

cross sections	Kinematic bin	Model dependent
$\frac{d\sigma}{dP_\mu d\cos\theta_\mu dP_{\pi^+} d\cos\theta_{\pi^+}}$	$\Delta x_i = \Delta P_{\mu,i}\,\Delta\cos\theta_{\mu,i}\,\Delta P_{\pi^+,i}\,\Delta\cos\theta_{\pi^+,i}$	No
$\frac{d\sigma}{dP_\mu d\cos\theta_\mu}$	$\Delta x_i = \Delta P_{\mu,i}\,\Delta\cos\theta_{\mu,i}$	No
$\frac{d\sigma}{dP_{\pi^+} d\cos\theta_{\pi^+}}$	$\Delta x_i = \Delta P_{\pi^+,i}\,\Delta\cos\theta_{\pi^+,i}$	No
$\frac{d\sigma}{dE_\nu}$	$\Delta x_i = \Delta E_{\nu,i}$	Yes
$\frac{d\sigma}{dW}$	$\Delta x_i = \Delta W_i$	Yes
$\frac{d\sigma}{dQ^2}$	$\Delta x_i = \Delta Q^2_i$	Yes

TABLE 4.1: Flux-integrated cross sections to be reported in this analysis (in Chapter 9).

This analysis will report several flux-integrated cross sections (see Table 4.1). In order to report a ν_μCC$1\pi^+$ cross section, reconstruction efficiency is defined as 5.8.

The metric used to evaluate the performance of cross section distributions (nominal/post fit) is χ^2 goodness test. This χ^2 is defined as follows:

$$\chi^2 = (\vec{\sigma}_i^{fit} - \vec{\sigma}_i^{true})V_{fit}^{-1}(\vec{\sigma}_i^{fit} - \vec{\sigma}_i^{true}), \tag{4.6}$$

where σ_i is the cross section for bin i^{th} for the post-fit and truth cross section, and V_{fit} is the post-fit covariance matrix; this quantifies the compatibility between the post-fit result and a chosen true distribution.

4.2.3 Fit method

This analysis uses a binned maximum likelihood method to perform a fit to the number of selected events in FGD1 (ND280) fiducial volumes as a function of outgoing muon and positive pion kinematics P_μ, $\cos\theta_\mu$, P_{π^+} and $\cos\theta_{\pi^+}$).

The maximum likelihood components are the total χ^2 (the test statistic minimized by the fit), the Poisson likelihood (how well the MC matches the data), and the penalty term (penalizes fit for moving systematic parameters away from nominal). We want to find a set of parameters that make the MC best describe the data in the fitting process. These parameters should describe the signal to extract (signal fitting parameters) and the background processes which either affect the best set of fit parameters or their error (nuisance parameters). The best fit parameters are those that maximize the likelihood:

$$\mathcal{L} = \mathcal{L}_{stat} \times \mathcal{L}_{syst} \tag{4.7}$$

Or minimizing the logarithm ($-2log(L)$), which approximates the (χ^2) for large data samples (Wilks' Theorem [71]).

$$\chi^2 = \chi^2_{stat} + \chi^2_{syst} = -2log(\mathcal{L}_{stat}) - 2log(\mathcal{L}_{syst}) \tag{4.8}$$

The statistical term ($\mathcal{L}_{stat}$) is the binned Poisson likelihood (using Stirling's approximation):

$$-2log(\mathcal{L}_{stat}) = \chi^2_{stat} = \sum_{j}^{reco\,bins} 2\left(N_j^{MC} - N_j^{DT} + N_j^{DT}\,log\frac{N_j^{DT}}{N_j^{MC}}\right), \tag{4.9}$$

where N_j^{MC} and N_j^{DT} are the number of events in each reconstructed bin j, for MC and data respectively, the systematic term (penalty term) describes how well the nuisance parameters agree with their nominal values, which are our prior on the nuisance parameters.

$$-2log(\mathcal{L}_{syst}) = \chi^2_{syst} = (\vec{a}^{syst} - \vec{a}^{syst}_{prior})^T (V^{syst}_{cov})^{-1} (\vec{a}^{syst} - \vec{a}^{syst}_{prior}), \tag{4.10}$$

where $\vec{a}^{syst}$ are the vector of nuisance parameters, $\vec{a}^{syst}_{prior}$ prior are their prior values, and V^{syst}_{cov} is the covariance matrix describing the confidence in the nominal parameter values as well as correlations between the parameters. The systematic penalty term allows for the use of prior knowledge in the fit from both theory and external experimental data. The systematic parameters are approximated and treated as Gaussian distributions in the fit.

Overall, $-2log(\mathcal{L}_{stat})$ describes how well the data and the simulation agree in reconstructed bins: the smaller the discrepancy, the smaller this term is, while, $-2log(\mathcal{L}_{syst})$ increases as parameters are moved far from their prior values (relative to the prior covariances set on them).

The analysis is tested by running a series of fits to a variety of data inputs produced by altering the nominal MC simulation designed to test a particular aspect of the analysis. The tests are essential to quantify the robustness of the fit to biases in the priors, accurately fit underlying physics, and identify possible failure modes of the fit.

The fit output contains a variety of information that can be used to assess the validity of the fit, including:

- The post-fit set of parameter values and covariance matrices: This can be used to judge if the pulls are reasonable given the input model, and the behavior of model parameters can be studied with fake data studies.
- Likelihood scans each parameter around the best fit point: Can check how Gaussian the likelihood is for a given parameter.
- Pre/post-fit reconstructed distributions and the χ^2 contribution per sample: Can be used to see how well the post-fit agrees with the fake or real data and calculate a p-value for the fake or real data fit.
- Error/log output from the fit routine[3]: Will indicate errors with the minimization, such as if the covariance was forced positive definite or if the fit failed to converge.

4.2.4 Unfolding method

Unfolding is a key part of cross section analyses. Almost all recent results which can be compared to theory/generator predictions are unfolded. The cross section result can be biased if the unfolding is done without care. Neutrino-nucleus interactions are not well understood and therefore should certainly not be confined to one model, so it is crucial to extract a result that is not dependent on the input signal model.

The unfolding method is implemented by allocating a free template weight parameter (denoted as c_i) to each bin of the true distribution, which acts as a normalization constant for that bin, in addition to the nuisance parameters; this allows model independence. The template weight can freely increase or decrease the number of selected

---

[3] like MINUIT output

signal events from the MC in a given bin of true variables (not altering the weight of background events). The effect of changing the number of events in a true bin on the number of events in a reconstructed bin needs to be known to compare to the data distribution.

The fit finds the combination of values for the template weights and the nuisance parameters, which minimizes the χ^2 described above, resulting in a set of post-fit parameters and their uncertainties. The post-fit parameter values are then used to calculate the number of signal events in the true distribution that best fits the data and is subsequently used to extract the cross section. An advantage of this method in contrast to other types of unfolding or a fit for model parameters is that, with fine enough bins, the result is not inherently biased to the shape of the input simulation as the template weights are entirely free to move the signal model since they have no prior constraint. The input simulation is still used to model the background processes, which can be validated by assessing the goodness of fit in control sample regions [1].

In the absence of any systematic fit parameters, these template weights influence the number of expected events (N_j^{MC} used to calculate the likelihood in Eq. 4.9), including background events, from the input simulation as:

$$N_j^{MC} = N_j^{MC,\,signal} + N_j^{MC,\,bkg} = \left[\sum_{i}^{truth\ bins} c_i \cdot \sum_{m}^{in\ bin\ i,j} w_m^{signal} \right] + \left[\sum_{m}^{in\ bin\ j} w_m^{bkg} \right], \quad (4.11)$$

where the index i runs over true kinematic bins, the index j runs over reconstructed kinematic bins, the index m runs over events in bin i, j and w_m is the weight assigned to the event m by the input simulation for signal and background. The background is typically categorized by topology (like CCother or, in this case, CC$1\pi^+1\pi^{\pm,0}$).

In addition to the template weights, the fit includes systematic parameters for cross section model[4], detector, and neutrino flux variations. The total number of selected events in a reconstructed bin can then be rewritten to include these as additional event weights:

$$\begin{aligned} N_j^{MC} = d_j \cdot \sum_{k}^{E_\nu\ bins} f_k \cdot \Bigg(\left[\sum_{i}^{truth\ bins} c_i \cdot \sum_{m}^{in\ bin\ i,j,k} (\sigma_m\, w_m)^{signal} \right] \\ + \left[\sum_{m}^{in\ bin\ j,k} (\sigma_m\, w_m)^{bkg} \right] \Bigg) \quad (4.12) \end{aligned}$$

- The f_k terms are the flux systematic parameters. They will change the modeled behavior of the neutrino flux and give additional weight to the events depending on which neutrino energy bin (k) they fall into. Their prior values describe the neutrino/antineutrino flux and its wrong-sign component. The prior values are defined as one and are constrained by the flux covariance matrix, which the Beam group supplies.

- The d_j terms are the detector systematic parameters. They describe the uncertainty of the way the detector reconstructs events. They act as weights to increase or decrease the total number of events in a reconstructed bin. The nominal values are defined to be one and are constrained by the detector covariance matrix,

---

[4] the theoretical modeling of our signal and background samples is not perfect and contains uncertainties

which is calculated using many toy throws of HighLAND2 detector systematic and enters in the penalty term given in Eq. 4.10.

- The σ_m terms are the model systematic parameters. These weights will depend on the event truth information related to the neutrino interaction and FSI, so they will need to be calculated and applied to each event individually. Each term acts as a weight to account for the effect of altering a model systematic parameter (like M_A^{RES}) that is constrained by the model covariance matrix and has pre-fit prior values obtained by fits to external data.

The fit will vary the template, flux, cross section, and detector parameters corresponding to both signal and nuisance parameters to find the values which best describe the data by minimizing χ^2. It will produce a set of post-fit values, errors, covariance, and correlations for each fit parameter. These best fit parameters (c_i, f_k, and d_j) will be used to re-weight the input simulation. The σ_m weights are computed event-by-event from the best fit values of the model systematic parameters. With this, we can obtain the unfolded number of signal events in the truth kinematics bins that will be used in Eq. 4.5 to obtain the double-differential and quadruple-differential neutrino cross sections:

$$N_i^{signal} = c_i \cdot \sum_{k}^{E_\nu\,bins} f_k \cdot \left[\sum_{j}^{reco\,bins} d_j \cdot \sum_{m}^{in\,bin\,i,j,k} (\sigma_m\, w_m)^{signal} \right] \tag{4.13}$$

This analysis is a blinded analysis where the entire analysis was developed with MC simulation without looking at the data. The procedure to unblind and perform the fit to data and check its validity is the following:

- Prepare and process data into the proper format for the fit.
- Run the control samples only fitting to data
- Check for mechanical fit failures from Minuit log output.
- Check reconstructed event distributions.
- Check post-fit values and errors by looking for parameters that were pulled outside their prior 1σ uncertainties, or for parameters with unrealistic post-fit constraints compared to the prior uncertainty using the Asimov studies as a guideline for expected sensitivity.
- Run full fit with signal and control samples.
- Check for mechanical fit failures as before.
- Check reconstructed event distributions.
- Check post-fit values and errors. Looking for the same criteria as the control samples.

Maximum likelihood fit has shown good performance in the past, and it will be the unfolding procedure for this analysis.

4.2.5 Monte Carlo and data sets

The data taking periods that are used in this analysis, and the corresponding MC and sand[5] samples, are detailed in Table 4.2 along with the number of protons on target (POT) for each sample. Detector conditions were taken into account by generating separate MC samples splitting runs into periods with water (w) and air (a) in the P0D sub-detector. The current results rely on MC processed with the production 6T[6] using runs 2, 3, 4, and 8. The same sand MC files are used with each data run.

Sample	MC magnet POT	Data POT	Sand POT	Period
Run 2w	1.20375×10^{21}	4.33502×10^{19}	1.04833×10^{21}	Nov. 2010 → Feb. 2011
Run 2a	1.68019×10^{21}	3.59885×10^{19}	1.04833×10^{21}	Feb. 2011 → Mar. 2011
Run 3a	3.05005×10^{21}	1.59337×10^{20}	1.04833×10^{21}	Mar. 2012 → Jun. 2012
Run 4w	2.18428×10^{21}	1.69529×10^{20}	1.04833×10^{21}	Oct. 2012 → Feb. 2013
Run 4a	2.10003×10^{21}	1.78927×10^{20}	1.04833×10^{21}	Feb. 2013 → May. 2013
Run 8w	9.60684×10^{21}	4.92944×10^{19}	1.04833×10^{21}	Oct. 2016 → Dec. 2016
Run 8a	1.48441×10^{21}	1.73408×10^{20}	1.04833×10^{21}	Jan. 2017 → Apr. 2017
Total	2.13095×10^{22}	8.09835×10^{20}	7.33831×10^{21}	

TABLE 4.2: T2K data-taking periods in neutrino mode and the POT used in this analysis for data and MC.

---

[5] 'Sand' refers to the interactions that occur outside of the N280 detector, and are simulated with a separate set of files to the standard MC(which is also known as 'Magnet MC')

[6] 'Production' refers to the MC that is generated using NEUT (version is 5.4.0. in this case). New MC is generated constantly

Chapter 5

Selection Development

This chapter presents the framework used, the selection development, and the performance of this new 4π acceptance selection.

5.1 HighLAND2 framework

The analysis was performed using a high-level framework called "HighLAND2" (High-Level ANalysis Development), which is designed to simplify the process of analyzing data in particle detectors. It allows the user to develop selections, run analyses, plot results, and evaluate the impact of systematic errors. Two sets of packages were implemented (HighLAND2 and PSyChE) to allow this.

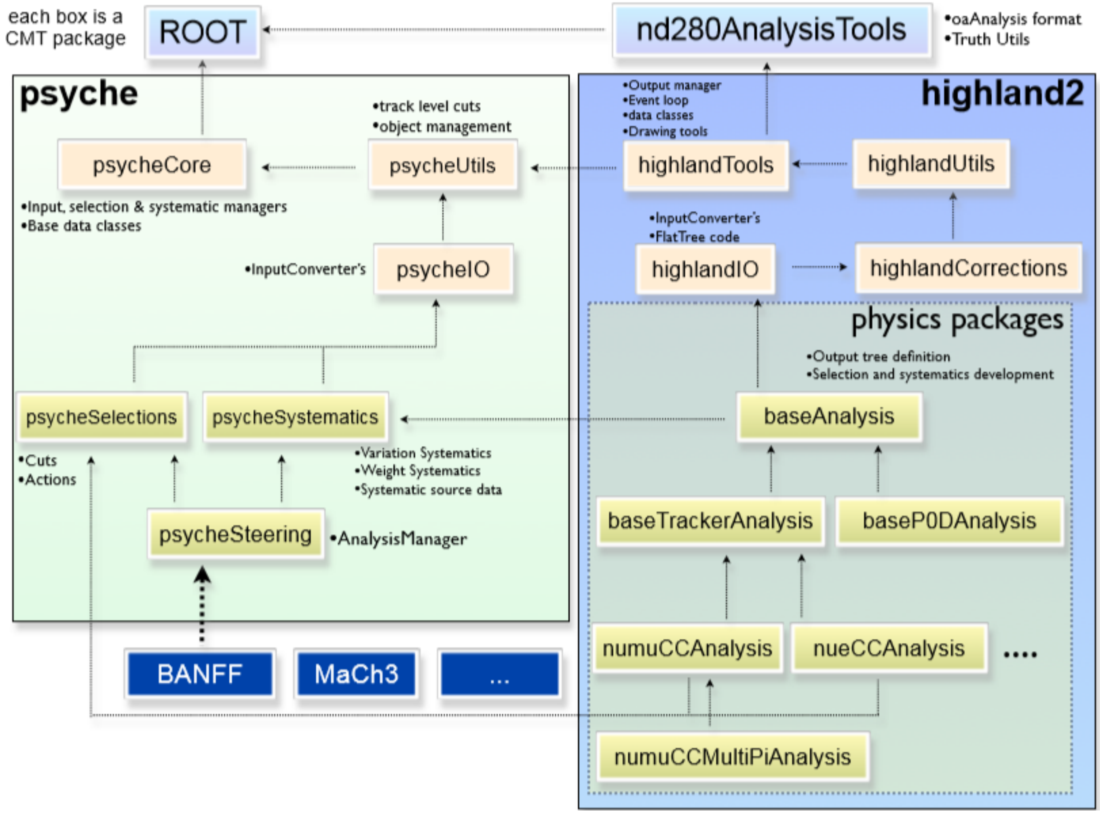

FIGURE 5.1: Structure of the framework and package hierarchy of HighLAND2

HighLAND2 uses the PSyChE (Propagation of Systematics and Characterization of Events) packages as the core. In practice PSyChE is part of the HighLAND2 distribution (Figure 5.1). PSyChE is a high-performance set of packages that perform event selection, propagation of systematics, and generalization of the BANFF interface. The main reason to keep PSyChE and HighLAND2 separated is that PSyChE should run directly by fitters on an event-by-event basis. The framework's core is usually developed only by HighLAND2 experts, while there is more freedom in the non-PSyChE part.

5.2 Previous selections

A selection needs to be developed (if not present in Highland2). In the case of this analysis, the objective was to study a CC1π^+ signal with 4π solid angle acceptance. Present in the code were two selections developed by previous IFAE students:

- NuMuCCMultiPi [61]: Developed by Raquel Castillo in 2015, this selection focused on multipion tracks signals and analyzed the only forward-going tracks. Figure 5.2 shows the efficiency of CC1π as a function of the muon kinematic of these samples.
- NuMuCC4pi [45]: Develop by Alfonso Garcia in 2017, this selection was the first one that tried to recover muons in 4π solid angle acceptance. Figure 5.3 shows an example of the kinematic of this sample.

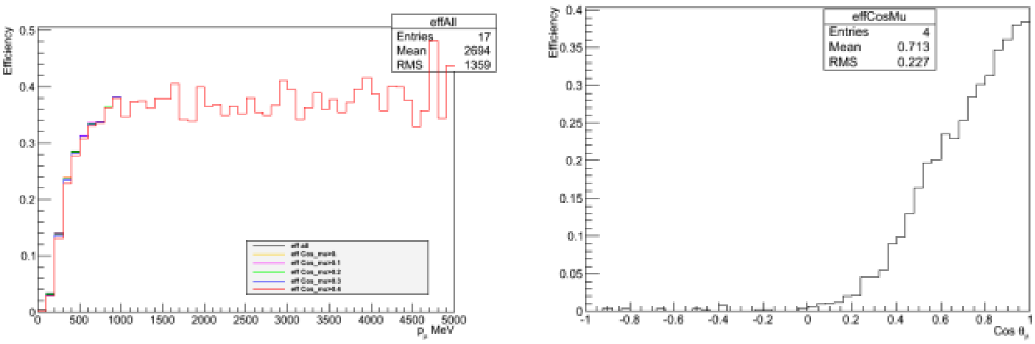

FIGURE 5.2: Efficiency CC1π as function of the muon kinematic using NuMuCCMultiPi selection [61].

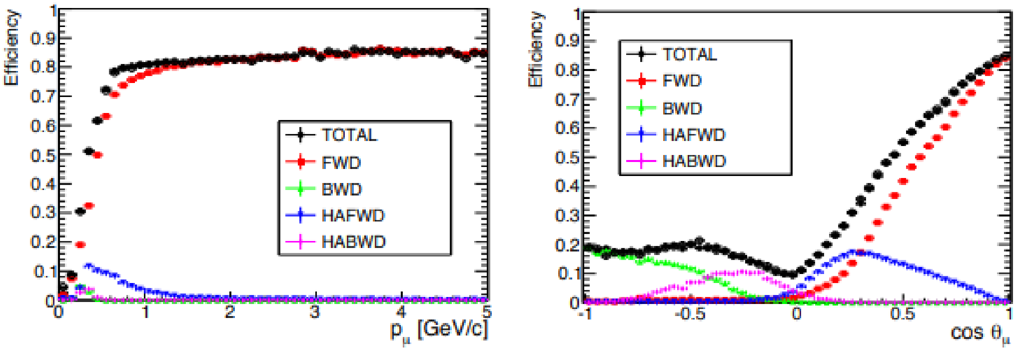

FIGURE 5.3: Efficiency CC1π as function of the muon kinematic using NuMuCC4pi selection [45].

So based on these selections, a new one was developed that allow us to study four main signals (CCinclusive, CC0π, CC$1\pi^+$ and CCother) and two sub-signals of CCother (CC$1\pi^+1\pi^\pm$ and CC$1\pi^+1\pi^0$) each with 4π acceptance.

5.3 Selection development

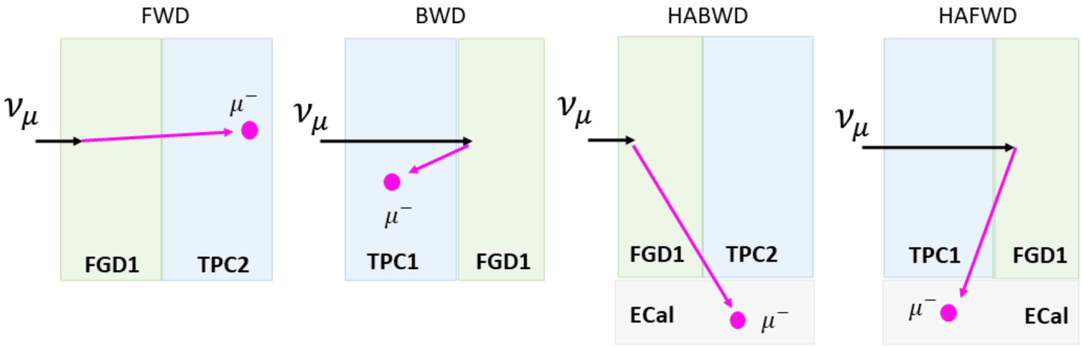

FIGURE 5.4: Schematic of the 4 directions of interest. FWD and BWD going tracks need to leave at least 19 reconstructed clusters in the TPC. HAFWD and HABWD tracks either have less than 19 TPC clusters or miss the TPC completely. TPCs are shown in light blue, FGD1 in light green, and ECals in light gray.

The present selection NuMuCC4piMultiPi[1] is based on the two selections described before. Events are split into different branches according to the direction of the muon candidate. It has been optimized to select forward-going (FWD) tracks (muon, proton, pions, etc.) originating in the FGDs and leaving at least 19 reconstructed clusters in the TPCs. With this selection, we aim to include backward-going (BWD) tracks applying the same cut as forward-going tracks but in the opposite direction. Additionally, high angle (HAFWD and HABWD) tracks with less than 18 (≤ 18) reconstructed clusters in the TPCs or completely missed them are also selected.

In the FWD and BWD branches, the muon candidate must have long TPCs segments (at least 18 reconstructed clusters as defined previously), while tracks with short or no TPC segment are used in the HAFWD and HABWD (Figure 5.4). After the separation by the different directions, the further categorization of the event is based on the topology. The selection is implemented following the scheme in Figure 5.5, where we have three blocks:

- General quality
- CC4pi inclusive
- CC4piMultiPi exclusive

Each of these blocks is formed by a certain number of steps. A detailed explanation for the most important selection steps (cuts and actions) is explained in this section.

---

[1] Tecnical steps to install the selection can be found on Appendix B

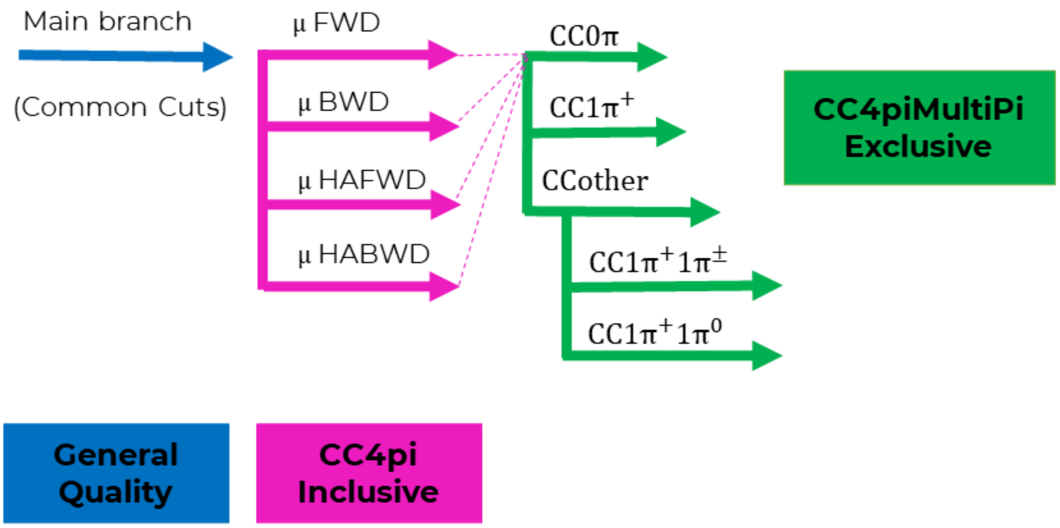

FIGURE 5.5: Schematic of the different stages of the selection.

5.3.1 Topology categorisation

The topology categorization is defined by looking at the true particle type for MC when they leave the nucleus after the neutrino interaction; this is what we refer to as a reaction-like interaction. The different topologies (Figure 5.6) are described below for forward horn current (FHC) events.

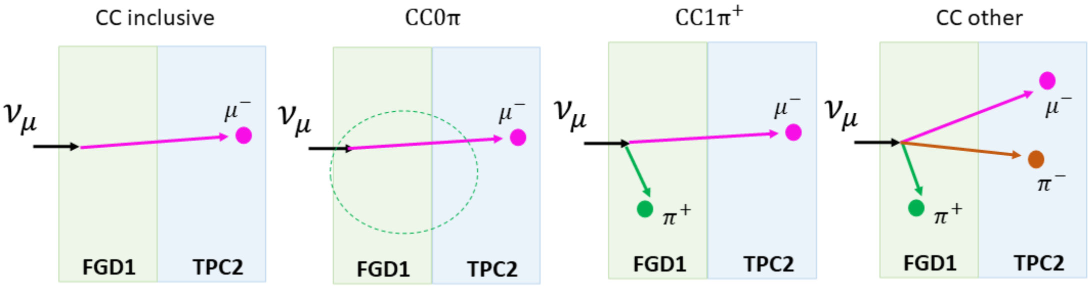

FIGURE 5.6: Schematic of the different signal topology. TPCs are shown in light blue and FGD1 in light green.

- *CC*0π: defined as events with a true negative muon and without any (charged or neutral) pions in the final state.
- *CC*$1\pi^+$: defined as events with a true negative muon and one positive pion and no negative or neutral pions in the final state. The positive pion can be observed in the TPC, in the ECaL, as an isolated track in the FGD, or via Michel electron tagging. (Figure 5.7).
- *CCother* corresponds to the rest of the CC events that are not in the first two topologies; this means events with a true negative muon and at least one neutral or negative pion, or with more than one positive pion. It also includes events with exotic particles (kaons or eta) that do not come from neutral current interactions.

- *Background (BKG)*: our background topology is composed of neutral current signals.
- *External (OOFV)*: we tag as external topology events, those where the vertex of the interaction is outside the FGD1 fiducial volume as defined in section 5.3.2.

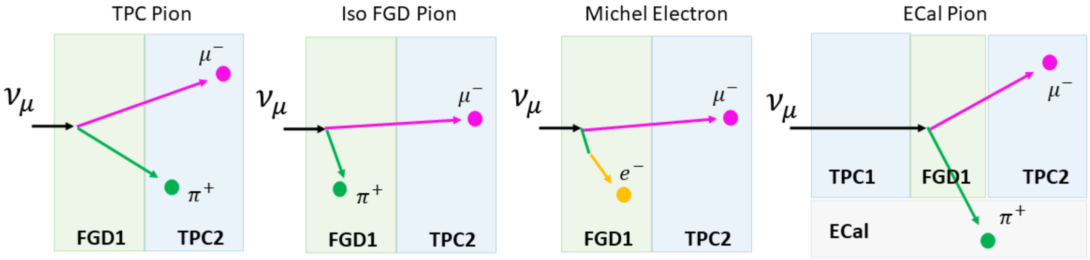

FIGURE 5.7: Schematic of the sub-detectors where we can find the positive pion for the CC1π^+ topology. TPCs are shown in light blue, FGD1 in light green, and ECals in light gray.

5.3.2 Selection steps

Now we will discuss the different steps implemented to form the selection.

Event quality cut

It is required that the full spill has an excellent global ND280 data quality flag. Events must occur within the bunch time windows of the neutrino beam. Since we can assign an event to a particular bunch based on its timing, we treat two neutrino interactions within the same spill but in different bunches as two independent events; this allows us to avoid a pile-up of events [27].

Event time quality cut

Since the 4π acceptance selections depend on the time of flight for the flipping of the track is very important to guarantee that the track has a good time quality. This cut is relatively new and implemented due to bad quality sub-runs in run number 8 of production 6T.

ToF flipping

It is known that there are data/MC discrepancies for the timing, so after removing the bad timing information, the MC prediction must be corrected, and systematic uncertainty must be evaluated. Since this work used a new production of MC (production 6T), these corrections had to be re-computed and implemented. In the past, only a set of corrections was computed for all the MC runs; one of my contributions was to re-compute these corrections for each run using neutrinos and antineutrinos. The ToF is used to determine when is forward or backward going tracks. It is crucial to correct the ToF before selecting the cut that will flip the track or not. To correct the ToF information, we need to comply with the following steps:

- Produce control samples with similar kinematics to muon like tracks in the selection (Figure 5.8 top left).

- For each control sample, fit data/MC ToF distributions using two Gaussian (Figures 5.8 top right).

- Use the sigma and mean differences of those Gaussian to smear the MC distributions (Figures 5.8 bottom).

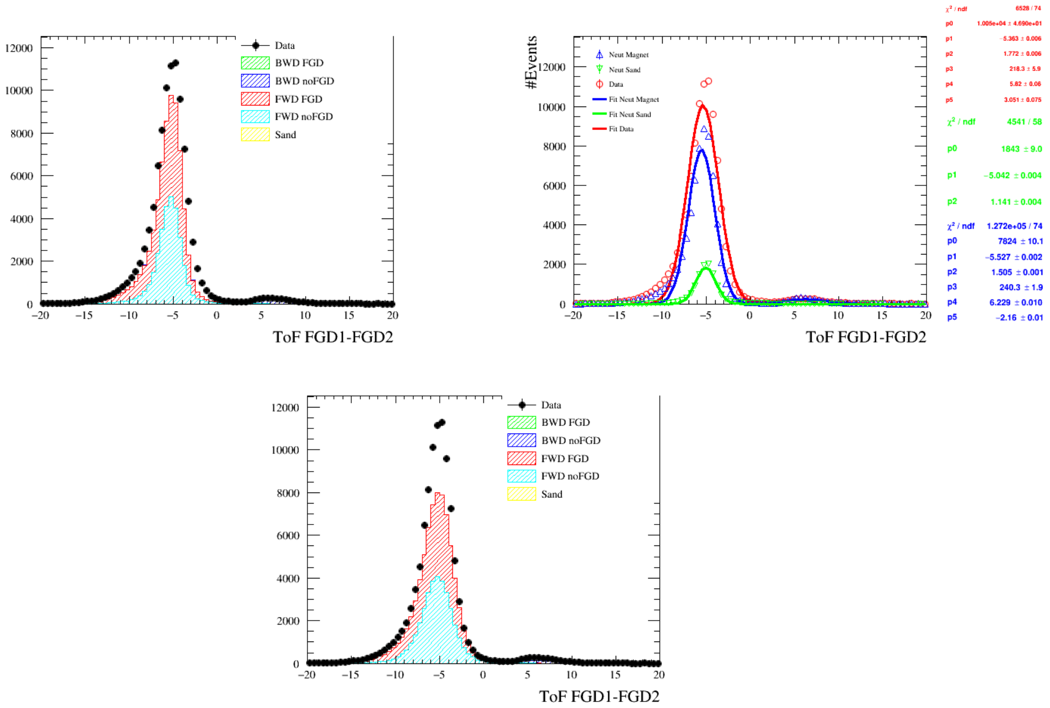

FIGURE 5.8: Number of events vs the ToF (in ns) distributions without any correction apply (top left), two Gaussian fit of the ToF distributions without any correction apply (top right) and ToF distributions after correction are apply (bottom). For runs 2 to 4 and for the FGD1_FGD2_MC_TrueFwd ToF topology.

Figure 5.8 presents each of the steps for obtaining the ToF correction for a specific ToF topology (the plots for all topologies are reported in the Appendix C). Now when we talk about ToF topology, it refers to a different path and true direction that the track has (Figure 5.9). The new correction values obtained for runs 2-4 and run 8 are presented in Table 5.1.

topology	runs 2-4		run 8	
	$\Delta\mu$[ns]	$\Delta\sigma$	$\Delta\mu$ [ns]	$\Delta\sigma$
kP0D_FGD1_MC_TrueFwd_Track	-1.100	0.220	0.130	0.000
kP0D_FGD1_MC_TrueBwd_Track	-1.000	2.160	0.000	0.540
kP0D_FGD1_Sand_Track	-0.145	1.940	-0.419	2.000
kP0D_FGD1_MC_TrueFwd_Shower	-1.190	4.420	-1.120	0.497
kP0D_FGD1_MC_TrueBwd_Shower	-0.730	0.417	-1.520	0.510
kP0D_FGD1_Sand_Shower	0.012	0.330	-0.205	1.450
kFGD1_FGD2_MC_TrueFwd	0.118	0.794	-1.300	2.050
kFGD1_FGD2_MC_TrueBwd	-0.562	5.590	-1.050	0.099
kFGD1_FGD2_Sand	-0.330	1.710	-0.347	1.498
kECaL_FGD1_MC_LAStartFgd_TrueFwd_Shower	0.169	1.840	0.397	1.310
kECaL_FGD1_MC_LAStartFgd_TrueBwd_Shower	1.600	3.030	1.800	2.050
kECaL_FGD1_MC_LAStartFgd_TrueFwd_Track	-0.189	2.080	0.157	1.720
kECaL_FGD1_MC_LAStartFgd_TrueBwd_Track	0.945	6.620	0.739	2.070
kECaL_FGD1_Sand_LAStartFgd_Shower	0.298	1.660	0.482	2.600
kECaL_FGD1_Sand_LAStartFgd_Track	-0.297	1.570	0.073	2.610
kECaL_FGD1_MC_LAEndFgd_TrueFwd_Shower	0.047	5.640	0.047	1.610
kECaL_FGD1_MC_LAEndFgd_TrueBwd_Shower	-0.531	0.570	-2.440	0.000
kECaL_FGD1_MC_LAEndFgd_TrueFwd_Track	-1.120	3.080	-1.060	1.270
kECaL_FGD1_MC_LAEndFgd_TrueBwd_Track	-1.030	3.500	-1.850	2.180
kECaL_FGD1_MC_HAStartFgd_TrueFwd_Showe	0.763	1.880	0.496	1.180
kECaL_FGD1_MC_HAStartFgd_TrueBwd_Shower	1.410	2.700	2.110	0.410
kECaL_FGD1_MC_HAStartFgd_TrueFwd_Track	0.468	1.980	0.537	0.990
kECaL_FGD1_MC_HAStartFgd_TrueBwd_Track	0.172	2.170	0.439	1.710
kECaL_FGD1_Sand_HAStartFgd_Shower	0.846	3.230	0.586	1.430
kECaL_FGD1_Sand_HAStartFgd_Track	-0.208	1.320	-0.093	1.610
kECaL_FGD1_MC_HAEndFgd_TrueFwd_Shower	0.830	4.420	1.930	0.820
kECaL_FGD1_MC_HAEndFgd_TrueBwd_Shower	0.778	0.556	1.800	0.000
kECaL_FGD1_MC_HAEndFgd_TrueFwd_Track	-0.475	1.420	-0.242	1.800
kECaL_FGD1_MC_HAEndFgd_TrueBwd_Track	0.009	3.750	-0.119	1.985
kECaL_FGD1_Sand_HAEndFgd_Shower	0.924	4.360	1.050	2.450
kECaL_FGD1_Sand_HAEndFgd_Track	-0.633	4.030	-0.317	2.060

TABLE 5.1: New ToF correction values computed for ν_μ.

After correcting the ToF then we can use it to flip the tracks (see Figure 5.10). For each couple of detectors (A and B), time of flight variables are defined as:

$$ToF_{A-B} = T_B - T_A \tag{5.1}$$

Cuts on the ToF variables have been optimized to separate backward from forward-going tracks; this means that if $ToF_{A-B} > 0$, the tracks originated in detector A. Based on this information, tracks can be flipped to the correct sense. When this happens, the start and end position of the track is switched, and the charge of the track is multiplied by -1[2].

---

[2] The momentum loss (in FGD1) will be affected with the flipping, so it is re-computed.

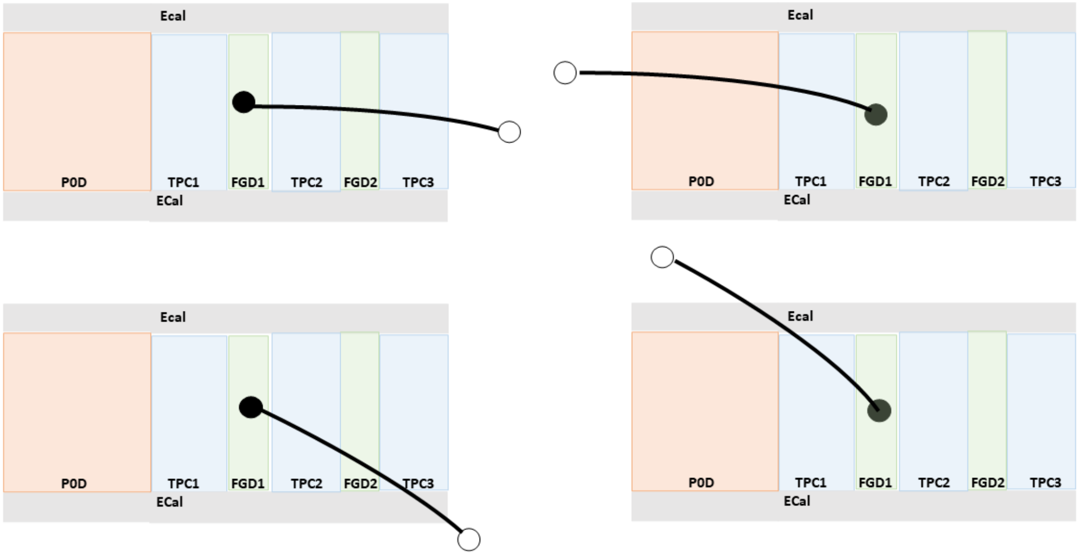

FIGURE 5.9: Different ToF topologies based in the start or end of the track and the angle. LowAngle-start (top left), LowAngle-end (top right), HighAngle-start (bottom left) and HighAngle-end (bottom right). Start point (solid) and end point (open) [27]. TPCs are shown in light blue, FGD1 in light green, ECals in light gray, and P∅D in light orange.

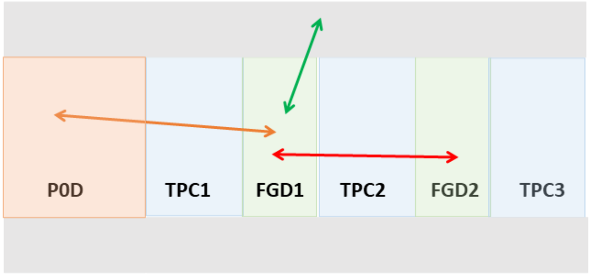

$$ToF_{P0D-FGD1} = t_{FGD1} - t_{P0D}$$
$$ToF_{ECal-FGD1} = t_{FGD1} - t_{BrECal}$$
$$ToF_{FGD1-FGD2} = t_{FGD2} - t_{FGD1}$$

FIGURE 5.10: Important ToF definitions for FGD1. TPCs are shown in light blue, FGD1 in light green, ECals in light gray, and P∅D in light orange.

Total multiplicity cut

The idea of these common steps is to reduce the number of events to those that at least have tracks reconstructed within either FGD1 or FGD2; this allows us to reduce the computational time for the following steps. Only those events where at least one reconstructed track crosses one of the FGDs are considered ([27]).

Sort tracks action

In this action, the tracks are sorted based on the sub-detectors segments into:

- Low angle tracks: tracks with long TPC segments that start or end in the FGDs.
- High angle tracks: tracks with short TPC segments that start or end in the FGDs or tracks with an ECaL segment that start or end in the FGDs.

A ”track” is defined as having a long TPC segment if it has more than 18 hits strictly; otherwise, it is defined as having a short TPC segment. For low-angle tracks, the TPC reconstruction can determine the momentum and particle identification. For high-angle tracks, momentum and particle identification use the particle range and ECaL information, respectively.

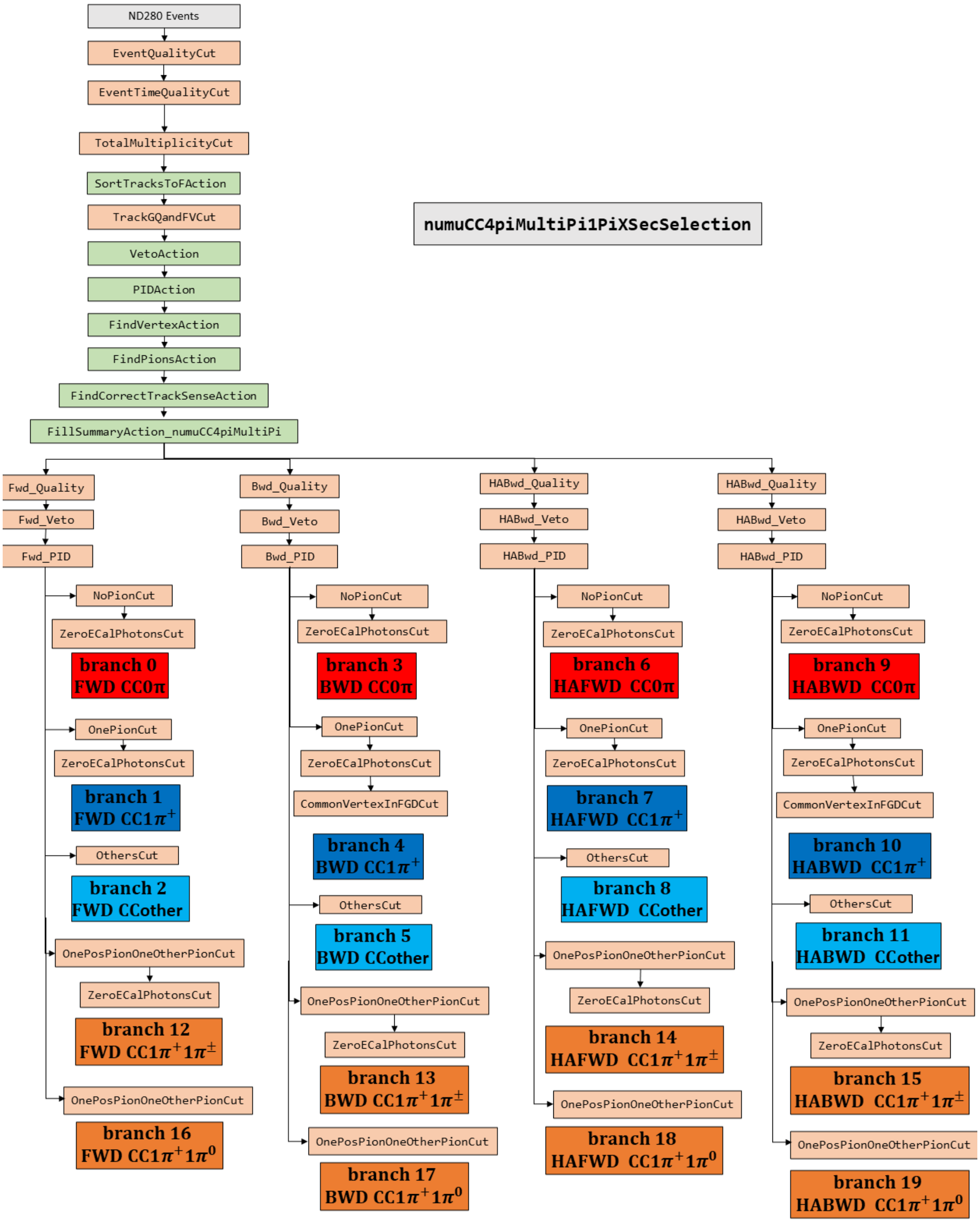

FIGURE 5.11: Schematic of the different cuts of the selection.

Track general quality and FV cut

It is checked that the track starts in the fiducial volume (FV) of either FGD1 or FGD2. The tracks are then distributed in the four directions based on the end position:

- Low angle tracks: FWD and BWD
- High angle tracks: HAFWD and HABWD

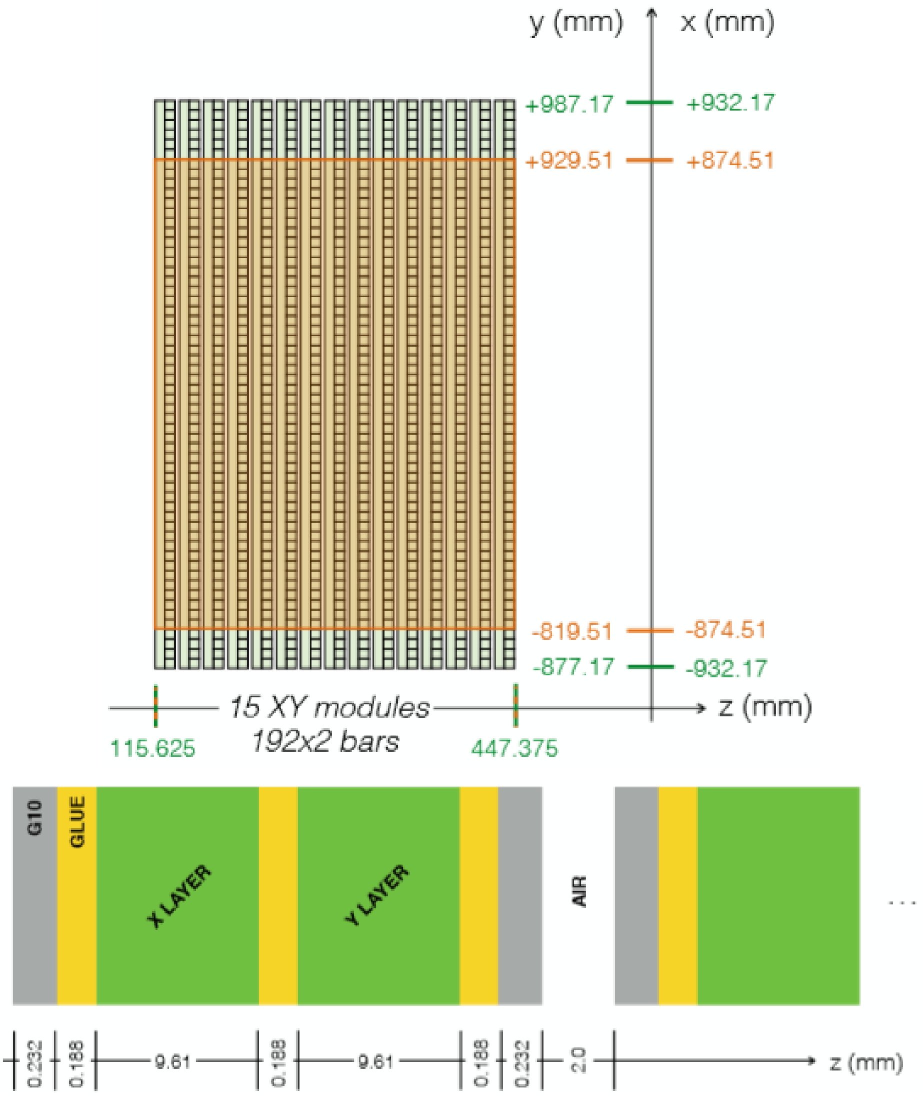

FIGURE 5.12: Top: FGD1 scheme. Orange lines indicate the fiducial volume. Bottom: Scintillator layers scheme

The interactions have to have their vertex within a certain fiducial volume in FGD1/FGD2. The fiducial volume definition depends on the direction of the muon track. For FGD1 it is defined as: $|x| < 874.51$ mm, $|y - 55| < 874.51$ mm, $125.750 < z < 447.375$ mm, where 55 mm offset in y-direction reflects 55 mm shift of the XY modules according to the center of the ND280 coordinate system (see Figure 5.12). Cuts in the X and Y direction accept only interactions with a vertex 5 bars distant from the edge of the XY module of FGD1. The definition of the fiducial volume cut in Z includes all 15 modules of FGD1, except the first. Additionally, for tracks with low or no TPC information (HA tracks), we remove the last layer along the beamline (along the Z-axis) of FGD1.

Veto action

Sometimes, a track enters the FGD and is broken by the reconstruction, thereby being mistaken for a muon starting in the FGD. We first look for the particle with the highest momentum after the muon candidate to find those broken tracks. We then use the momentum ratio and the distance between the start positions to cut on the background. We reject the event if:

- $Z_{Start,veto} - Z_{Start,\mu} < -100$ mm (-150 mm, -400 mm)
- $p_{veto}/p_{\mu} > 0.8(0.9, 0.9)$,

where the numbers in parentheses denote the cuts for the HAWFD and HABWD branches respectively.

For forward-going muons, we add another condition: if the muon candidate starts in the last two layers of the FGD and at the same time at least one other track in the FGD with no TPC segment, then we reject the event. For backward-going muons, we remove tracks that start in the second layer of the FGD, regardless of whether there is an additional activity or not. Note that this results in a tighter definition of the FV for backward-going tracks.

Muon PID cut

This cut is used to identify muon candidates. The cut treats low-angle (FWD and BWD) tracks differently from high-angle tracks.

Particle likelihoods are computed using particle pulls. A pull is defined as the difference of measured and expected energy deposition dE/dx, normalized by the energy resolution σ_i for this particle type (i):

$$Pull_i = \frac{\frac{dE}{dx}_{meas} - \frac{dE}{dx}_{expected,i}}{\sigma_i}. \tag{5.2}$$

These pulls can be transformed into a Gaussian with mean 0 and sigma 1 for the particle i by computing the exponential of the squared pull:

$$P_i = exp\left(-\frac{Pull_i * Pull_i}{2}\right). \tag{5.3}$$

The likelihood is finally computed by normalizing the Gaussian probability by all particle probabilities:

$$L_i = \frac{P_i}{\sum P_i}, \tag{5.4}$$

where the sum in the denominator goes over all particle hypotheses: muons, protons, electrons and pions.

Low angle tracks: These tracks have long segments in the TPC and therefore one can use the TPC PID information. Different PID conditions are defined for FWD and BWD tracks as shown in Figures 5.13 5.14 5.15 respectively. The optimization of the FWD muon PID cut can be found in [27].

- FWD tracks are selected as muons according to the following criteria:
  - if P $\geq$ 280 MeV then the track should not stop in FGD2,

  - if the track enters the barrel ECaL or stops in the downstream ECaL, it is required that the ECaL PIDMipEm[3] variable has a value lower than 15.
  - $L_\mu > 0.05$,
  - if $P < 500$ MeV then $L_{MIP} = \frac{L_\mu + L_\pi}{1 - L_p} > 0.8$.

- For the selection of BWD muons we have the following criteria:
  - if P < 200 MeV, then $L_{MIP} > 0.65$,
  - if P $\leq$ 200 MeV, then $L_\mu > 0.05$.

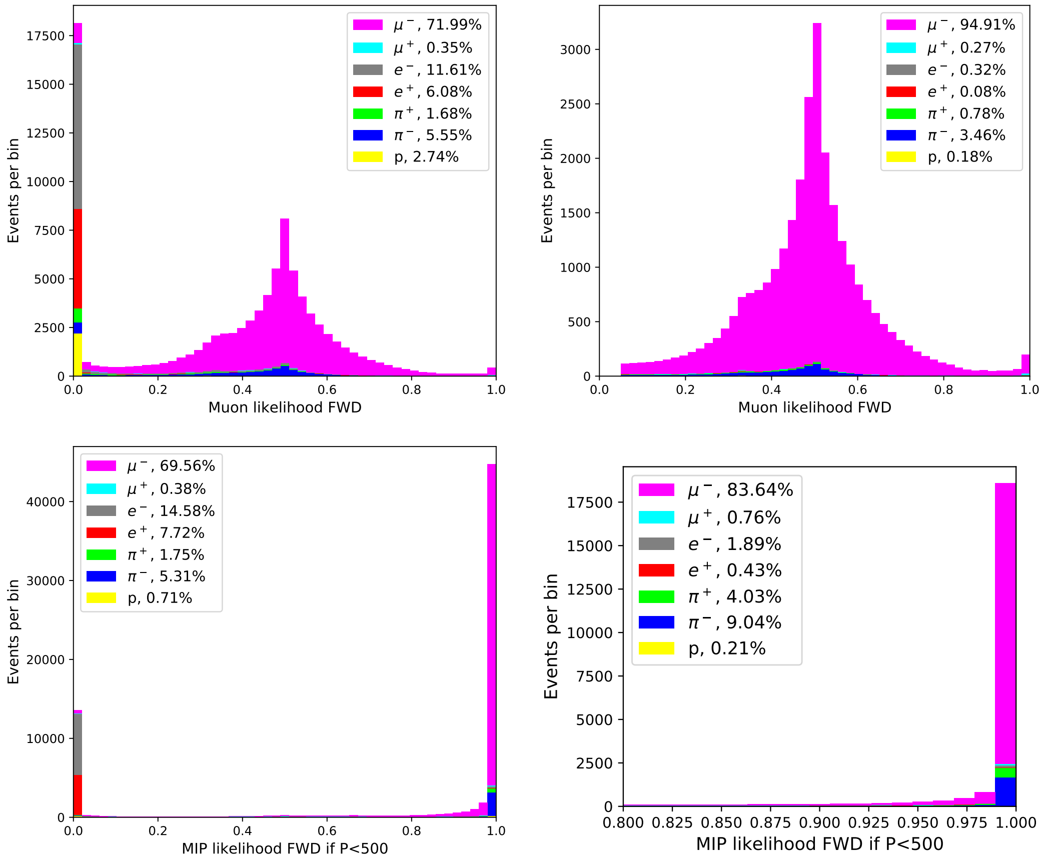

FIGURE 5.13: Muon likelihood L_μ before (top left) and after the cut (top right). Different variables used for muon PID in low angle tracks for the FWD. Minimum ionising particle likelihood L_{MIP} before (bottom left) and after the cut (bottom right).

---

[3] The PIDMipEm variable distinguishes between tracks and showers. Objects with negative values are track-like, while objects with positive PIDMipEm are shower-like.

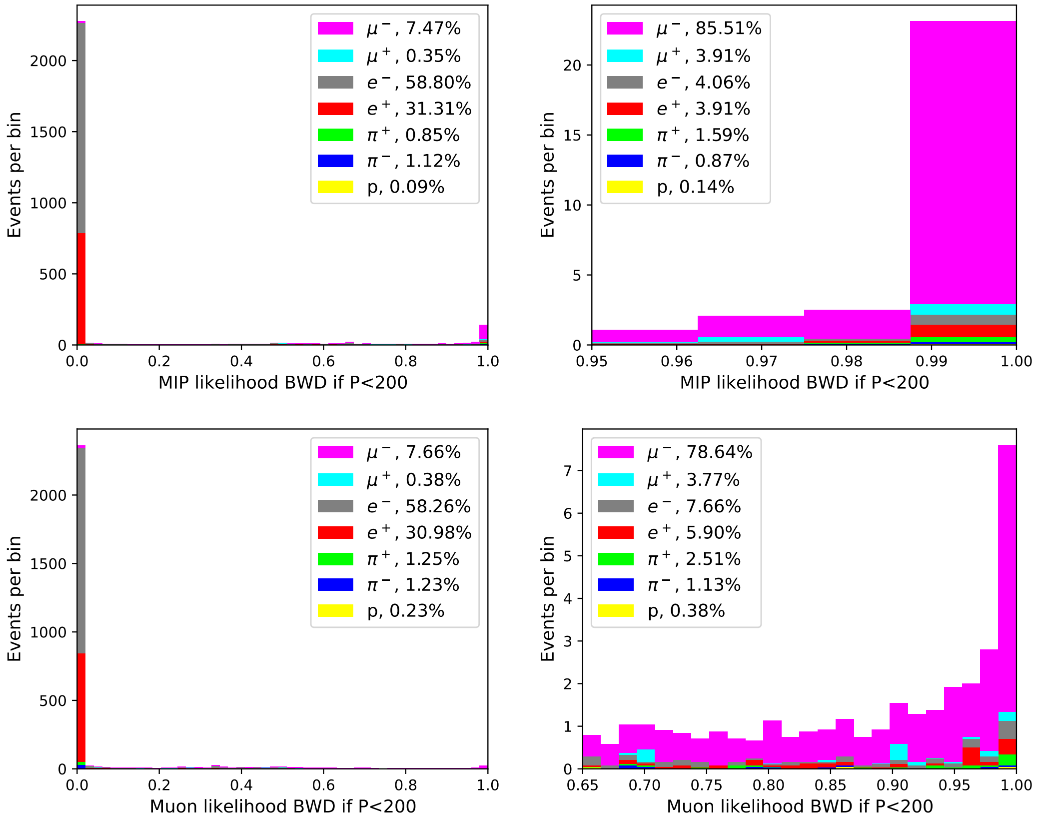

FIGURE 5.14: Different variables used for muon PID in low angle tracks for BWD muons with momentum $< 200\ MeV$. Minimum ionising particle likelihood L_{MIP} before (top left) and after the cut (top right). Muon likelihood L_μ before (bottom left) and after the cut (bottom right).

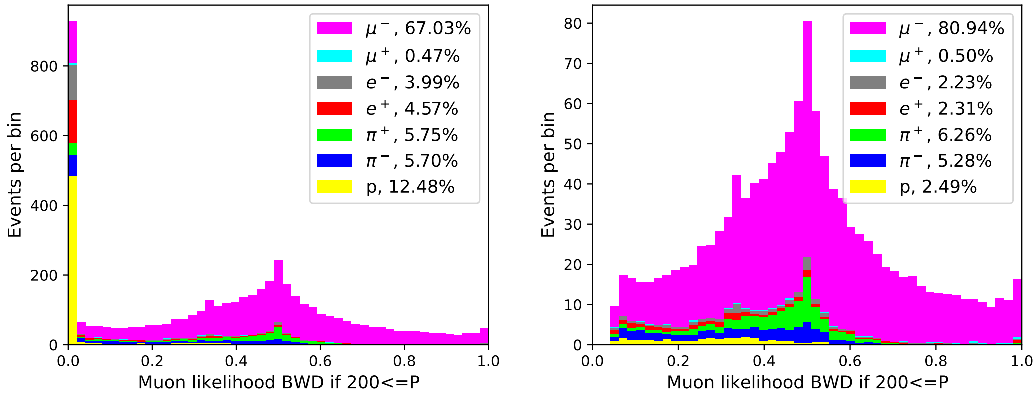

FIGURE 5.15: Different variables used for muon PID in low angle tracks for BWD muons with momentum $\geq 200\ MeV$. Muon likelihood L_μ before (left) and after the cut (right).

High angle tracks: These tracks do not leave enough information in the TPC, and therefore the PID has to be done differently using the information from the ECaL and the SMRD. We distinguish between tracks entering the SMRD and tracks stopping in the ECaL. If a track enters the SMRD, we tag it immediately as muon since this is strong enough criteria by itself. If the track stops before in the ECaL, then we cut on high-level PID variables (PIDMipEm) and the length and energy of the track (Figure 5.16):

- $-100 < \text{PIDMipEm} < 0$
- $1.0 < \text{Length/EMEnergy} < 2.6$

As explained before, the PIDMipEm variable differentiates between tracks and showers in the ECaL (PIDMipEm < 0 is track-like, and PIDMipEm > 0 is showers-like). The optimization of the HA muon PID cut can be found in [27].

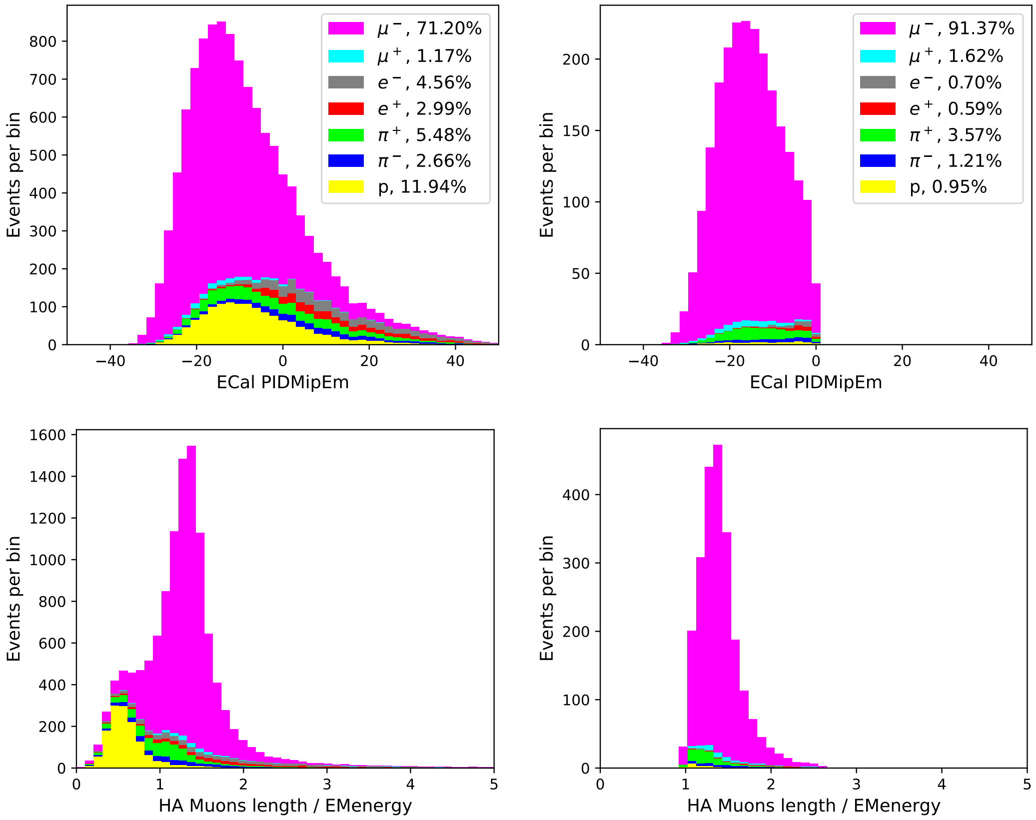

FIGURE 5.16: The variables used for identifying muons at HA. PIDMipEm (is a measure if a track is more track-like (< 0) or shower-like (> 0)) before (top left) and after the cut (top right). The ratio of track length and deposited electromagnetic energy in the ECaL before (bottom left) and after the cut (bottom right).

Pion PID cut

To select charged pions, we start by selecting two categories of tracks: tracks with good TPC information (tracks with at least 19 TPC hits) or isolated tracks confined to the FGD. We always make sure to ignore the main muon track to avoid double-counting of tracks; neutral pions are selected by detecting electrons and positrons in the TPC. The cuts for each category are explained in more detail in the following paragraphs.

TPC pions: We first look at positively charged tracks. We tag the tracks as the particle with the highest likelihood (as defined in Eq. 5.4). There is one exception to this rule: if the most positron likelihood is the highest, but the track's momentum is bigger than $900\ MeV$, we tag the particle as a proton. Negatively charged tracks are tagged as pions if $L_\pi > 0.8$. All other particles are tagged as electrons. Since a muon candidate has already been selected, there is no need to check the muon likelihood. The likelihood of the final pion candidates is shown in (Figure 5.17).

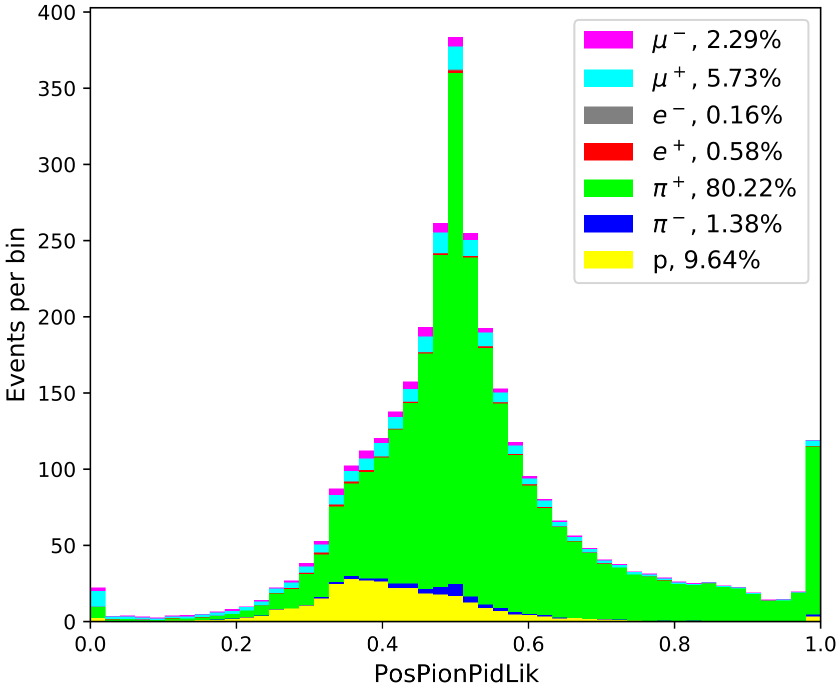

FIGURE 5.17: Distribution of the Pion likelihood used to select positive TPC pions.

Isolated FGD pions: When there is no information from the TPC, we can look at tracks contained in the FGD. For this, we only look at tracks that start and end in the FGD fiducial volume. We then require that the pion pull is within certain bounds (Figure 5.18):

$$-2.0 < Pull_\pi < 2.5 \tag{5.5}$$

The final cuts were optimized by looking at the product of selection efficiency (defined as the number of correctly selected pions divided by the total number of FGD contained pions) and the purity of the selected pions. The optimization of this cut can be found in [30].

Michel electron tagged pions: Low momentum pions that decay before reaching the TPC can be selected via Michel electron tagging. Michel electrons are selected by requiring at least 6 hits in FGD1 with a time delay of 100 ns or more. Further reading and detailed study of this cut can be found in [51].

Multiple pions cuts

The CCinclusive selection is split into three samples based on the number of reconstructed pions. The CC0π sample consists of events without any reconstructed pions, CC$1\pi^+$ are events with one reconstructed positive pion, and CCother sample consists of events with more than one reconstructed pion or one negative pion.

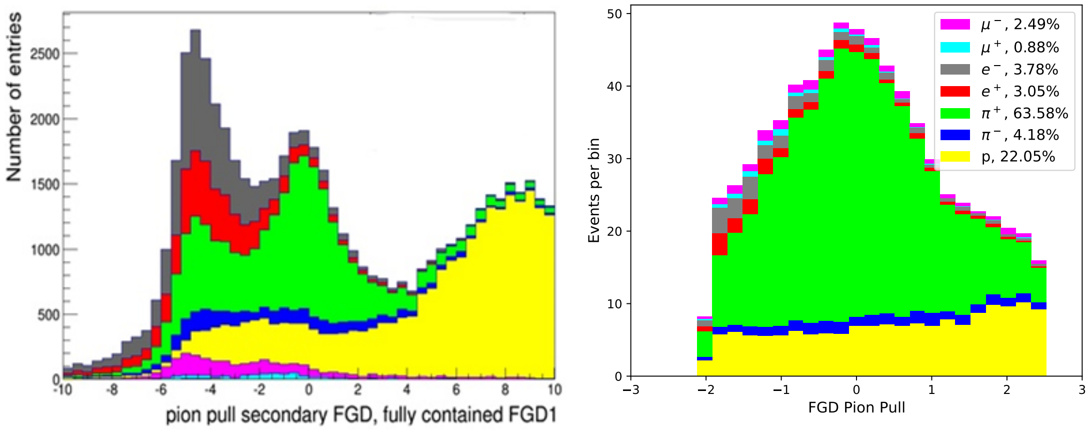

FIGURE 5.18: The left plot show the distribution of the FGD pion pull before selection, with the final selection shown in the right plot.

- **No Pion Cut:** In this cut events with charged pions, electrons or positrons in TPC are rejected, as well as the events with pions or michel electron (ME) in FGD.
- **One Positive Pion Cut:** Reject events with more than one pion, neutral pions, electrons or positrons in TPC and select events with either:
  - sum of π^+ in TPC + ME = 1
  - if $ME = 0$, sum of π^+ in (TPC + FGD) = 1 (Figure 5.7)

  The distinction between the two cases is needed to avoid a low momentum decaying pion being selected as an FGD isolated track and tagged via a Michel electron.
- **Other Cut:** Select events with at least one negative pion, neutral pion[4], or more than one positive pion.

Zero ECaL photons cut

The "Zero ECaL Photons Cut" works by identifying the γ-cluster partners and extrapolating this back to the decay point of the π^0 in the FGD block. The TPCs are used as vetoes for charged particles. In the π^0 momentum range of particular interest (between 200 and 800 MeV/c), approximately one-third of the FGD NC1π^0 events have both decay photons converting in the Barrel ECaL.

A π^0 candidate is selected, taking into account the low activity in the Tracker region and the identification of γ-like clusters. A photon is selected if the following conditions are fulfilled:

- There is an isolated object in the ECaL in the same time bunch as the muon candidate.
- The most energetic ECaL object is selected, and for this track, we set the following condition: MIPEM < 0 and the most upstream layer hit should be < 6.

If any photons are found in the event, the event is rejected from the CC0pi and CC1pi branches.

---

[4] Detected by counting the number of electrons and positrons in TPC

5.4 Selection performance

The first results with the selection, kinematics, purity, efficiency, and the event migration of each of the samples (CC inclusive, CC0π, CC1π^+ and CCother) are presented and discussed[5].

5.4.1 CC inclusive sample

The CC inclusive sample includes all events with a reconstructed muon regardless of any other particle. This sample was already studied in [45]. The CC inclusive sample consists mostly of CC0π with some contributions from CC1π^+ and CCother events. The purity of the sample shown in Table 5.2 is $\sim 95\%$ for FWD, $\sim 78\%$ for BWD, $\sim 89\%$ for HAFWD and $\sim 79\%$ for HABWD.

Topology composition [%]	FWD	BWD	HAFWD	HABWD
CC inclusive	94.62	78.50	88.92	79.46
BKG	1.76	0.86	2.97	0.85
OOFV	3.32	19.73	7.78	19.19
Sand μ	0.31	0.92	0.34	0.51
No. of events	555596	20920	60685	12168

TABLE 5.2: Topology composition of CC inclusive sample for the different directions: FWD, BWD, HAFWD, and HABWD.

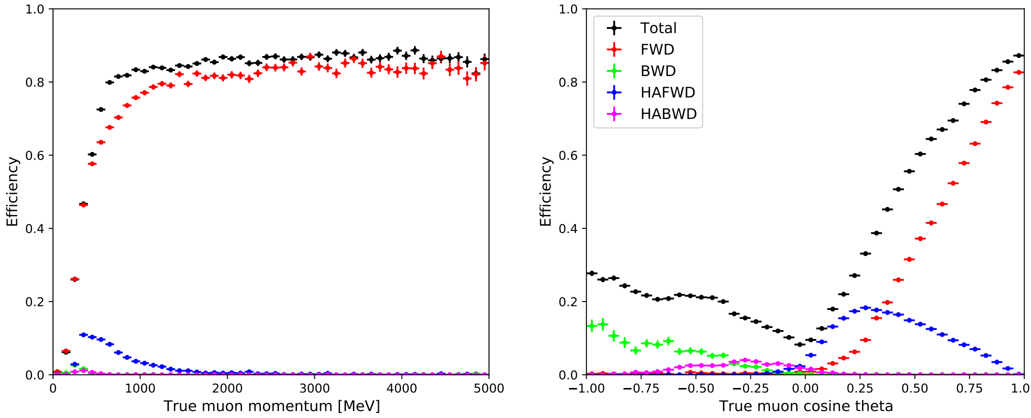

FIGURE 5.19: True muon momentum (left) and true cosine of theta (right) efficiency using highland2 v2r60 for CC inclusive sample.

Figure 5.19 shows the efficiency of the CC inclusive for 4π acceptance muon distributions. The efficiency is computed as follows:

$$\frac{Number\ of\ selected\ muons\ in\ kinematic\ bin\ in\ reconstructed\ branch}{total\ number\ of\ muons\ in\ kinematic\ bin} \tag{5.6}$$

This efficiency shows an improvement of $\sim 4\%$ points over the one reported in [45] (Figure 5.3) for backward-going muons. This improvement is based, in part, on

---

[5] The distributions plots for each topology and each direction are presented in the Appendix **??**.

the improvement correction values for the ToF. For forward-going muons, we see a decrease in the efficiency from $\sim 84\%$ to $\sim 80\%$.

5.4.2 CC zero pion sample

The CC0π sample is the main contribution to the CC inclusive signal, and it is the most CCQE-like of all the signals. The selected CC0π events broken down by true topology are shown in Table 5.3 and true particle type in Table 5.4. The signal purity in those samples is lowest for the BWD branch ($\sim$ 74%) and highest for the FWD branch ($\sim$ 75%). The main background for the FWD branch is CC$1\pi^+$ events, while for all other branches, the OOFV contribution dominates the background. For the BWD and HABWD branches, the out-of-fiducial volume background is rather large, with a contribution of 19%. Comparing Tables 5.3 and 5.4 owe can see that the regions with the highest OOFV events coincide with regions where positive particles get misidentified more often as muons.

Topology composition [%]	FWD	BWD	HAFWD	HABWD
CC0π	74.97	73.99	78.97	75.47
CC$1\pi^+$	9.21	2.23	5.40	1.83
CCother	10.44	2.28	4.55	2.16
BKG	1.76	0.86	2.97	0.85
OOFV	3.32	19.73	7.78	19.19
Sand μ	0.31	0.92	0.34	0.51
No. of events	380834	16037	49964	10998

TABLE 5.3: Topology composition of CC0π sample for the different directions: FWD, BWD, HAFWD, and HABWD.

Particle composition [%]	FWD	BWD	HAFWD	HABWD
μ^-	96.08	90.46	93.91	95.39
μ^+	0.20	0.35	1.87	0.44
e^-	0.33	1.12	0.44	0.65
e^+	0.10	0.99	0.30	0.58
π^+	0.51	3.11	1.92	1.69
π^-	2.59	2.29	0.77	0.63
p	0.19	1.68	0.80	0.63

TABLE 5.4: Particle composition of muon selection for the different directions: FWD, BWD, HAFWD, and HABWD.

Since the muon selection performs very well, with 90% to 96% muons correctly identified as shown in Table 5.4, the OOFV background does not come from misidentified particles. Instead, it comes mostly from events originating in the FGD but outside the FV definition and to a lesser extent from events originating in the P∅D. We, therefore, assume that positive forward-going (backward-going) particles, which get flipped by mistake and thus resemble a backward-going (forward-going) muon, only play a minor role.

The efficiency of the CC0π selection as a function of true muon kinematics is shown in Figure 5.20. The efficiency is computed as:

$$\frac{Number\ of\ selected\ true\ CC0\pi\ events\ in\ kinematic\ bin\ in\ reconstructed\ branch}{total\ number\ of\ true\ CC0\pi\ in\ kinematic\ bin} \tag{5.7}$$

It is very similar to the CC inclusive efficiency, which is expected since it is dominated by the muon selection efficiency and only to a lesser extent to the pion selection efficiency. On top of that, the CC0π events make up almost 75% of the CC inclusive events. The efficiency is flat for muons (4π acceptance) with momenta higher than 500 MeV but varies depending on the direction of the muon. For forward-going muons, the efficiency is higher than for backward-going muons. It is lowest (5%) for muons going perpendicular to the neutrino direction. These muons do not enter the TPC and only leave small traces in the FGD before entering the ECaL.

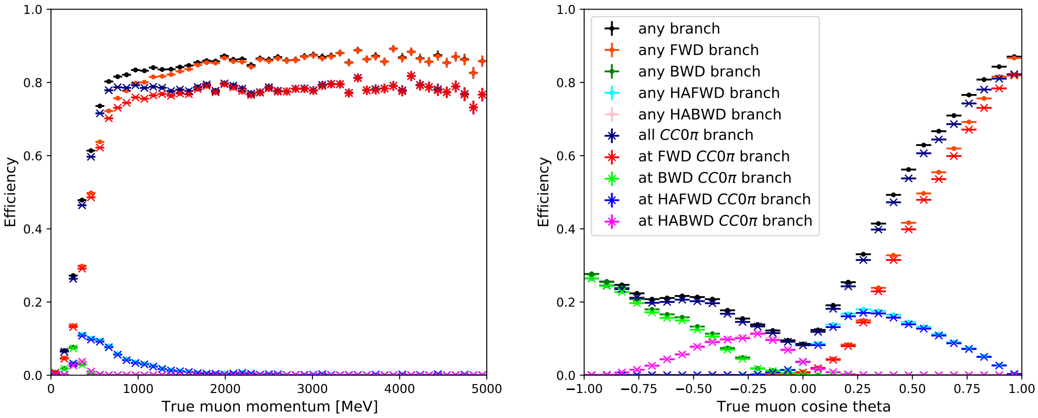

FIGURE 5.20: Muon momentum (left), muon cosine of theta (right) efficiency for CC0π sample.

5.4.3 CC one positive pion sample

Table 5.5 shows events broken down by true topology. The CC1π^+ reconstructed events are based on at least two tracks, one muon, one positive pion, and any number of nucleons. The signal purity in these samples is lowest for the BWD branch ($\sim 23\%$) and highest for the FWD branch ($\sim 57\%$).

Topology composition [%]	FWD	BWD	HAFWD	HABWD
CC0π	6.47	16.91	15.29	35.89
CC1π^+	57.34	23.12	53.52	40.31
CCother	25.91	4.26	15.03	10.36
BKG	4.96	2.36	2.98	2.11
OOFV	4.87	49.01	13.17	11.32
Sand μ	0.45	4.34	0.0	0.0
No. of events	91076	2418	6771	585

TABLE 5.5: Topology composition of CC1π^+ sample for the different directions: FWD, BWD, HAFWD, and HABWD.

Particle composition [%]	FWD	BWD	HAFWD	HABWD
μ^-	89.72	62.47	90.91	95.39
μ^+	0.80	2.66	1.26	0.38
e^-	0.30	0.79	0.37	0.38
e^+	0.02	0.71	0.28	0.0
π^+	1.93	15.25	4.30	1.73
π^-	7.07	14.46	2.01	2.11
p	0.15	3.66	0.87	0.0

TABLE 5.6: Particle composition of muon selection for the different directions: FWD, BWD, HAFWD, and HABWD.

The main background for the FWD branch is CCother events, while for the HAFWD branch, it is CC0π and CCother events. In the case of BWD and HABWD branches, the two main backgrounds are CC0π and OOFV events. The muon selection performs very well, with $\sim 62\%$ to $\sim 95\%$ muons correctly identified as shown in Table 5.6. The positive pion purity depends on the selection method, with $\sim 45\%$ to $\sim 81\%$ correctly identified in the TPC and $\sim 16\%$ to $\sim 68\%$ correctly identified in the FGD1 as shown in Table 5.7 and Table 5.8.

Particle composition [%]	FWD	BWD	HAFWD	HABWD
μ^-	1.92	13.37	4.58	4.13
μ^+	5.56	4.85	5.29	4.41
e^-	0.15	0.32	0.32	0.0
e^+	0.57	0.80	0.39	0.0
π^+	81.53	45.11	77.29	61.71
π^-	0.89	21.88	0.82	1.65
p	9.39	13.68	11.30	28.10

TABLE 5.7: Particle composition of TPC positive pion selection for the different directions: FWD, BWD, HAFWD, and HABWD.

The primary source of the misidentification are protons and, in the TPC, to a lesser extent, positive muons. In the case of the TPCs, the misidentified protons have momenta higher than 1200 MeV, while for FGD1, the protons are at low momentum. In both cases, we observed that a higher percentage of misidentification occurred when we had backward-going muons, and the forward-going proton was selected as a positive pion.

Particle composition [%]	FWD	BWD	HAFWD	HABWD
μ^-	1.69	1.43	7.77	5.13
μ^+	0.95	0.0	0.65	0.0
e^-	3.97	3.93	3.27	0.0
e^+	3.23	2.50	2.86	1.28
π^+	68.08	32.50	38.18	19.87
π^-	4.38	2.86	2.62	1.92
p	17.11	56.79	44.64	71.79

TABLE 5.8: Particle composition of FGD positive pion selection for the different directions: FWD, BWD, HAFWD, and HABWD.

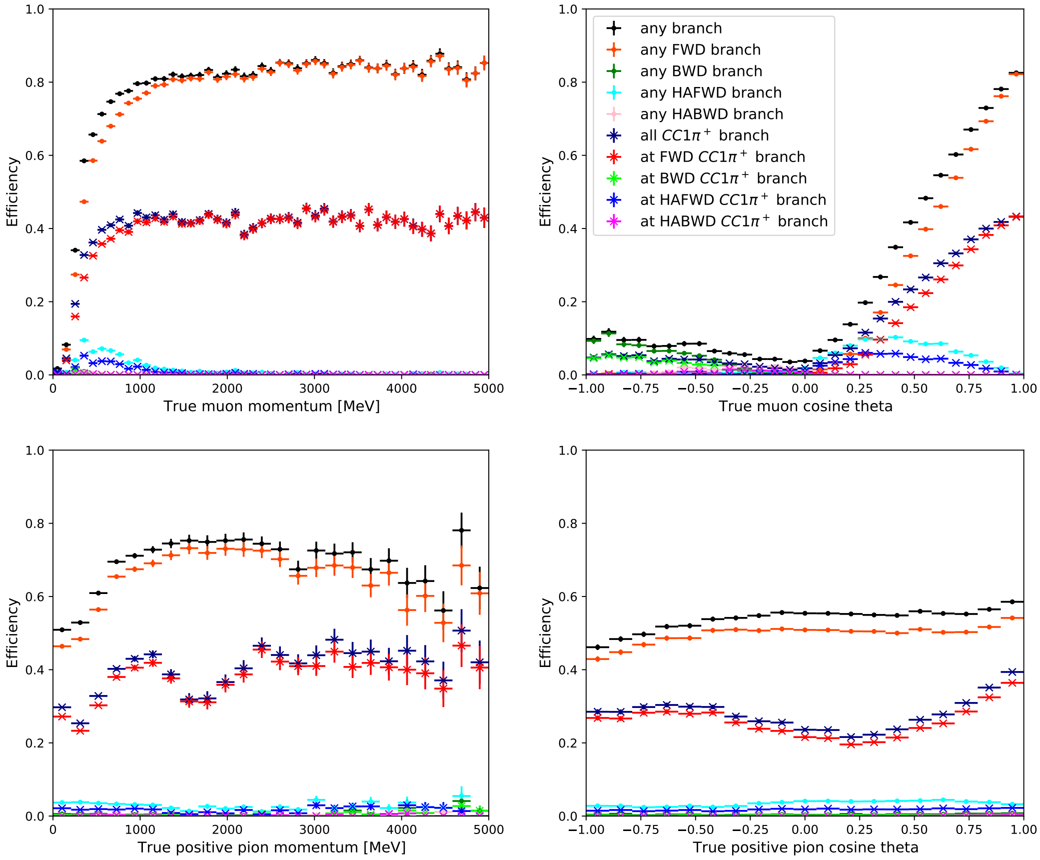

FIGURE 5.21: Muon momentum (top left), muon cosine of theta (top right), positive pion momentum (bottom left) and positive pion cosine of theta (bottom right) efficiency for CC1π^+ sample.

The efficiency is computed as:

$$\frac{Number\ of\ selected\ true\ CC1\pi^+\ events\ in\ kinematic\ bin\ in\ reconstructed\ branch}{total\ number\ of\ true\ CC1\pi^+\ in\ kinematic\ bin} \tag{5.8}$$

The efficiency of the CC1π^+ selection as a function of true muon and positive pion kinematics are shown in Figure 5.21. We can observe a dip in the efficiency for pion momenta at 1600 MeV; this corresponds to the energy range where the TPC cannot distinguish pions from protons based on the dE/dx.

5.4.4 CC other sample

The CCother events are a mixture of deep inelastic scattering (DIS) and resonant (RES) events, with additional creation of pions. Table 5.9 and Table 5.10 show the signal broken down by topology and particle content.

As can be seen, the CCother samples are the least pure ones, from $\sim 12\%$ for BWD to $\sim 66\%$ for FWD, with the BWD branch dominated by OOFV events. The particle content is striking to see that backward-going, high momentum positive particles characterize the OOFV events strongly suggests that these particles are forward-going but have been flipped by mistake, thus appearing as a negative particle. For the FWD branch, $\sim 13\%$ of the muons are misidentified negative pions, while for other branches, a wide range of particles are misidentified as muons. Strikingly the BWD sample has a significant contribution of misidentified electrons and positrons, besides the misidentified charged pions.

Topology composition [%]	FWD	BWD	HAFWD	HABWD
CC0π	7.80	10.55	15.22	23.08
CC1π^+	11.42	4.99	15.24	10.09
CCother	66.70	12.82	42.48	32.48
BKG	6.32	2.19	7.01	6.67
OOFV	6.95	67.74	19.87	26.50
Sand μ	0.81	1.70	0.18	1.20
No. of events	83686	2465	3950	585

TABLE 5.9: Topology composition of CCother for the different directions: FWD, BWD, HAFWD, and HABWD.

Particle composition [%]	FWD	BWD	HAFWD	HABWD
μ^-	80.82	34.36	74.54	67.18
μ^+	0.36	1.03	3.47	3.25
e^-	3.43	13.04	1.37	4.27
e^+	0.73	13.82	1.77	2.22
π^-	1.09	15.99	10.55	17.95
π^+	12.53	15.70	4.06	4.27
p	1.04	6.07	4.23	0.85

TABLE 5.10: Particle composition of muon selection for the different directions: FWD, BWD, HAFWD, and HABWD.

This is expected since the muons in these branches do not leave enough information in the TPC. The efficiency (5.22) is computed as:

$$\frac{Number\ of\ selected\ true\ CCother\ events\ in\ kinematic\ bin\ in\ reconstructed\ branch}{total\ number\ of\ true\ CCother\ in\ kinematic\ bin} \tag{5.9}$$

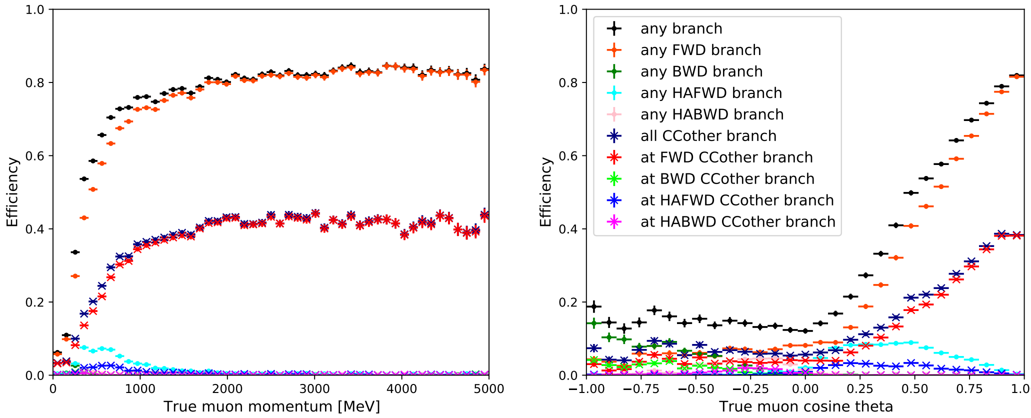

FIGURE 5.22: Muon momentum (left), muon cosine of theta (right) efficiency for CCother sample.

5.4.5 Event migration

The primary contamination on each sample comes from events that are wrongly assigned to the sample. In this section, we discuss the reason for this.

- **Events reconstructed as CC0π:** The main contamination in this sample comes from CCother ($\sim$ 9%) and CC$1\pi^+$+ events ($\sim$ 8%) as shown on Table 5.2. The CCother contamination is due mainly to charged current events with more than two pions or one or more other particles like kaon; this is called CCrest. (Table 5.11).
- **Events reconstructed as CC$1\pi^+$:** The main contamination in the sample comes from CCother ($\sim$ 24%) and CC0π ($\sim$ 8%) as shown on Table 5.2. The CCother events are composed of $\sim$ 56% CC$1\pi^+\pi^{-,0}$, $\sim$ 19% CC$2\pi^+$ and $\sim$ 24% CCrest (Table 5.12).
- **Events reconstructed as CCother:** The main contamination in the sample comes from CC$1\pi^+$ ($\sim$ 11%) and CC0π ($\sim$ 8%) as shown on Table 5.2. The Table 5.13 and 5.14 shows the composition of this migrated evens.

Reaction composition [%]	FWD	BWD	HAFWD	HABWD
CCQE	1.55	25.68	3.48	24.79
2p2h	0.26	0.0	0.48	0.0
RES	54.50	58.20	61.34	51.26
DIS	43.69	16.12	34.70	23.95

TABLE 5.11: Reaction composition of CCother events classified as CC0π for the different directions: FWD, BWD, HAFWD, and HABWD.

The "Zero ECaL Photon Cut" already reduced the CCother contribution in the samples CC0π and CC1π^+ but still, we can observe some migrated events to CCother. If a pion is absorbed, we can miss it and target a true CCother event as CC1π^+, or if a nucleon (that results from the neutrino interaction) interacts and produces a pion, we can target a true CC0π event as CC1π^+ or a true CC1π^+ event as CCother. In the case of true protons that are identified as positive pions and vise-versa, this occurs mainly in the TPC and for energies superior to 1200 MeV (see Figure 3.10).

Reaction composition [%]	FWD	BWD	HAFWD	HABWD
CCQE	0.38	8.74	1.18	4.46
2p2h	0.04	0.0	0.0	0.0
RES	11.17	17.48	17.09	32.14
DIS	88.41	73.79	81.73	63.39

TABLE 5.12: Reaction composition of CCother events classified as CC1π^+ for the different directions: FWD, BWD, HAFWD, and HABWD.

Reaction composition [%]	FWD	BWD	HAFWD	HABWD
CCQE	63.27	83.46	74.54	90.37
2p2h	15.28	2.69	9.65	2.96
RES	18.55	12.69	13.98	6.67
DIS	2.90	1.15	1.83	0.0

TABLE 5.13: Reaction composition of CC0π events classified as CCother for the different directions: FWD, BWD, HAFWD, and HABWD.

Reaction composition [%]	FWD	BWD	HAFWD	HABWD
CCQE	0.77	3.25	2.16	5.08
2p2h	0.07	0.0	0.33	0.0
RES	78.28	86.99	87.54	76.27
DIS	17.22	9.76	9.97	18.64
COH	3.61	0.0	0.0	0.0
other	0.05	0.0	0.0	0.0

TABLE 5.14: Reaction composition of CC1π^+ events classified as CCother for the different directions: FWD, BWD, HAFWD, and HABWD.

5.4.6 OOFV contribution

The Figures 5.23 and 5.24 show the true vertex position of the events that are classified as OOFV on the BWD and HA samples, respectively. The main contributions come from P∅D ECaL and the first and last layers of the FGDs in the case of BWD samples. For HA samples, the events start mainly in the ECaL and the limits of the FGD1.

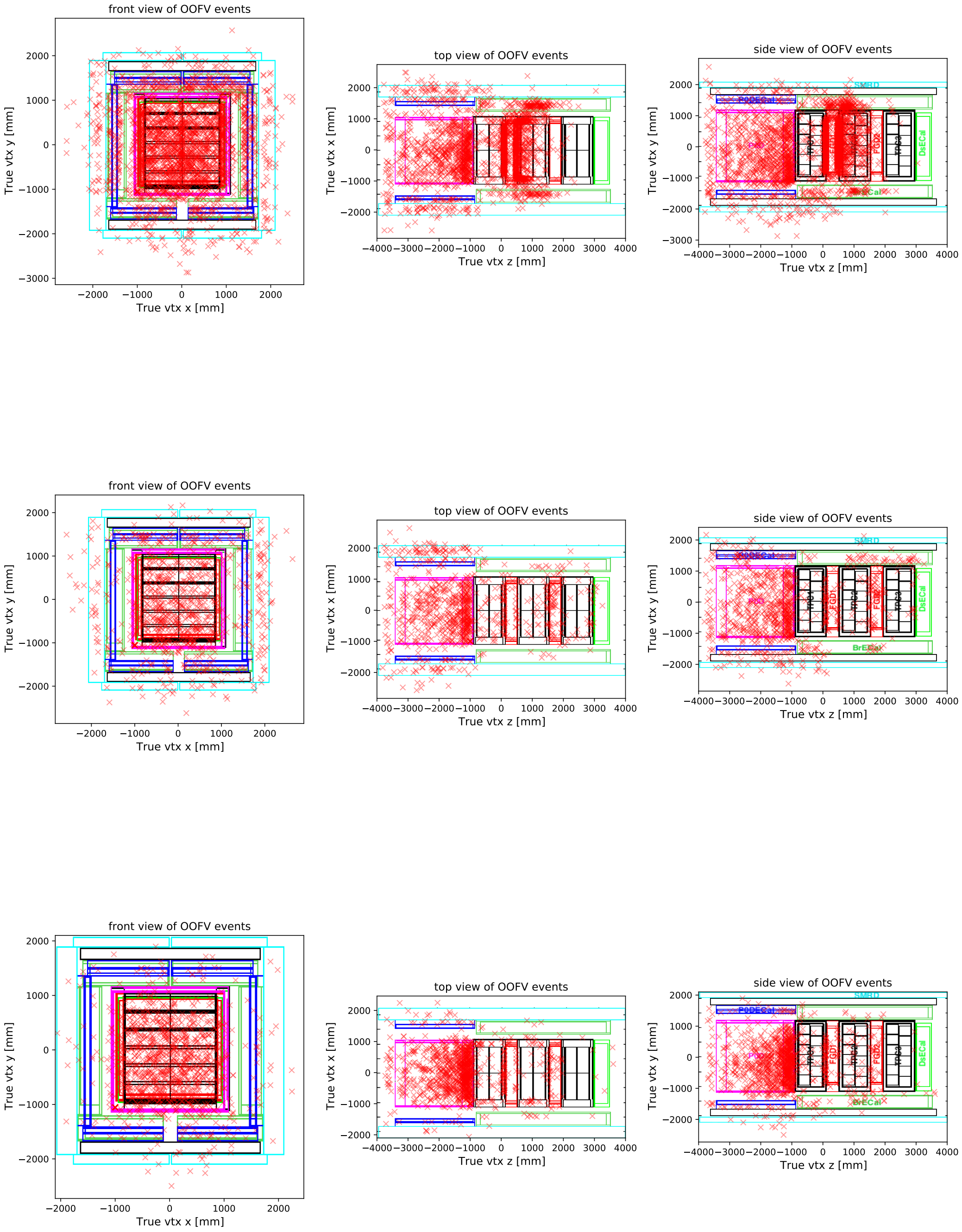

FIGURE 5.23: Events that are classified as OOFV on BWD sample of CC0π (top), CC1π^+ (center) and CCother (bottom).

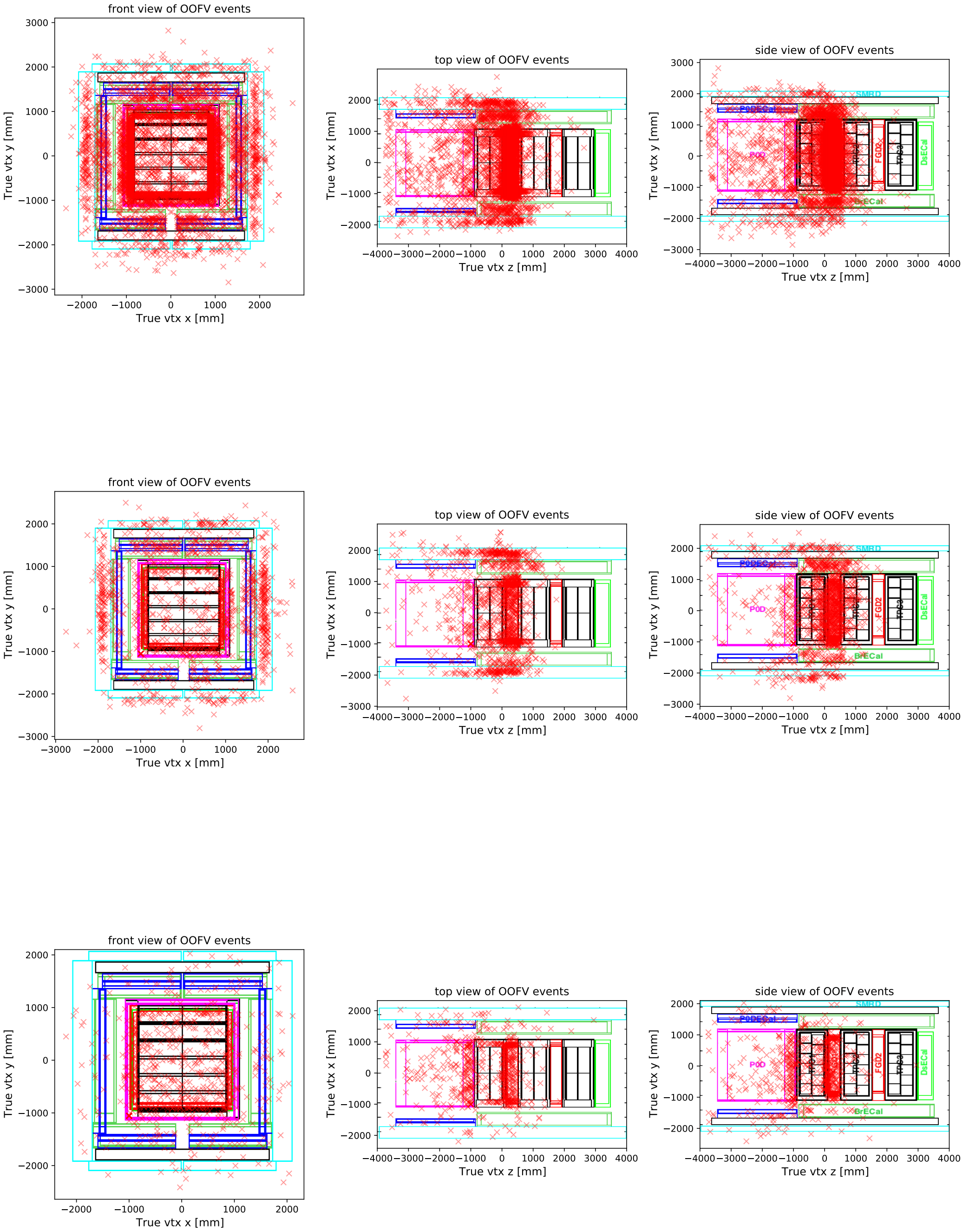

FIGURE 5.24: Events that are classified as OOFV on HA samples of CC0π (top), CC1π^+ (center) and CCother (bottom).

5.5 Summary and possibles improvements

Regarding the CC inclusive sample, the muon purity is very high (> 90 %) for the forward, and angle tracks branches. It is slightly lower for backward-going muons and muons at high-angles, which additionally suffer from low statistics. Compared to previous selections seeking to select muons with a 4π coverage, the efficiency for backward-going muons has been improved to 25%. This selection shows an improved muon selection purity. For CCother, the OOFV contributions are huge for the backward and high-angle directions. An essential future improvement would be developing and optimizing cuts to clean up the BWD sample. Currently, the selection is restricted to events in FGD1. For an extension to FGD2, dedicated selection cuts are needed to select muons with full angular coverage.

This selection can be further improved. A better cut to reduce the contamination of protons when selecting the FGD pion can be implemented, deepening on the direction of the track (see Table 5.8). Michel electrons reconstructed kinematics information can be included (this has been developed as part of a Ph.D. thesis at ND280, and the results shown are outstanding). Improve the timing information and the detector efficiency for backward and high angle branches. This two will be achieved with the ND280 upgrade.

Chapter 6

Signal definition

The signal is defined as the experimentally observable particles exiting the nucleus, commonly called ’topologies’. As it was shown in previous chapters, several interaction modes[1] will contribute to each topology (we will call them ’reactions’). In chapter 5 we described the selection developed and its performance. This selection makes it possible to study four main signals (CCinclusive, CC0π, CC1π^+ and CCother), with 4π acceptance.

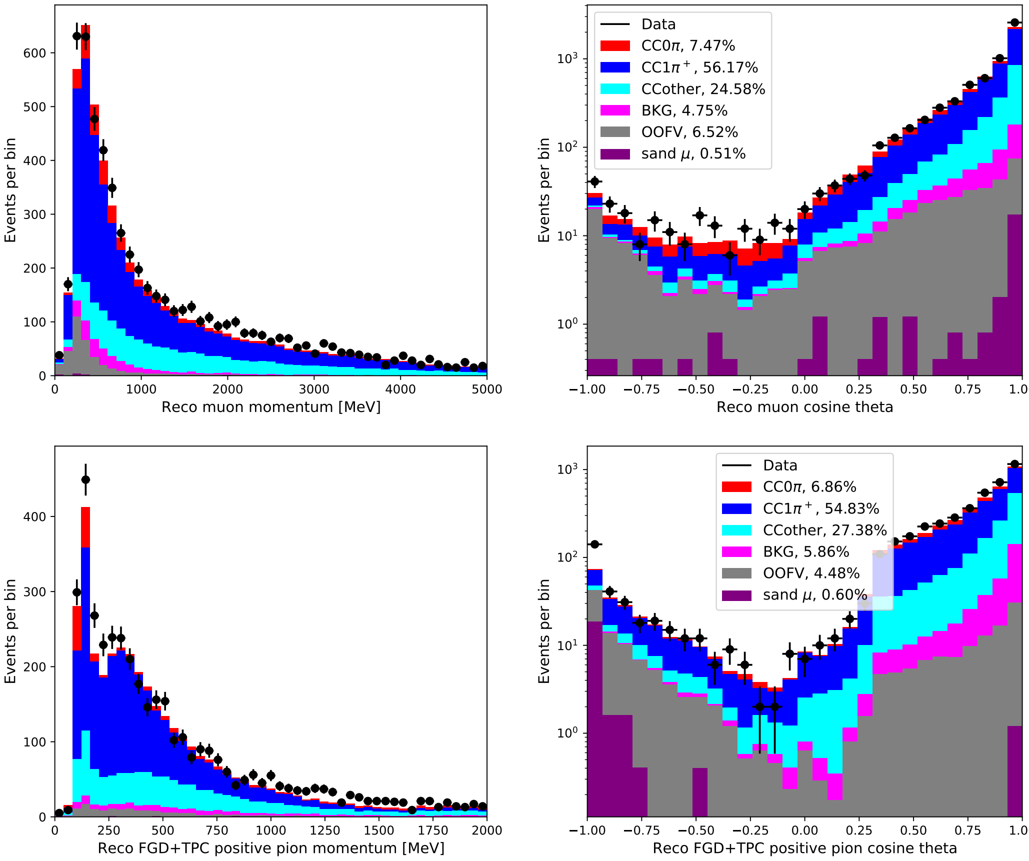

FIGURE 6.1: Muon momentum (top left), muon cosine of theta (top right), positive pion (FGD + TPC) momentum (bottom left) and positive pion (FGD + TPC) cosine of theta (bottom right) distribution of CC1π^+ with 4π acceptance. Using the true topology definition and ND280 data (black points).

---

[1] This refers to the neutrino-nucleon interaction before the intra-nuclear cascade (like QE, RES or DIS).

6.1 Signal: CC one positive pion

The CC1π^+ reconstructed events are based on two tracks events, one muon and one positive pion, both in 4π solid angle acceptance. The event is rejected if additional pions, either charged or neutral, or photons are identified in the event. These pions can be identified by looking at TPC tracks, FGD tracks, Mickel electrons, or electromagnetic showers in ECal. Ecal pions will not be used in this analysis due to the poor purity and the small number of events of that sample.

Figure 6.1 shows the muon and positive pion kinematics[2] distributions (reconstructed momentum and cosine of theta). The signal purity in these samples is 56.17%. The main background is CCother ($\sim 24\%$) events. This CCother events are composed, mostly, of CC1$\pi^+\pi^{\pm,0}$ (Table 5.12). This contamination is coming from missing or misidentifying pions as discussed in chapter 5. The difference between the purity of the sample is due to the variable being plotted. If we look at muon kinematics, we will obtain all events selected as the signal, while when we look at the positive pions kinematics variable, we will miss some events that are identified using Michel Electrons (since we do not have this kinematic information from ME).

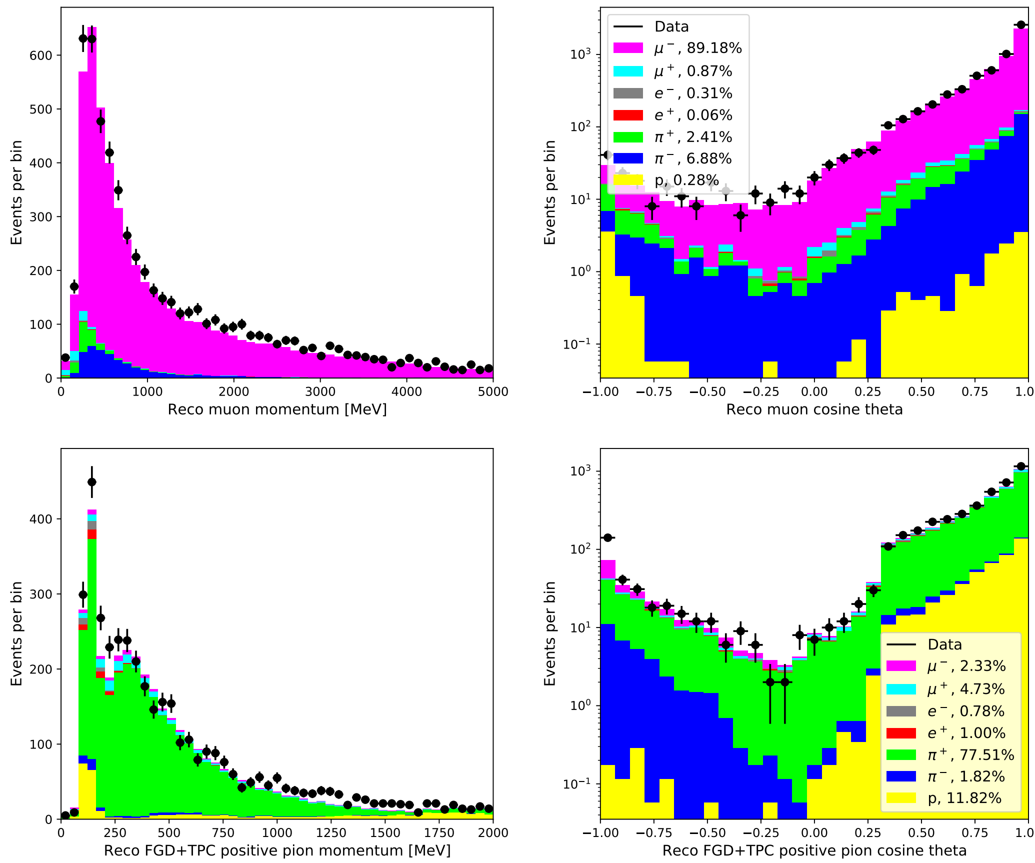

FIGURE 6.2: Muon momentum (top left), muon cosine of theta (top right), positive pion (FGD + TPC) momentum (bottom left) and positive pion (FGD + TPC) cosine of theta (bottom right) distribution of CC1π^+ with 4π acceptance. Using the true particle definition and ND280 data (black points).

---

[2] Because of the missing information from ME for the pion kinematics only FGD and TPC pions are used.

Looking at the data points (black dots) in 6.1 angular distributions figure, we can see that the MC describe relatively well the data except for high angles backward (HABWD) muons and positive pions tracks (-0.5 < $cos\theta$ < 0.0) were the MC underestimate the data; this was expected due to the very low statics in the HABWD sample (see Table 5.5). When looking at the momentum distribution, this underestimation is more visible in the pick of the distribution.

The muon selection performs very well, with 89.19% muons correctly identified as shown in Figure 6.2 (top row). For CC1π^+ events, the OOFV background comes from charged pions misidentified as muons. The positive pion purity is 77.51%[3] correctly identified in the FGD1 and TPC as shown in Figure 6.2 (bottom row). The main source of the misidentification of pions is protons. We observed that a higher percentage of misidentification occurred when we have backward-going muons, and the forward-going proton is selected as a positive pion.

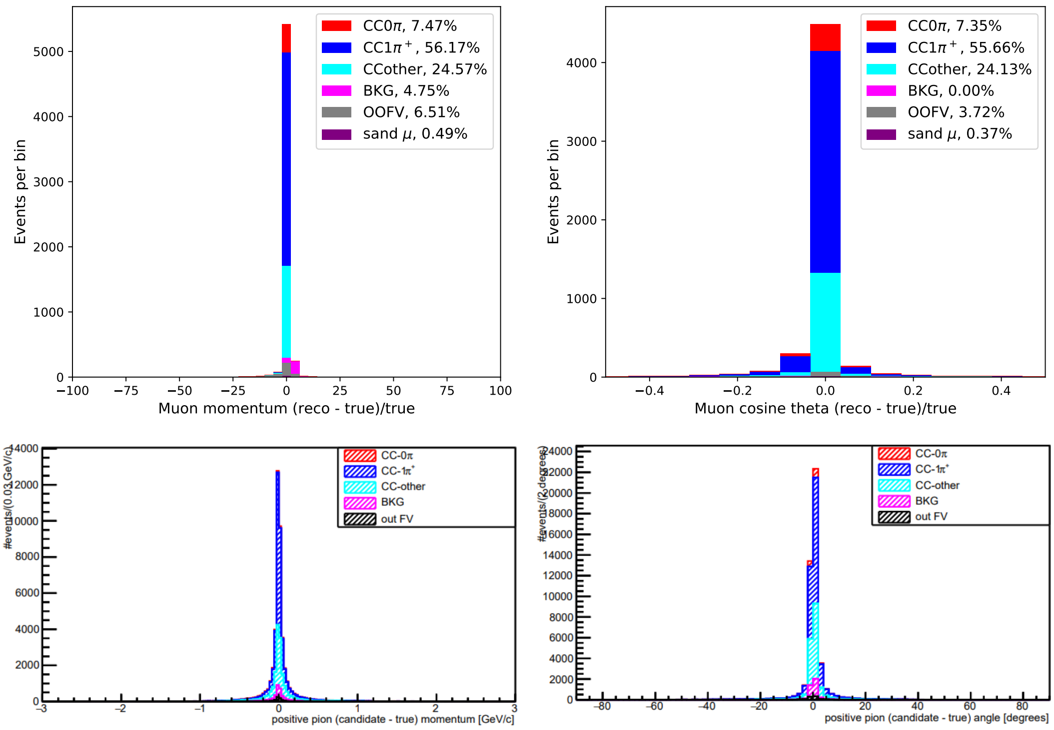

FIGURE 6.3: Resolution between reconstructed and true for muon momentum (top left), muon cosine of theta (top right), positive pion (FGD + TPC) momentum (bottom left) and positive pion (FGD + TPC) cosine of theta (bottom right) of CC1π^+ with 4π acceptance. Using the true topology definition.

Figure 6.3 shows the difference between reconstructed and true for the muon and positive pion kinematics variables distribution of CC1π^+ with 4π acceptance. We observed a good agreement between reconstructed and true variables for both muon and positive pion.

Figure 6.4 shows the true vs. reconstructed distributions for muon and positive pion kinematics of CC1π^+ signal events (that were reconstructed correctly) with 4π acceptance. These plots indicate how well the kinematics variables are reconstructed when looking at CC1π^+ signal events.

---

[3] The positive pion purity in the TPC sample is 80.39% and from the FGD1 sample is 63.43%

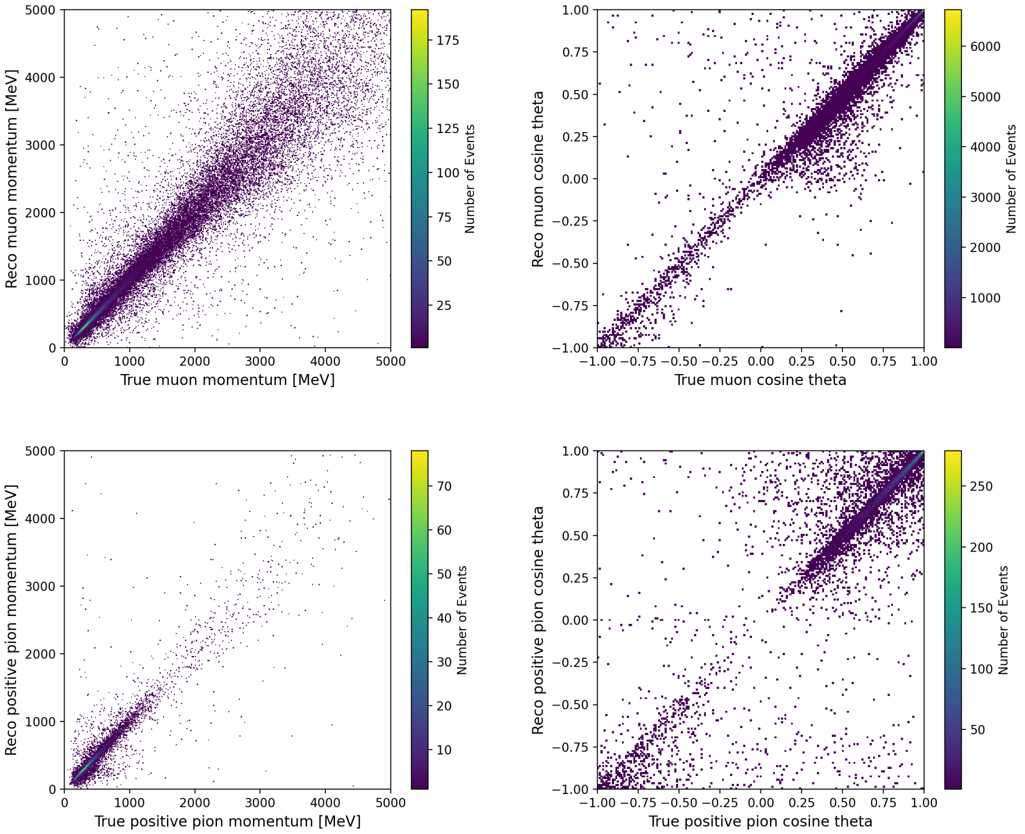

FIGURE 6.4: True vs reconstructed distributions for muon momentum (top left), muon cosine of theta (top right), positive pion (FGD + TPC) momentum (bottom left) and positive pion (FGD + TPC) cosine of theta (bottom right) of CC1π^+ signal events (that were reconstructed correctly) with 4π acceptance.

- **Muon momentum (top left):** We observe a good agreement between the reconstructed and true muon momentum regardless of the method used. We are using a 4π solid angle acceptance; for HA samples, we calculate the muon momentum by the range of the track, while for LA tracks, it is done using the TPC information. The Figure 6.5 shows the contributions by separated.

- **Muon cosine of theta (top right):** We observe a good agreement between the reconstructed and true muon cosine of theta. A small amount of events are reconstructed with a lower cosine of theta as we can see that correspond to events with true muon cosine of theta between 0.3 and 0.7 (0.3 < $\cos^{true}\theta_\mu$ < 0.7).

- **Positive pion momentum (bottom left):** We observe a good agreement between the reconstructed and true positive pion momentum regardless of the detector used. For FGD positive pions, the momentum is calculated by the range of the track, while for the TPC positive pions, it is done by using the TPC information.

- **Positive pion cosine of theta (bottom right):** We observe almost non-events in HA because in this analysis, as mentioned before ECal pions sample is not used. The few events in HA are due to FGD pions[4]. We can also see a small number of

---

[4] FGD pions as we presented before are pions that start and end inside the FGD.

reconstructed backward events when the true positive pion cosine of theta indicates that the track should go forward; this could be due to tracks being wrongly flipped when using ToF information, FGD pions with short tracks, or/and TPC pions with short tracks.

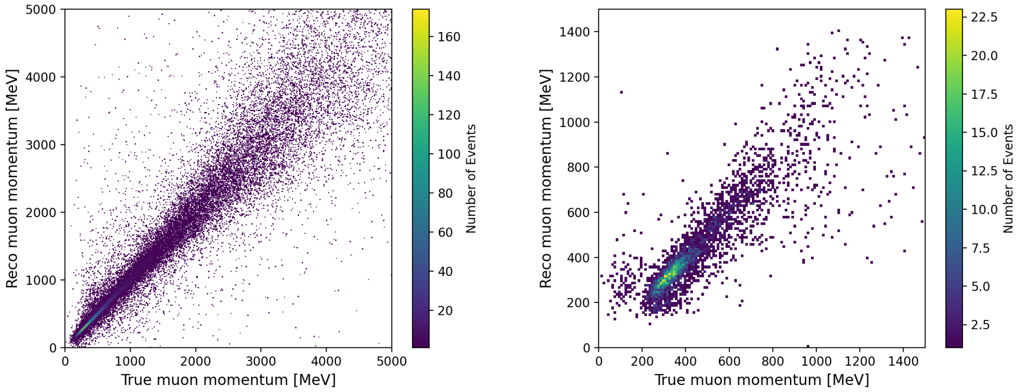

FIGURE 6.5: True vs reconstructed distributions of LA (left) and HA (right) muon momentum of CC1π^+ signal events (that were reconstructed correctly) with 4π acceptance.

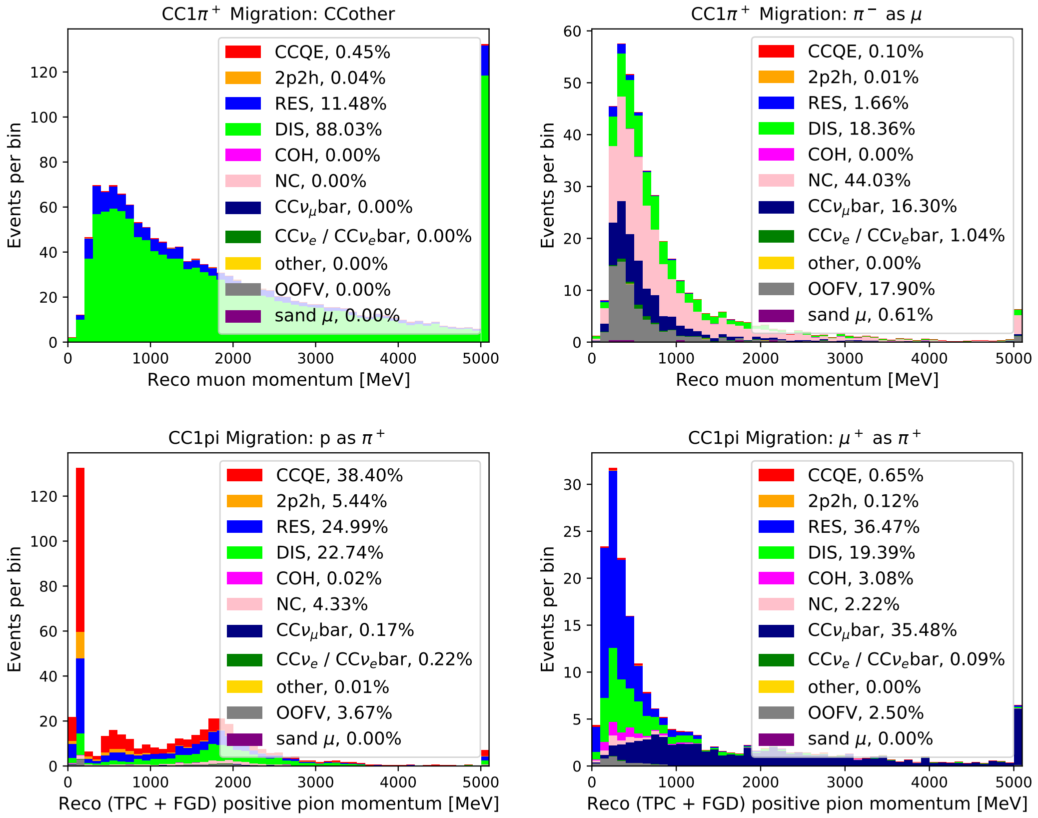

FIGURE 6.6: Muon momentum distributions for the migrates events. CCother as CC1π (top left), negative pion as muons (top right), protons as positive pions (bottom right) and antimuon as positive pions (bottom right). Using the true reaction definition.

6.1.1 Event Migration

As discussed in the chapter 5, the main contamination on CC1π^+ comes from CCother events. Most specifically from CC1π^+1$\pi^{\pm,0}$. Another migrations comes from misidentified muons and positive pions as shown on Figure 6.2. The Figure 6.6 shows the muon momentum distributions for the migrates events. Around a 7% of the times the muon is misidentify as a negative pion (Figure 6.6 top right). In the case of positive pions the main source of the mis-identification are protons (with $\sim$ 12%, represented in Figure 6.6 bottom right) and antimuon (with $\sim$ 5%, represented in Figure 6.6 bottom right).

6.1.2 Phase-Space constrains

The detector acceptance is limited depending on the path of the track. Choosing the exact phase-space limitations to apply is not trivial. Ideally, the efficiency correction should be entirely independent of the neutrino interaction model. In this analysis, this is even more complicated since both muons and pions are identified, and therefore it is necessary to use 4D-kinematic phase-space where both are consistently reconstructed. Since the observables directly measured in the detector are the kinematics variables of muons and pions, these are used to select the phase-space constraints. The 4D space efficiency was divided into six 2D phase-spaces, which fully encompass the correlations between the kinematic variables. The Figure 6.7 shows this 2D efficiency plots.

From this evaluation of the efficiency the following constraints are to be placed on muon and pion kinematics in the signal definition for the cross section extraction:

- True muon momentum > 200 MeV/c,
- True pion momentum > 160 MeV/c.

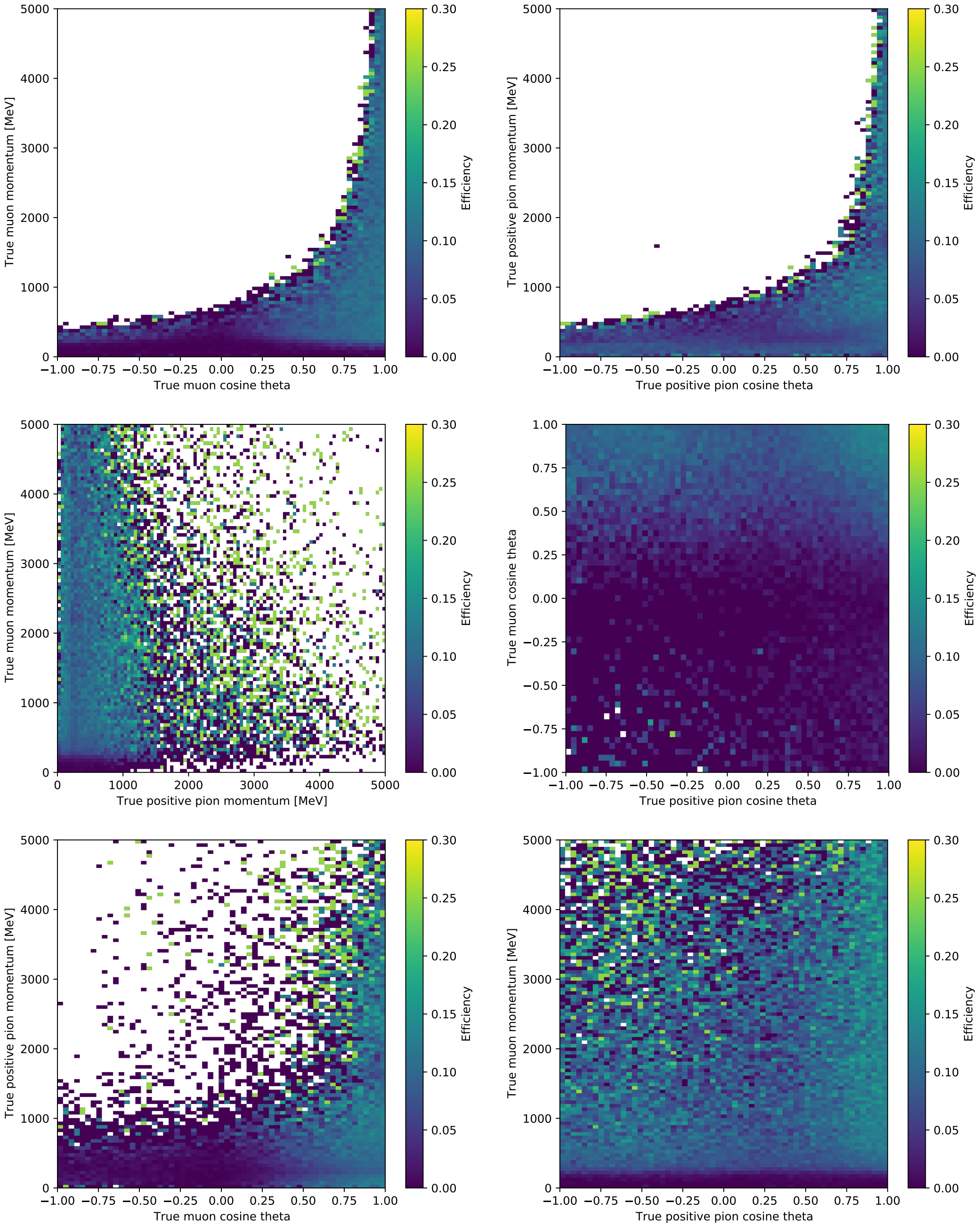

FIGURE 6.7: The CC1π^+ efficiency, true muon momentum vs. true muon cosine theta (top left), true pion momentum vs. true pion cosine theta (top right), true muon momentum vs. true pion momentum (center left), true muon cosine theta vs. true pion cosine theta vs (center right), true pion momentum vs. true muon cosine theta (bottom left), and true muon momentum vs. true pion cosine theta (bottom right). These plots are used to choose phase-space limits to create a more realistic and less model dependent signal definition. This is done by looking for regions of consistently high efficiency across the 4D phase-space.

6.2 Control sample: CC one positive pion and one charged or neutral pion

Control samples are selected to constrain the MC background components. Each control sample is selected to be representative of a specific background, and it is required to minimize the content of CC1π^+ in order to be considered a side-band sample independent of the signal sample.

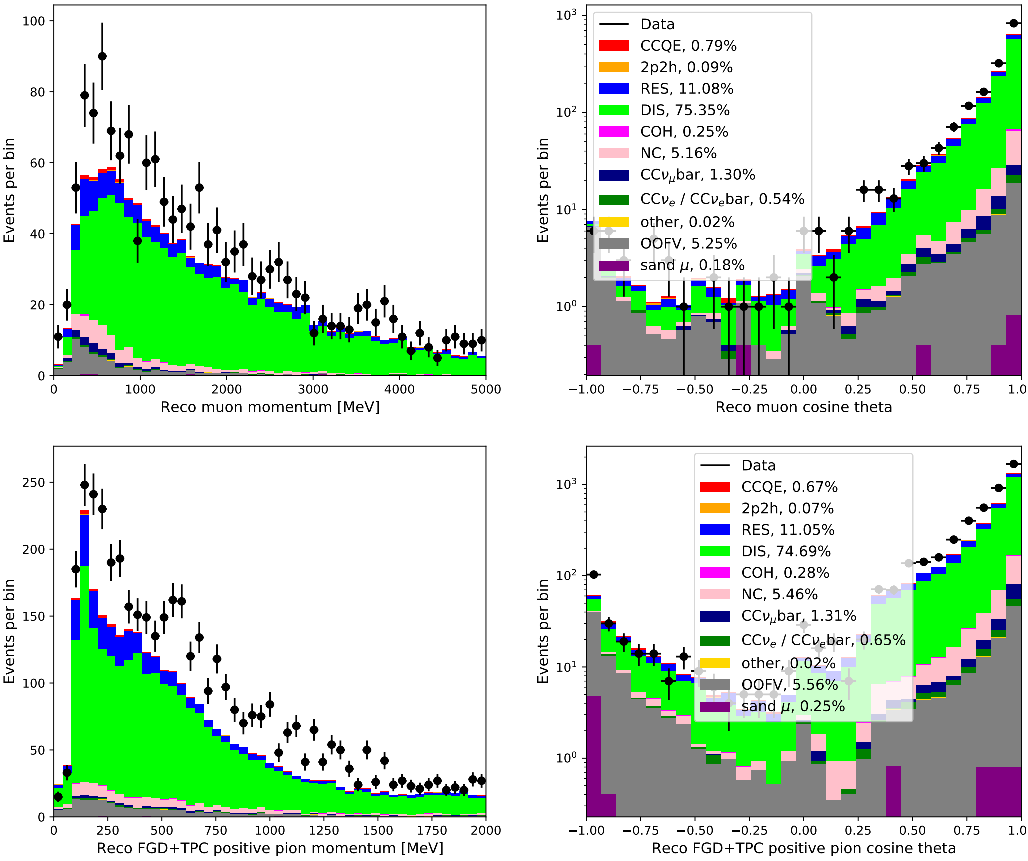

FIGURE 6.8: Muon momentum (top left), muon cosine of theta (top right), positive pion momentum (bottom left) and positive pion cosine of theta (bottom right) distributions of CC1$\pi^+1\pi^{\pm,0}$ with 4π acceptance. Using the true reaction definition and ND280 data (black points).

Control samples are also required to be independent of each other (mutually exclusive). For this analysis, we have defined a control sample that is a sub-sample of CCother: CC1$\pi^+1\pi^{\pm,0}$. Figures 6.8 and 6.9 show the control sample broken down by reaction and particle content as a function of the muon and positive pion (FGD + TPC) kinematics.

It can be seen that in these samples are mostly DIS ($\sim 55\%$ from muon kinematics distributions and $\sim 75\%$ from positive pion kinematics) events with a small contribution from RES ($\sim 21\%$ from muon kinematics distributions and $\sim 11\%$ from positive pion kinematics) events. The muons are misidentified negative pions $\sim 12\%$ of the times as shown in Figure 6.9 (top row). The positive pion purity is $\sim 71\%$ correctly identified in the TPC + FGD as shown in Figure 6.9 (bottom row). The main source of the misidentification of pions is protons.

In the Figures 6.8 and 6.9[5], we can see that the MC underestimated the data; this was expected due to the very low statics and the fact that these samples are based on events with more than two tracks, which introduce a higher possibility of missing a track.

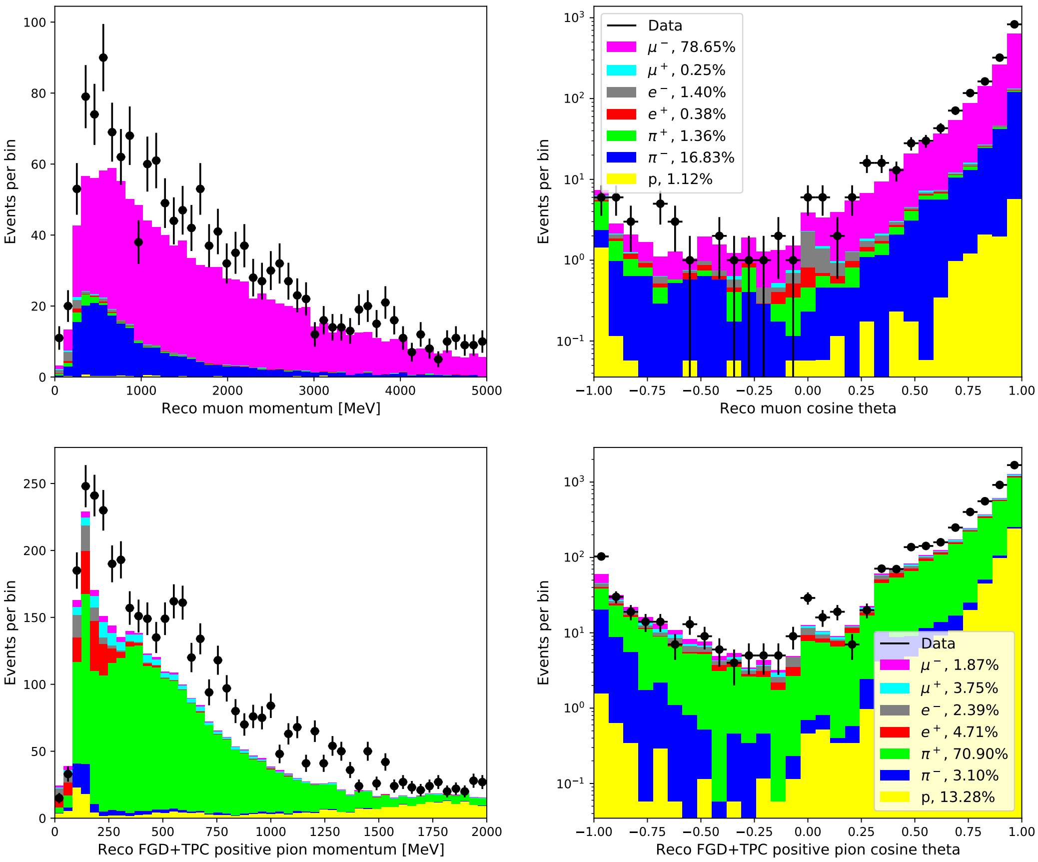

FIGURE 6.9: Muon momentum (top left), muon cosine of theta (top right), positive pion momentum (bottom left) and positive pion cosine of theta (bottom right) distributions of CC$1\pi^+1\pi^{\pm,0}$ with 4π acceptance. Using the true particle definition and ND280 data (black points).

6.3 Reconstructed variables using muon and pion kinematic

The neutrino energy (E_ν) is reconstructed using energy-momentum conservation. Based on the Figure 2.1 we can express the energy conservation like:

$$E_\nu = E_{bind} + E_{N'} \tag{6.1}$$

since this definition of the neutrino energy assumes that the target nucleon is at rest. E_{bind} is the target nucleon binding energy ($25 MeV$ in NEUT for a carbon target), and $E_{N'}$ is the energy of the scattered nucleon. Using the Mandelstam variables 2.1 and considering the neutrino as massless, we obtain:

---

[5] The distributions for the full CCother are shown in the Figures D.9 and D.10.

$$E_{\nu_{reco}} = \frac{{m_p}^2 - (m_p - E_{bind} - E_\mu - E_\pi)^2 + |\vec{P}_\mu + \vec{P}_\nu|^2}{2(m_p - E_{bind} - E_\mu - E_\pi + \hat{k}_\nu(\vec{P}_\mu + \vec{P}_\nu))} \tag{6.2}$$

Were $(E_\mu, \vec{P}_\mu)$ and $(E_\pi, \vec{P}_\pi)$ are the four-momenta of the muon and the pion, $\hat{k}_\nu$ is the neutrino direction, and m_p is the free proton mass. This assumption introduces a bias in the reconstruction of E_ν. The motion of the nucleons inside the nucleus (Fermi motion) causes smearing on the E_ν. It is important to understand these nuclear effects to reconstruct the E_ν.

The hadronic invariant mass can be reconstructed directly from the final state pion and proton kinematics:

$$W^2 = \Big(E_\pi - E_p\Big)^2 - \Big(\vec{P}_\pi - \vec{P}_p\Big)^2 \tag{6.3}$$

In this case, we do not know the final proton kinematics, so W is reconstructed from the neutrino and muon kinematics instead. Once we have reconstructed the E_ν, this allows us to calculate the hadronic invariant mass of the system as:

$$W^2 = \Big((E_\nu + m_p) - E_\mu\Big)^2 - \Big(|\vec{P}_\mu| - |\vec{P}_\nu|\Big)^2 \tag{6.4}$$

The hadronic invariant mass provides an indication of the relative population of the dominant resonant production versus non–resonant production. The four-momentum transfer[6] is defined as:

$$Q^2 = -q^2 = (\vec{P}_\mu - \vec{P}_\nu)^2 \tag{6.5}$$

Were $(E_\nu, \vec{P}_\nu)$ is the neutrino four-momentum vector. For the calculation of Q^2 and W, the reconstructed neutrino energy obtained before is used, making them model-dependent.

Figure 6.10 shows the reconstructed and true distribution of E_ν, W and Q^2 for selected for CC$1\pi^+$ events with 4π solid angle acceptance according to their true reaction. The MC simulation includes an accurate description of the E_ν, Q^2, and W angular distributions and the agreements with the data it can be considered good.

Although, when comparing the reconstructed to true distributions (in each of these variables), we can observe that in the true distributions, the different reactions are relatively well defined while, for the reconstructed variables, this is not the case. For the high values of neutrino energy ($E_\nu > 2\,GeV$), hadronic invariant mass ($W > 2\,GeV$) and four-momentum transfer ($Q^2 > 210^{-3}GeV^2$) deep inelastic scattering background dominates. In the case of the hadronic invariant mass, $2\,GeV$ constitutes the threshold that defines the DIS region in NEUT; this can give a sense of the transition from RES production to DIS in Monte Carlo.

---

[6] The reason for this definition is that q^2 is negative; this can be easily seen by calculating the Lorentz-invariant q^2 in the laboratory frame.

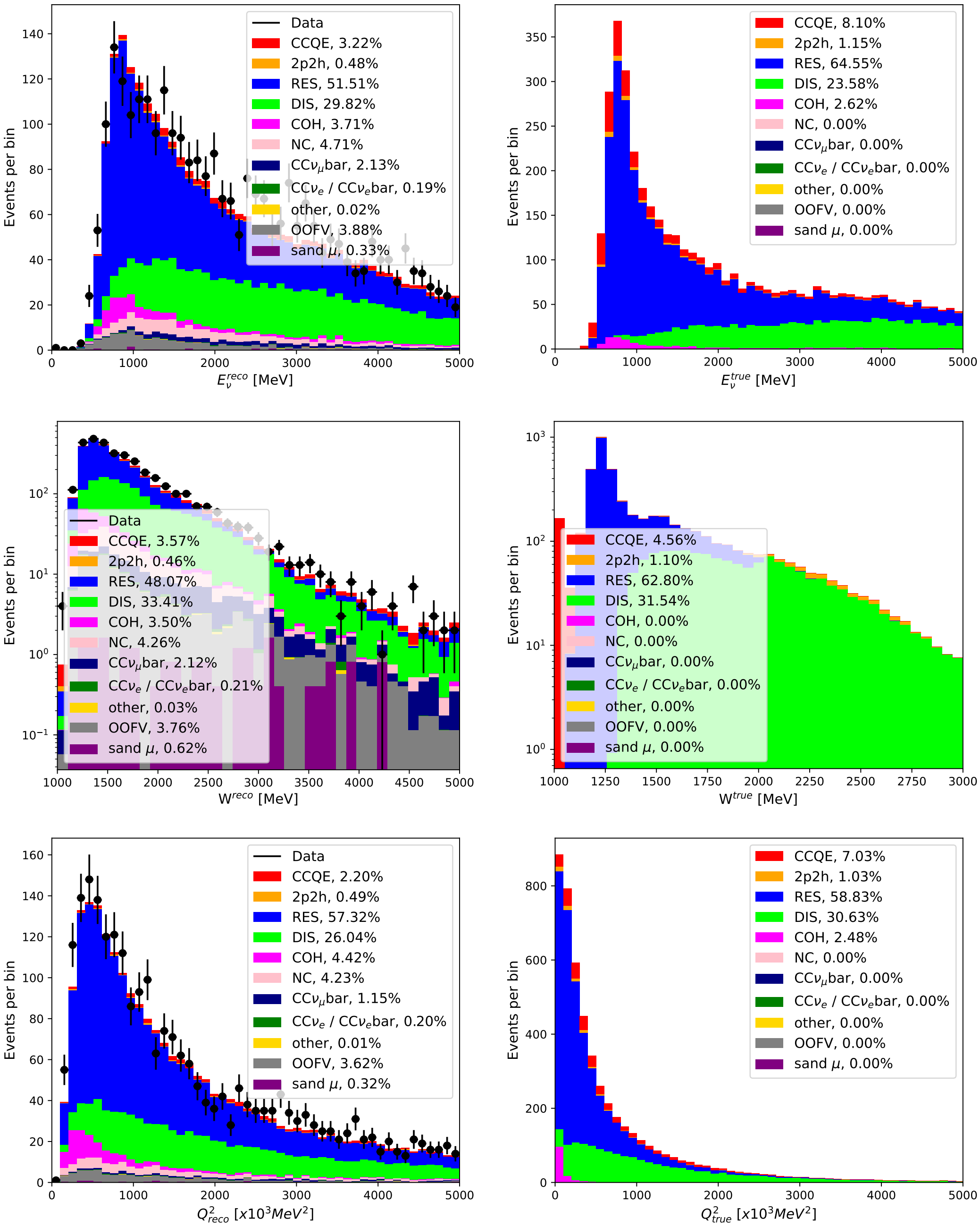

FIGURE 6.10: Reconstructed and true neutrino energy (top row), hadronic invariant mass (central row) and four-momentum transfer (bottom row) for CC1π^+ events correctly identified with 4π solid angle acceptance. Using the true reaction definition and ND280 data (black points).

Figure 6.11 shows the 2D distributions for true vs. reconstructed distribution of the neutrino energy[7], the hadronic invariant mass, and the four-momentum transfer for CC1π^+ signal events (that were reconstructed correctly) with 4π acceptance. Each of these plots indicates the accuracy of the reconstruction.

---

[7] Because of the missing information from ME for the pion kinematics only FGD and TPC pions are used.

- **Neutrino energy (left):** We observe a good agreement between the reconstructed and true neutrino energy regardless of the method used for reconstructing the muons and pions kinematic.
- **Hadronic invariant mass (center):** It shows some events that are reconstructed with a higher value than expected, more specifically for $W = 1.25\ GeV$. This is happening for events reconstructed using FGD pion information related to misreconstructions on the FGD positive pion kinematics.
- **Four-momentum transfer (right):** It shows some events that are reconstructed with a higher value than expected.

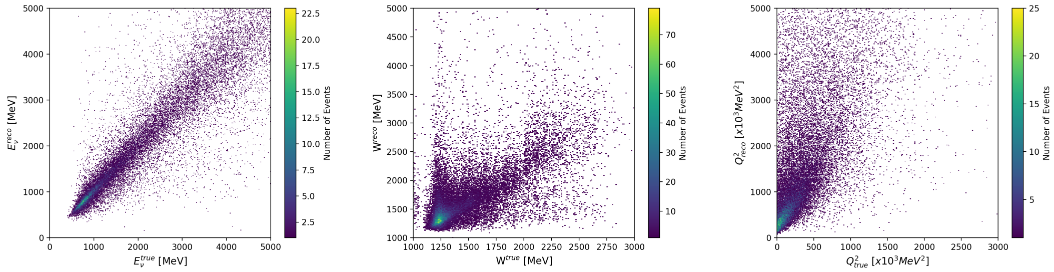

FIGURE 6.11: True vs reconstructed distributions for neutrino energy (left), hadronic invariant mass (center), and four-momentum transfer (right) for CC1π^+ events with 4π acceptance.

6.3.1 Adler angles

It is possible to measure the Adler angles in neutrino-nucleus scattering. The results based on the NEUT Monte Carlo show:

- That one can determine the transverse polarization of the Δ resonance because the information is reasonably well maintained despite the FSI and the need to reconstruct the energy of the incoming neutrino from the experimental data [39].
- The longitudinal polarization is shown to depend strongly on the kinematics of the emerging pion, but it appears, on the CC1π^+ tracks emerging from the nucleus, to allow investigation of [39]:
  - the effects of pion re-scattering,
  - high mass resonances,
  - deep inelastic processes.

The two Adler angles are properly defined at the nucleon interaction level, but they are altered by the final state interactions and the Fermi momentum of the target nucleon. They carry information about the polarization of the Δ resonance the interference with non-resonant single pion production, and they can provide hints of parity violation due to the lack of preference in the Δ direction. Underneath, there is a nucleon-level effect that has information about the neutrino-nucleon interactions concerning the polarization of the Δ. The problem is that the nuclear effects are large.

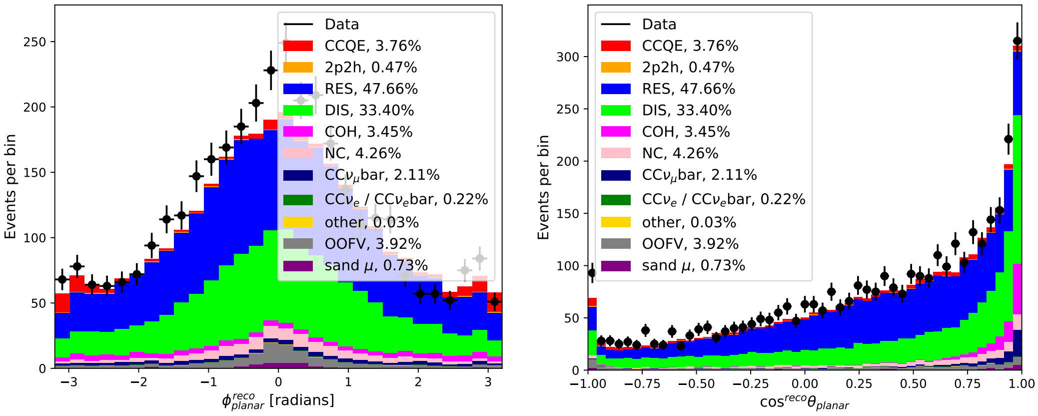

FIGURE 6.12: Reconstructed Adler angles, ϕ_{planar} and $\cos\,\theta_{planar}$ (left) for CC1π^+ (right) with 4π solid angle acceptance. Using the true topology and reaction definition and ND280 data (black points).

Figure 6.12 shows the reconstructed Adler angle distributions for ϕ_{planar} and $\cos\theta_{planar}$. Looking at both distributions, we can observe that the MC, overall, underestimates the data. If we focus on the ϕ_{planar} MC distribution comparison of data with MC, this can give us valuable insights into how well our model simulates the FSI and nuclear effects.

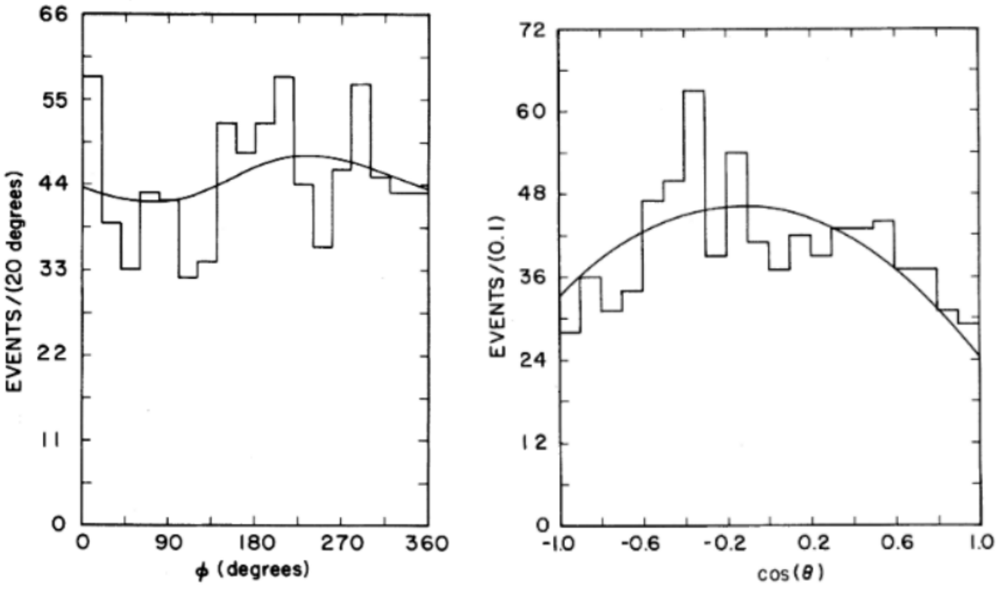

FIGURE 6.13: Adler angle distributions for ϕ_{planar} (left) and $\cos\,\theta_{planar}$ (right). Results presented by ANL using a target of deuterium and the same definition of Adler angles [20].

The Rein-Sehgal model assumes that these angular distributions should not have a preferred direction that translates to a flat distribution. When analyzing the previous result (Figure 6.13), this is what we observe. Contrary to this, we do not see flat distributions (Figure 6.12). The main differences between our analysis and the analysis by ANL are the target[8] used and the phase–space covered (see 6.1.2). Considering these

---

[8] ANL using a target of deuterium (minimizing the FSI effect) [20]

differences, the observed non-flat behavior could be coming from nuclear medium effects and FSI due to the heavier target used.

A comparison was performed to understand this a bit more. Figure 6.14 shows the comparison between reconstructed and true Adler angle distributions for ϕ_{planar} and cos θ_{planar} using CC1π^+ events regardless of in which sample they were in (CC1π^+ events within CCinclusive, CCother+CC1π^+ and CC1π^+). This allows us to see the effect that the reconstruction and the selection of CC1π^+ events has in the Adler angle distributions. In this case, we observe that when plotting the true distribution, we have the flat-ish distribution that was expected and that the constraints in the samples (from CCinclusive to CC1π^+) will affect the number of events, but the shape will be very similar (Figure 6.14 orange, pink and red curves).

For the cos θ_{planar}[9] reconstructed distribution (Figure 6.14 (right) violet, green and blue curves), the number of events decreases for negative values; this corresponds to positive pions with low momentum after the boost, resulting from mis-reconstructing low momentum pions. The ϕ_{planar} reconstructed distribution shows a peak around zero. In general, when applying the further criteria to select CC1π^+ events, the distributions show non–flat distribution.

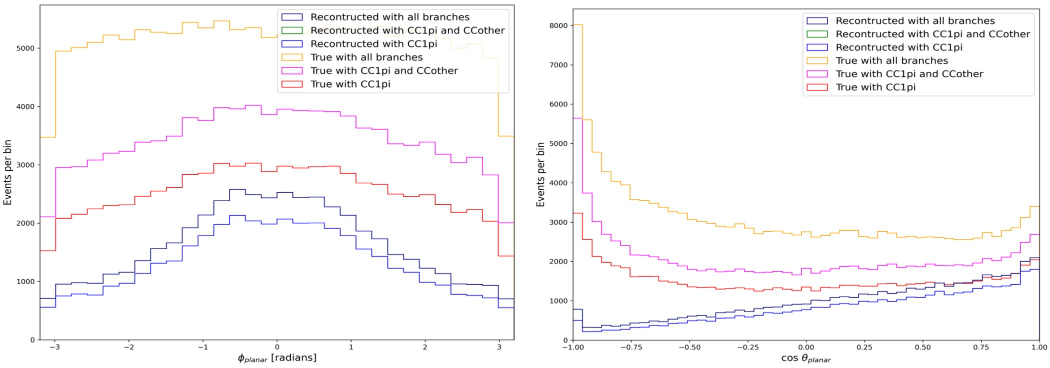

FIGURE 6.14: Comparison between reconstructed and true Adler angle distributions for ϕ_{planar} (left) and cos θ_{planar} (right).

Due to the current high-statistics experiments, we can the Adler angles as a function of the kinematic parameters of the scattering process (such as E_ν, W, and Q^2) transfer [39]. Figure 6.15 shows the 2D distributions of the reconstructed Adler angles as a function of the energy of the neutrino, the hadronic invariant mass, and four-momentum transfer.

---

[9] cos θ_{planar} Adler angle characterize the pion with regard to the direction of the Δ (after the boost).

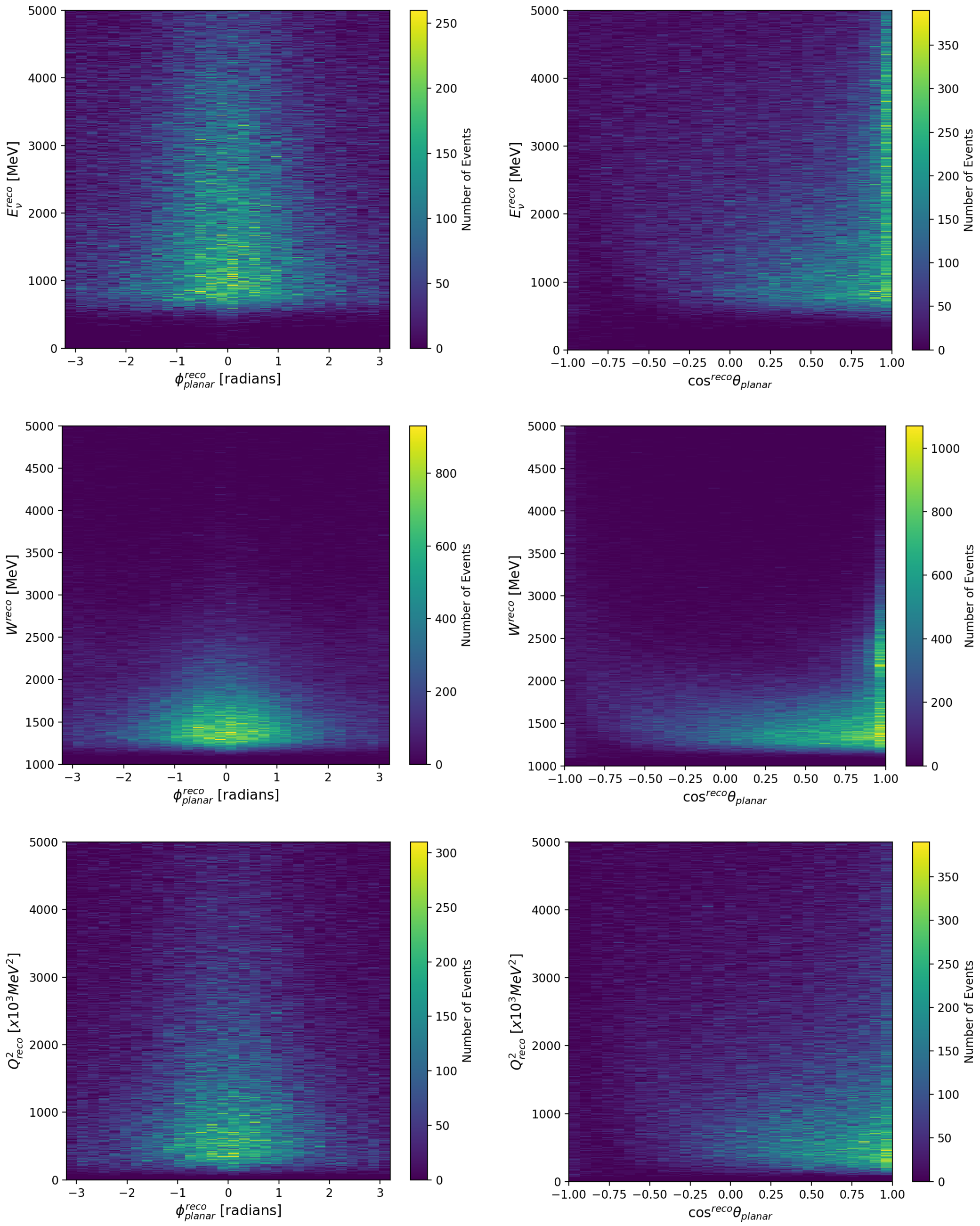

FIGURE 6.15: 2D distributions of the reconstructed neutrino energy (top row), hadronic invariant mass (central row) and four-momentum transfer (bottom row) as function of ϕ_{planar} (left column) and $\cos\ \theta_{planar}$ (right column).

Chapter 7

Evaluation of systematic uncertainties

The detector, flux, and model systematic uncertainties will alter the number of events in the corresponding truth or reconstructed bin. For these uncertainties, prior knowledge is necessary to constrain them, so a covariance matrix is computed correctly. This chapter briefly explains the different sources of systematic uncertainties accounted for in this analysis.

7.1 Detector Systematic Uncertainties

In this section, the detector systematic has been evaluated using a dedicated control sample that mimics the properties of the events in this selection. We present the relative error on the total number of events selected for the CC1π selection with 4π solid angle acceptance of systematic uncertainty. The way to propagate systematic uncertainties can be split into two categories variation and weight.

7.1.1 Propagation of variation systematics

In the case of variation systematics, there is an uncertainty on the scale or resolution of a reconstructed observable (for example, TPC PID, momentum, ToF, ...). For the error propagation, this observable is varied, and the effect on the number of selected events is checked by rerunning the whole selection. While for weight systematics, there are two classes of weight systematics, *efficiency-like* systematics, and *normalization-like* systematics. The former describes an uncertainty on reconstruction or detection efficiencies (for example, matching or tracking efficiencies); the latter change the rate of events (for example, OOFV events). The uncertainty can be encoded in an event weight in both cases without rerunning the whole selection. Two problems can arise:

1. If our observable is deduced from other underlying parameters (for example, the momentum of a track depends on the magnetic field), then an uncertainty on those parameters will be reflected in an uncertainty on the true value of our observable.
2. There are possible differences between the MC and data regarding our observable scale (mean) and resolution. Figure 7.1 shows two possible scenarios. In general, the data could be shifted and have a different resolution to the MC. We need to correct this bias; however, there might be an uncertainty on the bias, which we need to consider. Correcting these differences is part of the error propagation process without clearly separating the two. Here, we aim to describe where corrections and error propagation occurs. The error propagation can then be seen as propagating our uncertainties on the accurateness of the correction.

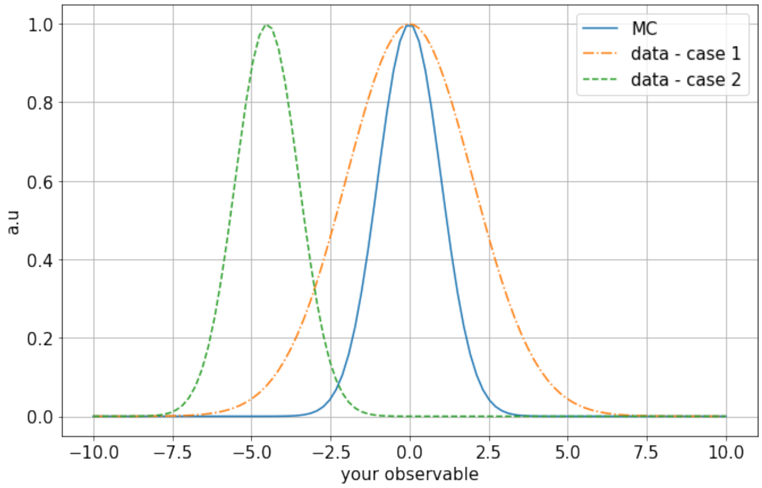

FIGURE 7.1: Two different scenarios of differences between MC and data are shown. In case 1, the data shows a different resolution twice as large as the one in MC. In case 2, the resolution is the same, however the mean value of the observable is shifted. The general case would be a combination of shifting the mean and changing the resolution.

In both cases, varying the observable might affect the number of selected events or migrate events between different analysis bins. The observable is varied according to the uncertainty, and the whole selection is rerun to estimate this effect. Note that an observable can be affected by several uncertainties. For example, the momentum is affected by field distortions, the scale of the B-field, and differences between MC and data. The variation is done in the following way:

- Case 1: The reconstructed observable x is varied according to the propagated uncertainty from the underlying parameter:

  $$x_{toy} = x_{rec}^{MC} + \alpha\delta x, \tag{7.1}$$

  where α is a random parameter, usually drawn from a Gaussian distribution centered in 0 and with width 1 (exception B-field distortions, which have a uniform PDF).

- Case 2: A small variation is added to the corrected observable x according to the uncertainty of the correction. We need to distinguish between variations of the mean or of the resolution. In the case of the mean we find:

  $$x_{toy} = x_{corr}^{MC} + \alpha\delta\Delta\bar{x} \tag{7.2}$$
  $$\text{with:} \quad x_{corr}^{MC} = x_{rec}^{MC} + \Delta\bar{x} \quad \text{and:} \quad \Delta\bar{x} = x_{rec}^{data} - x_{rec}^{MC}.$$

  If we need to vary the observable because of a difference of resolution between MC and data, we apply the following:

  $$x_{toy} = x_{true} + (1 + \alpha\delta s)(x_{corr}^{MC} - x_{true}) \tag{7.3}$$
  $$\text{with:} \quad x_{corr}^{MC} = x_{true} + s(x_{rec}^{MC} - x_{true}) \quad \text{and:} \quad s = \frac{\sigma_{data}}{\sigma_{MC}}.$$

The errors $\delta\Delta\bar{x}$ and δs are readout of data files saved in the code.

7.1.2 Propagation of weight systematics

As the name implies, we assign a weight for weight systematics, which will then scale the number of events up or down according to the uncertainty of our systematic. For efficiency-like systematics, the event weight is only applied to relevant events, and several weights can be applied to the same event (for example, one weight per TPC track for the TPC Track-Efficiency systematic). For normalization systematics, only one event weight is applied to each event. The calculation of the weights differs for the two categories and will be explained in the following sections.

Efficiency-like systematic:

These systematics are tightly linked to the performance of the reconstruction and selection. There can be different efficiencies in data and MC. Therefore the MC is corrected with the help of an event weight to reflect the data better. The propagation of this correction's uncertainty consists of varying the event weight. The event correction is determined by comparing the efficiencies in data and MC in dedicated control sample, and assuming that the ratio of efficiencies in the control sample r^{CS} is the same as the ratio of efficiencies in the analysis sample:

$$\epsilon_{data} = \frac{\epsilon_{data}^{CS}}{\epsilon_{MC}^{CS}} \epsilon_{MC} = r^{CS} \epsilon_{MC}. \tag{7.4}$$

We can assign an efficiency or inefficiency weight to the event as followed:

$$w_{eff} = \frac{\epsilon_{data}}{\epsilon_{MC}} \quad , \quad w_{ineff} = \frac{1-\epsilon_{data}}{1-\epsilon_{MC}}. \tag{7.5}$$

For the error propagation we simply change these weights by varying the ratio r^{CS} and recalculating the efficiency in data ϵ'_{data}:

$$\epsilon'_{data} = (r^{CS} + \alpha \delta r^{CS}) \epsilon_{MC}, \tag{7.6}$$

where as before α is a random parameter, drawn from a Gaussian distribution centered in 0 and with width 1. The error δr^{CS} is a combination of relative difference between MC and data $(1 - r^{CS})$ and statistical uncertainty (computed using Gaussian error propagation):

$$\begin{aligned} \delta r^{CS} &= \sqrt{(1 - r^{CS})^2 + \left(r^{CS}_{stat}\right)^2} & (7.7) \\ &= \sqrt{(1 - r^{CS})^2 + (r^{CS})^2 \left[\left(\frac{\delta \epsilon_{data}}{\epsilon_{data}} \right)^2 + \left(\frac{\delta \epsilon_{data}}{\epsilon_{data}} \right)^2 \right]}. & (7.8) \end{aligned}$$

Normalisation-like systematic:

Normalisation-like systematics describe uncertainties we have on the total event rate of CC-inclusive events. In that case we can immediately vary the event weight:

$$w_{event} = 1 + w_{corr} + \alpha \delta, \tag{7.9}$$

where w_{corr} [1] is a potential correction, and δ quantifies the rate uncertainty related to the systematic.

7.1.3 Analysis uncertainties

All the results are obtained after throwing 500 toys[2]. It is important to notice that the weights associated with the systematics are truncated at ten due to large weights in this analysis mainly coming from secondary interactions of pion and proton.

Each selection has its list of systematics which are relevant for it. In the selection, the systematics are tuned depending on the path and the topology (Figure 7.2). This tuning was introduced to reduce the computing time of certain systematics and only apply the important systematics for each track; this is called "fine-tuning". The fine-tuning allows us only to apply a specific systematic if the systematic itself has to be considered for the track (true or reconstructed).

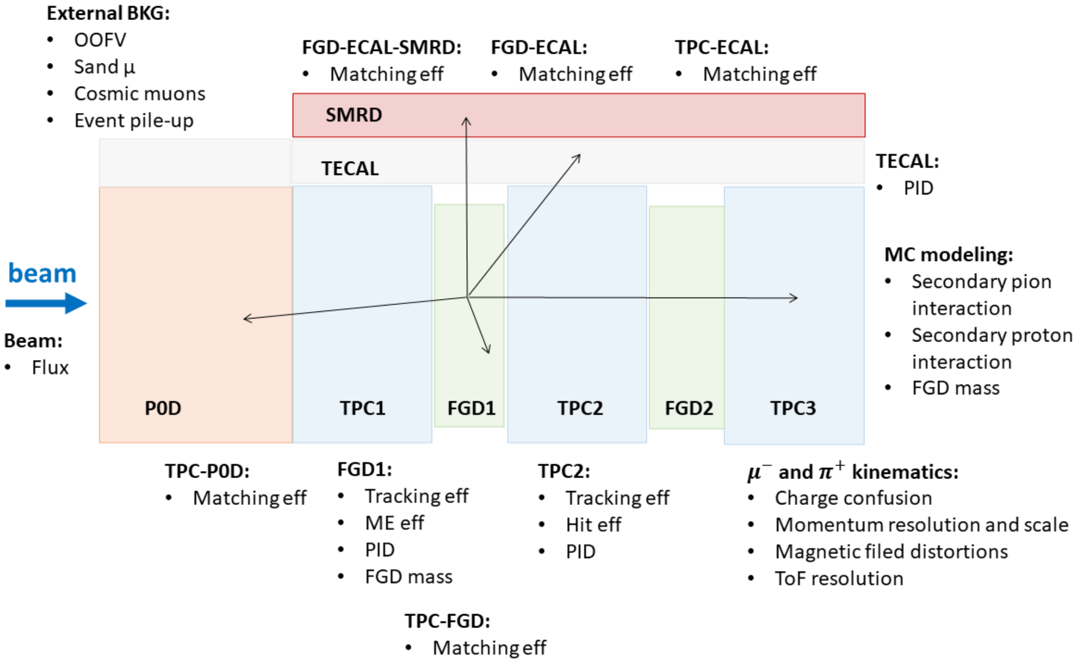

FIGURE 7.2: Sketch of the sub-detectors relevant for this analysis with the corresponding associated systematic components and example of possibles tracks paths. TPCs are shown in light blue, FGD1 in light green, ECals in light gray, and P∅D in light orange

Figures 7.3 shows the relative errors using NEUT and GENIE as a function of muon and positive pion kinematics variables when all systematics (7.2) are thrown together for the CC1π^+ sample. We can correlate the higher values of the relative errors to the low statistic bins. Overall the relative error values when running all the systematics together is less than 10%. The main contribution comes from the systematics: SandMu, OOFV, TpcTrackEff, and TpcPid (in that order).

---

[1] The correction is done by producing a control sample with similar kinematics and fitting data/MC.

[2] Random variations of parameter based on the uncertainty in order to propagate the systematic when it is not possible to do it analytically. This toy gives a different number of reconstructed events in each bin for each sample for each toy

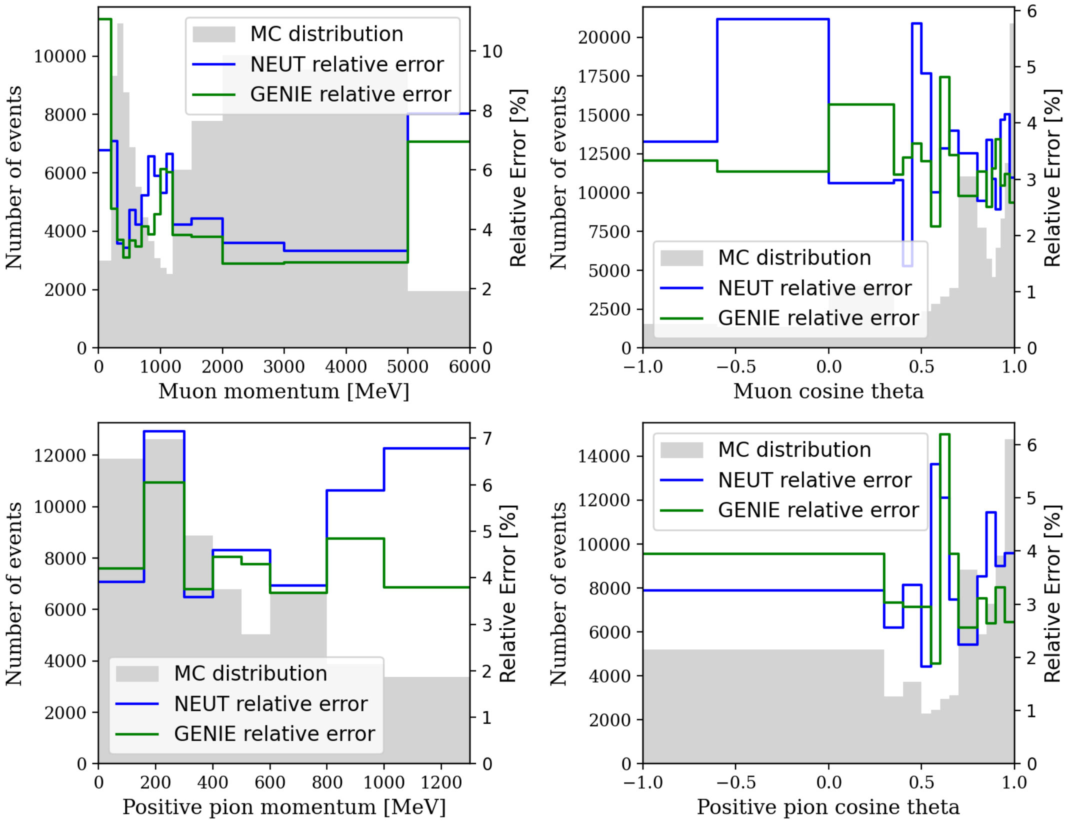

FIGURE 7.3: Relative errors using NEUT (blue line), GENIE (green line) and MC distribution (gray area) as function of muon momentum (top left), muon cosine of theta (top right), positive pion momentum (bottom left) and positive pion cosine of theta (bottom right) when all systematics are thrown together for the CC1π^+ sample.

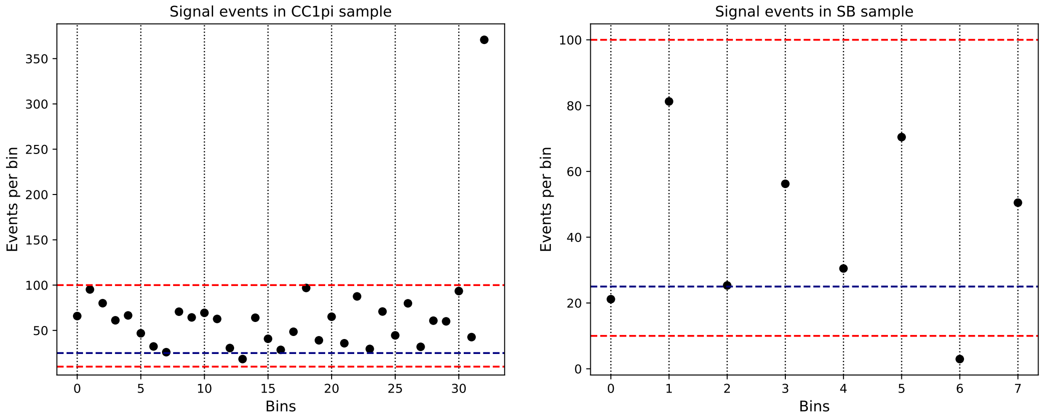

FIGURE 7.4: Number of signal events for signal (left) and control sample (right) binning in reconstructed variables. Red dash lines are marking the values of 100 and 10 number of events and the navy dash line is at the 25 mark of the number of events.

Table 7.1 displays the integrated systematic errors for CC1π^+, which are computed using a single bin of $\cos\ \theta_\mu$ and of $\cos\ \theta_{\pi^+}$, between 1 and -1. While some of the errors appear small, this is because it is the error on the total number of events in the selection, and it is more insightful to study the systematic plots as a function of the kinematics variables. The single systematic contributions are reported in the Appendix E.

A detector covariance matrix is calculated (Figure 7.5) using the toys and the reconstructed bins separately for each sample. We used two different binning for the reconstructed variables in the signal and control sample (Table 7.2).

Systematics error source	Total error in (%) for CC1π^+			
	$\cos\theta_\mu$		$\cos\theta_{\pi^+}$	
	NEUT	GENIE	NEUT	GENIE
BFieldDist	0.017624	0.005980	0.130875	0.096558
MomResol	0.866122	0.504343	0.316884	0.184534
MomScale	0.020693	0.007286	0.081739	0.056419
MomRangeResol	0.002364	0.006813	0.0	0.0
MomBiasFromVertexMigration	0.779635	0.613562	0.098412	0.164463
TpcPid	3.683760	3.566778	2.173667	2.011243
FgdPid	0.024432	0.229338	0.121291	0.147329
ECalEMResol	0.777001	1.030165	0.208751	0.245543
ECalEMScale	1.517380	2.356713	0.640884	0.396490
ToFResol	1.632360	0.211305	0.039595	0.084370
FGDMass	0.997506	0.942836	1.010963	1.014107
ChargeIDEff	0.411911	0.440164	0.368582	0.377031
TpcClusterEff	0.053152	0.010746	0.027075	0.028444
TpcTrackEff	4.573733	5.833676	3.833696	4.250435
TpcFgdMatchEff	0.249033	0.238992	0.606406	0.341882
FgdHybridTrackEff	0.550206	0.456092	0.351068	0.280922
MichelEleEff	0.377419	0.489003	0.450003	0.484340
PileUp	0.206773	0.170297	0.203324	0.194000
OOFV	3.198059	4.368523	5.383160	4.647081
SandMu	20.65164	0.0	14.06794	0.0
TpcECalMatchEff	0.013080	0.061223	0.020254	0.044160
TpcP0dMatchEff	1.697825	0.628949	0.758224	0.535866
FgdECalMatchEff	0.544337	0.731544	0.798125	0.572270
FgdECalSMRDMatchEff	1.293214	2.971061	1.965877	2.145872
ECalTrackEff	0.092746	0.092812	0.158717	0.066572
SIPion	0.769612	0.563504	0.592483	0.473299
SIProton	0.730587	0.511500	0.804703	0.779778
Total uncertainty (All)	8.276472	6.808587	6.633964	7.314640

TABLE 7.1: Integrated relative errors (in %) for each source of detector systematics for CC1π^+ by using NEUT and GENIE.

	$cos\theta_\mu$		P_μ [MeV]		$cos\theta_{\pi^+}$		P_{π^+} [MeV]	
Bin No.	begin	end	begin	end	begin	end	begin	end
Signal								
0	-1.0	0.6	200	30000	-1.0	0.7	160	30000
1	-1.0	0.6	200	400	0.7	1.0	160	30000
2	-1.0	0.6	400	30000	0.7	1.0	160	30000
3	0.6	0.8	200	600	-1.0	0.7	160	30000
4	0.6	0.8	200	600	0.7	1.0	160	400
5	0.6	0.8	200	600	0.7	1.0	400	30000
6	0.6	0.8	600	30000	-1.0	0.7	160	30000
7	0.6	0.8	600	30000	0.7	1.0	160	400
8	0.6	0.8	600	30000	0.7	1.0	400	30000
9	0.8	0.9	200	1000	-1.0	0.7	160	30000
10	0.8	0.9	200	1000	0.7	1.0	160	400
11	0.8	0.9	200	1000	0.7	1.0	400	30000
12	0.8	0.9	1000	30000	-1.0	0.7	160	30000
13	0.8	0.9	1000	30000	0.7	1.0	160	400
14	0.8	0.9	1000	30000	0.7	1.0	400	30000
15	0.9	1.0	200	1000	-1.0	0.7	160	300
16	0.9	1.0	200	1000	-1.0	0.7	300	30000
17	0.9	1.0	200	1000	0.7	1.0	160	300
18	0.9	1.0	200	1000	0.7	1.0	300	30000
19	0.9	1.0	1000	2500	-1.0	0.7	160	300
20	0.9	1.0	1000	2500	-1.0	0.7	300	30000
21	0.9	1.0	1000	2500	0.7	1.0	160	300
22	0.9	1.0	1000	2500	0.7	1.0	300	600
23	0.9	1.0	1000	2500	0.7	1.0	600	800
24	0.9	1.0	1000	2500	0.7	1.0	800	30000
25	0.9	1.0	2500	30000	-1.0	0.7	160	300
26	0.9	1.0	2500	30000	-1.0	0.7	300	30000
27	0.9	1.0	2500	30000	0.7	1.0	160	300
28	0.9	1.0	2500	30000	0.7	1.0	300	500
29	0.9	1.0	2500	30000	0.7	1.0	500	800
30	0.9	1.0	2500	30000	0.7	1.0	800	30000
31	-1.0	1.0	0	200	-1.0	1.0	160	30000
32	-1.0	1.0	200	30000	-1.0	1.0	0	160
Control sample								
33	-1.0	0.85	200	30000	-1.0	1.0	160	300
34	-1.0	0.85	200	30000	-1.0	1.0	300	30000
35	0.85	1.0	200	30000	-1.0	0.8	160	300
36	0.85	1.0	200	30000	-1.0	0.8	300	30000
37	0.85	1.0	200	30000	0.8	1.0	160	500
38	0.85	1.0	200	30000	0.8	1.0	500	30000
39	-1.0	1.0	0	200	-1.0	1.0	160	30000
40	-1.0	1.0	200	30000	-1.0	1.0	0	160

TABLE 7.2: Signal + control sample binning in reconstructed variables.

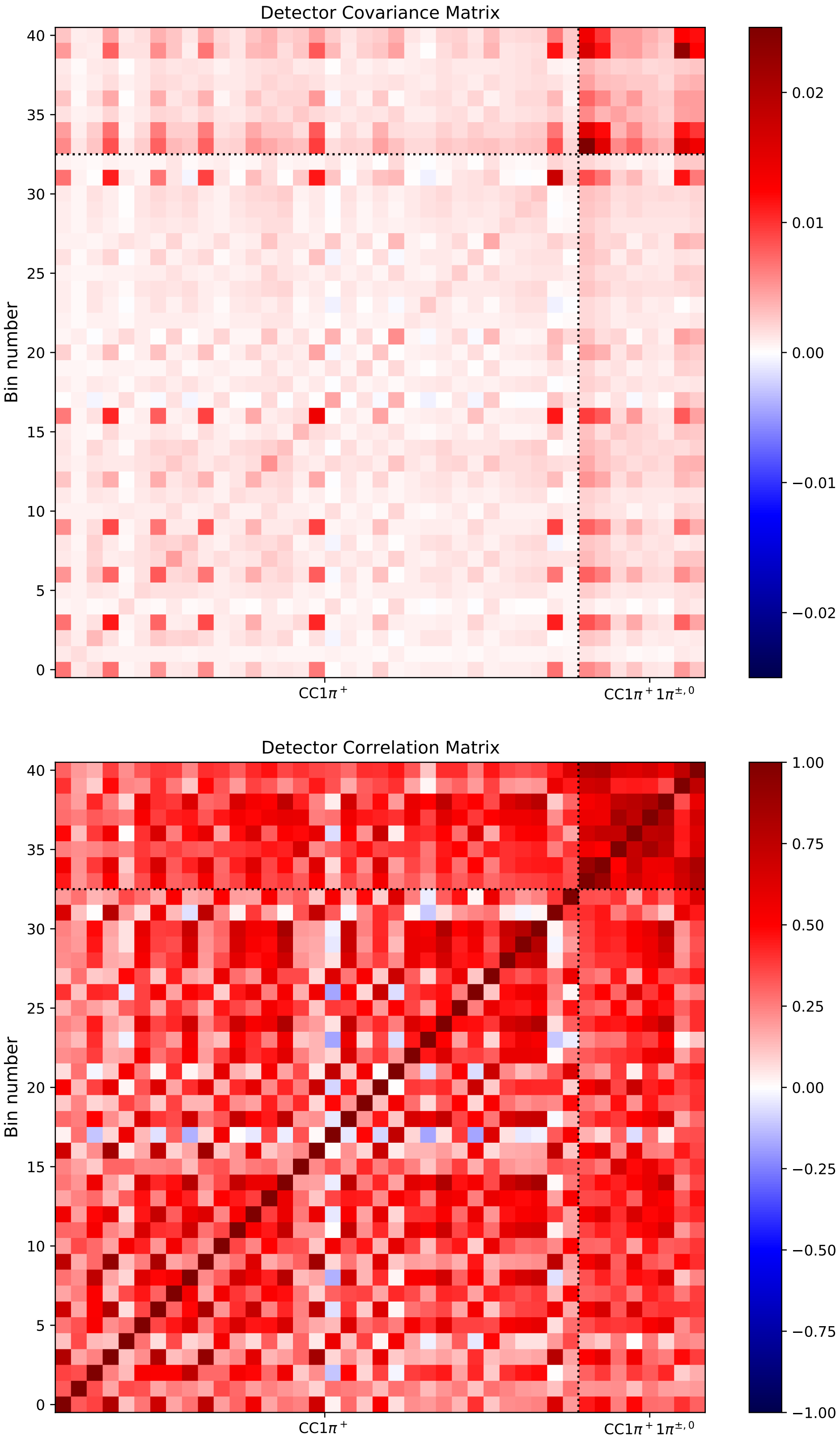

FIGURE 7.5: ND280 detector covariance (top) and correlation (bottom) matrices. With 41 bins used for the detector covariance and correlation matrix (signal + control sample). Binnig reported in Table 7.2.

7.2 Flux systematic uncertainties

The Beam MC group provides the flux systematic uncertainties in a covariance matrix with submatrices for each horn polarity and neutrino flavor combination. In this analysis, we used only the FHC ν_μ covariance matrix (Figure 7.7) of the *21bv2*[3] flux release with 20 bins on the neutrino energy.

	E_ν [MeV]			E_ν [MeV]	
Bin No.	begin	end	Bin No.	begin	end
0	0	100	10	1200	1500
1	100	200	11	1500	2000
2	200	300	12	2000	2500
3	300	400	13	2500	3000
4	400	500	14	3000	3500
5	500	600	15	3500	4000
6	600	700	16	4000	5000
7	700	800	17	5000	7000
8	800	1000	18	7000	10000
9	1000	1200	19	10000	30000

TABLE 7.3: Flux binning on the neutrino energy.

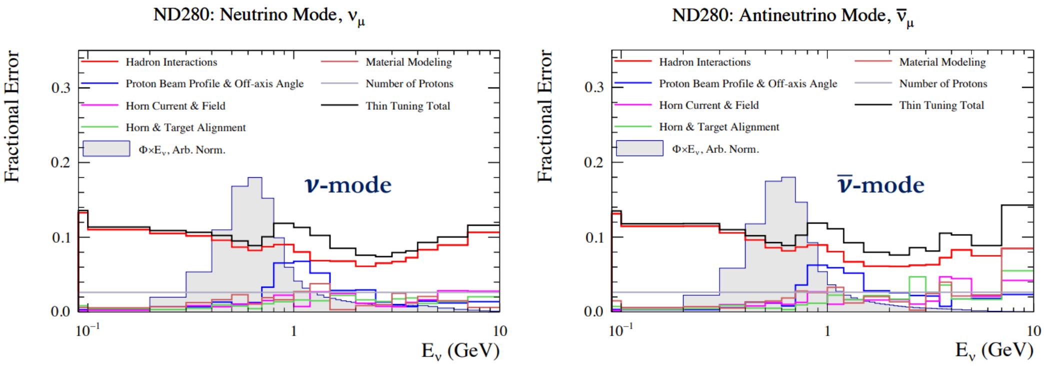

FIGURE 7.6: The relative flux uncertainty for ND280 for neutrinos (right) and antineutrinos (left) as a function of neutrino energy, separated by the uncertainty source. The flux uncertainty is dominated by the uncertainty in the hadron interaction model.

The flux covariance matrix is calculated by performing toy throws of the nominal flux prediction for each systematic and combining the uncertainty from each into a single covariance matrix. The sources of uncertainty (Figure 7.6) in the flux prediction are separated into two broad categories: hadron production uncertainties (such as pion kinematics and multiplicities) and non-hadron production uncertainties (such as the horn current or off-axis angle).

---

[3] The version of the tuning used for the P6T processing is 21bv2, which features 21b nominal flux with NA61 2010 replica thin-target, which for the first time includes $K^{\pm}$ and proton yields from the surface of a T2K replica target.

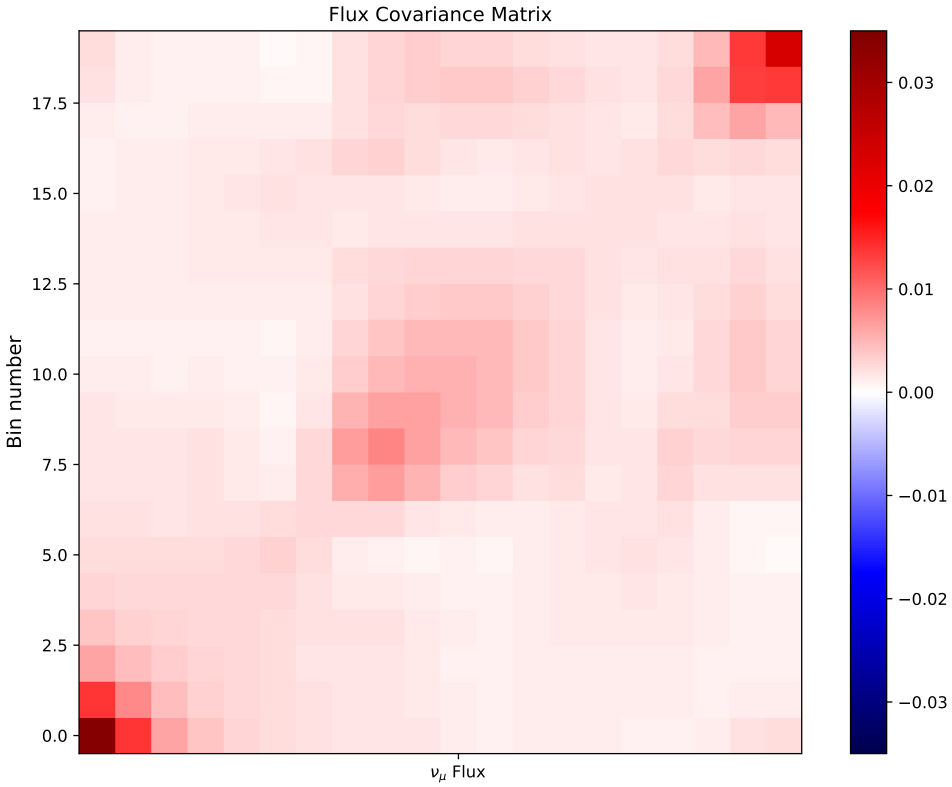

FIGURE 7.7: Flux covariance matrix for ND280 detector for both ν_μ in FHC. First 20 × 20 bins of the full covariance matrix. Binning show in Table 7.3.

7.3 Modeling systematic uncertainty

The BANFF systematic parameters for oscillation analysis are used to parametrize the model variation in our fit. Oxygen parameters are omitted since they should not affect the FGD1 (Hydrocarbon) analysis. The parameters used in this analysis are shown in Table 7.4 and the Figure 7.8 shows the corresponding covariance and correlation matrices. Functionally in the analysis, each parameter's nominal value and error are normalized to have a nominal value of one and corresponding fractional error. T2KReweight is used to form splines that describe the effect of changing a model parameter, categorized by event sample, final state topology, true and reconstructed kinematic variable analysis bins (for the splines plots, see Appendix F).

Index	Parameter	Type[4]	Prior ± Error
0	M_A^{QE}	shape	1.21 ± 0.30
1	2p2h ν norm	normalization	1.0 ± 1.0
2	2p2h ν shape	shape	1.0 ± 1.0
3	M_A^{RES}	shape	0.95 ± 0.15
4	C_A^5	shape	1.01 ± 0.12
5	Bkg Resonant	normalization	1.3 ± 0.20
6	CC1π $E_\nu < 2.5GeV$	normalization	1.0 ± 0.50
7	CC1π $E_\nu > 2.5GeV$	normalization	1.0 ± 0.50
8	DIS	shape	1.0 ± 0.40
9	CC DIS	normalization	1.0 ± 0.50
10	CC Multi-π	normalization	1.0 ± 0.50
11	CC Coherent on C	normalization	1.0 ± 1.0
12	NC Coherent	normalization	1.0 ± 0.30
13	NC Other	normalization	1.0 ± 0.30
14	FSI Inelastic $< 0.5GeV$	shape	1.0 ± 0.41
15	FSI π absorbtion	shape	1.1 ± 0.41
16	FSI Charge exchange, $< 0.5GeV$	shape	1.0 ± 0.57
17	FSI Inelastic, $> 0.5GeV$	shape	1.8 ± 0.34
18	FSI π production	shape	1.0 ± 0.50
19	FSI Charge exchange, $> 0.5GeV$	shape	1.8 ± 0.28

TABLE 7.4: cross section modeling parameters used in this analysis along with their type, prior, and error. Values taken from [1].

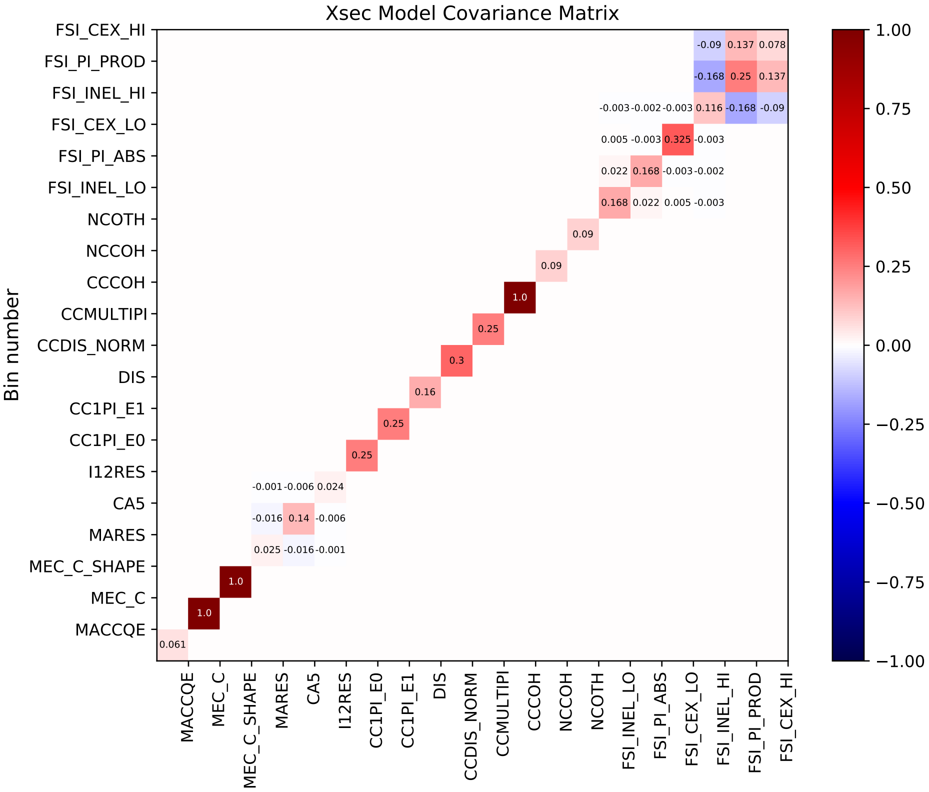

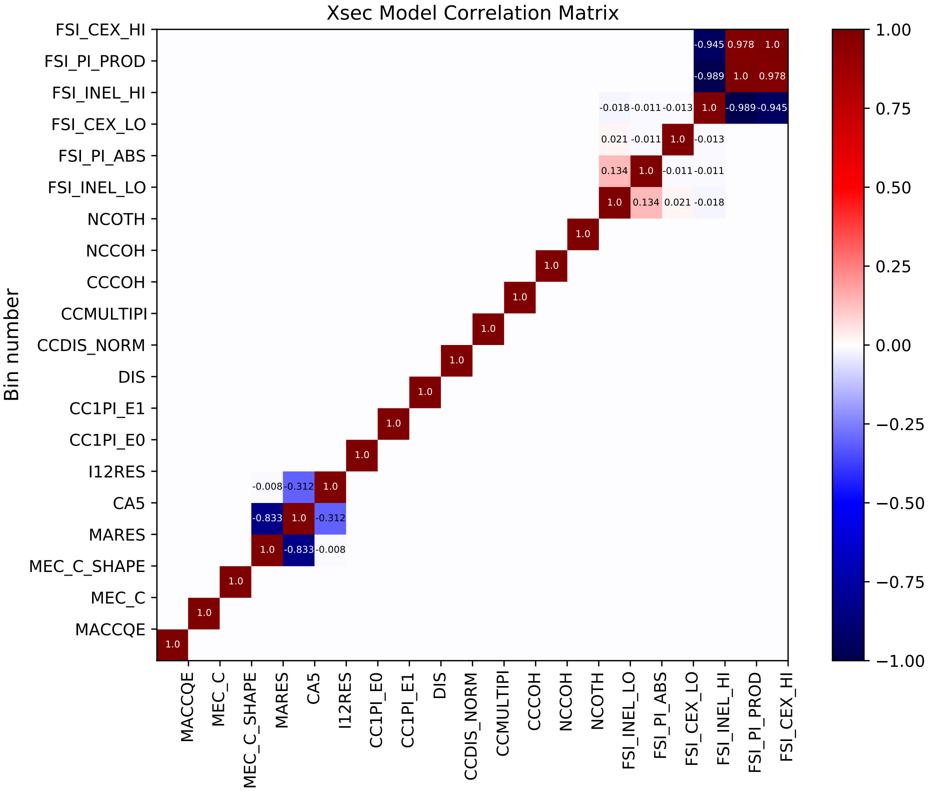

FIGURE 7.8: cross section model covariance matrix (top) and correlation matrix (bottom).

7.4 Signal binning

In order to avoid a strong anti-correlation between nearby bins, the binning choice becomes extremely important. The aim is to balance the number of selected events per bin and the detector's resolution. The truth binning in kinematic variables of the signal events used in cross section extraction is presented in Table 7.5. The binning contains two extra out of phase-space constrains (OOPS as reported in 6.1.2) bins to include the events that fail the kinematic phase space cut, which provides information for the fitter to scale the OOPS background properly.

	$cos\theta_\mu$		P_μ [MeV]		$cos\theta_{\pi+}$		$P_{\pi+}$ [MeV]	
Bin No.	begin	end	begin	end	begin	end	begin	end
0	-1.0	0.6	200	30000	-1.0	1.0	160	30000
1	0.6	0.8	200	400	-1.0	1.0	160	30000
2	0.6	0.8	400	30000	-1.0	1.0	160	30000
3	0.8	0.9	200	1000	-1.0	0.7	160	30000
4	0.8	0.9	200	1000	0.7	1.0	160	30000
5	0.8	0.9	1000	30000	-1.0	1.0	160	30000
6	0.9	1.0	200	1000	-1.0	1.0	160	300
7	0.9	1.0	200	1000	-1.0	1.0	300	30000
8	0.9	1.0	1000	2500	-1.0	0.7	160	30000
9	0.9	1.0	1000	2500	0.7	1.0	160	600
10	0.9	1.0	1000	2500	0.7	1.0	600	30000
11	0.9	1.0	2500	30000	-1.0	0.7	160	30000
12	0.9	1.0	2500	30000	0.7	1.0	160	30000
OOPS								
13	-1.0	1.0	0	200	-1.0	1.0	160	30000
14	-1.0	1.0	200	30000	-1.0	1.0	0	160

TABLE 7.5: Signal binning in true variables.

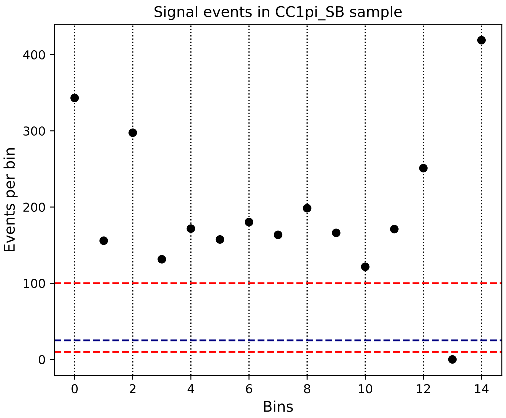

FIGURE 7.9: Number of signal events for signal binning in true variables. Red dash lines are marking the values of 100 and 10 number of events and the navy dash line is at the 25 mark of the number of events.

The main limitation in determining the cross section binning is the available statistics. To have a reasonably small statistical error in the final cross section result in each bin, we need at least 100 events/bin (Figure 7.9), and we would need to consider the detector resolution to avoid significant bin-by-bin anti-correlation due to event migration. Finally, the cross section extracted will be reported using these bins without including the OOPS bins.

When extracting the cross section on model dependant variables, the signal binning used is according to the variable (E_ν, Q^2 and W).

E_ν [MeV]			Q^2 [$\times 10^3$ MeV^2]			W [MeV]		
Bin No.	begin	end	Bin No.	begin	end	Bin No.	begin	end
0	500	750	0	0	160000	0	1000	1400
1	750	1000	1	160000	480000	1	1400	4000
2	1000	1500	2	480000	1120000			
3	1500	2000	3	1120000	5000000			
4	2000	3000						
5	3000	5000						
6	5000	30000						

TABLE 7.6: Signal binning in true E_ν, Q^2 and W variables.

Chapter 8

Fit validation

In this chapter, the inputs necessary for the fitter are presented, and we perform a comprehensive validation of the fit procedure to find out any possible misbehavior of the fitter framework to ensure the extracted cross sections are not biased by the input MC model and can always return the truth values within error bars. The fit takes as input a number of signal and background samples for each detector which are described in detail in chapter 6.

As it was defined and explained in sections 4.2.3 and 4.2.4, the fit is free to alter the template, flux, cross section, and detector parameters corresponding to both signal and nuisance parameters to find the values which best describe the data by minimizing χ^2.

The fit will produce a set of best post-fit values, errors, covariance, and correlations for each fit (template, flux, cross section, and detector) parameter that then will be used to obtain the double differential and quadruple differential neutrino cross sections.

Fit name	Description
Asimov fit	data identical to MC simulation (Sec. 8.1.1).
Random template priors	Asimov fit where the prior values of the template parameters have been randomized (Sec. 8.1.2).
MC statistical fluctuations	Asimov fit with variations of truth bins according to Poisson fluctuations (Sec. 8.1.3).
Altered OOFV weights	Data fit to decreased the oofv events weights (0.9*weight) (Sec. 8.2.1).
Altered CCother weights	Data fit to decreased the control sample events weights (0.9*weight) (Sec. 8.2.2).
Altered OOPS kinematics weights	Data fit to increased the weights (1.1*weight) of events with $P_{\mu} \leq 200\ MeV$ or $P_{\pi^+} \leq 160\ MeV$ (Sec. 8.2.3).
Altered resonant weights	Data fit to increased the resonant events weights (1.3*weight) (Sec. 8.2.4).
GENIE MC	Data fit to MC events generated with the GENIE neutrino interaction simulation (Sec. 8.2.5).

TABLE 8.1: List of fake data studies performed to validate the analysis, with short description.

The fit validation for this analysis was done is done by a series of fits utilizing fake data[1]. Table 8.1 shows the list of fake data performed in this analysis and the description.

8.1 Basic Checks

8.1.1 Asimov fit

The most basic fit that can be done is an Asimov fit (fit where the" data" is the same as the input MC simulation). The movement of any parameter will not lower the χ^2 (or raise the likelihood) because this fit starts at the true best-fit point, and it should return the same nominal parameters; this will be the first validation that the fit works and estimate the range of the final errors on the cross section. We should expect that the post-fit values remain at their nominal values (for all parameters) as shown in Figure 8.1. The parameter error bars show the magnitude of the variances.

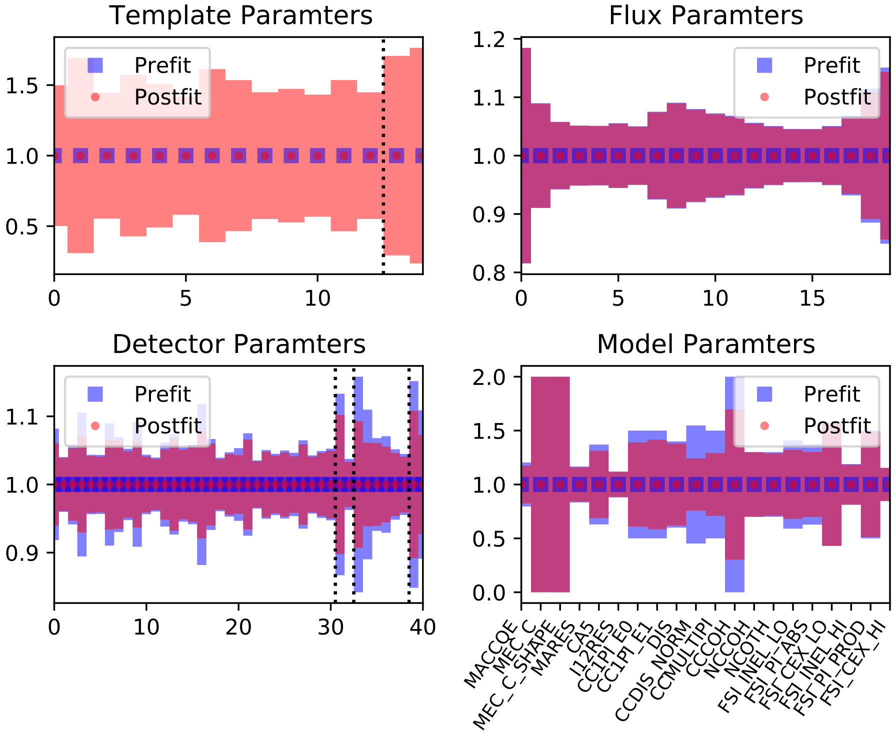

FIGURE 8.1: Pre/post-fit parameter plots for the Asimov fit with nominal priors. The black dash line on template parameters separates the last two OOPS bins, in the detector parameters point to the bins with the same kinematics as the OOPS bins for signal and control sample. Red points in the left plot show the post-fit parameters values and standard deviations alongside the light red lines, while the blue points and lines show each parameter's prior values and standard deviation. The model parameters' nominal values are normalized.

- **Template parameters[2] (top left):** The error are strongly correlated with the available statistics. So as expected, in bins with fewer events, we obtain larger errors,

---

[1] 'fake data', (also known as pseudo/mock data) is generated by altering MC.

[2] The number of template parameters is determinate by the number of true bins (analysis binning 7.4).

but overall, the errors are very similar because the binning was selected in a way that the number of the events is similar in each bin.

- **Flux parameters (top right):** The errors are almost the same as the prior.
- **Detector parameters (bottom left):** Nearly all errors saw some reduction, with the spike pattern largely a result of the statistics in a given bin.
- **Model parameters[3] (bottom right):** The errors saw a reduction in selected bins (mainly the one more related to the signal). The control samples indeed help constrain these parameters.

The pre-fit and post-fit values per bin for each sample (CC1π^+ and CC1$\pi^+1\pi^{\pm,0}$) match perfectly as expected in an Asimov fit (resulting in a zero χ^2) as shown in Figure 8.2.

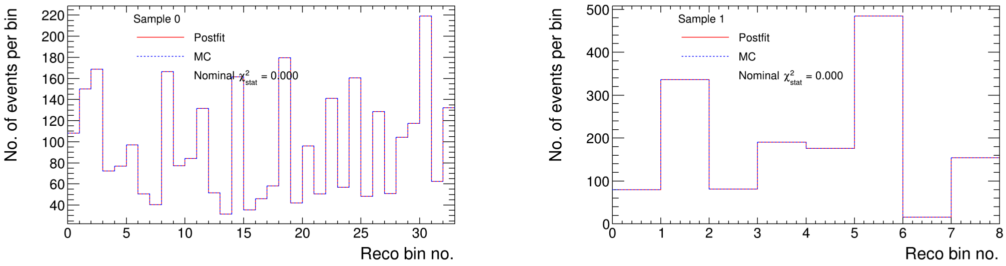

FIGURE 8.2: Pre/post-fit reconstructed event plots for the Asimov fit with nominal priors, signal (left) and control sample (right) samples.

8.1.2 Random template priors

This fake data is an Asimov fit with a slight variation. Since it is an Asimov fit, the" data" is the same as the input MC simulation, but the set to random prior values. The random number to set the prior is drawn from a Gaussian distribution with a mean of one and width of ten percent. Since the fit does not start precisely at the best-fit point, we can evaluate whether the fitter can find the correct minimum when it starts from a random point.

The fitter correctly finds the minimum no matter where it starts, as shown in Figure 8.3. The post-fit parameter errors show similar behavior to the nominal Asimov fit. The reconstructed event distributions for each sample are shown in Figure 8.4. They match perfectly as expected. The fit is expected to return a χ^2 of zero.

---

[3] These nominal values are normalized in this and all the following plots.

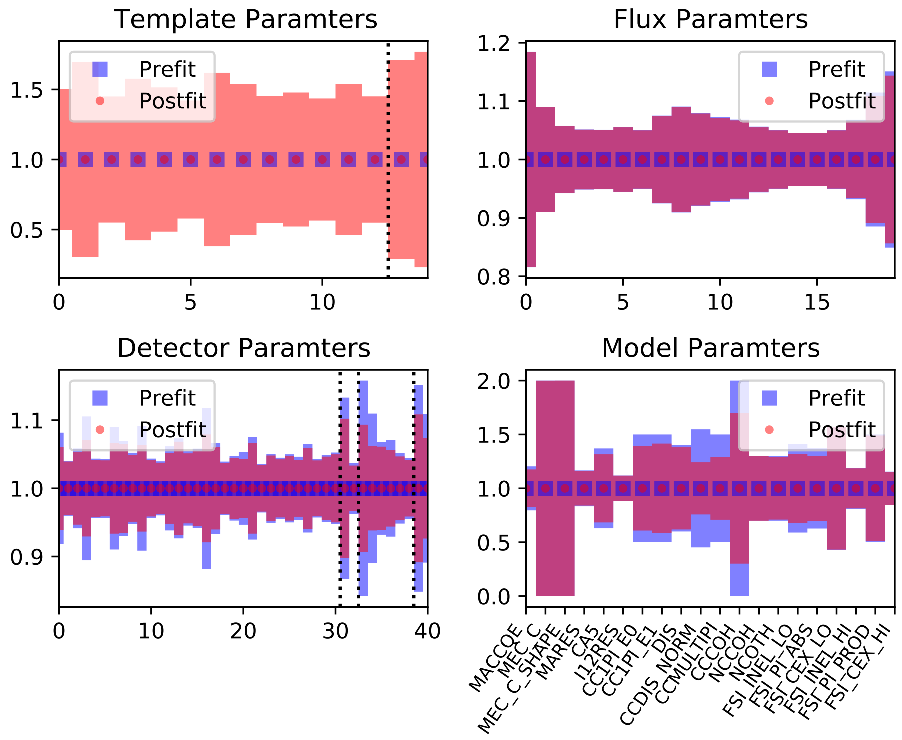

FIGURE 8.3: Pre/post-fit parameter plots for the Asimov fit with random priors. The black dash line on template parameters separates the last two OOPS bins, in the detector parameters point to the bins with the same kinematics as the OOPS bins for signal and control sample. Red points in the left plot show the post-fit parameters values and standard deviations alongside the light red lines, while the blue points and lines show each parameter's prior values and standard deviation. The model parameters' nominal values are normalized.

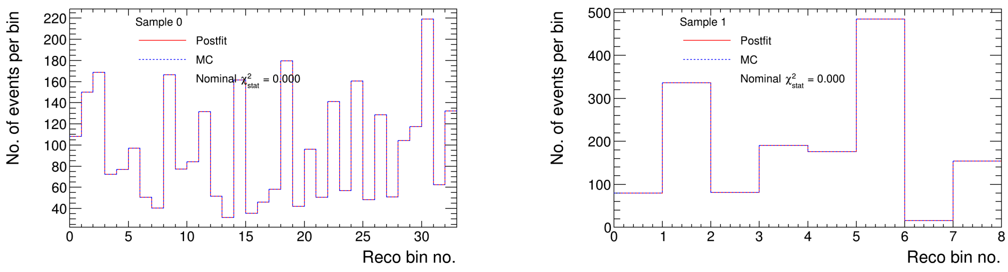

FIGURE 8.4: Pre/post-fit reconstructed event plots for the Asimov fit with random priors, signal (left) and control sample (right) samples.

8.1.3 MC statistical fluctuations

This fake data is an Asimov fit with a slight variation on the first. The fit was run with all parameters at their nominal prior but now fitting to a statistical fluctuated data set that is not identical to the input MC. A statistical fluctuation of the nominal MC was built by altering the number of events in the truth bins according to a Poisson distribution using the nominal MC prediction as average. Since the fit does not start exactly at the best-fit point, we can evaluate whether the fitter can find the correct minimum when it starts from a random point, and it is no longer expected a χ^2 of zero.

- **Template parameters (top left):** show a good behaviour under statistical fluctuations.
- **Flux parameters (top right):** The errors were more or less uniformly reduced.
- **Detector parameters (bottom left):** all parameters saw some reduction in error, with the spike pattern largely a result of the statistics in a given bin.
- **Model parameters (bottom right):** Nearly all parameters saw a varied reduction in error.

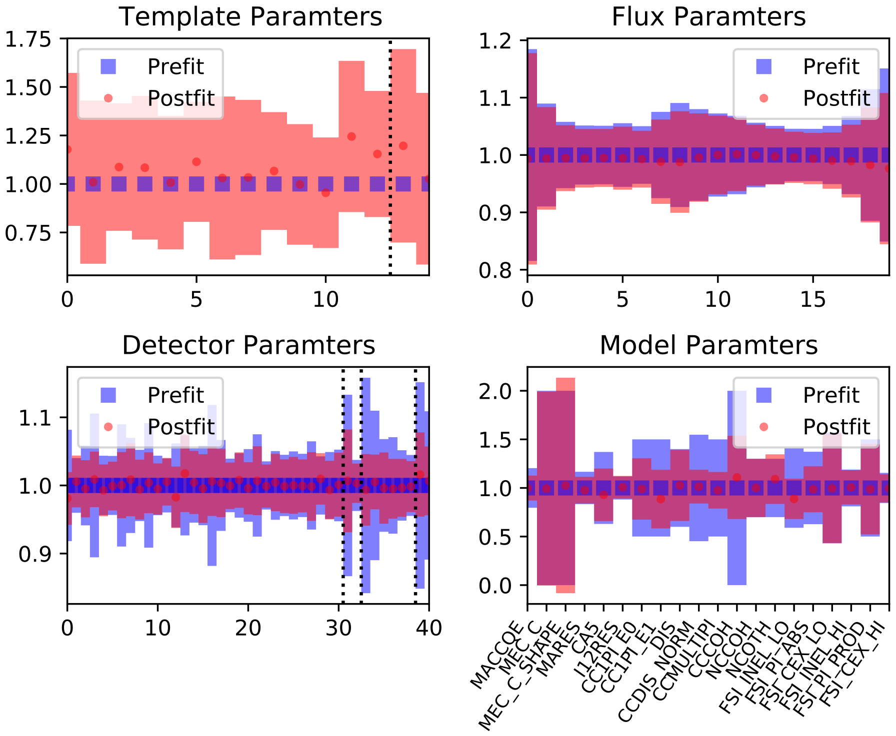

FIGURE 8.5: Pre/post-fit parameter plots for the Asimov fit with nominal priors and with statistical fluctuation. The black dash line on template parameters separates the last two OOPS bins, in the detector parameters point to the bins with the same kinematics as the OOPS bins for signal and control sample. Red points in the left plot show the post-fit parameters values and standard deviations alongside the light red lines, while the blue points and lines show each parameter's prior values and standard deviation. The model parameters' nominal values are normalized.

The reconstructed event distributions for each sample are shown in Figure 8.6. The pre-fit and post-fit event distributions show a good agreement with a non-zero χ^2 as expected since there are some discrepancies between the data and the simulation in reconstructed bins.

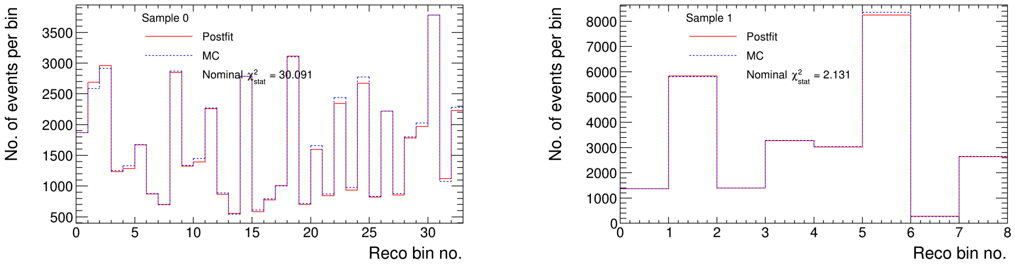

FIGURE 8.6: Pre/post-fit reconstructed event plots for the Asimov fit with nominal priors and with statistical fluctuation, signal (left) and control sample (right) samples.

8.2 Fake data studies

These studies are done by using fake data where the signal events in the nominal MC simulation were weighted to see if the fit could correctly and exactly recover the change. This fake data set were built by weighting only the determined events in the nominal MC simulation event-by-event.

In the case of altering the signal events, since the template parameters have no prior error or penalty for moving, they should recover a simple normalization variation where none of the systematic parameters should move. In these cases, the weighting function is more complicated; for example, based on the resonant components of the signal events, then the slight movement would be expected in the systematic parameters. Table 8.1 shows the list of fake data studies used to validate the analysis. These fake data studies are used to evaluate if the fitter is responding properly to its changes.

8.2.1 Altered OOFV weights

In chapter 5 we observed that OOFV events play a fundamental role in BWD samples since they constitute the main contribution in this direction. This fake data was generated by only altering the weight of the OOFV events in the analysis samples based on the topology. OOFV events are reweighed by a factor of 0.9. Given that OOFV is present in both the signal and control samples, we expect this change will alter our detector parameters, mostly the control sample bins, because of the higher contribution.

The fit results show the expected behavior (Figure 8.7). The template and model parameters moved their values slightly while the detector parameters were pulled down mainly in the control sample bins.

The reconstructed event distributions show, overall, a good agreement between the post-fit distribution and the fake data points for both samples achieving an almost perfect fit (Figure 8.8).

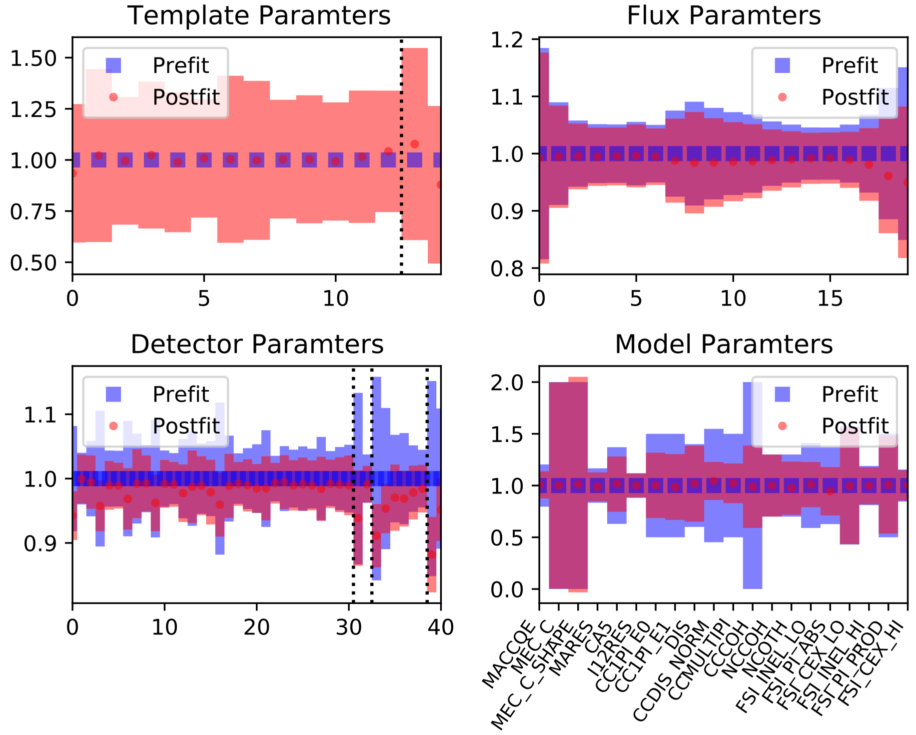

FIGURE 8.7: Pre/post-fit parameter plots for the fake data with altered OOFV events. The black dash line on template parameters separates the last two OOPS bins, in the detector parameters point to the bins with the same kinematics as the OOPS bins for signal and control sample. Red points in the left plot show the post-fit parameters values and standard deviations alongside the light red lines, while the blue points and lines show each parameter's prior values and standard deviation. The model parameters' nominal values are normalized.

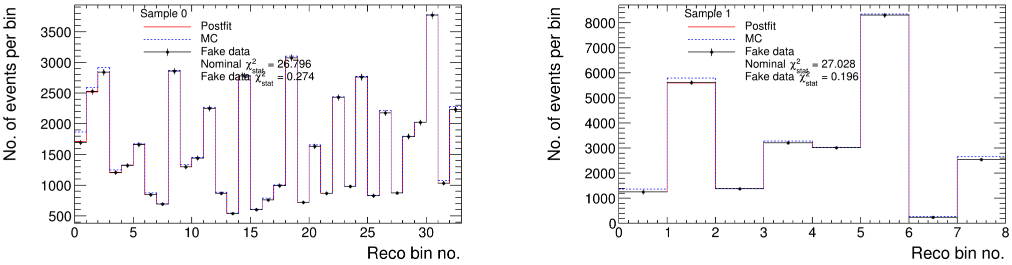

FIGURE 8.8: Pre/post-fit reconstructed event plots for the fake data with altered OOFV events, signal (left) and control samples (right) samples.

8.2.2 Altered CCother weights

The main background to the CC1pi^+ signal events (as discussed before in chapter 6) are CCother events. This fake data was generated by only altering the weight of the CCother events in the analysis samples based on the topology. CCother events are reweighed by a factor of 0.9. Given that the control sample is a sub-sample of CCother we would expect that this is well constrained in the detector parameters and will slightly move the model parameter related to multiple pions, DIS and CC1π. The fitter is performing properly for a reduction of the CCother background with the template parameters moving to correct the values as shown on the Figure 8.9.

The reconstructed event distributions show, overall, a good agreement between the post-fit distribution and the fake data points for both ND280 samples (Figure 8.10).

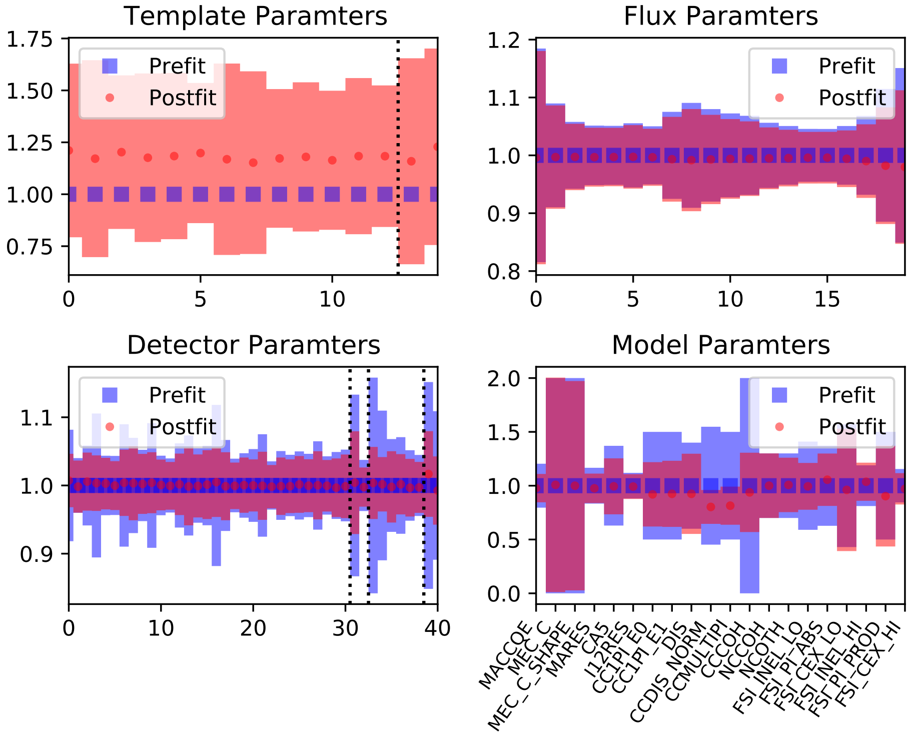

FIGURE 8.9: Pre/post-fit parameter plots for the fake data with altered CCother events. The black dash line on template parameters separates the last two OOPS bins, in the detector parameters point to the bins with the same kinematics as the OOPS bins for signal and control sample. Red points in the left plot show the post-fit parameters values and standard deviations alongside the light red lines, while the blue points and lines show each parameter's prior values and standard deviation. The model parameters' nominal values are normalized.

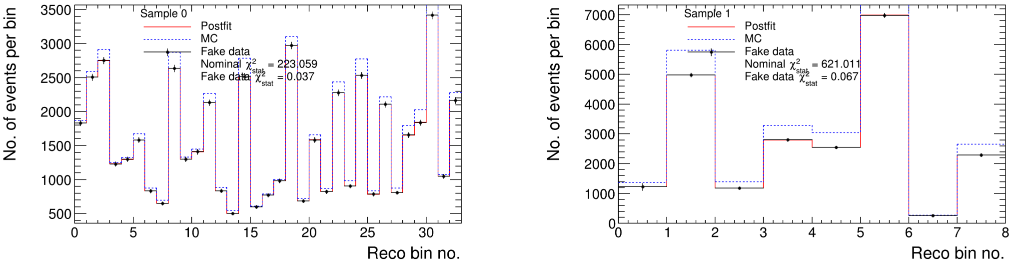

FIGURE 8.10: Pre/post-fit reconstructed event plots for the fake data with altered CCother events, signal (left) and control samples (right) samples.

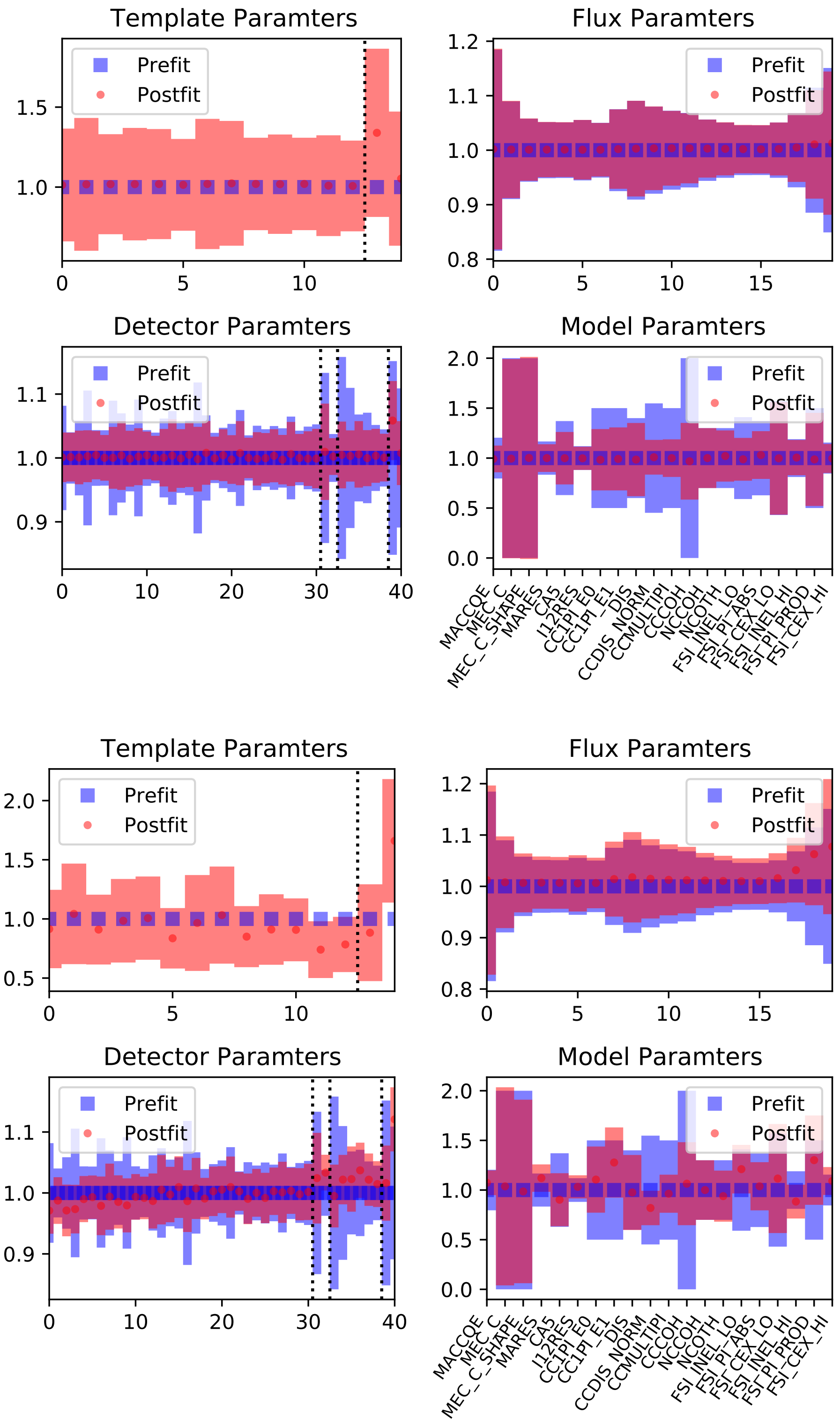

FIGURE 8.11: Pre/post-fit parameter plots for the fake data with altered OOPS muon momentum (top two rows) and positive pion momentum (bottom two rows) events. The black dash line on template parameters separates the last two OOPS bins, in the detector parameters is pointing to the bins with the same kinematics as the OOPS bins for signal and control sample. Red points in the left plot show the post-fit parameters values and their standard deviations alongside the light red lines, wile the blue points and lines show each parameter's prior values and standard deviation. The model parameters' nominal values are normalized.

8.2.3 Altered OOPS kinematics weights

In the template parameters, the last two bins correspond to the OOPS (see Sec. 6.1.2), and since the binning of the detector (signal +control sample) were selected in a way to properly separated the OOPS kinematics, two sets of fake data were generated by reweighing the OOPS events based on kinematic; this would allow us to study the effect of the OOPS events on the fit. In the first fake data set, events with $P_\mu \leq 200MeV$ were reweighed by a factor of 1.1. On the second fake data set, events with $P_{\pi+} \leq 160\ MeV$ were reweighed by a factor of 1.1. The fitter is performing properly for the weight increase of OOPS kinematics as shown in Figure 8.11.

We observe that the template parameters (especially the OOPS bin containing this event) move up to correct the values. In the reconstructed binning of the signal and control sample, these kinematics bins were also separated, so we should observe a movement in the bins. As expected, template parameter number 13 and detector parameters 31 and 39 are pulled up to correct the values for the first fake data set.

For the second fake data set, the pion kinematics will affect the model parameter mostly related to multiple pions, DIS, CC1π and FSI_s moving the value but reducing their errors. As expected, the template parameters and detector parameters are moved, but the most significant pull is observed for the bins with that kinematic (bin 14 for template parameters for detector parameter (signal and control sample) the bins 32 and 40) to correct the values. The fitter is performing properly for the weight change in the OOPS kinematics.

The reconstructed event distributions show, overall, a good agreement between the post-fit distribution and the fake data points, as shown in Figure 8.12.

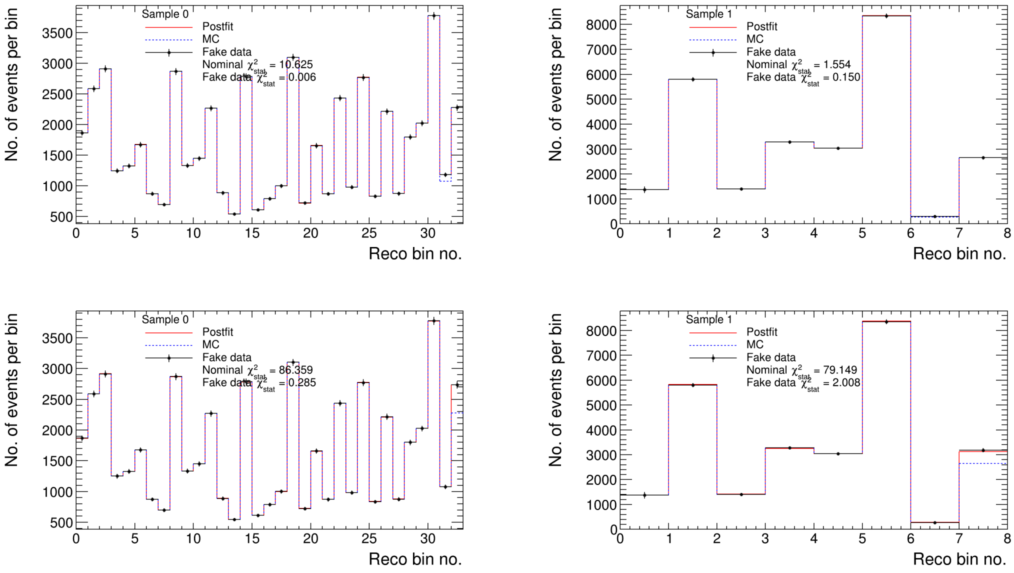

FIGURE 8.12: Pre/post-fit reconstructed event plots for the fake data with altered OOPS muon momentum signal (top left), muon momentum control sample (top right), positive pion momentum signal (bottom left), and positive pion momentum control sample (bottom right) events.

8.2.4 Altered resonant weights

The two main contributions to our signal events are RES ($\sim 52\%$) and DIS ($\sim 26\%$). This fake data was generated by only reweighing the resonant events in the analysis samples based on the reaction. Resonant events are reweighed by a factor of 1.3. The signal events are mostly resonant, and in the control sample, this is the second highest contribution. The fitter is performing properly for an increase of the resonant weight with the template parameters moving up to correct the values as shown in Figure 8.13.

The fit results show the expected behavior, the systematic parameters slight moving values (Figure 8.13). The reconstructed event distributions show, overall, a good agreement between the post-fit distribution and the fake data points, with all the ND280 samples achieving an almost perfect fit (Figure 8.14).

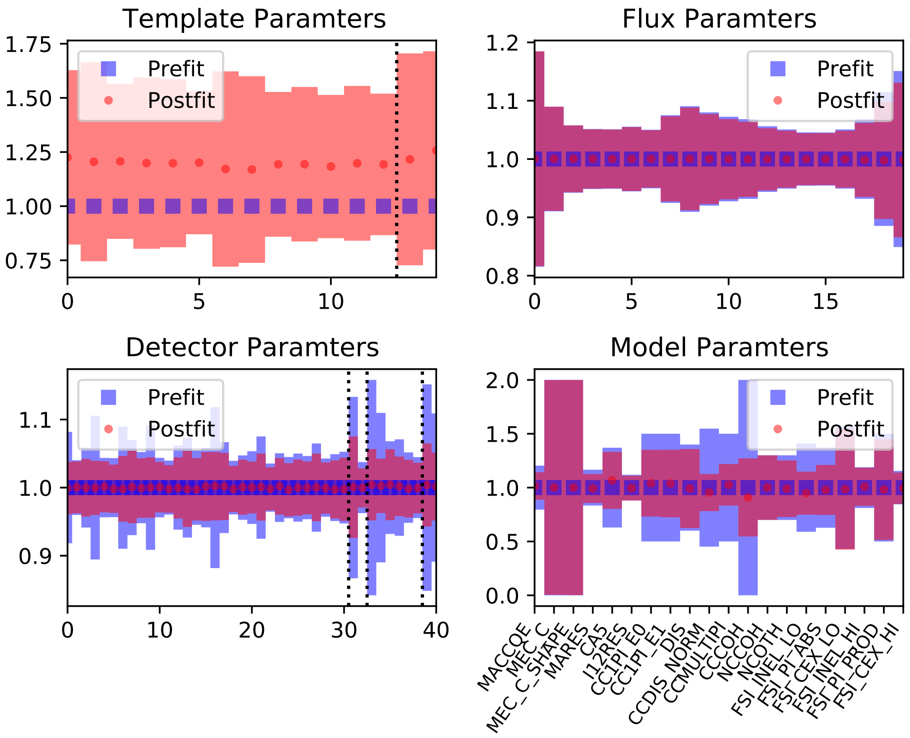

FIGURE 8.13: Pre/post-fit parameter plots for the fake data with altered resonant events. The black dash line on template parameters separates the last two OOPS bins, in the detector parameters point to the bins with the same kinematics as the OOPS bins for signal and control sample. Red points in the left plot show the post-fit parameters values and standard deviations alongside the light red lines, while the blue points and lines show each parameter's prior values and standard deviation. The model parameters' nominal values are normalized.

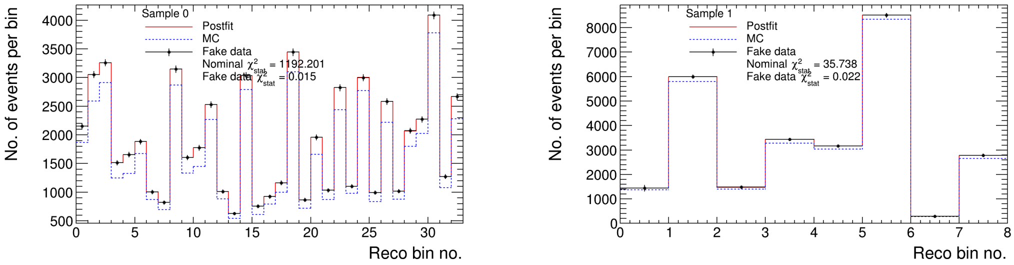

FIGURE 8.14: Pre/post-fit reconstructed event plots for the fake data with altered resonant events, signal (left) and control samples (right) samples.

8.2.5 GENIE

We generated the fake data using the GENIE MC (scaled to data POT). This test will probe if the fitter has good flexibility since the FSI and DIS implementation for GENIE is very different from NEUT. The set of best-fit parameters for this fake data is shown in Figure 8.15.

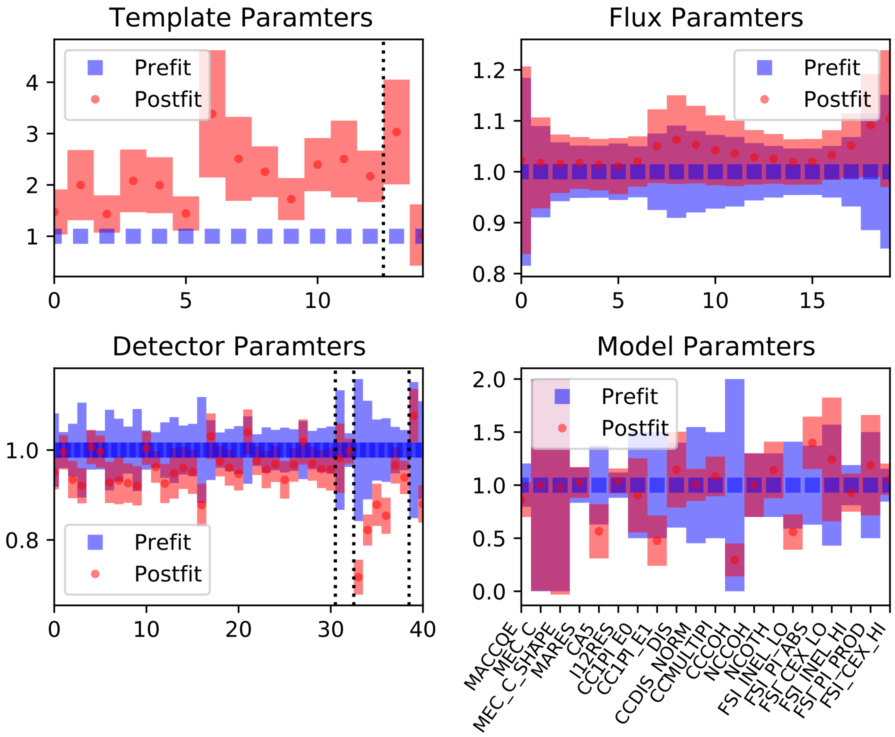

FIGURE 8.15: Pre/post-fit parameter plots for the fake data using GENIE. The black dash line on template parameters separates the last two OOPS bins, in the detector parameters point to the bins with the same kinematics as the OOPS bins for signal and control sample. Red points in the left plot show the post-fit parameters values and standard deviations alongside the light red lines, while the blue points and lines show each parameter's prior values and standard deviation. The model parameters' nominal values are normalized.

The reconstructed event distributions show, overall, a good agreement between the post-fit distribution and the fake data points for both signal and control sample (Figure 8.16). We can see the multiple pions, DIS, CC1π and FSI_s model parameters are moved quite a lot from the nominal. The detector parameters are pull-down (higher for the control sample), while the template parameters are pushed up to correct the values.

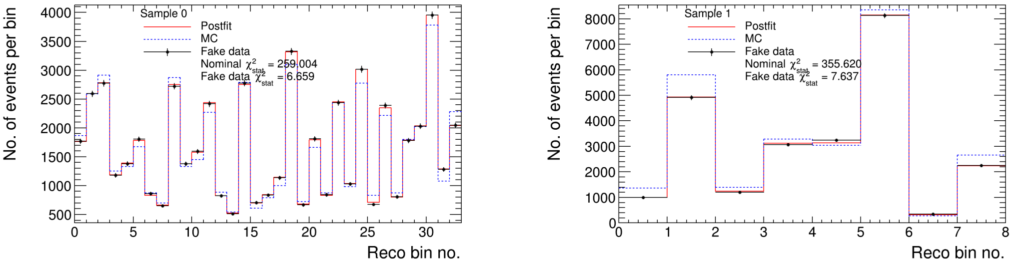

FIGURE 8.16: Pre/post-fit reconstructed event plots for the fake data using GINIE, signal (left) and control samples (right) samples.

8.3 Summary

The fitter framework performed well in every validation test described in this chapter, being capable of identifying single changes. These studies of the fitter constitute the baseline for the fit performance and an indication of the validity of the real data fit. When unblinding the data, the fit parameters should show similar post-fit error bars to these studies. We know if the fit has enough freedom by checking the agreement between the pre-fit nominal MC and the post-fit distributions. Looking at the χ^2 values in general, we can see that the data prefers the post-fit distribution in each fake data study. Table 8.2 summarizes the χ^2 values per study for nominal to post-fit and data to post-fit.

Fit name	χ^2_{stat} CC1π^+		χ^2_{stat} CC1π^+1$\pi^{\pm,0}$	
	Nominal	Fake data	Nominal	Fake data
Asimov fit	0.0	—	0.0	—
Random template priors	0.0	—	0.0	—
MC statistical fluctuations	30.091	—	2.131	—
Altered OOFV weights	26.796	0.274	27.028	0.196
Altered CCother weights	223.059	0.037	621.011	0.067
Altered OOPS P_μ weights	10.625	0.006	1.554	0.150
Altered OOPS P_{π^+} weights	86.359	0.285	79.149	2.008
Altered resonant weights	1192.201	0.015	35.738	0.022
GENIE MC	259.004	6.659	355.620	7.637

TABLE 8.2: Summary the χ^2_{stat} values per fake data study for nominal to post-fit and data to post-fit.

Chapter 9

Cross section measurement and results

The previous chapter showed that the fit framework is fully functional and has a very low bias for the set of fake data studies made. Now, this chapter presents the best fit results (same procedure fallow for fake data in chapter 8) for the real data, and the extraction of the cross sections results from this analysis. The method used to extract a (CC1π^+) differential cross section in kinematic variables was described in chapter 4.

Index	Parameter	Nominal	Pre-fit constraints
0-14	Template weight in each analysis bin	1.0	
9-29	Flux weight for events in each FHC $\nu_m u$ flux bin	1.0	flux covariance matrix
30-49	Model weights for each parameter	1.0	model covariance matrix
50-83	Weight for events in CC1π^+ in each reconstructed bin	1.0	detector covariance matrix
84-90	Weight for events in CC1π^+1$\pi^{\pm,0}$ in each reconstructed bin	1.0	detector covariance matrix

TABLE 9.1: All parameters included in the fit (the are discuss it in chapter 7). The model parameters nominal values are normalized.

This analysis will report several flux-integrated cross sections (see Table 4.1). Table 9.1 shows a summary of all parameters included in the fit and in the same order that we will see then in the matrix.

9.1 Fit results

The fitter outputs with both signal and control sample unblinded in the fit using the real data are presented using NEUT. In Figures 9.1, 9.2, 9.3 and 9.4 the post-fit correlation matrix and fit parameters results are presented where the template parameters are binned in different variables; this will allow us to extract the cross section in each of this variables. We can observe a strong correlation in the flux post-fit covariance matrix; this is compatible with the pre-fit flux predictions (Figure 7.7). In addition, the flux is, as expected, anti-correlated with the template parameters and indifferent cross section model parameters, While template parameters are highly anti-correlated to those cross section model parameters.

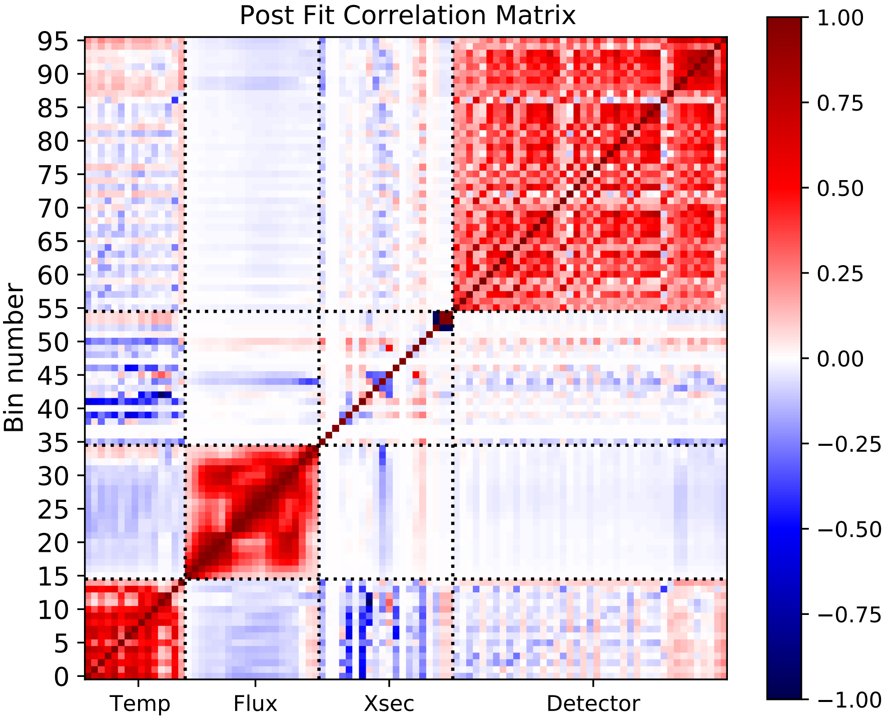

(A) Post-fit correlation matrix

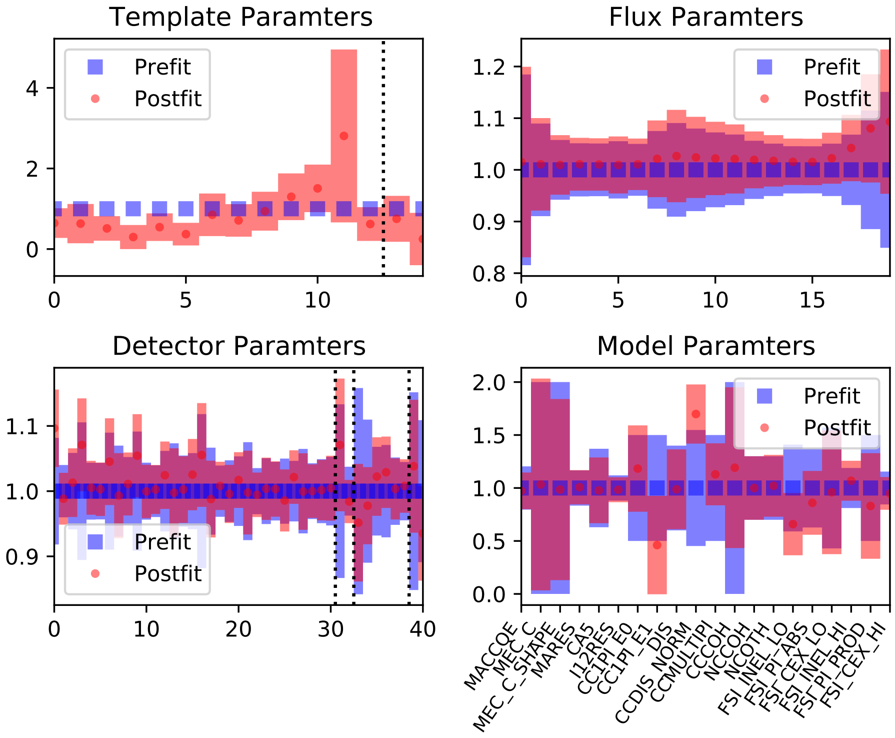

(B) Pre/post-fit parameter

FIGURE 9.1: Post-fit correlation matrix for the ND280 real data (A) and pre/post-fit parameter plots for the ND280 real data (B). The black dash line on the template parameters is separating the last two OOPS bins while in the detector parameters is pointing to the bins with same kinematics as the OOPS bins for signal and control sample. Red points in the left plot show the post-fit parameters values and their standard deviations alongside the light red lines, wile the blue points and lines show each parameters prior values and standard deviation. Binning the template parameters on P_{μ}, $\cos\theta_{\mu}$, P_{π^+} and $\cos\theta_{\pi^+}$ kinematic variables.

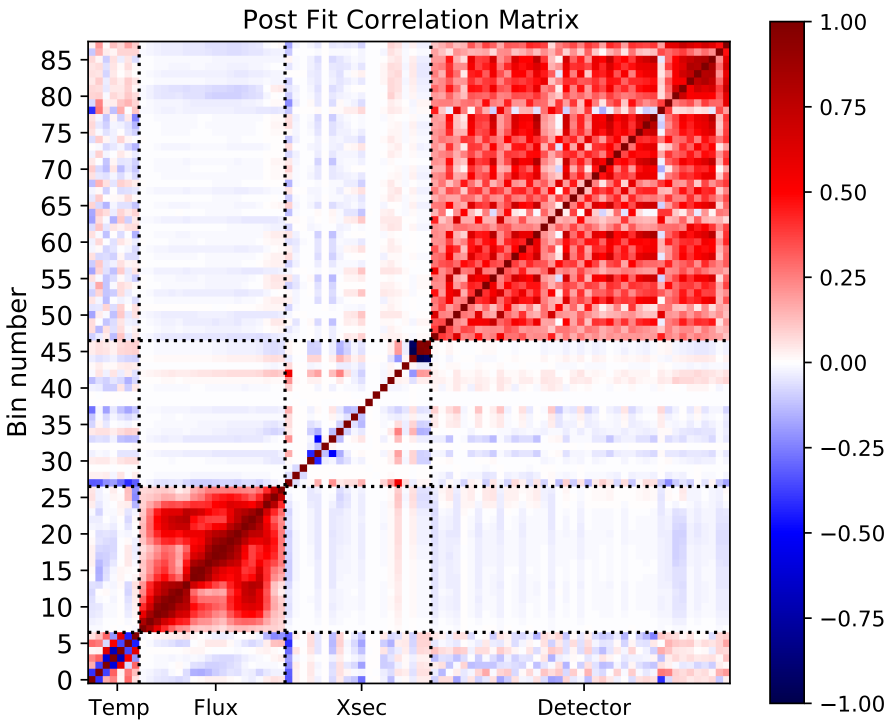

(A) Post-fit correlation matrix

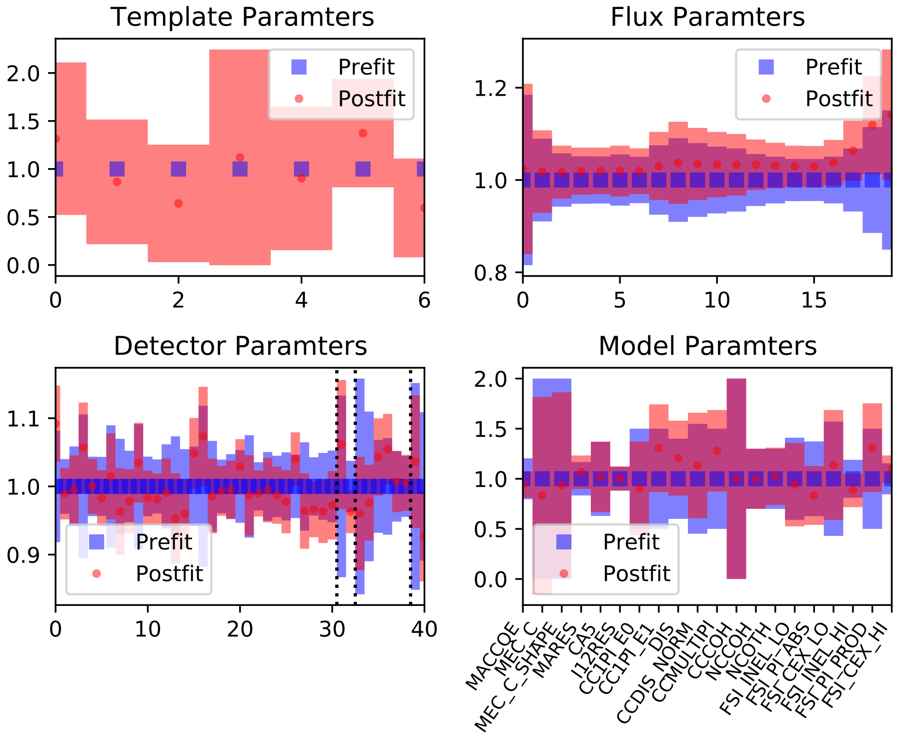

(B) Pre/post-fit parameter

FIGURE 9.2: Post-fit correlation matrix for the ND280 real data (A) and pre/post-fit parameter plots for the ND280 real data (B). The black dash line on the detector parameters is pointing to the bins with same kinematics as the OOPS bins for signal and control sample. Red points in the left plot show the post-fit parameters values and their standard deviations alongside the light red lines, wile the blue points and lines show each parameters prior values and standard deviation. Binning template parameters on E_ν variable.

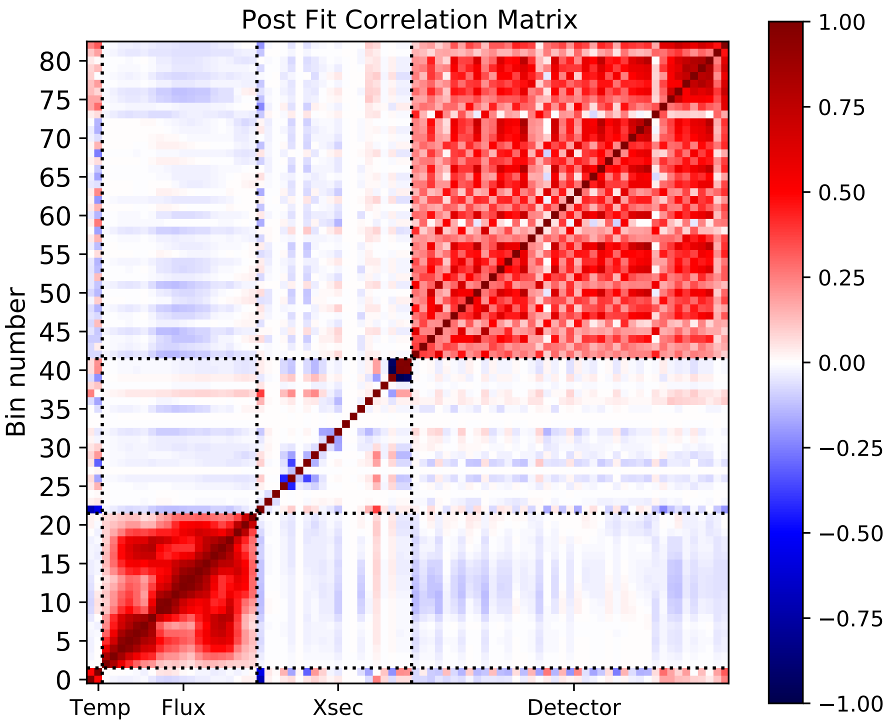

(A) Post-fit correlation matrix

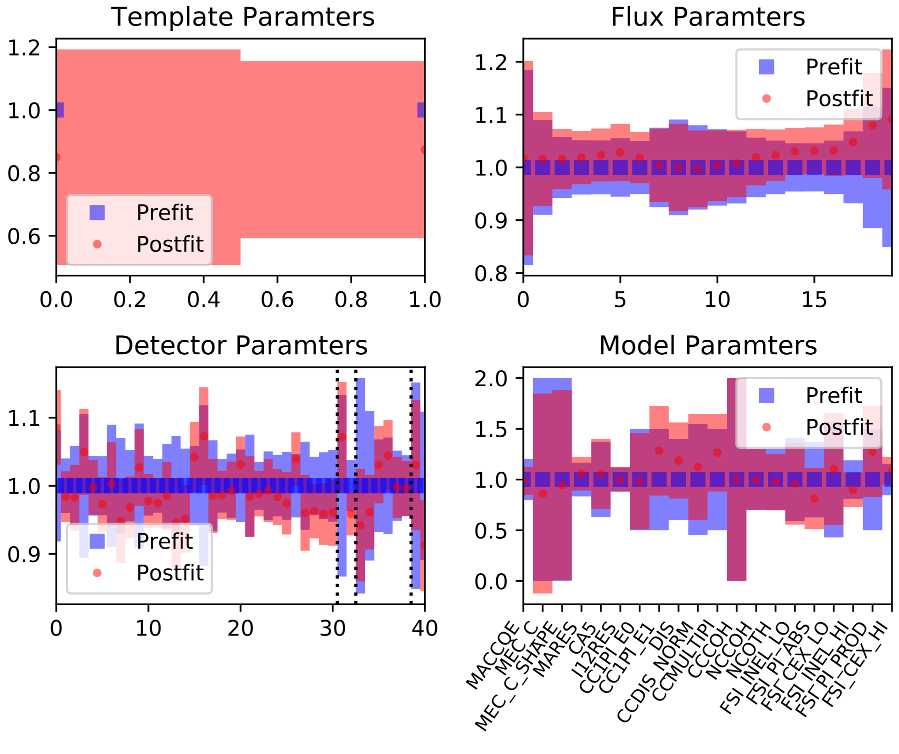

(B) Pre/post-fit parameter

FIGURE 9.3: Post-fit correlation matrix for the ND280 real data (A) and pre/post-fit parameter plots for the ND280 real data (B). The black dash line on the detector parameters is pointing to the bins with same kinematics as the OOPS bins for signal and control sample. Red points in the left plot show the post-fit parameters values and their standard deviations alongside the light red lines, wile the blue points and lines show each parameters prior values and standard deviation. Binning the template parameters on W variable.

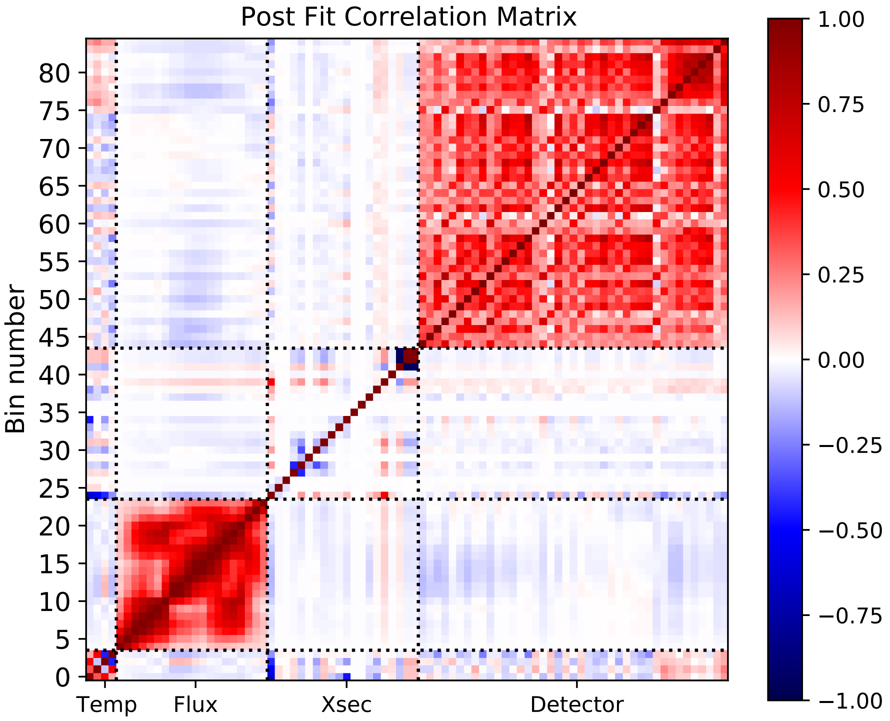

(A) Post-fit correlation matrix

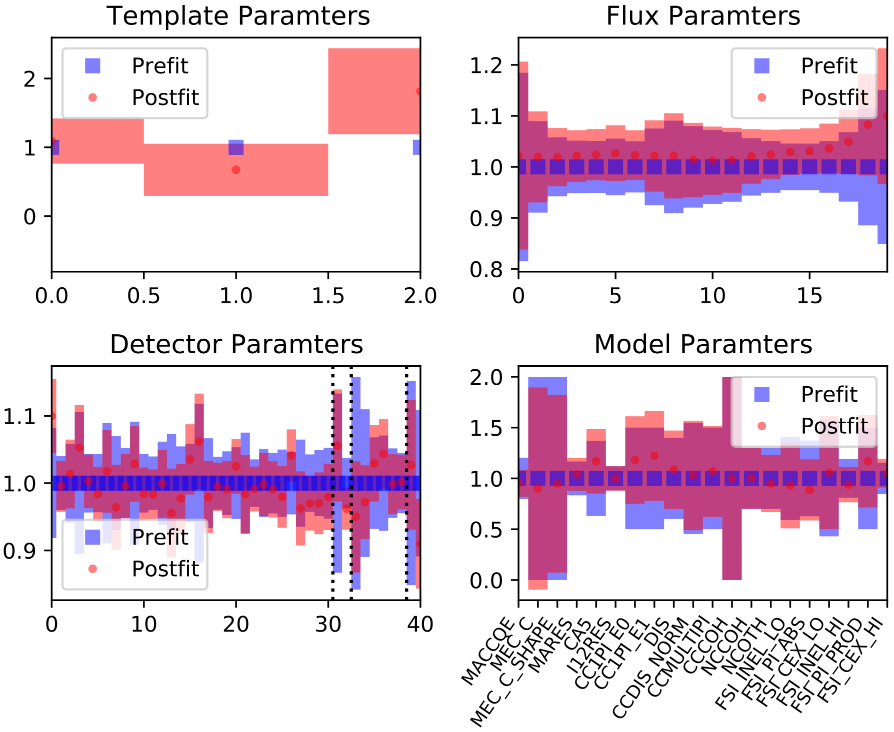

(B) Pre/post-fit parameter

FIGURE 9.4: Post-fit correlation matrix for the ND280 real data (A) and pre/post-fit parameter plots for the ND280 real data (B). The black dash line on the template parameters is separating the last two OOPS bins while in the detector parameters is pointing to the bins with same kinematics as the OOPS bins for signal and control sample. Red points in the left plot show the post-fit parameters values and their standard deviations alongside the light red lines, wile the blue points and lines show each parameters prior values and standard deviation. Binning the template parameters on Q^2 variable.

The fit parameters plots show the expected behavior, with the template parameters moving to correct the values. The flux and detector parameters show some deviations from their nominal but stay at 12% and within the errors limit. For the detector parameters, the fit reduced the relative errors in almost every bin.

The cross section model parameters were affected; those significantly impacted were those related to CC Multi pions, CC1π, Coherent, and Pion FSI; this indicates that the fit has good sensitivity towards them and a correct model in the nominal Monte Carlo simulation. We also observe a big pull up of the CCMultiPions parameter and pull down of CC1π with $E_\nu > 2.5GeV$ (see Figure 9.5).

The reconstructed event distributions show, overall, a good agreement between the post-fit distribution and the real data points at the reconstructed level, as shown in Figure 9.5. The post-fit distribution better describe the data as it is clear from the χ^2_{stat} values (obtained as Eq. 4.9).

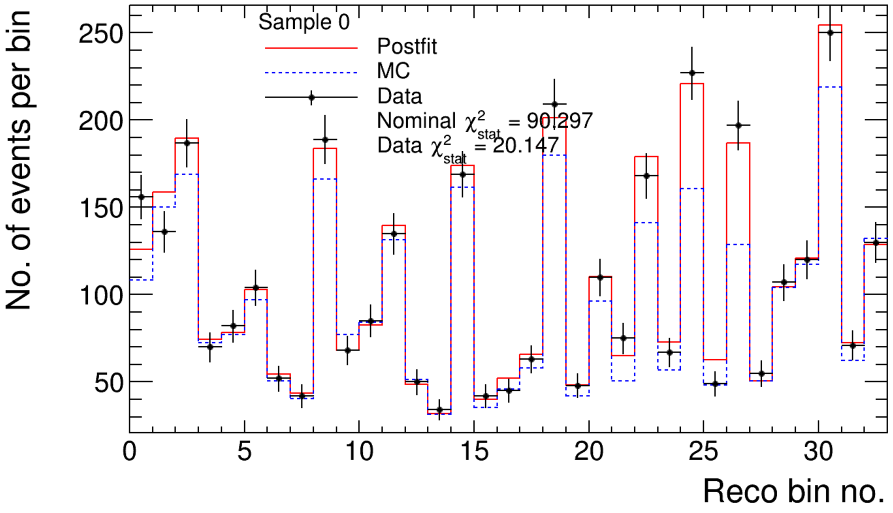

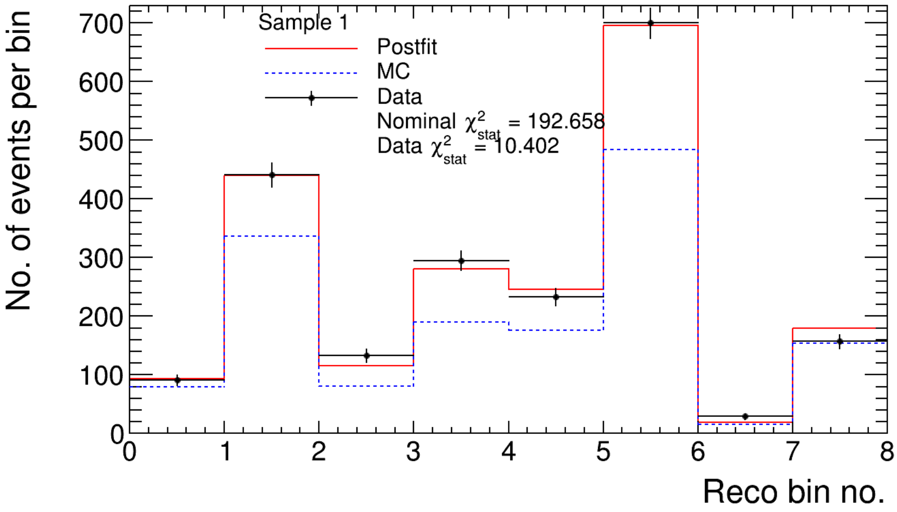

FIGURE 9.5: Pre/post-fit reconstructed event plots for the real data, signal (top) and control samples (bottom) using ND280 real data. Binning show in Table 7.2.

9.2 Cross section measurements

Here we present the final extracted cross section results from real ND280 data. In each plot, we compared the results for the real data fit the nominal MC prediction. The extracted cross section is calculated using Eq. 4.5. The fake data studies (see chapter 8) performed demonstrate that there is no bias in the cross section extraction method.

Figure 9.6 contains the primary result of this analysis showing the quadruple differential cross section per bin (the binning is shown in Table 7.5) and the associated correlation matrix obtained by fitting to real data. The quadruple differential cross section on muon and pion kinematics results indicate a disagreement extracted cross section than what was predicted by the input simulation using both NEUT and GENIE.

$$\frac{d\sigma}{dP_\mu \; dcos\theta_\mu \; dP_{\pi^+} \; dcos\theta_{\pi^+}} = \frac{N_i^{signal}}{\epsilon_i^{signal,MC} \Phi N_{nucleons}^{FV}} \times \frac{1}{\Delta P_{\mu,i} \; \Delta \cos\theta_{\mu,i} \; \Delta P_{\pi^+,i} \; \Delta \cos\theta_{\pi^+,i}} \tag{9.1}$$

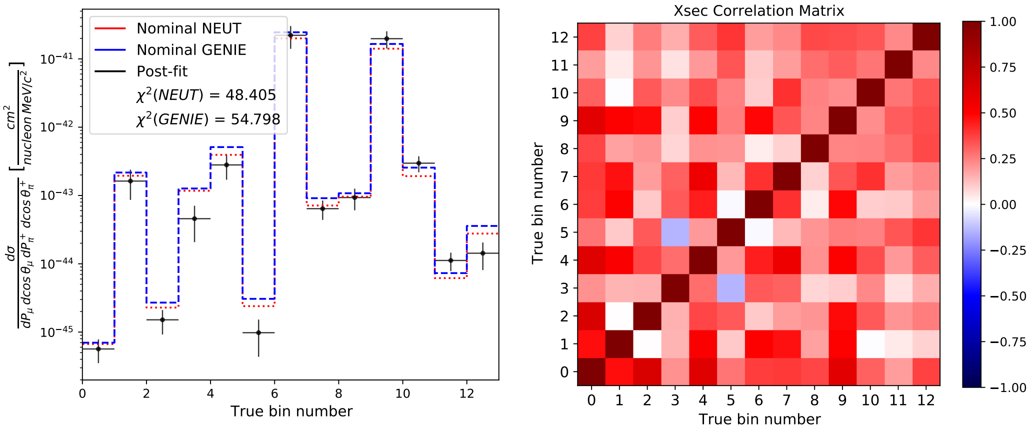

FIGURE 9.6: The quadruple differential cross section per bin and the associated correlation matrix obtained by fitting to real data using NEUT MC (red line) and GENIE MC (blue line). The extracted cross section is the primary result of this thesis.

The integrated cross section can be computed using these results by:

$$\sigma = \sum_i \frac{d\sigma}{dP_{\mu,i} \; dcos\theta_{\mu,i} \; dP_{\pi^+,i} \; dcos\theta_{\pi^+,i}} \Delta P_{\mu,i} \; \Delta \cos\theta_{\mu,i} \; \Delta P_{\pi^+,i} \; \Delta \cos\theta_{\pi^+,i} \tag{9.2}$$

This value integrates the number of signal events and the efficiency without the OOPS regions. This result needs to be interpreted with a pinch of salt since the detector's efficiency varies between the different muons and positive pion angles.

$$\sigma_{NEUT} = 3.536 \times 10^{-41} \frac{cm^2}{nucleon}$$
$$\sigma_{GENIE} = 4.266 \times 10^{-41} \frac{cm^2}{nucleon}$$
$$\sigma_{DATA} = (4.300 \pm 1.415) \times 10^{-41} \frac{cm^2}{nucleon}$$

Dividing the integrated cross section by the mean energy of the neutrino flux[1] this result can be compared with other experiments.

A previous results[2] for T2K CC1π^+ integrated cross section is reported on [13].

$$\sigma_{DATA} = (11.76 \pm 2.83) \times 10^{-40} \frac{cm^2}{nucleon}$$

By integrating the quadruple differential cross section (Eq. 9.1) over positive pion kinematics or muon kinematics, the double differential cross sections were obtained.

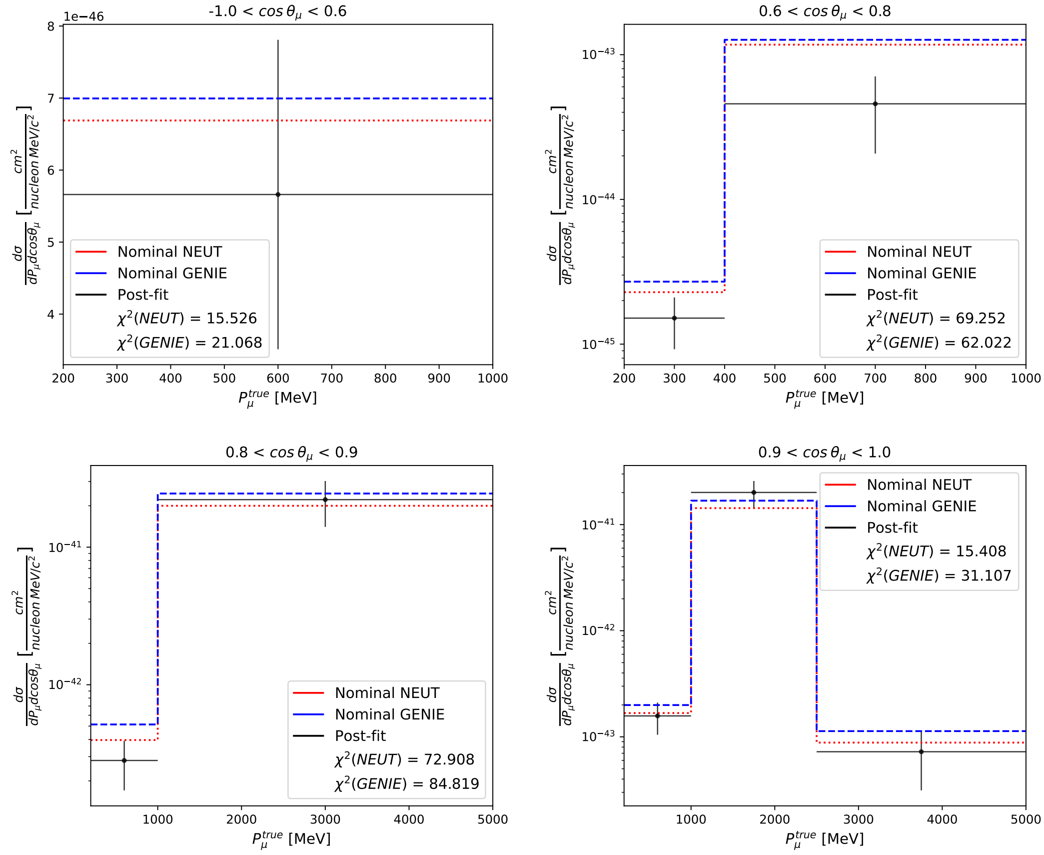

FIGURE 9.7: The double differential cross section as function of muon kinematics split in different slices of true muon angle using NEUT MC (red line) and GENIE MC (blue line). The last momentum bins extend all the way to 30 GeV.

---

[1] For T2K, the mean energy is 850 MeV and it is slightly shifted due to the high energy tail

[2] The full CCπ^+ candidate sample is considered, including pions identified by the Michel electron tag, only uses FWD going tracks [13]

$$\frac{d\sigma}{dP_{\mu}\ dcos\theta_{\mu}} = \frac{N_i^{signal}}{\epsilon_i^{signal,MC}\Phi N_{nucleons}^{FV}} \times \frac{1}{\Delta P_{\mu,i}\,\Delta\cos\theta_{\mu,i}} \tag{9.3}$$

$$\frac{d\sigma}{dP_{\pi^+}\ dcos\theta_{\pi^+}} = \frac{N_i^{signal}}{\epsilon_i^{signal,MC}\Phi N_{nucleons}^{FV}} \times \frac{1}{\Delta P_{\pi^+,i}\,\Delta\cos\theta_{\pi^+,i}} \tag{9.4}$$

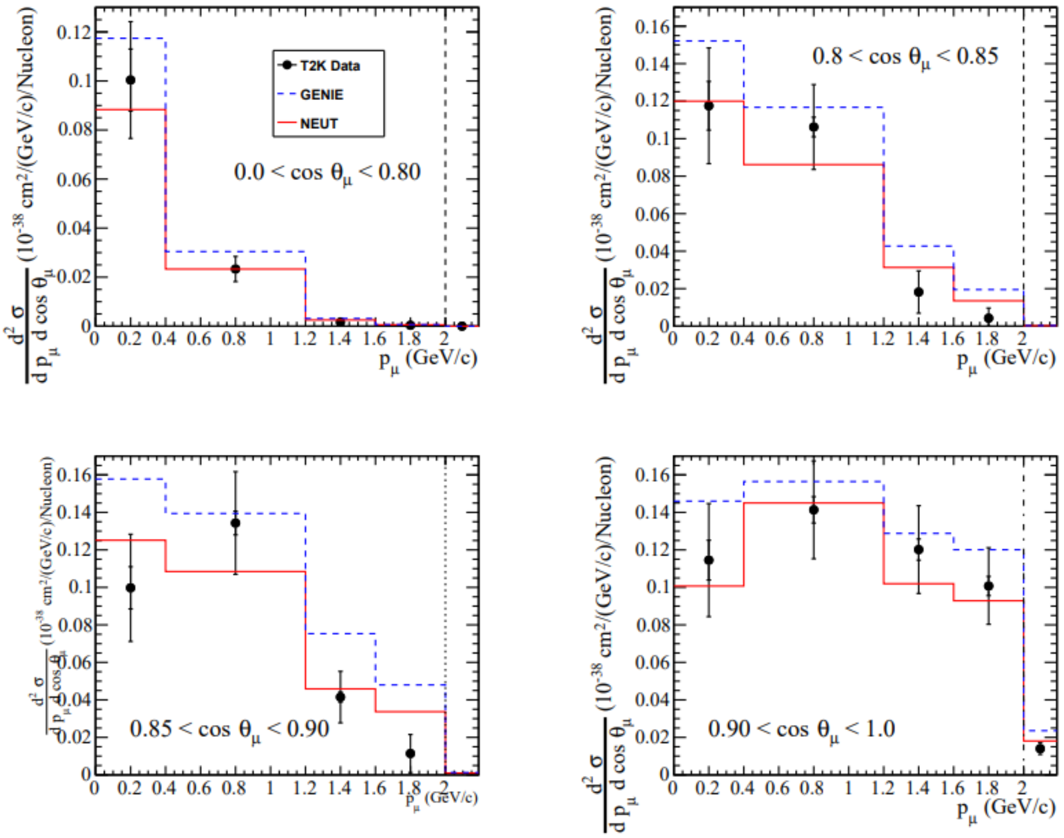

FIGURE 9.8: The double differential cross section as function of muon kinematics split in different slices of true muon angle using NEUT MC (red line) and GENIE MC (blue line). Reported by[13].

Figure 9.7 shows the double differential cross section on muon kinematics split in different slices of true muon angle and plotted as a function of true muon momentum.

- For $-1.0 < cos\theta_{\mu} < 0.6$ the differential cross section shows a good agreement with the input simulation with values staying within the error limits.
- For $0.6 < cos\theta_{\mu} < 0.8$ the differential cross section shows all bins at a lower extracted cross section than what was predicted by the input simulation.
- For $0.8 < cos\theta_{\mu} < 0.9$ the differential cross section shows lower extracted cross section for muons with momentum less that 1GeV and a good agreement (within the error limits) for muons with momentum more that 1GeV.
- For $0.9 < cos\theta_{\mu} < 1.0$ the differential cross section shows lower extracted cross section for muons with momentum beteewn 1 GeV and 2.5 GeV, for the rest it

shows a good agreement with the input simulation with values staying within the error limits.

This can be an indication of a deficiency in our theoretical models when describing specific regions like muons with $0.6 < cos\theta_{\mu} < 0.8$ and for $0.8 < cos\theta_{\mu} < 0.9$ if the momentum is $< 1GeV$. Previous results reported in [13] (Figure 9.8) was observe a good description of the data for CC$1\pi^{+}$ events in all the muon kinematics observables.

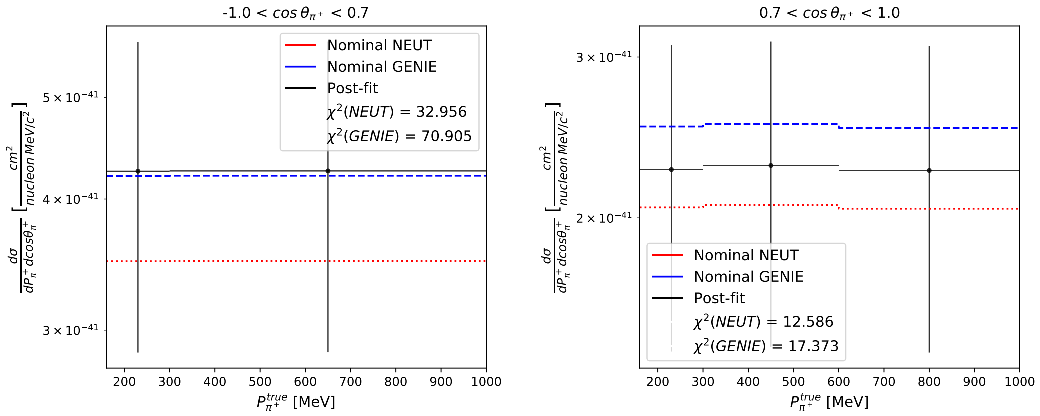

FIGURE 9.9: The differential cross section as function of the true positive pion momentum using NEUT MC (red line) and GENIE MC (blue line). The last momentum bins extend all the way to 30 GeV

Figure 9.9 shows the double differential cross section on positive pion kinematics split into different slices of true positive pion angle and plotted as a function of true positive pion momentum.

- For $-1.0 < cos\theta_{\pi^{+}} < 1.0$ the differential cross section shows a good agreement with the input simulation with values staying within the error limits.

Figure 9.10 contains the differential cross sections per bin (the binning is shown in Table 7.6) and their associated correlation matrix obtained by fitting to real data.

$$\frac{d\sigma}{dE_{\nu}} = \frac{N_i^{signal}}{\epsilon_i^{signal,MC}\Phi N_{nucleons}^{FV}} \times \frac{1}{\Delta E_{\nu,i}} \tag{9.5}$$

$$\frac{d\sigma}{dW} = \frac{N_i^{signal}}{\epsilon_i^{signal,MC}\Phi N_{nucleons}^{FV}} \times \frac{1}{\Delta W_i} \tag{9.6}$$

$$\frac{d\sigma}{dQ^2} = \frac{N_i^{signal}}{\epsilon_i^{signal,MC}\Phi N_{nucleons}^{FV}} \times \frac{1}{\Delta Q_i^2} \tag{9.7}$$

Now, let us break down each of the cross sections in Figure 9.10. The differential cross section on neutrino energy and the differential cross section on hadronic invariant mass showed a good agreement with the input simulation with values staying within the error limits. The differential cross section on four-momentum transfer shows all bins at higher or lower extracted cross section than what was predicted by the input simulation.

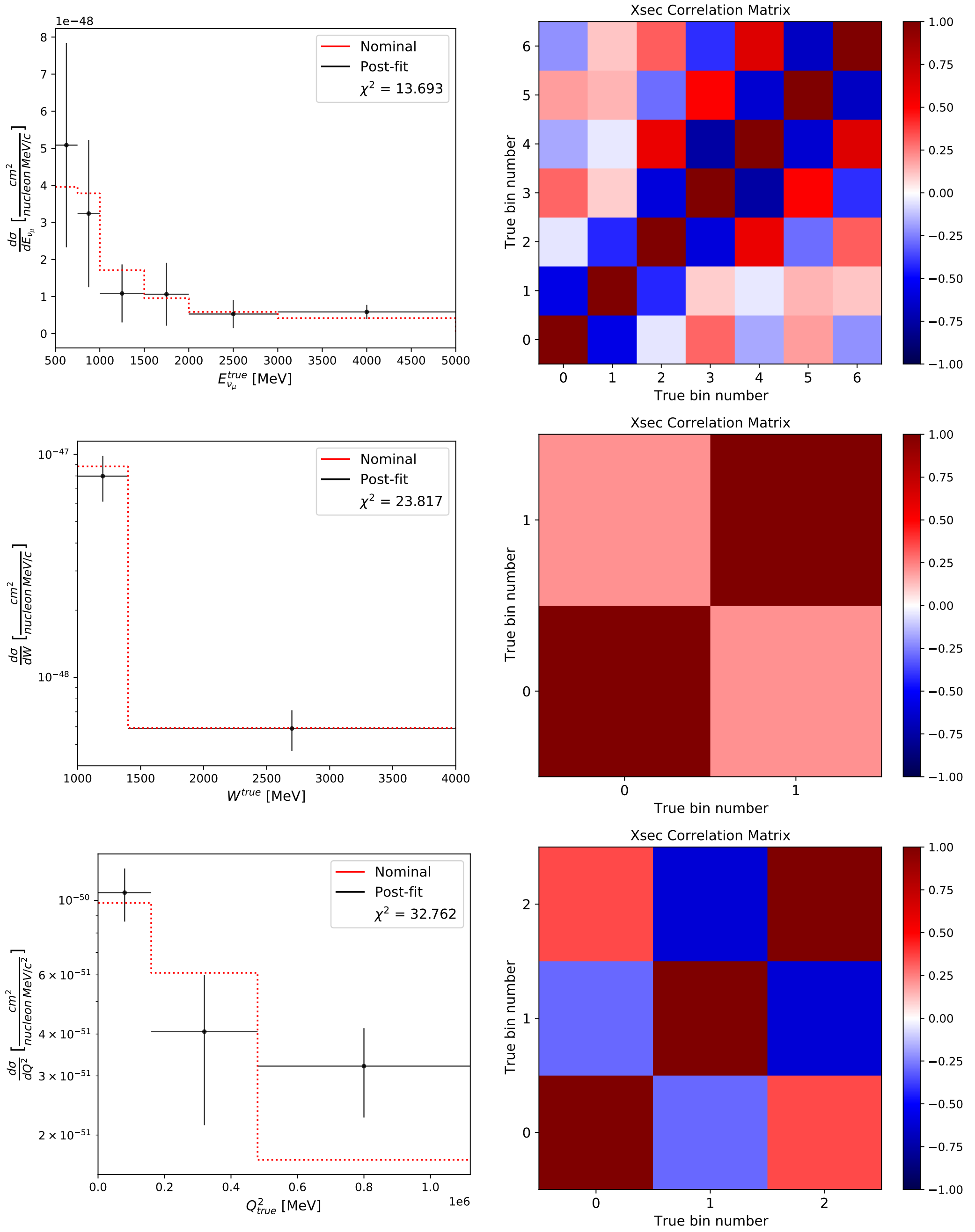

FIGURE 9.10: The differential cross section as function of E_ν (top row), W (central row), and Q^2 (bottom row) and the associated correlation matrix obtained by fitting to real data. The extracted cross section is the primary result of this thesis.

The χ^2 value is calculated from the full statistical and systematic penalties as in Eq. 4.6. Table 9.2 summarize the χ^2 goodness values obtained.

cross section	MC	χ^2 goodness
$\frac{d\sigma}{dP_\mu d\cos\theta_\mu dP_{\pi^+} d\cos\theta_{\pi^+}}$	NEUT	48.405
	GENIE	54.798
$\frac{d\sigma}{dP_\mu d\cos\theta_\mu}$	NEUT	15.526 ($-1.0 < cos\theta_\mu < 0.6$)
		69.252 ($0.6 < cos\theta_\mu < 0.8$)
		72.908 ($0.8 < cos\theta_\mu < 0.9$)
		15.408 ($0.9 < cos\theta_\mu < 1.0$)
	GENIE	21.068 ($-1.0 < cos\theta_\mu < 0.6$)
		62.022 ($0.6 < cos\theta_\mu < 0.8$)
		84.819 ($0.8 < cos\theta_\mu < 0.9$)
		31.107 ($0.9 < cos\theta_\mu < 1.0$)
$\frac{d\sigma}{dP_{\pi^+} d\cos\theta_{\pi^+}}$	NEUT	32.956 ($-1.0 < cos\theta_{\pi^+} < 0.7$)
		12.586 ($0.7 < cos\theta_{\pi^+} < 1.0$)
	GENIE	70.905($-1.0 < cos\theta_{\pi^+} < 0.7$)
		17.373 ($0.7 < cos\theta_{\pi^+} < 1.0$)
$\frac{d\sigma}{dE_\nu}$	NEUT	13.693
$\frac{d\sigma}{dW}$	NEUT	0.211
$\frac{d\sigma}{dQ^2}$	NEUT	53.781

TABLE 9.2: Summary the χ^2 goodness values per cross section presented.

9.3 Asymmetry studies

The event generator used (NEUT) uses the Rein-Sehgal [62] model to simulate neutrino-induced single pion production, an ad-hoc model to simulate multiple pion production up to a hadronic invariant mass of $2.0GeV/c^2$ and a microscopic cascade model to simulate FSI of hadrons taking place within the nuclear medium. The FWD-BWD asymmetry of θ_{planar} with respect to the direction of the plane $\vec{q} = \vec{p}_\nu - \vec{p}_\mu$:

$$A_{FB} = \frac{N_{cos\theta>0} - N_{cos\theta<0}}{N_{cos\theta>0} + N_{cos\theta<0}} = \frac{N_{cos\phi>0} - N_{cos\phi<0}}{N_{cos\phi>0} + N_{cos\phi<0}} \tag{9.8}$$

with W below 1400 MeV in order to select events dominated by Δ^{++} and Δ^{+} resonant contributions (as shown in Figure 6.10). The A_{FB} values obtained and the reported in the bibliography are summarize in Table 9.3.

To try to understand this asymmetry and the influence of the nuclear models and FSI on it, a few configurations were used to compute it as shown in Table 9.3. The NEUT generator simulates neutrino interactions with the T2K beam flux. Assuming a carbon target, neutrino interactions are simulated by four nuclear models: local Fermi gas (LFG), (global) relativistic Fermi gas (RFG), Bodek-Ritchie model (BRRFG), and effective spectral function (SF), with or without FSI being enabled. Without FSI (NoNuclFSI), the cascade is not run for nucleons, but it is for pions. More FSI (MoreNuclFSI) means that the cross sections in the FSI cascade are 30 % higher. MA103 is the value of the axial mass used, and C or CH represents the target (Carbon or Hydrocarbon). The nuclear models affect nuclear properties like the nucleon momentum distribution, Fermi energy, binding energy, etc. However, for the RES (and DIS) channel in the effective SF model, the SF feature of interaction on correlated nucleon pair, or the correlation of outgoing nucleons, is not implemented. The FSI process may also be dependent on the nuclear model as the nuclear potential for hadron propagation is often determined from the underlying nuclear model.

	FWD-BWD asymmetry	
	$\cos\ \theta_{planar}$	$\cos\ \phi_{planar}$
Reconstructed using true MC with different NEUT configurations		
	$\times 10^{-05}$	$\times 10^{-5}$
neut_C_noFSI_LFG	-0.241 ± 1.83	-0.013 ± 1.810
neut_CH_RFGRPA_lessNucFSI	-0.212 ± 1.72	-0.014 ± 1.697
neut_CH_RFGRPA_moreNucFSI	-0.212 ± 1.69	-0.011 ± 1.705
neut_CH_RFGRPA_noNucFSI	-0.203 ± 1.72	-0.009 ± 1.709
neut_CH_SF_MA103_flatSF	-0.207 ± 1.61	-0.012 ± 1.604
neut_CH_SF_MA103_lessNucFSI	-0.201 ± 1.63	-0.013 ± 1.617
neut_CH_SF_MA103_moreNucFSI	-0.213 ± 1.62	-0.017 ± 1.603
neut_CH_SF_MA103_noNuclFSI_noPB	-0.217 ± 3.25	-0.014 ± 3.223
neut_CH_SF_MA103_noNuclFSI_noPB_flatSF	-0.204 ± 3.24	-0.013 ± 3.231
Reported by [39]		
True value	-0.007 ± 0.003	
Reconstructed using true MC	-0.179 ± 0.003	
Obtained with this analysis		
Reconstructed using true NEUT MC	-0.619 ± 0.005	-0.083 ± 0.004
Reconstructed using true GENIE MC	-0.647 ± 0.005	-0.230 ± 0.003
Experimental variables	-0.641 ± 0.008	-0.592 ± 0.008

TABLE 9.3: FWD-BWD asymmetry values for different nuclear models and FSI configurations together with values reported in previous literature ([39]) and the ones obtained with this study. This is done using the CC1pi^+ sample and limiting the W to below 1400 MeV.

The observed bias is produced by the FSI and Fermi momentum within the nucleus because θ_{planar} is significantly modified, as shown in Figure 6.13. The dependence of the θ angle on the FSI and Fermi momentum makes it a very useful observable when investigating the nuclear effects on the results of the reaction [39].

Chapter 10

Conclusions

The main objective of the near detectors in an oscillation neutrino experiment (like T2K) is the reduction of systematic errors in the oscillation analysis. One of the limitations is the interactions uncertainties that are the dominant systematic on current measurements of the oscillation parameters. These interactions are fundamental for understanding the nuclear effects contributing to the cross section and inaccuracies in reconstructing the neutrino energy. Cross sections at the nucleon level are not perfectly known, the nuclear medium effects modify them, and these primary interactions are embedded in the nucleus, where nuclear effects can modify the event topology.

The analysis carried out in this thesis has produced a set of flux integrated ν_μ CC1π^+ cross sections on hydrocarbon using the T2K off-axis near detector data. The primary output of this thesis is the first CC1π^+ fiducial quadruple differential cross section in bins of muon and positive pion kinematic variables, using T2K's ND280 off-axis near detector.

The muon and positive pion kinematics variables are directly observable in the detector, while the other reconstructed variables (the neutrino energy, the hadronic invariant mass, and the four-momentum transfer) depend on the underlying model of the cross section.

A new selection was developed to study this signal with a full solid angle coverage of the ND280 detector. This new selection is capable in identifying and selecting backward and high angles tracks, increasing the efficiency in this region; this is the second selection developed with a full solid angle coverage and the first one that allows us to study the different contributions to CC inclusive interactions with a full solid angle coverage. The events selected at the near detector are used to constrain the flux and cross section parameters. Using NEUT as the default MC generator, we observe a 56.17% purity of the CC1π^+ signal.

The signal is defined as one negatively charged muon, one positive charged pion, and any number of nucleons as the final state particles. It depends on the primary vertex and FSI, as pion can be produced in the primary vertex, produced or absorbed in FSI, and affected by charge exchange.

The detector acceptance is limited depending on the path of the track. The following constraints were placed on muon and pion kinematics in the signal definition for the cross section extraction:

- True muon momentum > 200 MeV/c,
- True pion momentum > 160 MeV/c.

The preliminary cross section results achieved so far have shown disagreements between the MC prediction and the post-fit results. An agreement with the input simulation (with values staying within the error limits) was observed for:

- $\frac{d\sigma}{dP_\mu d\cos\theta_\mu}$ with $-1.0 < cos\theta_\mu < 0.6$,

- $\frac{d\sigma}{dP_{\mu}d\cos\theta_{\mu}}$ with $0.8 < cos\theta_{\mu} < 0.9$ and $P_{\mu} > 1.0GeV$,
- $\frac{d\sigma}{dP_{\mu}d\cos\theta_{\mu}}$ with $0.9 < cos\theta_{\mu} < 1.0$ and $2.5\,GeV < P_{\mu} < \, 1.0GeV$
- $\frac{d\sigma}{dP_{\pi^{+}}d\cos\theta_{\pi^{+}}}$
- $\frac{d\sigma}{dE_{\nu}}$
- $\frac{d\sigma}{dW}$

This can be an indication of a deficiency in our theoretical models when describing specific regions like muons with $0.6 < cos\theta_{\mu} < 0.8$ and for $0.8 < cos\theta_{\mu} < 0.9$ if the momentum is $< \, 1GeV$.

Some of the variables studied were the Adler angles (ϕ_{planar} and θ_{planar}). They will be most helpful for comparison with neutrino interaction models. The Adler angles can be used to improve our interaction models. They are properly defined at the nucleon interaction level, but they are altered by the final state interactions and the Fermi momentum of the target nucleon. The θ_{planar} Adler angle is with the one that characterizes the pion with regard to the direction of the Δ (after the boost). The Adler angles carry information about the polarization of the Δ resonance the interference with non-resonant single pion production, and they can provide hints of parity violation due to the lack of preference in the Δ direction.

The non-flat behavior observed in the reconstructed Adler angle distributions could be coming from nuclear medium effects and FSI due to the heavier target used. We are missing low momentum pions in the reconstruction due to nuclear effects. The missing low momentum pions can be observed in the lack of events with negative values of the cos θ_{planar} distribution.

In general, this analysis can be further improved. Starting with the selection, a better cut to reduce the contamination of protons when selecting the FGD pion can be implemented, deepening on the direction of the track (see Table 5.8). Michel electrons reconstructed kinematics information can be included; this has been developed as part of a Ph.D. thesis at ND280 and the results shown are outstanding. Improve the timing information and the detector efficiency for BWD and HA tracks. This two will be achieved with the ND280 upgrade. Furthermore, reducing the statistical uncertainties is more complicated since it depends on our knowledge of the neutrino interaction.

Appendix A

Energy thresholds for neutrino production

The thresholds for the incoming neutrino energy are given by simple relativistic kinematics. Assuming the notation presented before, this give an minimum neutrino energy (in the lab frame):

$$E_\nu = \frac{m_l^2 + m_{N'}^2 + 2m_l m_{N'} - m_N^2}{2m_N} \tag{A.1}$$

The numerical values for different processes are given in Table A.1 and for the Δ resonance we used $m_{N'} = m_\Delta$ (Table A.2).

TABLE A.1: Threshold energies for QE and RES production (in GeV).

	E_{ν_e}	E_{ν_μ}	E_{ν_τ}
CCqe	~ 0	0,111	3,450
CCres	0,177	0,305	3,940
NCe	0	0	0
NCres	0,175	0,175	0,175

TABLE A.2: Δ (1232) resonance information [29].

	Spin	Mass (MeV)	Γ (MeV)	Decay
Δ^{++}	$\frac{3}{2}$	1232	118	$\pi^+ + p$
Δ^+				$\pi^+ + n$
				$\pi^0 + p$
Δ^0				$\pi^0 + n$
				$\pi^- + p$

Appendix B

Changes to Highland2

Some changes needs to be done to the basic nd280 and highlad2 software in order to work with the selection. Here are the basic steps to fallow depending if you are working with GIT/cmake verison.

1. installing nd280 software
    - git clone https://git@git.t2k.org/nd280/pilot/nd280SoftwarePilot.git
    - cd nd280SoftwarePilot
    - ./configure.sh
    - . nd280SoftwarePilot.profile
    - nd280-install -j16 12.31
    - cd ..
2. installing Highland2 software
    - git clone https://git@git.t2k.org/nd280/highland2Software/highland2SoftwarePilot.git
    - nd280-fetch-package highland2Software/highland2UserAnalyses highlandRecPack highlandRecPack master
    - in /highlandCorrections_2.24/cmake/highlandCorrectionsND280_USE.cmake
        - uncoment: ND280_USE(highlandRecPack)
    - in /ND280/highlandCorrections_2.24/src/FlipKinematicsCorrection.cxx
        - uncoment: #define UseRecPack
    - in /ND280/highlandCorrections_2.24/src/MomRangeCorrection.cxx
        - uncoment: #define UseRecPack
    - . highland2SoftwarePilot/highland2SoftwarePilot.profile
    - highland-install -j16 2.65
3. installing numuCC4piMultiPiAnalysis package
    - nd280-fetch-package highland2Software/highland2UserAnalyses numuCC4piMultiPiAnalysis master
    - cd numuCC4piMultiPiAnalysis_master; mkdir Linux-CentOS_7-gcc_4.8-x86_64; cd Linux-CentOS_7-gcc_4.8-x86_64
    - cmake ../cmake
    - ../bin/makeAll.sh
    - . ../bin/setup.sh

Appendix C

ToF correction

ToF distributions for runs 2 to 4 and 8 for the different ToF topologies.

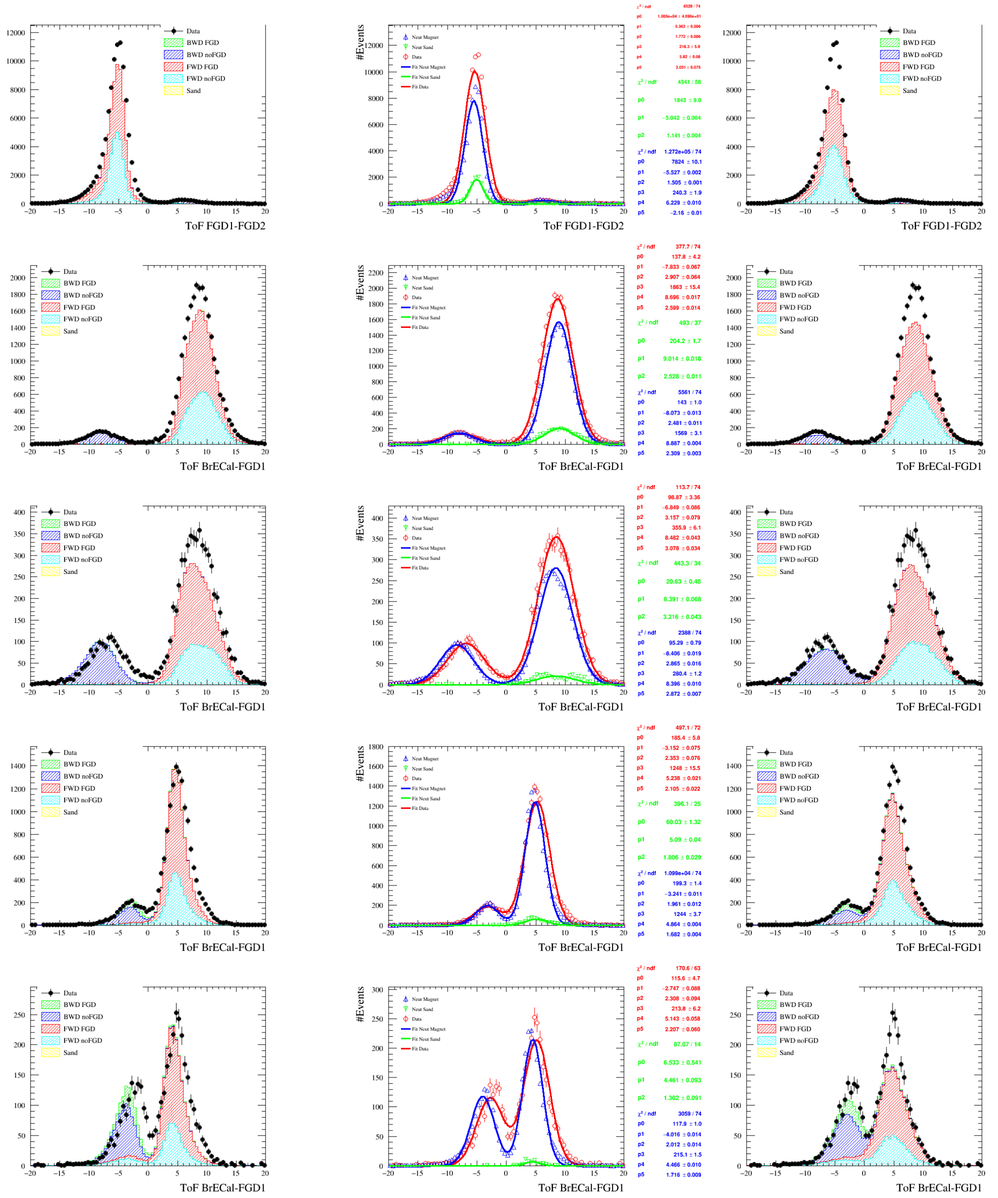

FIGURE C.1: ToF distributions without any correction apply (left column), two Gaussian fit of the ToF distributions without any correction apply (central column) and ToF distributions after correction are apply. For run 2 to 4 and for different ToF topologies.

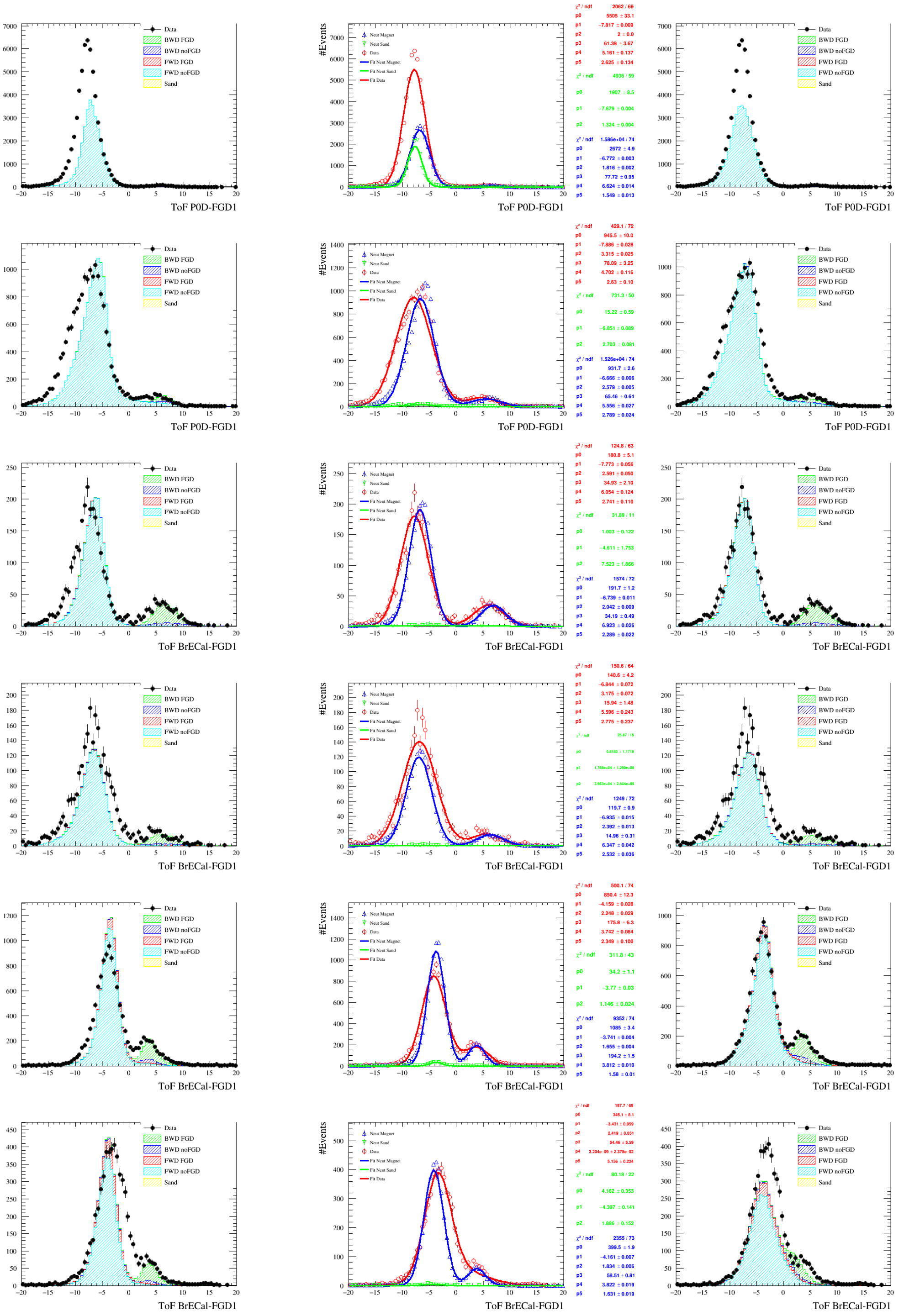

FIGURE C.2: ToF distributions without any correction apply (left column), two Gaussian fit of the ToF distributions without any correction apply (central column) and ToF distributions after correction are apply. For runs 2 to 4 and for different ToF topologies.

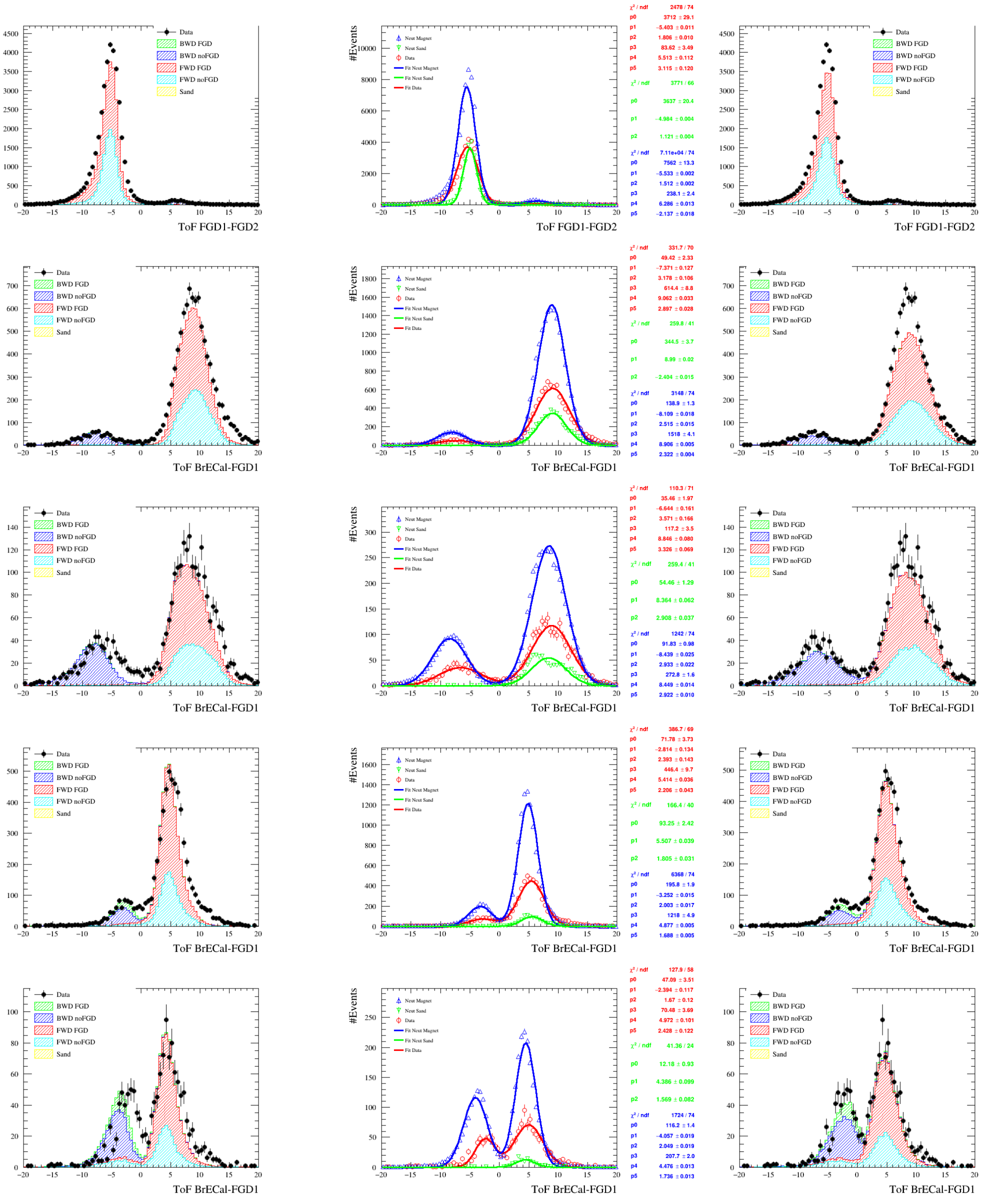

FIGURE C.3: ToF distributions without any correction apply (left column), two Gaussian fit of the ToF distributions without any correction apply (central column) and ToF distributions after correction are apply. For run 8 and for different ToF topologies.

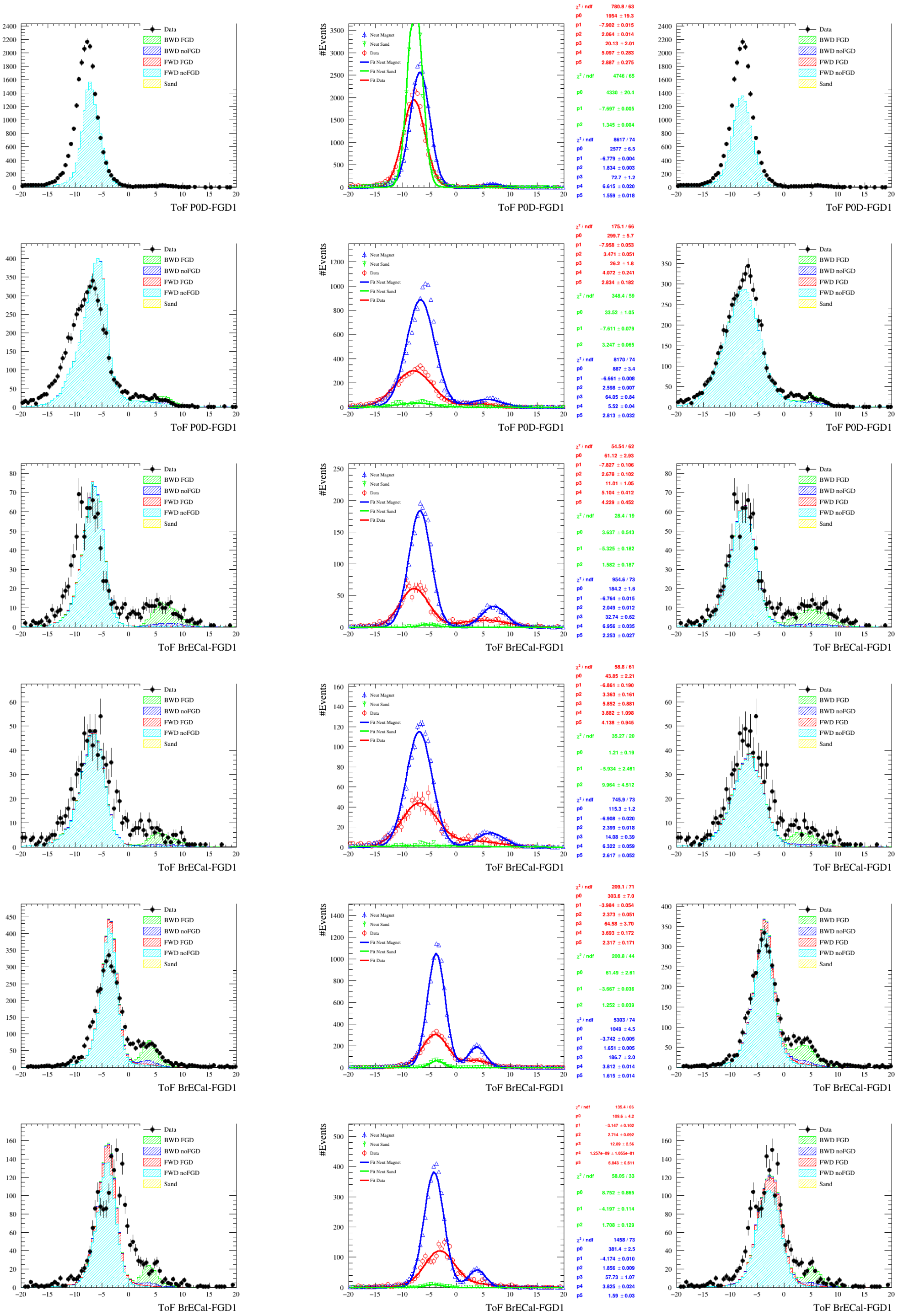

FIGURE C.4: ToF distributions without any correction apply (left column), two Gaussian fit of the ToF distributions without any correction apply (central column) and ToF distributions after correction are apply. For run 8 and for different ToF topologies.

Appendix D

Distributions

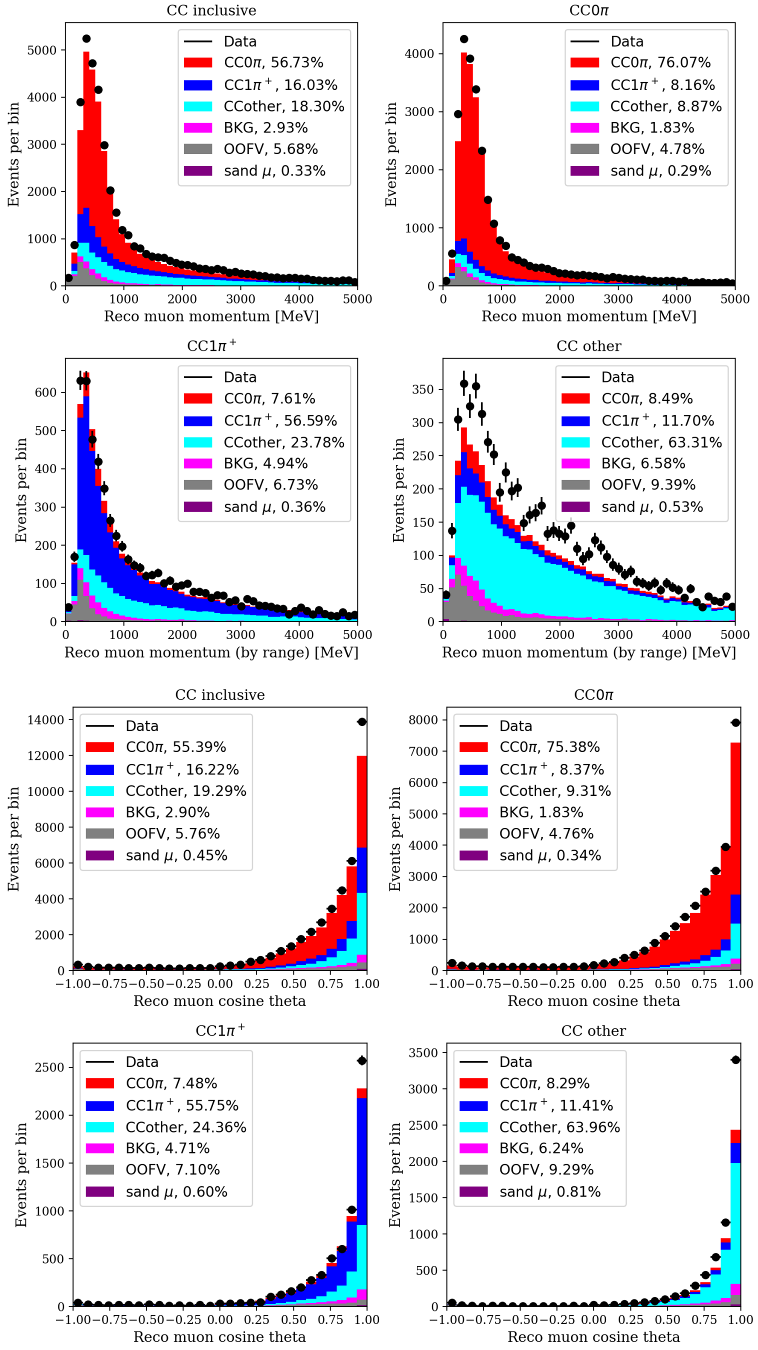

FIGURE D.1: Muon momentum (top two rows) and cosine of theta (bottom two rows) distributions for the CC inclusive samples (top left), and for the CC0π (top right), the CC1π^+ (bottom left) and CCother samples (bottom right) for 4π acceptance. Using the true topology definition.

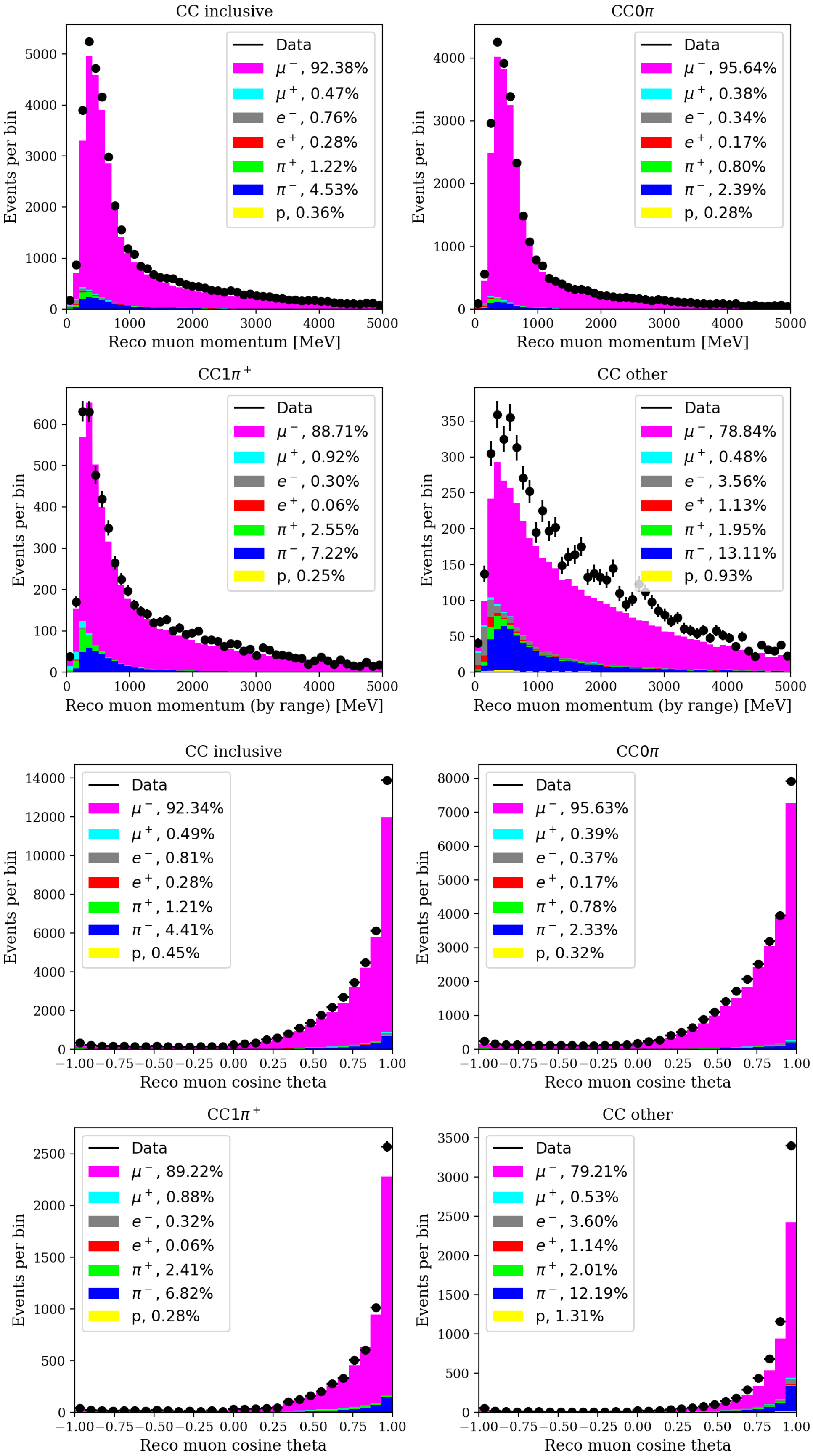

FIGURE D.2: Muon momentum (top two rows) and cosine of theta (bottom two rows) distributions for the CC inclusive samples (top left), and for the CC0π (top right), the CC1π^+ (bottom left) and CCother samples (bottom right) for 4π acceptance. Using the true particle definition.

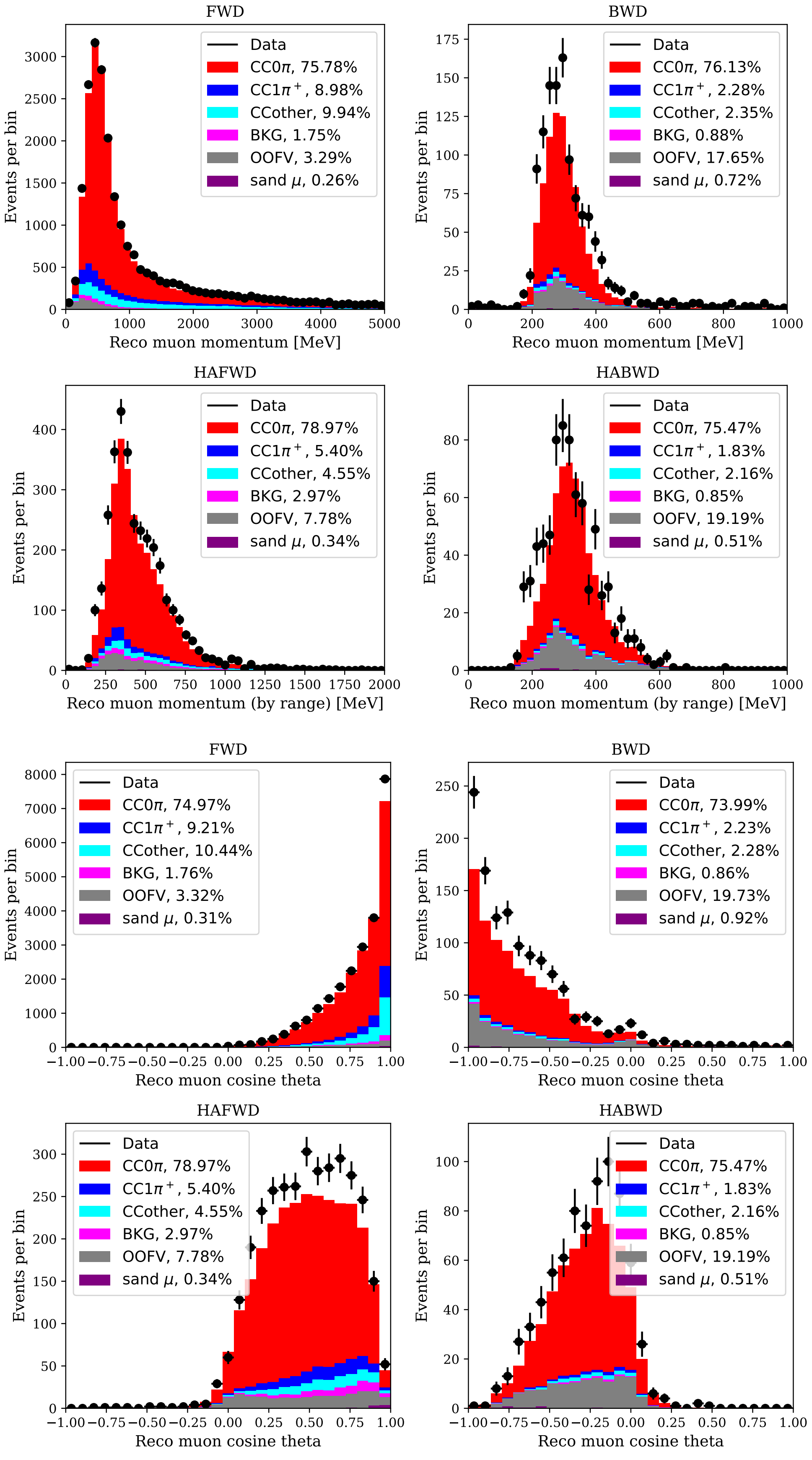

FIGURE D.3: Muon momentum (top two rows) and cosine of theta (bottom two rows) distributions of CC0π for the different directions: FWD (top left), BWD (top right), HAFWD (bottom left) and HABWD (bottom right) using the true topology definition.

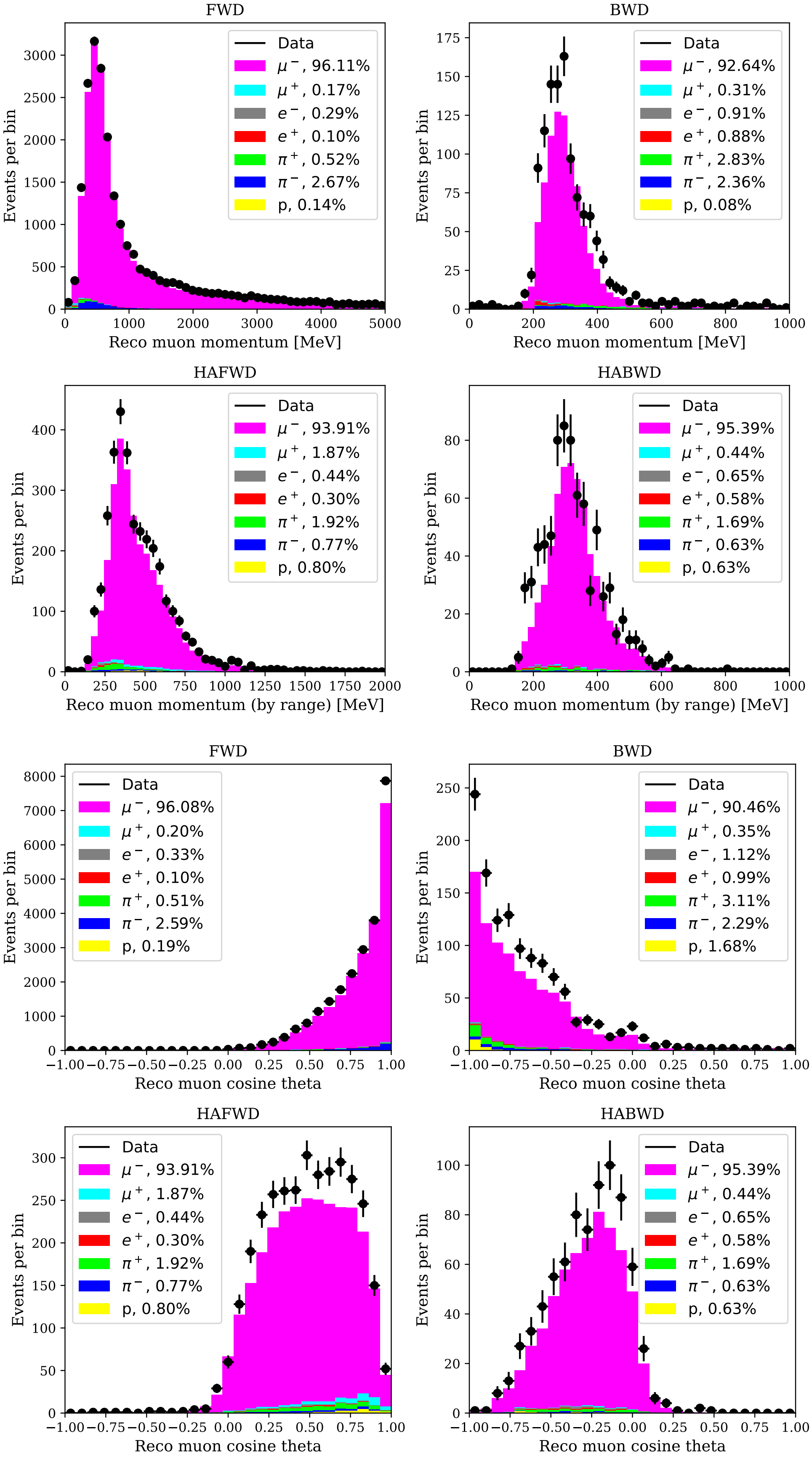

FIGURE D.4: Muon momentum (top two rows) and cosine of theta (bottom two rows) distributions of CC0π for the different directions: FWD (top left), BWD (top right), HAFWD (bottom left) and HABWD (bottom right) using the true particle definition.

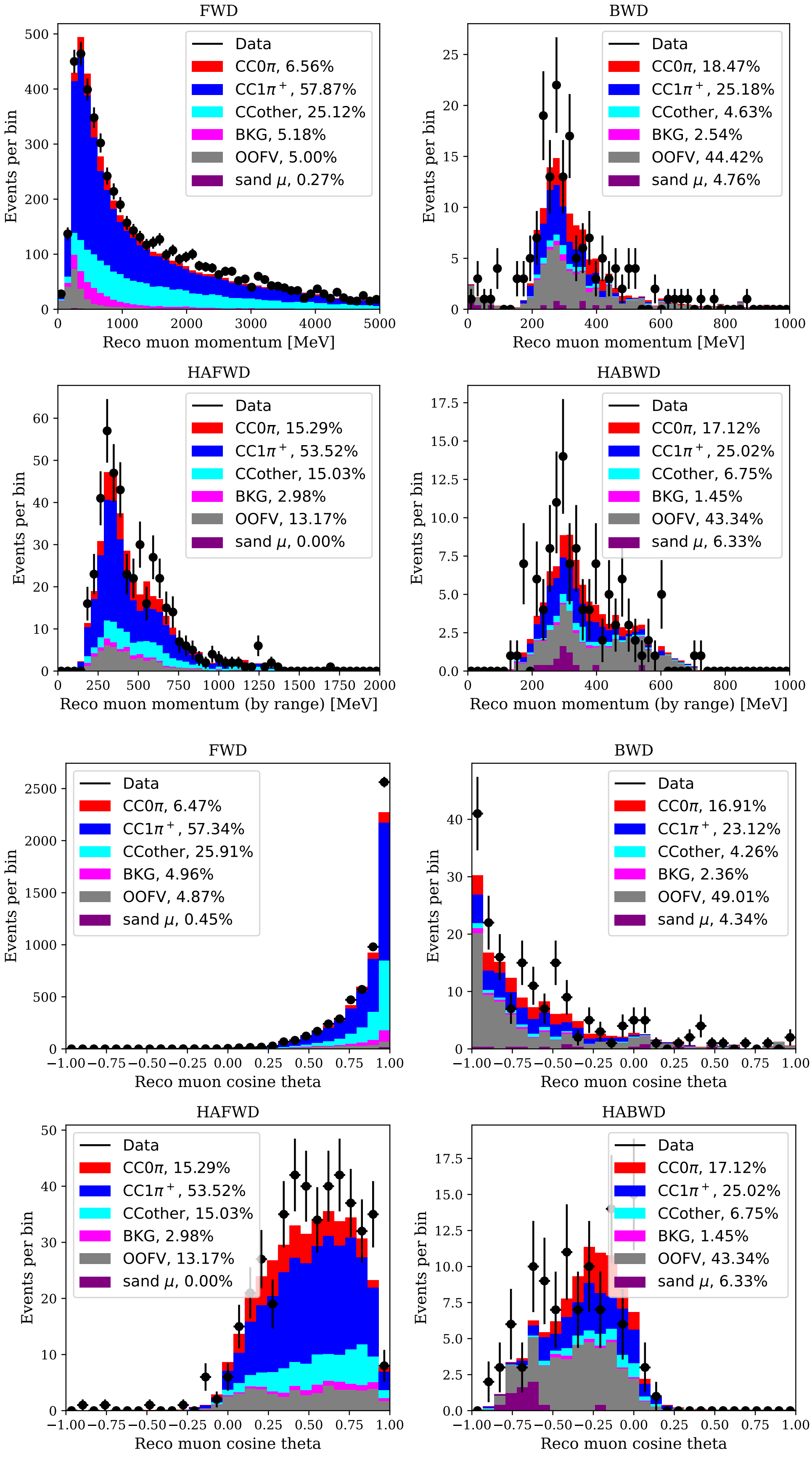

FIGURE D.5: Muon momentum (top two rows) and cosine of theta (bottom two rows) of $CC1\pi^+$ for the different directions: FWD (top left), BWD (top right), HAFWD (bottom left) and HABWD (bottom right), using the true topology definition.

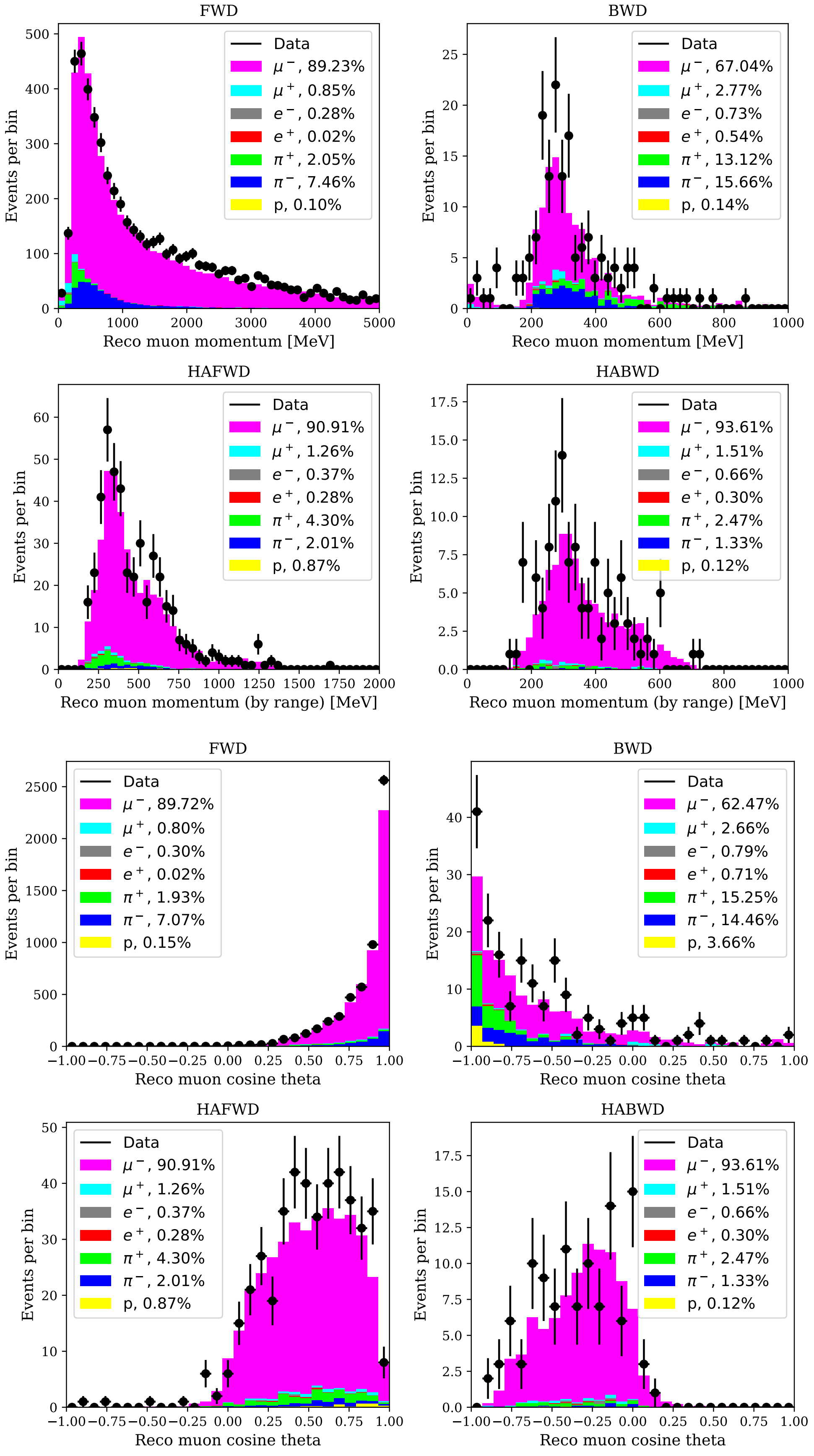

FIGURE D.6: Muon momentum (top two rows) and cosine of theta (bottom two rows) distributions of CC1π^+ for the different directions: FWD (top left), BWD (top right), HAFWD (bottom left) and HABWD (bottom right), using the true particle definition.

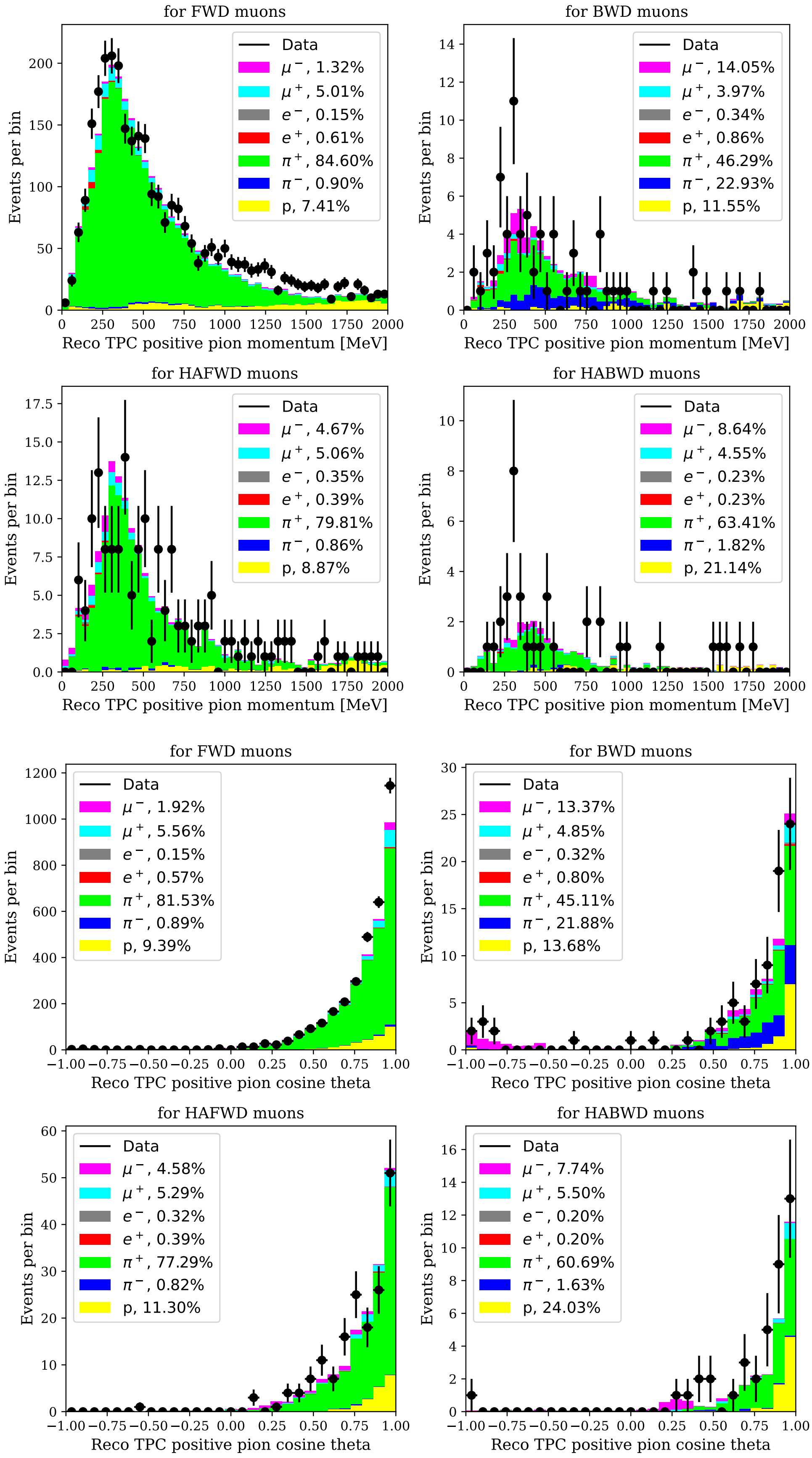

FIGURE D.7: Positive pion momentum (top two rows) and cosine of theta (bottom two rows) distributions of CC1π^+ for TPC pions,for the different muon directions: FWD (top left), BWD (top right), HAFWD (bottom left) and HABWD (bottom right), using the true particle definition.

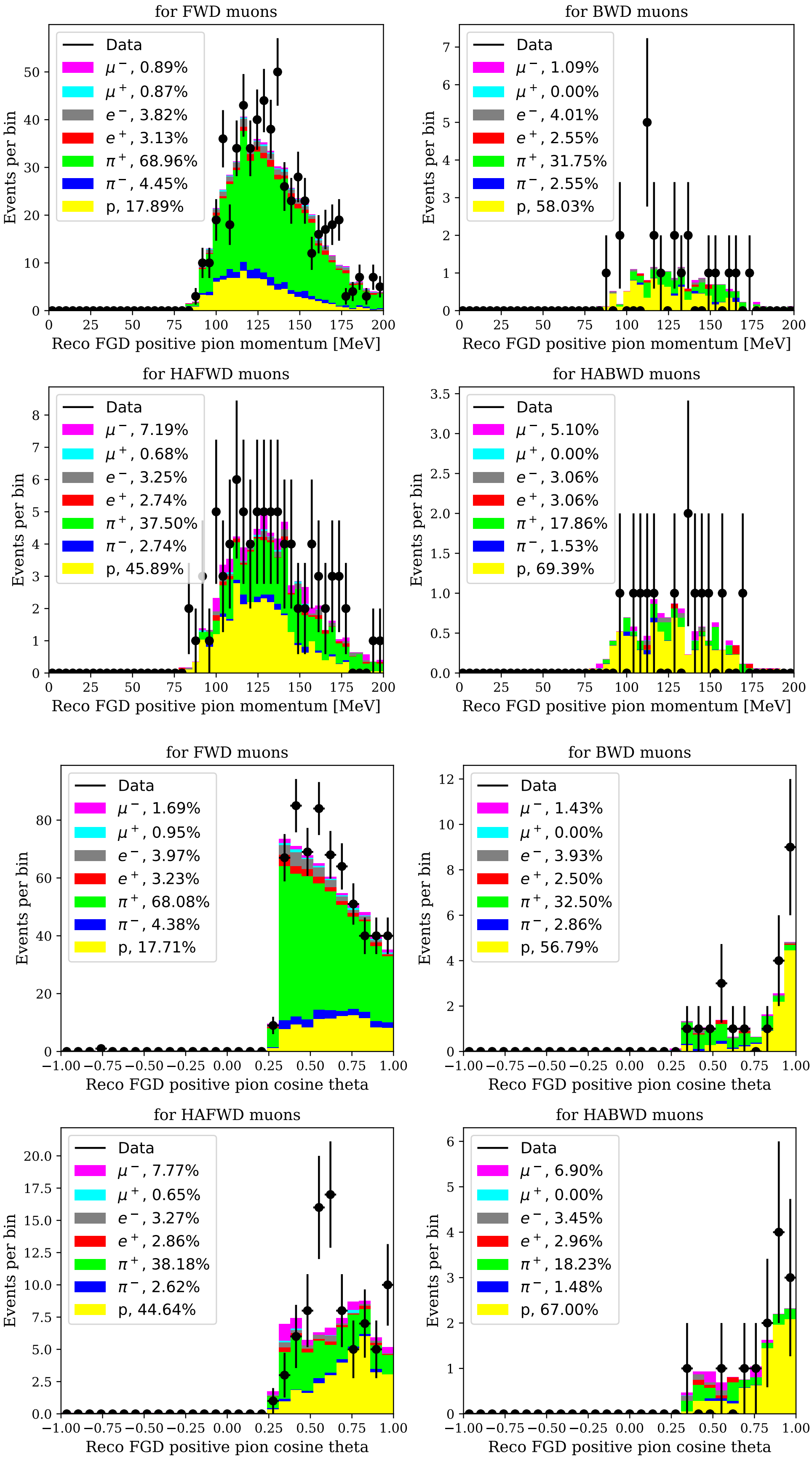

FIGURE D.8: Positive pion momentum (top two rows) and cosine of theta (bottom two rows) distributions of CC1π^+ for FGD pions,for the different muon directions: FWD (top left), BWD (top right), HAFWD (bottom left) and HABWD (bottom right), using the true particle definition.

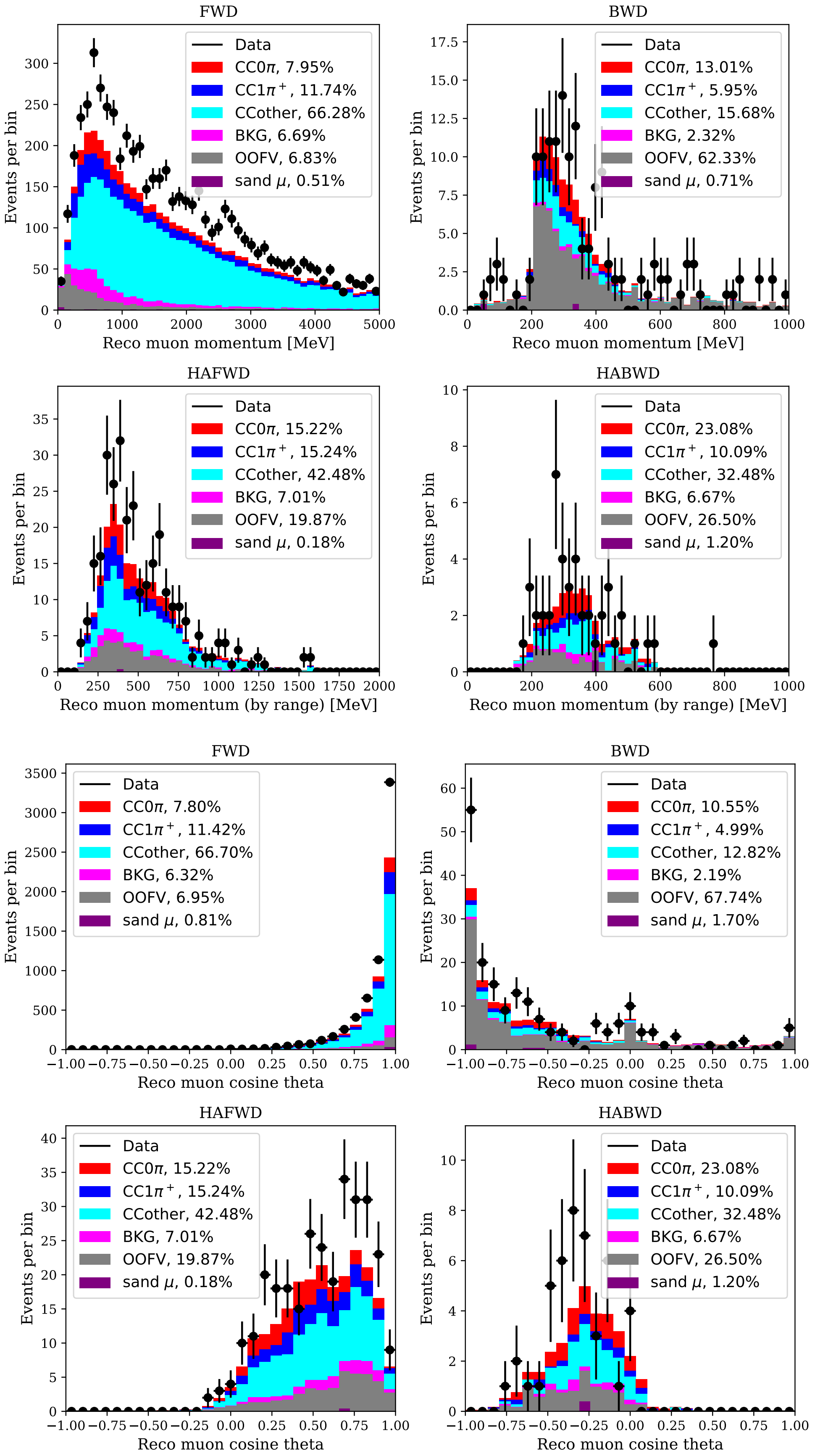

FIGURE D.9: Muon momentum (top two rows) and cosine of theta (bottom two rows) of CCother for the different directions: FWD (top left), BWD (top right), HAFWD (bottom left) and HABWD (bottom right), using the true topology definition.

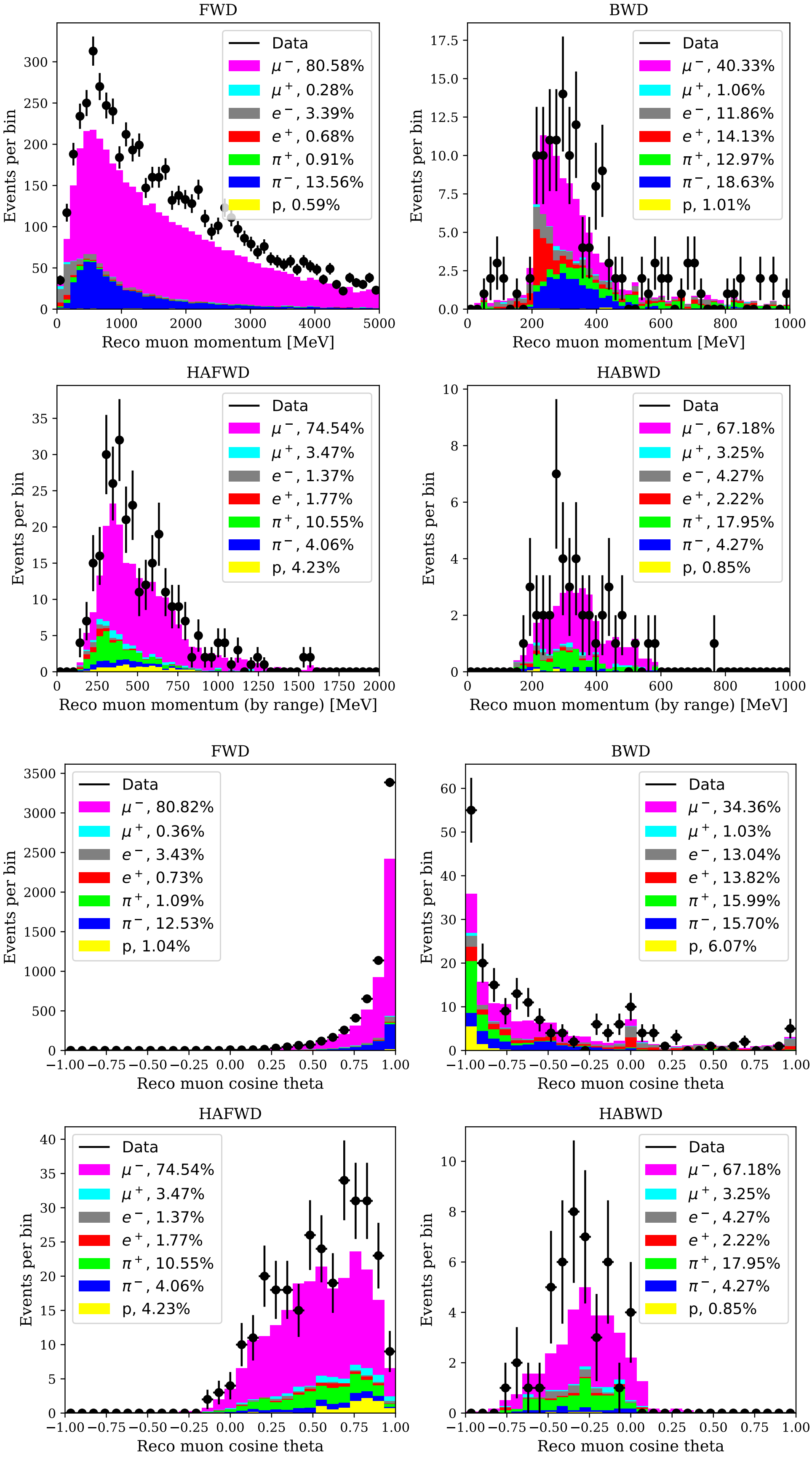

FIGURE D.10: Muon momentum (top two rows) and cosine of theta (bottom two rows) distributions of CCother for the different directions: FWD (top left), BWD (top right), HAFWD (bottom left) and HABWD (bottom right), using the true particle definition.

Appendix E

Single detector systematic contributions

- **BFieldDist:** It is due to the modelling of the TPC magnetic field distortions and the associated errors. It uses a flat density probability function and is a variation-like systematic (Figure **??**).
- **ToFResol:** It is used for each ToF is set equal to the maximum bias. It uses a Gaussian density probability function and is a variation-like systematic (Figure E.6a).
- **MomResol:** It is due to how well it is modelled in the MCs. It uses a Gaussian density probability function and is a variation-like systematic (Figure E.2a).
- **MomScale:** It affects more the migration between bins than the total number of events passing the selection cuts. It uses a Gaussian density probability function and is a variation-like systematic (Figure E.2b).
- **MomRangeResol:** It depends of the detector that was used to compute the momentum by range and the direction of the track. It uses a Gaussian density probability function and is a variation-like systematic (Figure E.3a).
- **MomBiasFromVertexMigration:** It is due to the current resolution of the FGD. It uses a Gaussian density probability function and is a variation-like systematic (Figure E.3b).
- **TpcPid:** It is due to the simulation of the TPC PID performance. It uses a Gaussian density probability function and is a variation-like systematic (Figure E.4a).
- **FgdPid:** It is due to the simulation of the FGD PID performance. It uses a Gaussian density probability function and is a variation-like systematic (Figure E.4b).
- **ECalEMResol:** It depends on the particle type and ECAL subdetector. It uses a Gaussian density probability function and is a variation-like systematic (Figure E.5a).
- **ECalEMScale:** It depends on the particle type and ECAL subdetector. It uses a Gaussian density probability function and is a variation-like systematic (Figure E.5b).
- **ChargeIDEff:** It depends of the ability of the MC and data to correctly identify the charge of a particle based on its curvature in the TPCs. It uses a Gaussian density probability function and is a efficiency-like systematic (Figure E.7a).

- **TpcClusterEff:** It is now applied to FGD-TPC objects that have 19 TPC NNodes. It uses a Gaussian density probability function and is a efficiency-like systematic (Figure E.7b).
- **TpcTrackEff:** It is due to the efficiency of reconstructing TPC tracks. It uses a Gaussian density probability function and is a efficiency-like systematic (Figure E.8a).
- **TpcFgdMatchEff:** It accounts for the efficiency of matching TPC to FGD tracks and is only applied for tracks with 1 or 2 hits at the end of the TPC. It uses a Gaussian density probability function and is a efficiency-like systematic (Figure E.8b)).
- **FgdHybridTrackEff:** It covers differences in FGDs tracking efficiencies due to the presence of TPC-FGD object(s). It uses a Gaussian density probability function and is a efficiency-like systematic (Figure E.9a).
- **MichelEleEff:** It is introduced due to the ability to correctly tag such signals. It uses a Gaussian density probability function and is a efficiency-like systematic (Figure E.9b).
- **PileUp:** The effect of pile up considered here is due to sand muons that are in coincidence with magnet events. It uses a Gaussian density probability function and is a normalisation-like systematic (Figure E.10a).
- **OOFV:** It is due to the number of events entering the selection due to interactions that occur outside of the FGD FV is due to a combination of vertex migration and neutral particles. It uses a Gaussian density probability function and is a normalisation-like systematic (Figure E.10b).
- **SandMu:** It is due to the simulation of interactions in the sand that enter ND280. It uses a Gaussian density probability function and is a normalisation-like systematic (Figure E.11a).
- **TpcECalMatchEff:** It depends on the particle type, momentum and ECAL subdetector. It uses a Gaussian density probability function and is a efficiency-like systematic (Figure E.11b).
- **TpcP0dMatchEff:** It depends of the timing information between TPC and P0D. It uses a Gaussian density probability function and is a efficiency-like systematic (Figure E.12a).
- **FgdECalMatchEff:** It depends on the direction of the track. It uses a Gaussian density probability function and is a efficiency-like systematic (Figure E.12b).
- **FgdECalSMRDMatchEff:** It depends on the direction of the track. It uses a Gaussian density probability function and is a efficiency-like systematic (Figure E.13a).
- **ECalTrackEff:** It depends on the particle type, momentum and ECAL subdetector. It uses a Gaussian density probability function and is a efficiency-like systematic (Figure E.13b).
- **SIPion:** It is due to the modelling of pion secondary interactions. It uses a Gaussian density probability function and is a normalisation-like systematic (Figure E.14a).

- **SIProton:** It is due to the modelling of proton secondary interactions. It uses a Gaussian density probability function and is a normalisation-like systematic (Figure E.14b).
- **FGDMass:** It is due to the uncertainty on the areal density for XY modules, or for FGD1s mass density inside the fiducial volume. It uses a Gaussian density probability function and is a normalisation-like systematic (Figure E.6b).

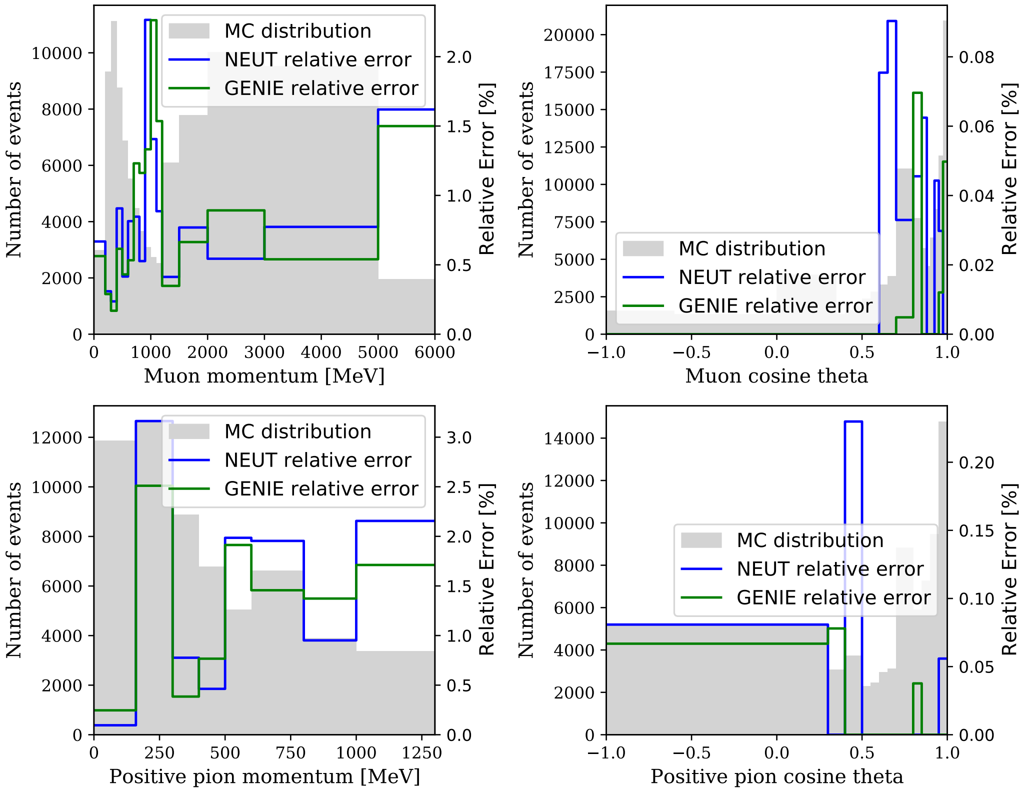

FIGURE E.1: Relative errors using NEUT (blue line), GENIE (green line) and MC distribution (gray area) as function of muon momentum (top left), muon cosine of theta (top right), positive pion momentum (bottom left) and positive pion cosine of theta (bottom right) for "BFieldDist" variation systematics for the CC1π^+ sample.

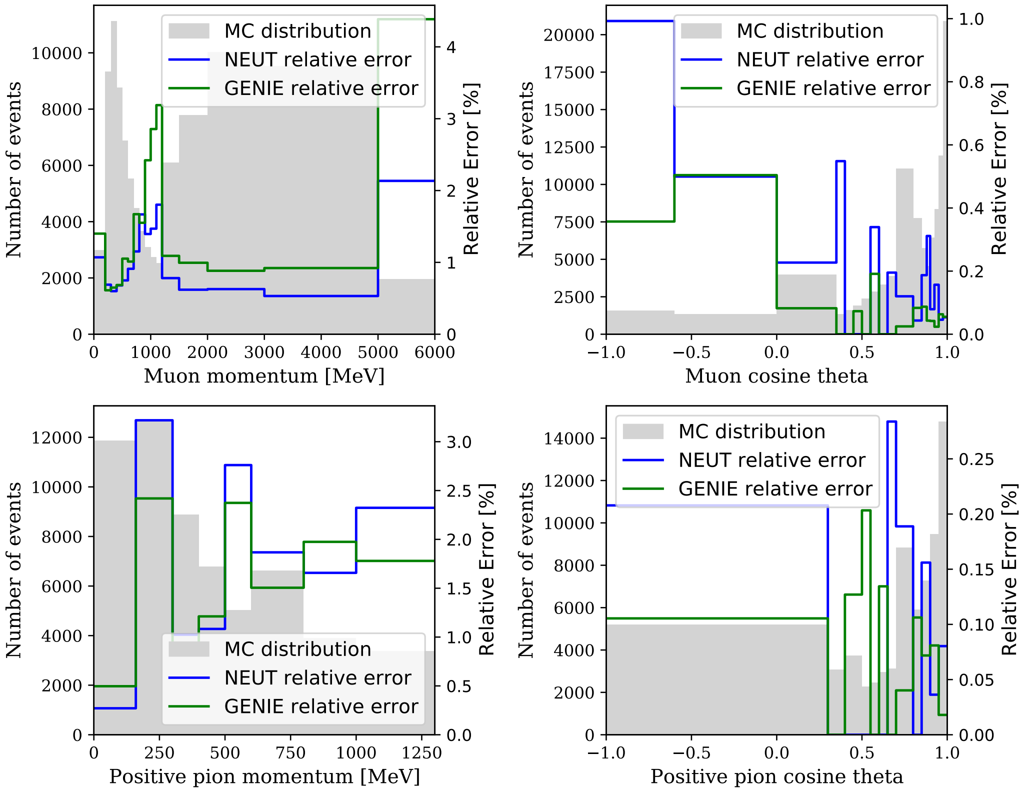

(A) MomResol

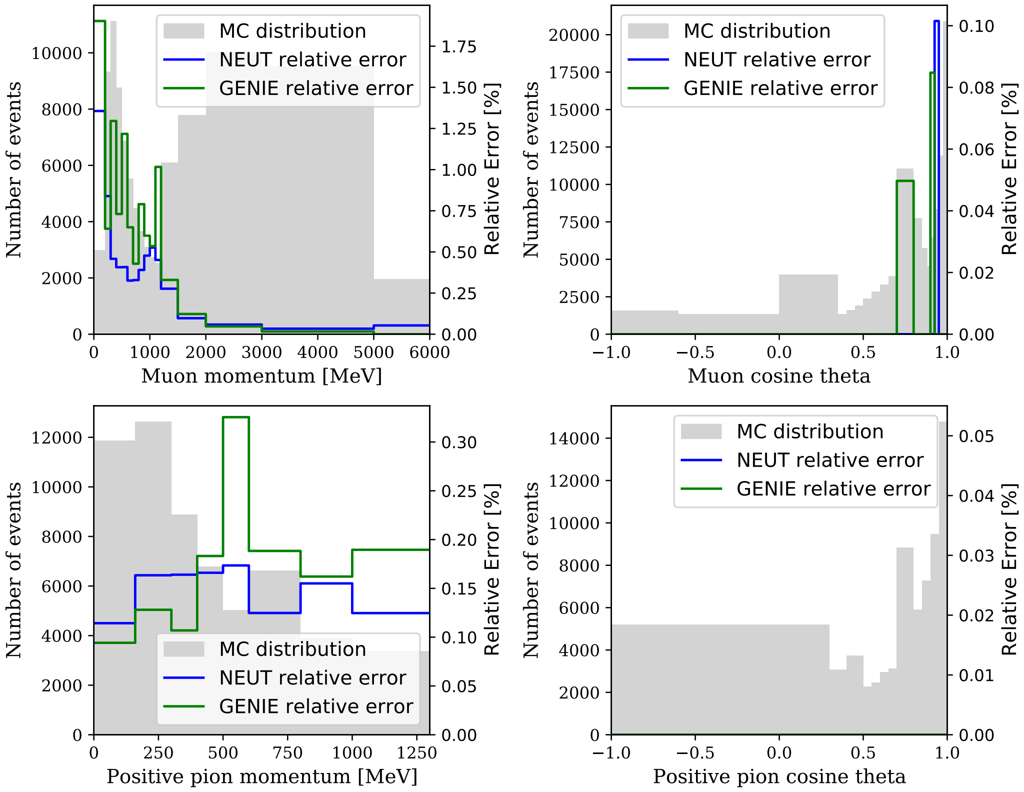

(B) MomScale

FIGURE E.2: Relative errors using NEUT (blue line), GENIE (green line) and MC distribution (gray area) as function of muon momentum (top left), muon cosine of theta (top right), positive pion momentum (bottom left) and positive pion cosine of theta (bottom right) for "MomResol" (a) and "MomScale" (b) variation systematics for the CC1π^+ sample.

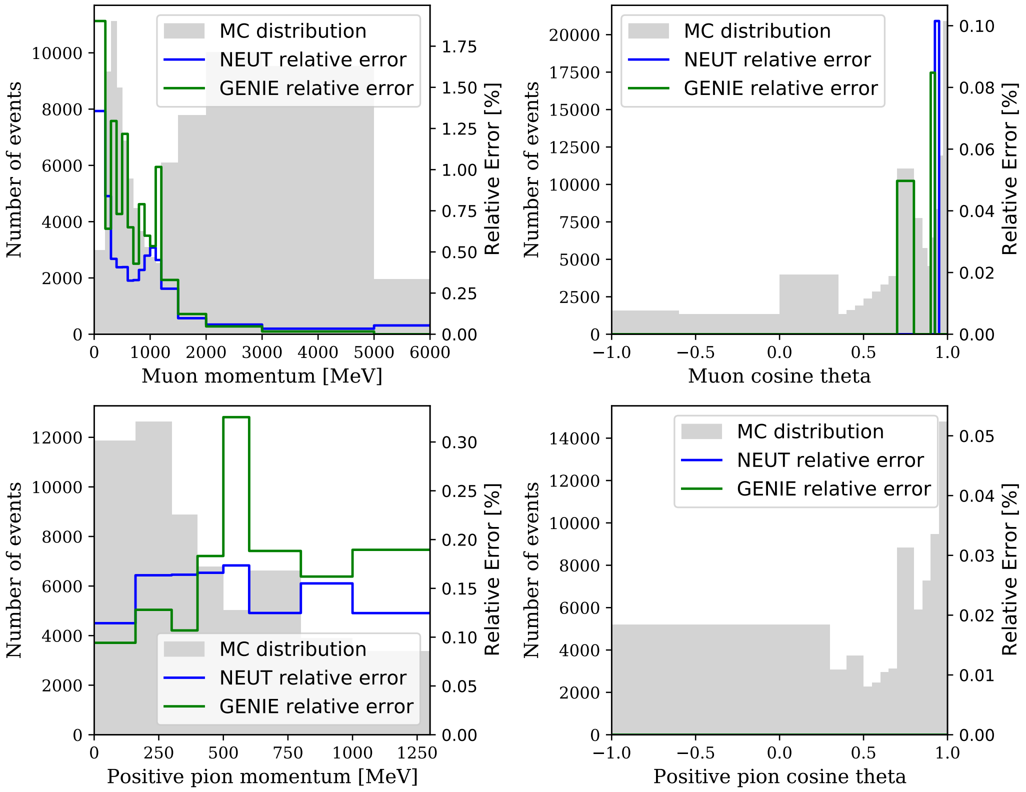

(A) MomRangeResol

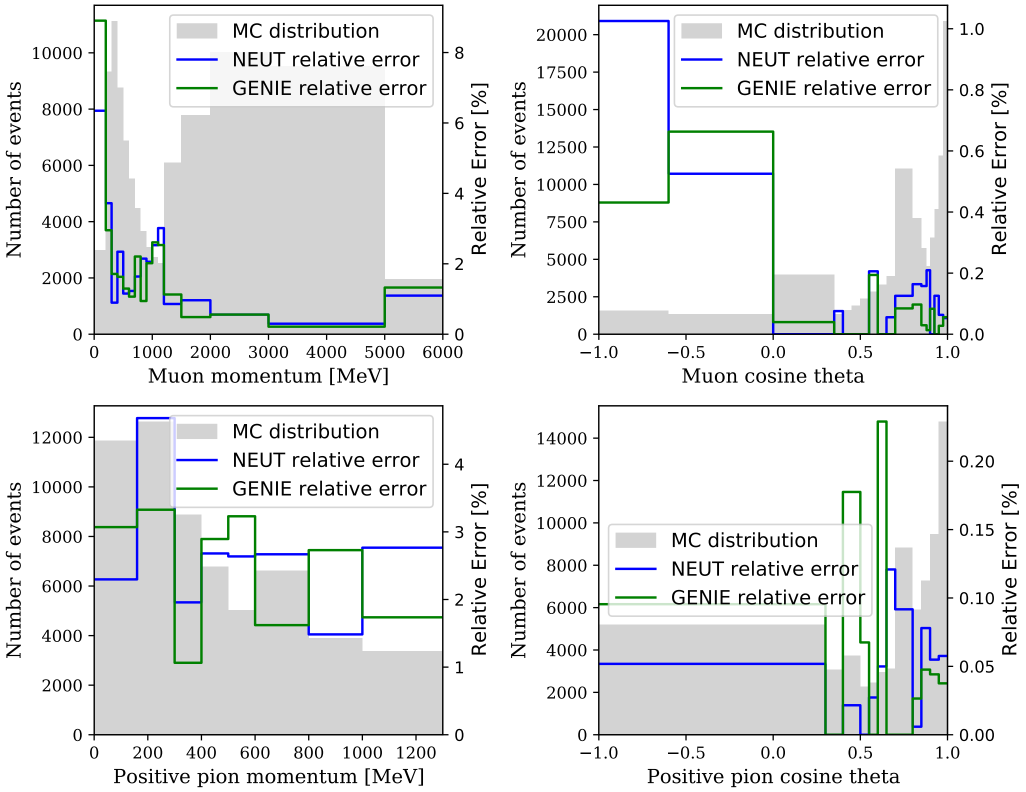

(B) MomBiasFromVertexMigration

FIGURE E.3: Relative errors using NEUT (blue line), GENIE (green line) and MC distribution (gray area) as function of muon momentum (top left), muon cosine of theta (top right), positive pion momentum (bottom left) and positive pion cosine of theta (bottom right) for "MomRangeResol" (a) and "MomBiasFromVertexMigration" (b) variation systematics for the CC1π^+ sample.

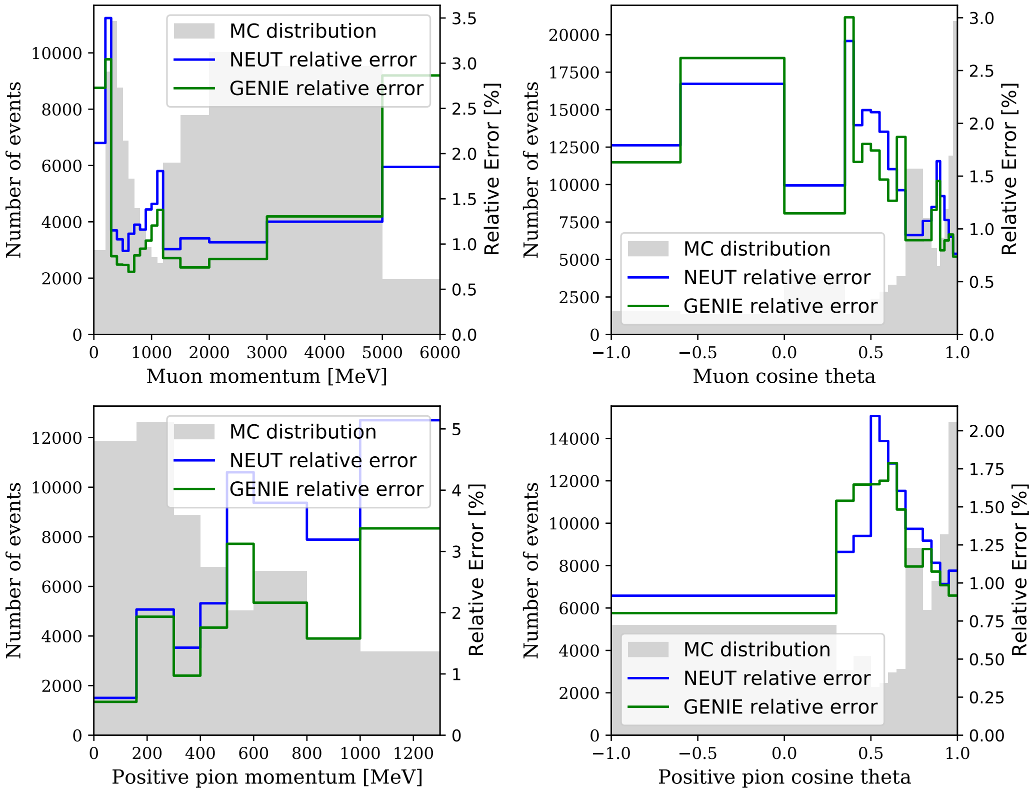

(A) TpcPid

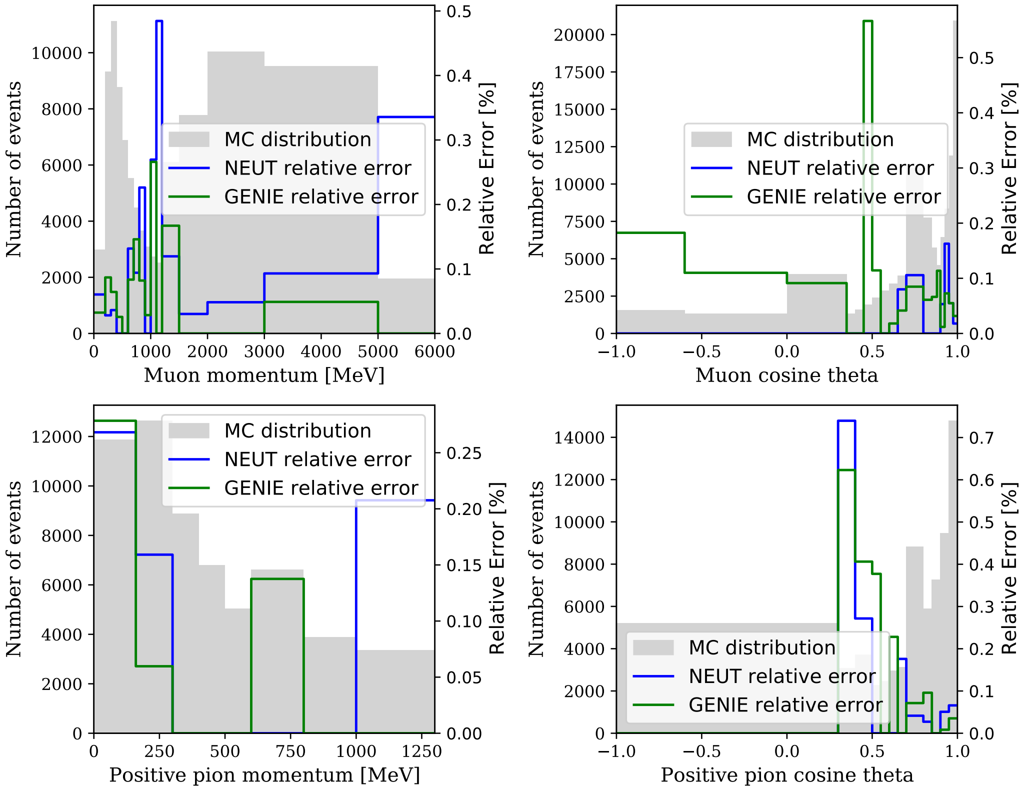

(B) FgdPid

FIGURE E.4: Relative errors using NEUT (blue line), GENIE (green line) and MC distribution (gray area) as function of muon momentum (top left), muon cosine of theta (top right), positive pion momentum (bottom left) and positive pion cosine of theta (bottom right) for "TpcPid" (a) and "FgdPid" (b) variation systematics for the CC1π^+ sample.

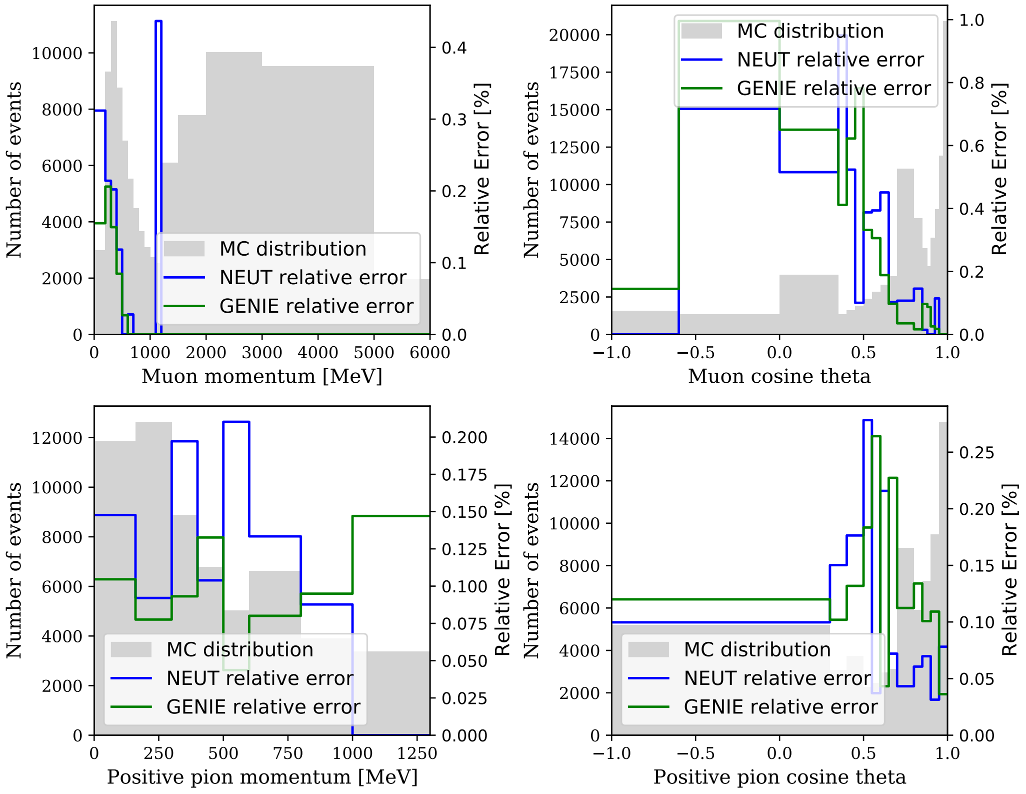

(A) ECalEMResol

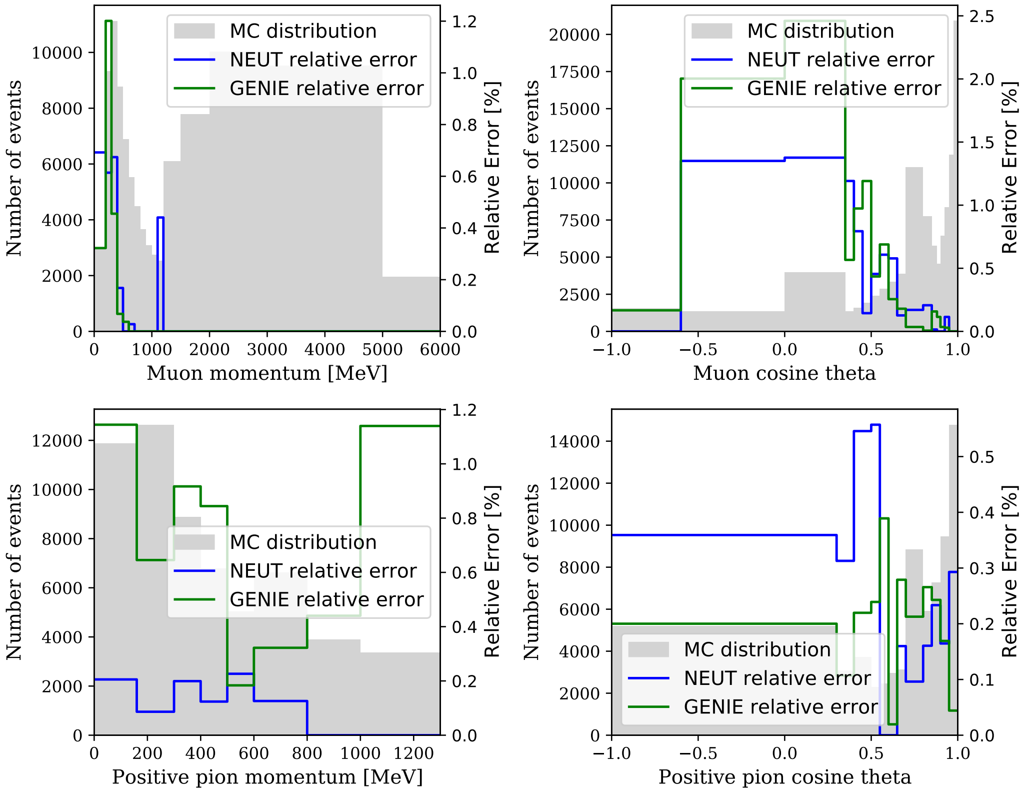

(B) ECalEMScale

FIGURE E.5: Relative errors using NEUT (blue line), GENIE (green line) and MC distribution (gray area) as function of muon momentum (top left), muon cosine of theta (top right), positive pion momentum (bottom left) and positive pion cosine of theta (bottom right) for "ECalEMResol" (a) and "ECalEMScale" (b) variation systematics for the CC1π^+ sample.

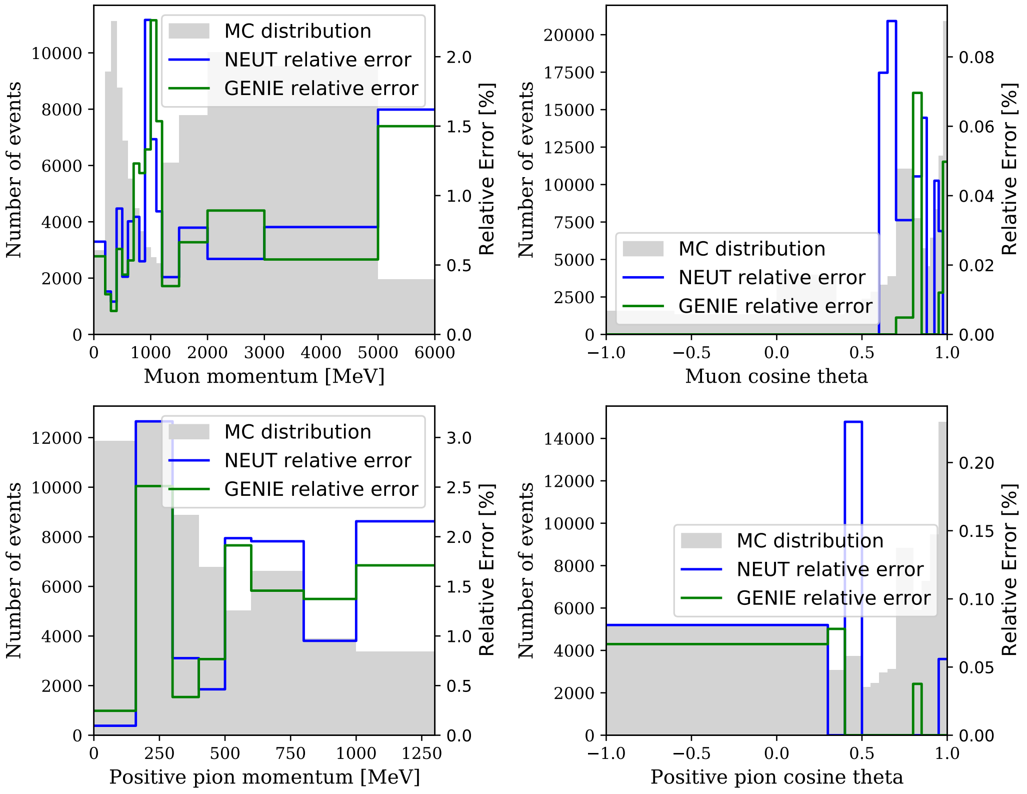

(A) ToFResol

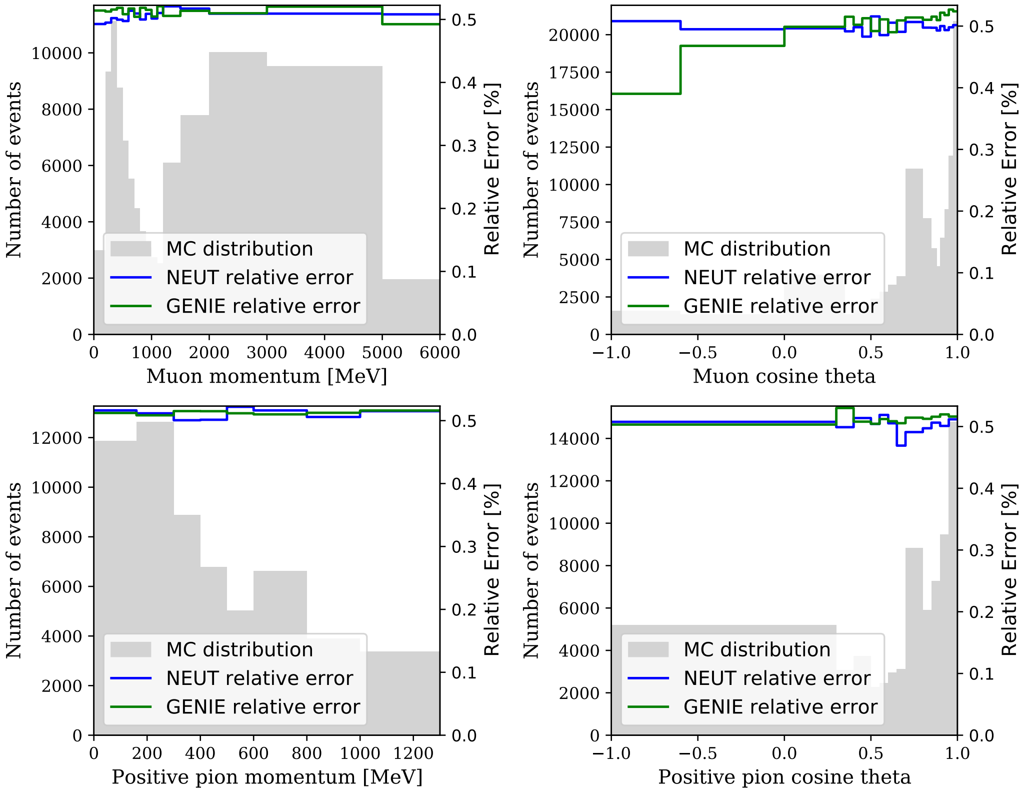

(B) FGDMass

FIGURE E.6: Relative errors using NEUT (blue line), GENIE (green line) and MC distribution (gray area) as function of muon momentum (top left), muon cosine of theta (top right), positive pion momentum (bottom left) and positive pion cosine of theta (bottom right) for "ToFResol" variation systematics (a) and "FGDMass" weight systematics (b) variation systematics for the CC1π^+ sample.

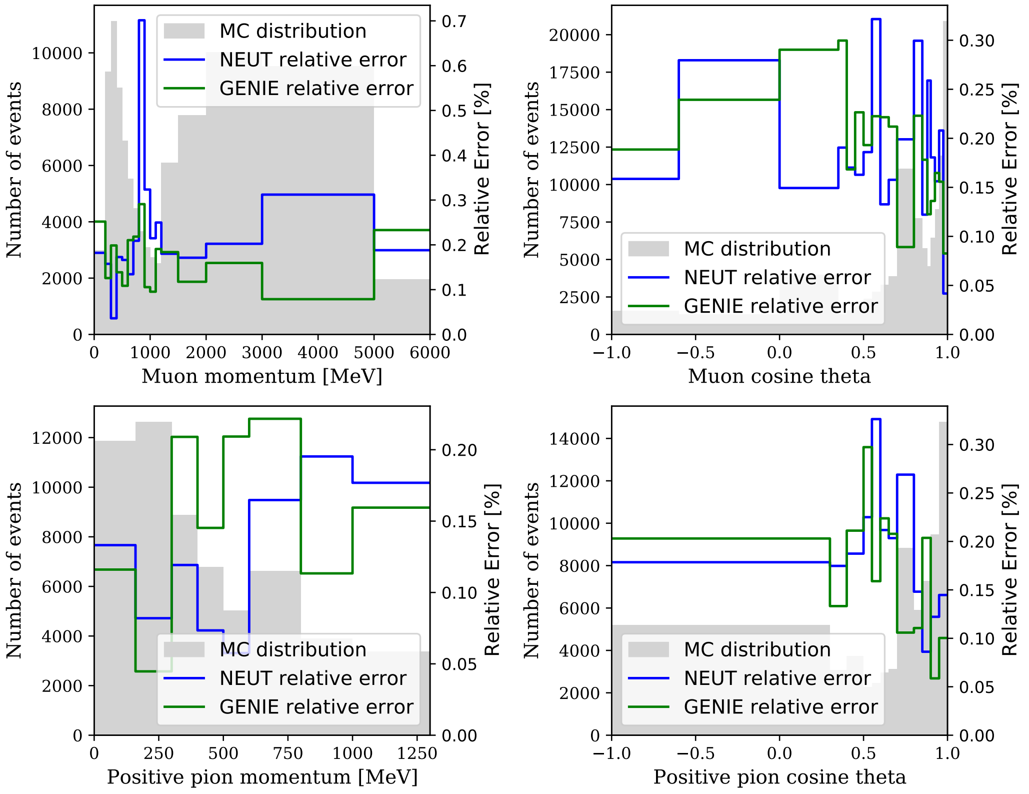

(A) ChargeIDEff

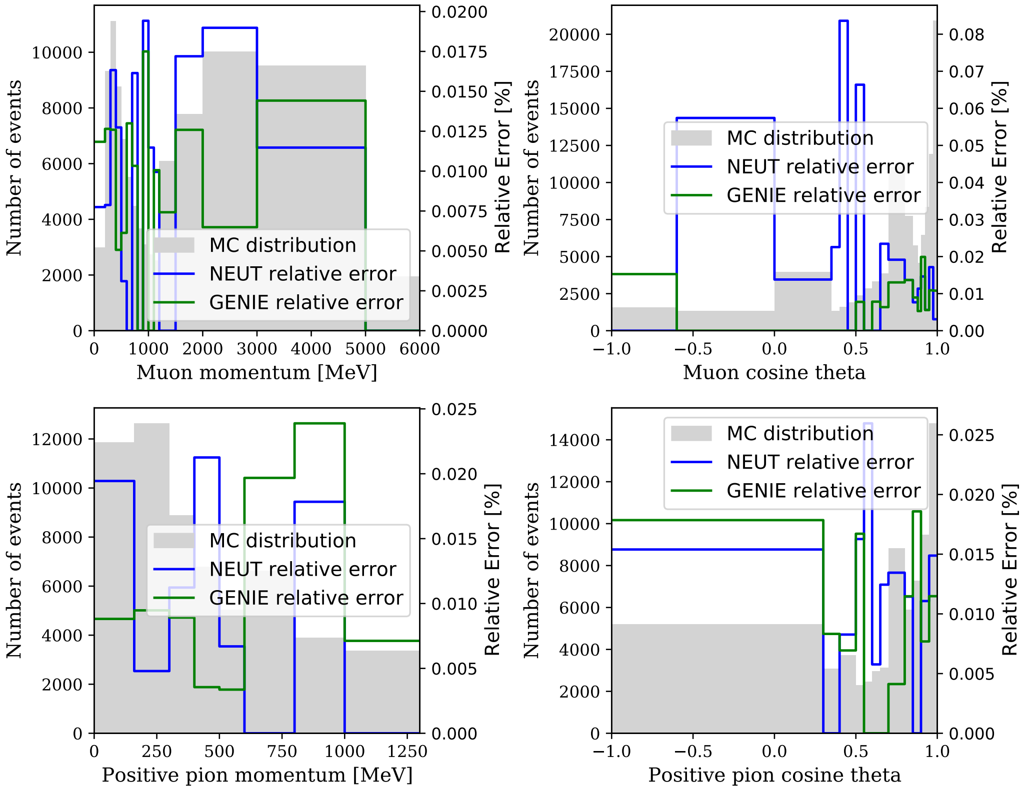

(B) TpcClusterEff

FIGURE E.7: Relative errors using NEUT (blue line), GENIE (green line) and MC distribution (gray area) as function of muon momentum (top left), muon cosine of theta (top right), positive pion momentum (bottom left) and positive pion cosine of theta (bottom right) for "ChargeIDEff" (a) and "TpcClusterEff" (b) weight systematics for the CC1π^+ sample.

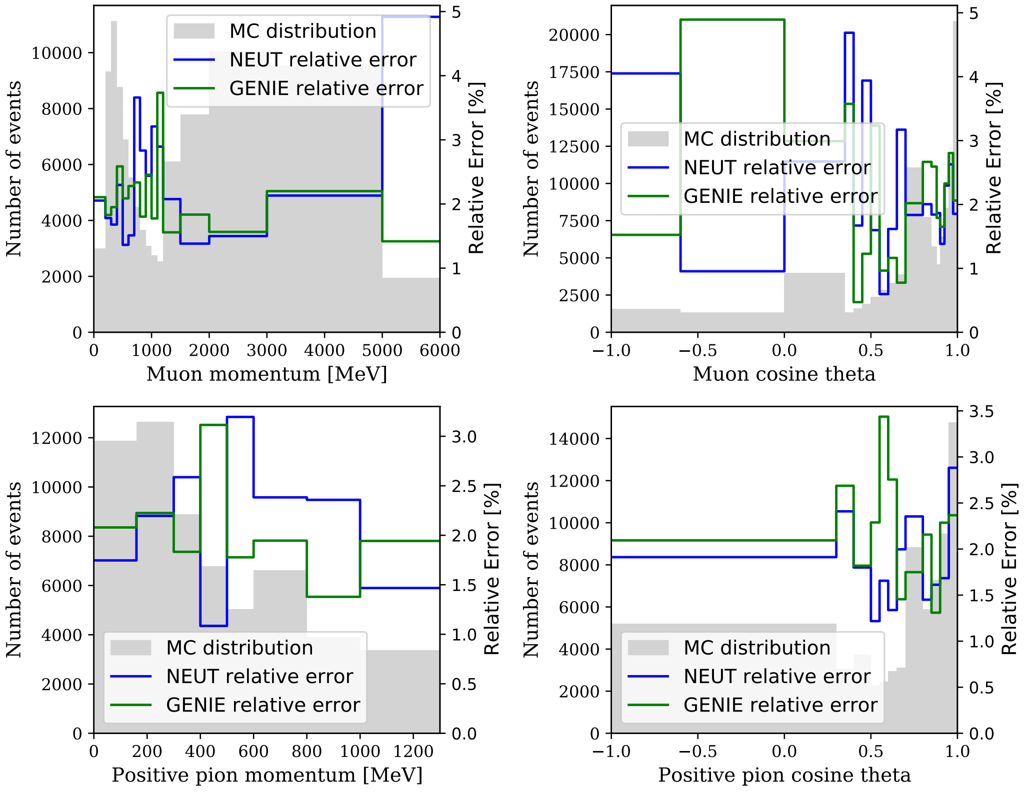

(A) TpcTrackEff

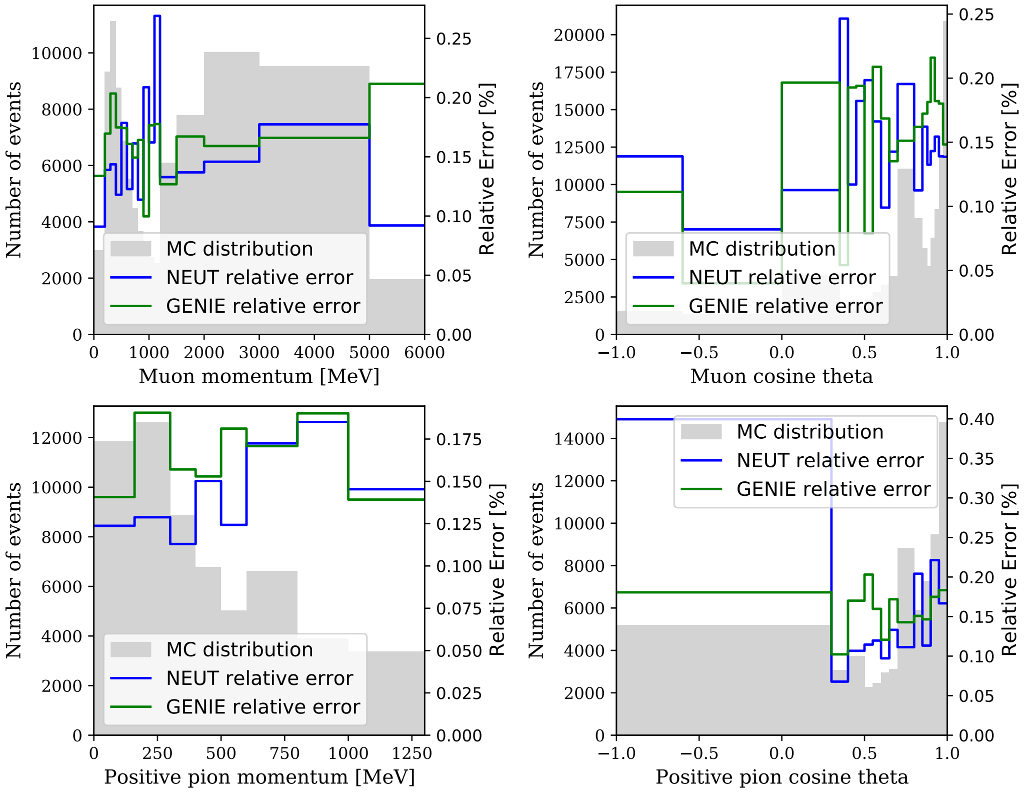

(B) TpcFgdMatchEff

FIGURE E.8: Relative errors using NEUT (blue line), GENIE (green line) and MC distribution (gray area) as function of muon momentum (top left), muon cosine of theta (top right), positive pion momentum (bottom left) and positive pion cosine of theta (bottom right) for "TpcTrackEff" (a) and "TpcFgdMatchEff" (b) weight systematics for the CC1π^+ sample.

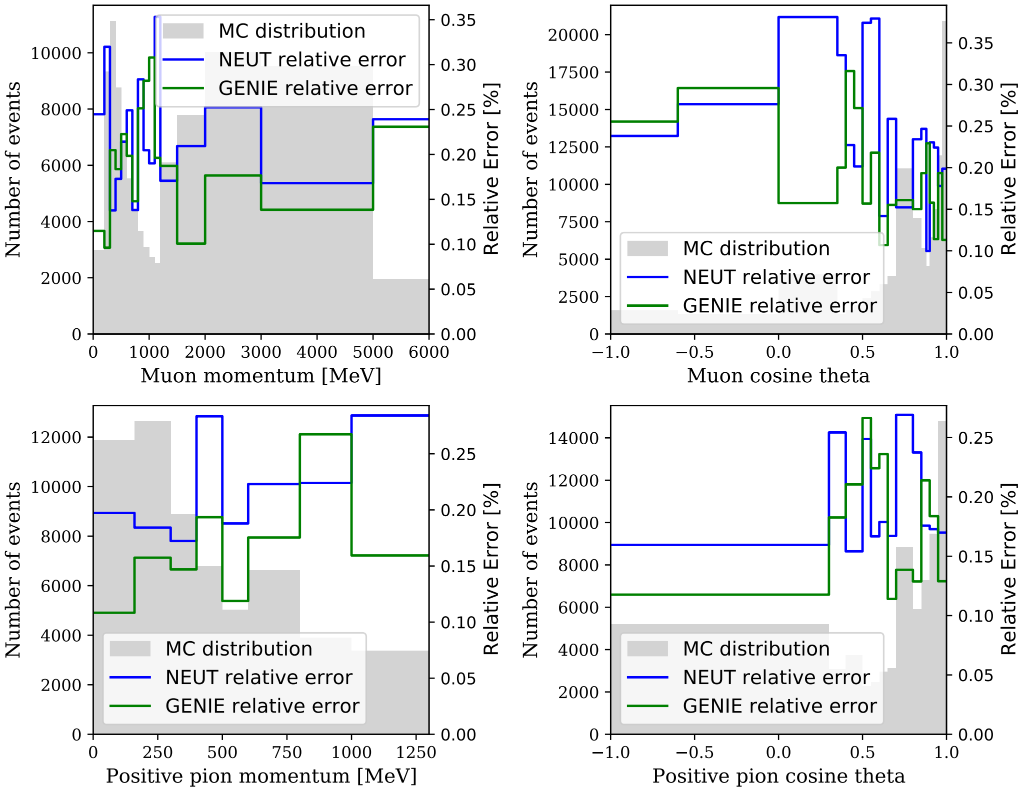

(A) FgdHybridTrackEff

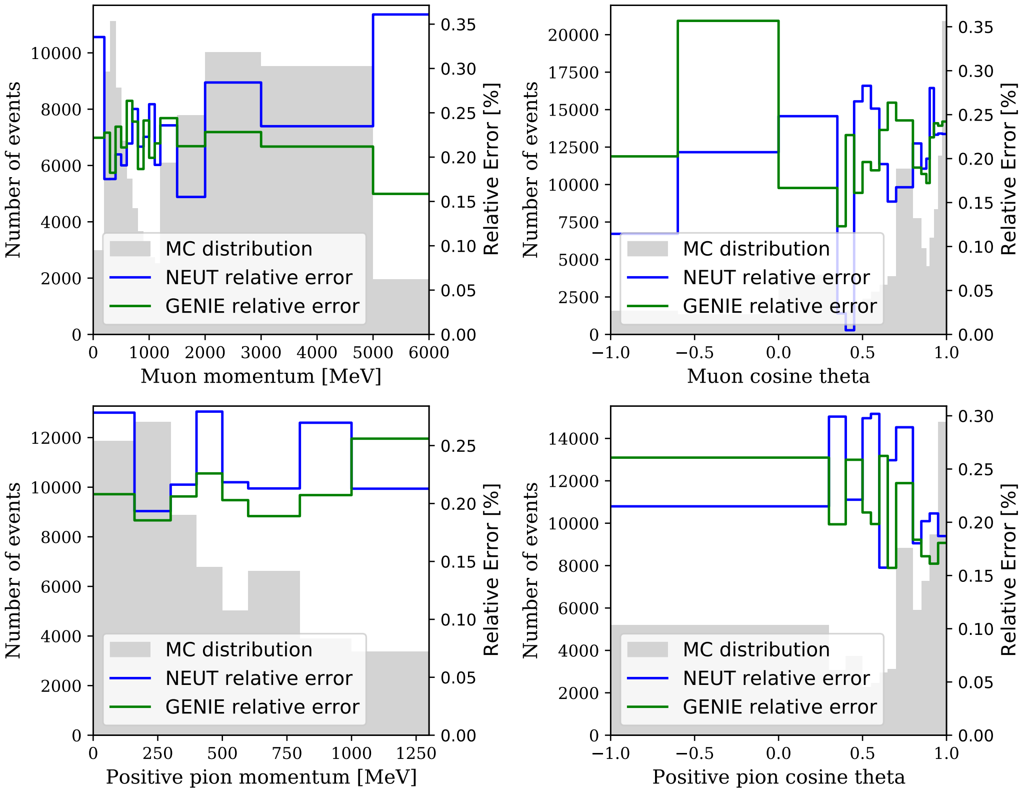

(B) MichelEleEff

FIGURE E.9: Relative errors using NEUT (blue line), GENIE (green line) and MC distribution (gray area) as function of muon momentum (top left), muon cosine of theta (top right), positive pion momentum (bottom left) and positive pion cosine of theta (bottom right) for "FgdHybridTrackEff" (a) and "MichelEleEff" (b) weight systematics for the CC1π^+ sample.

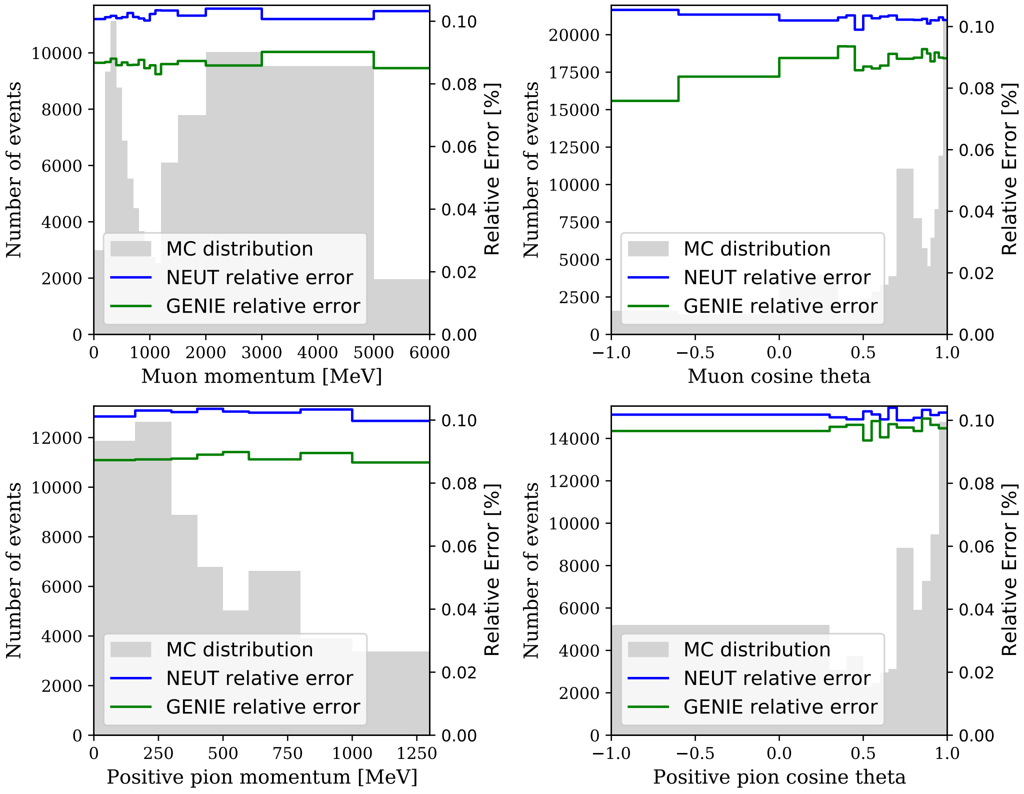

(A) PileUp

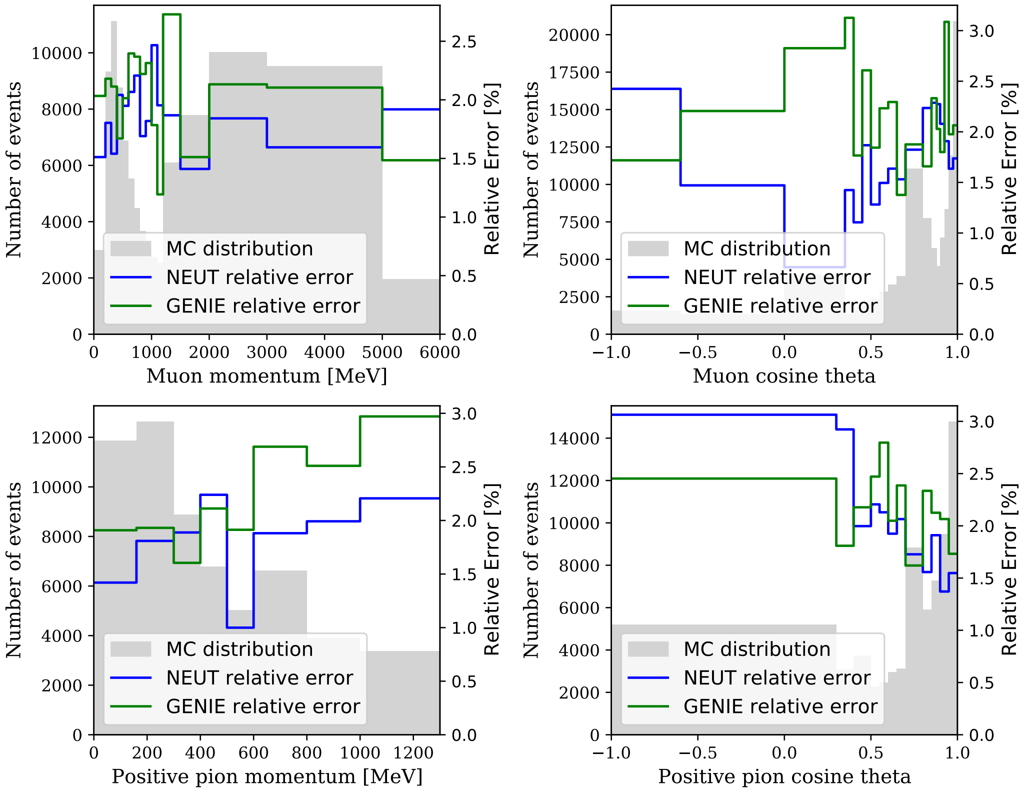

(B) OOFV

FIGURE E.10: Relative errors using NEUT (blue line), GENIE (green line) and MC distribution (gray area) as function of muon momentum (top left), muon cosine of theta (top right), positive pion momentum (bottom left) and positive pion cosine of theta (bottom right) for "PileUp" (a) and "OOFV" (b) weight systematics for the CC1π^+ sample.

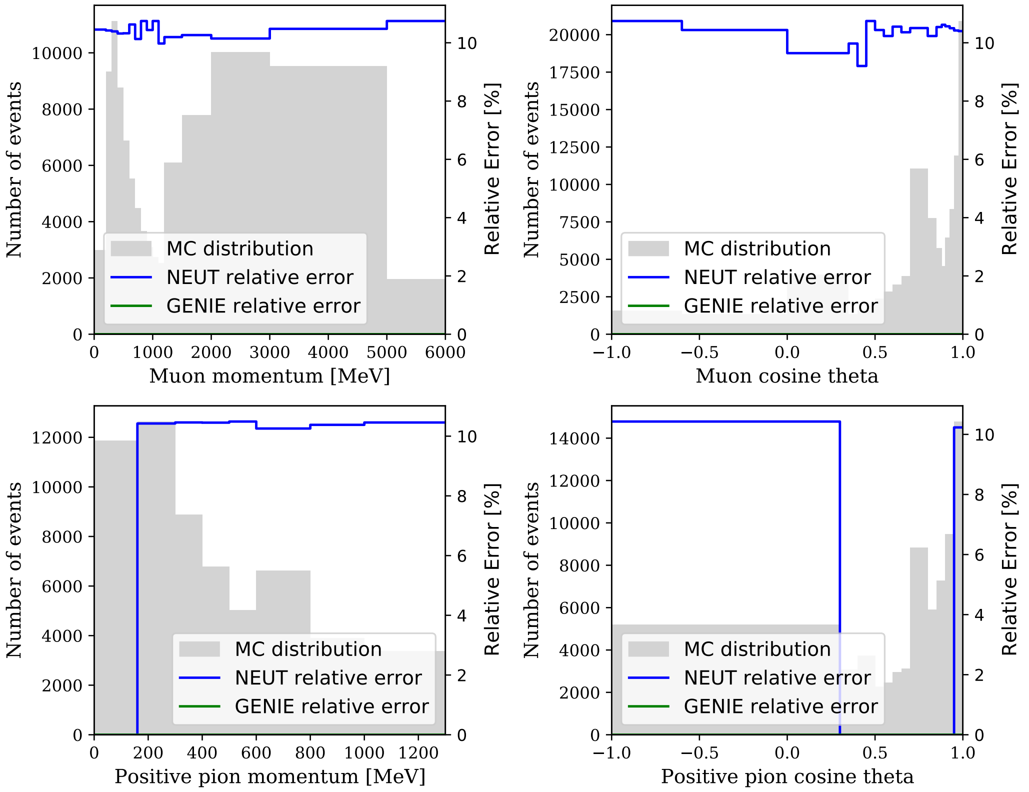

(A) SandMu

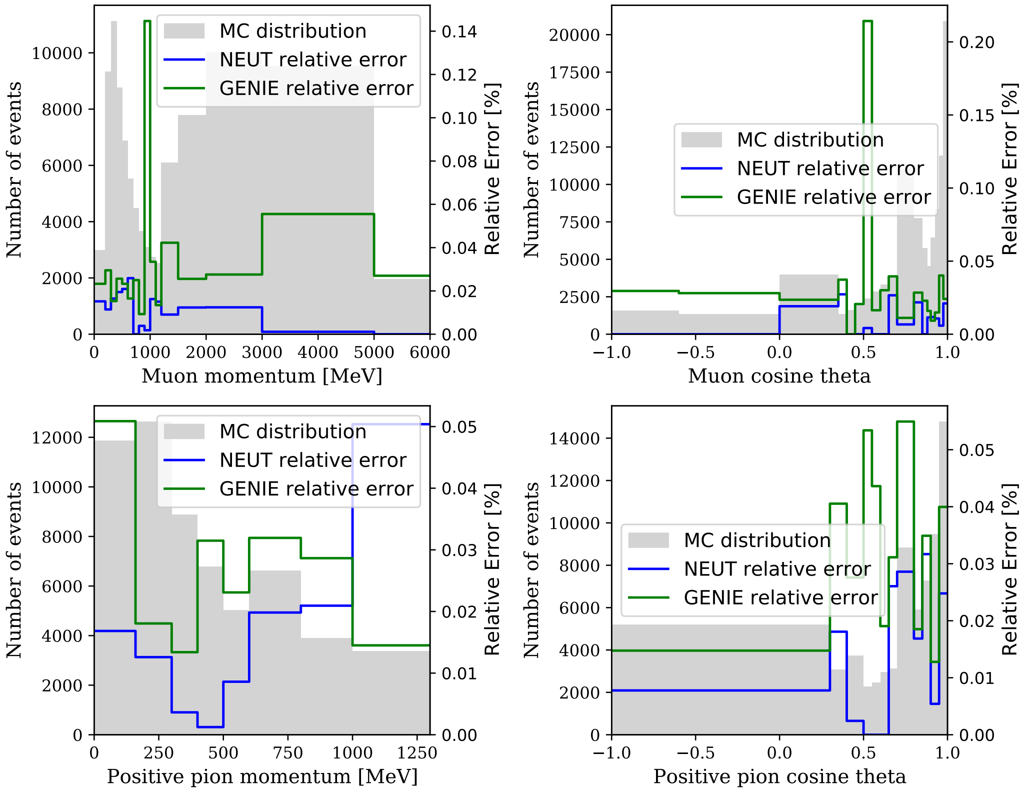

(B) TpcECalMatchEff

FIGURE E.11: Relative errors using NEUT (blue line), GENIE (green line) and MC distribution (gray area) as function of muon momentum (top left), muon cosine of theta (top right), positive pion momentum (bottom left) and positive pion cosine of theta (bottom right) for "SandMu" (a) and "TpcECalMatchEff" (b) weight systematics for the CC1π^+ sample.

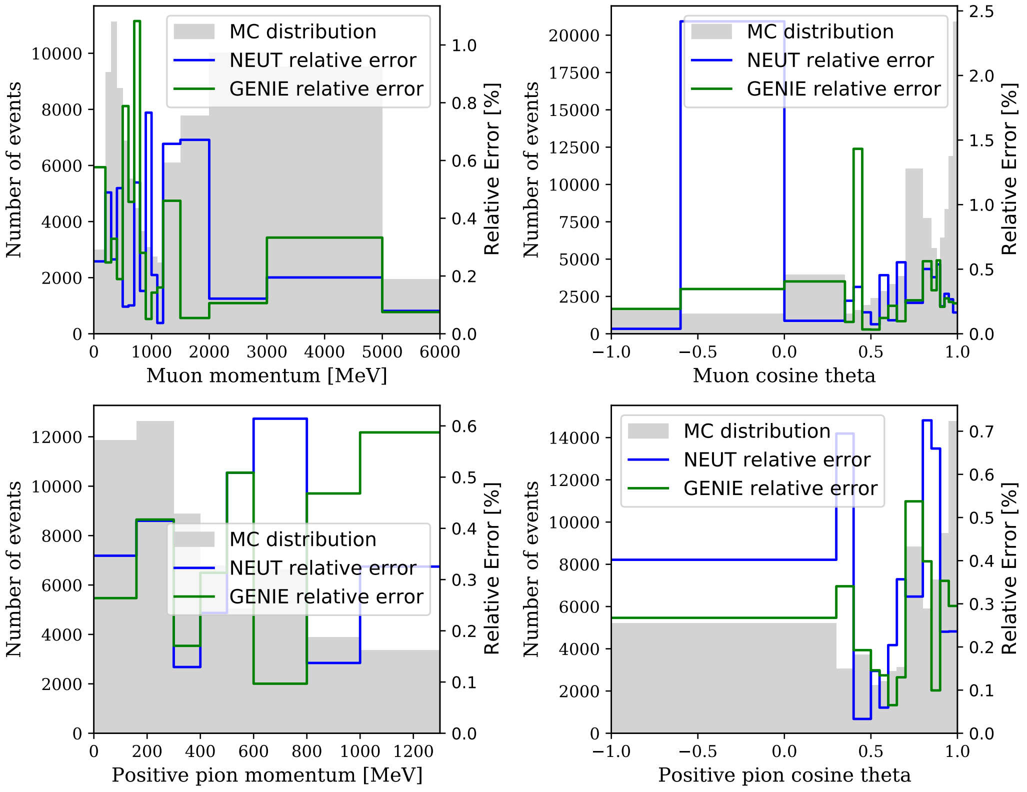

(A) TpcP0dMatchEff

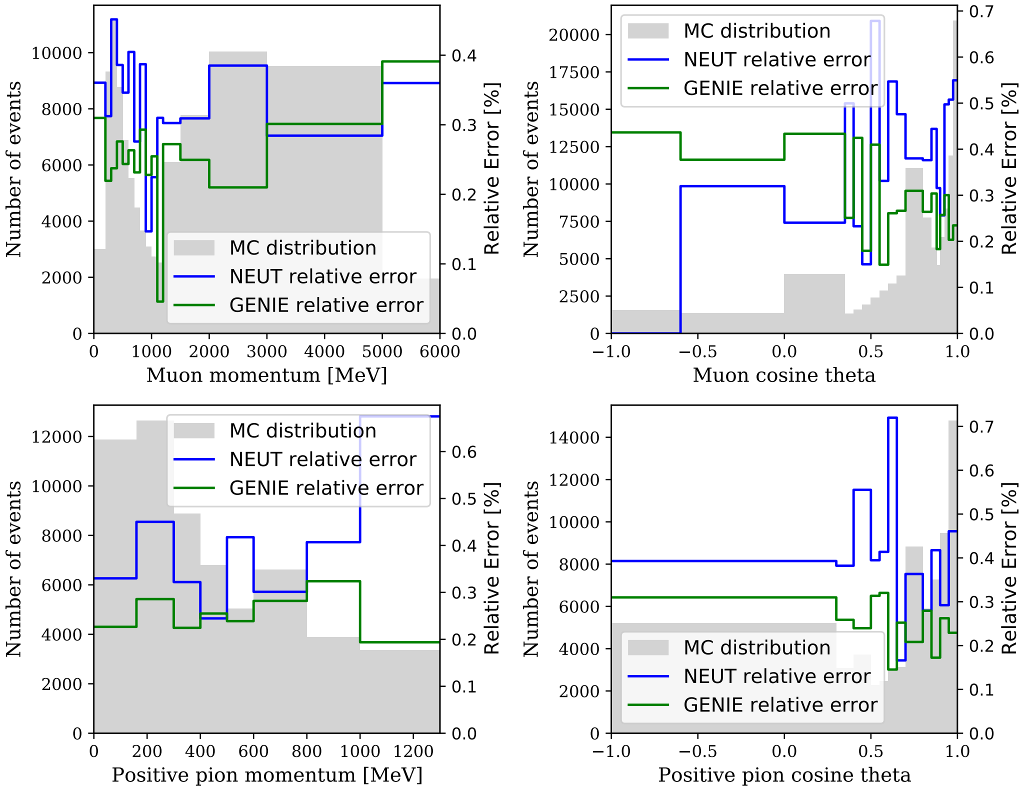

(B) FgdECalMatchEff

FIGURE E.12: Relative errors using NEUT (blue line), GENIE (green line) and MC distribution (gray area) as function of muon momentum (top left), muon cosine of theta (top right), positive pion momentum (bottom left) and positive pion cosine of theta (bottom right) for "TpcP0dMatchEff" (a) and "FgdECalMatchEff" (b) weight systematics for the CC1π^+ sample.

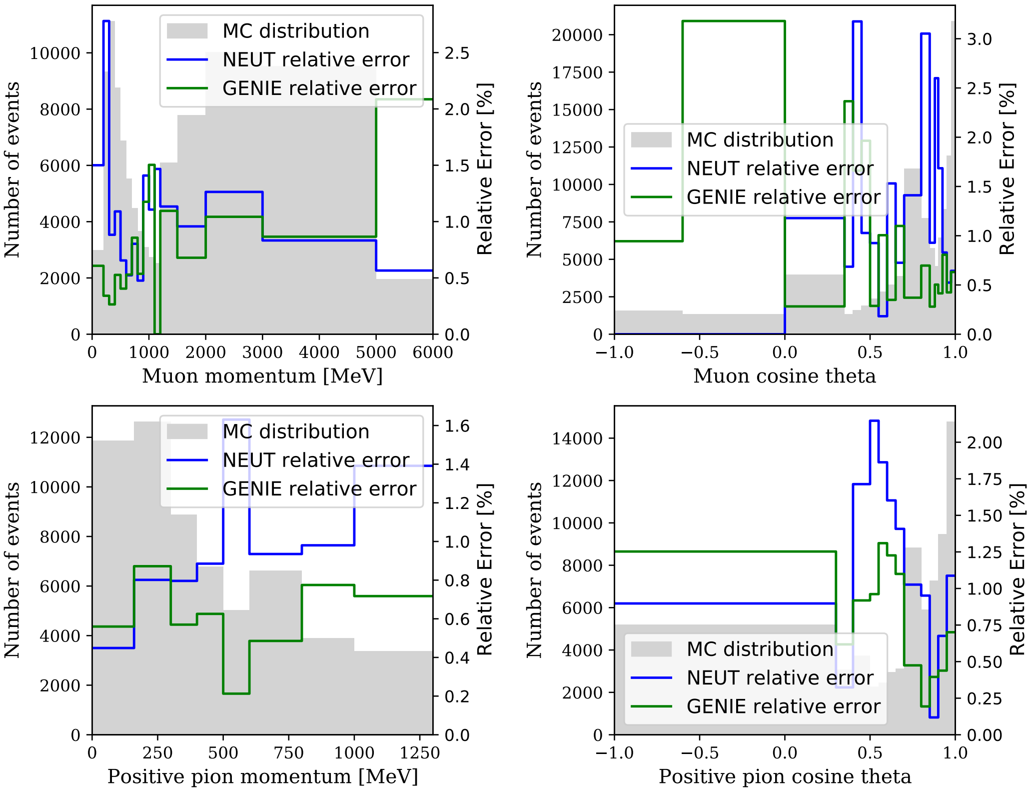

(A) FgdECalSMRDMatchEff

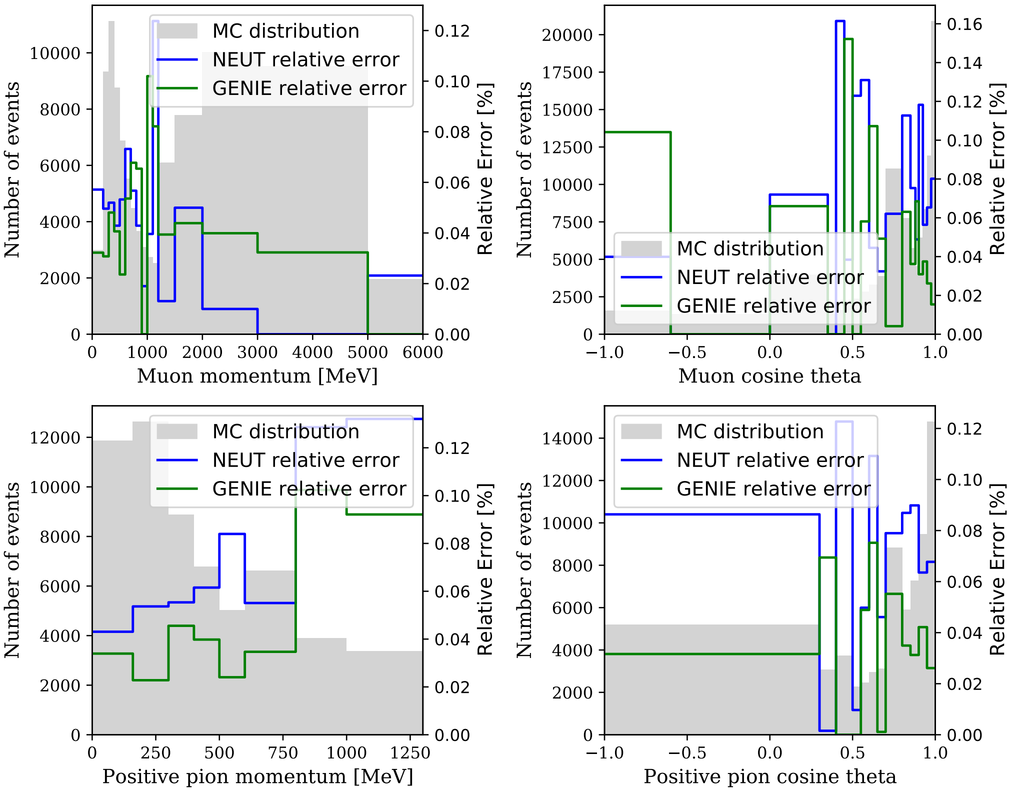

(B) ECalTrackEff

FIGURE E.13: Relative errors using NEUT (blue line), GENIE (green line) and MC distribution (gray area) as function of muon momentum (top left), muon cosine of theta (top right), positive pion momentum (bottom left) and positive pion cosine of theta (bottom right) for "FgdECalSMRDMatchEff" (a) and "ECalTrackEff" (b) weight systematics for the CC1π^+ sample.

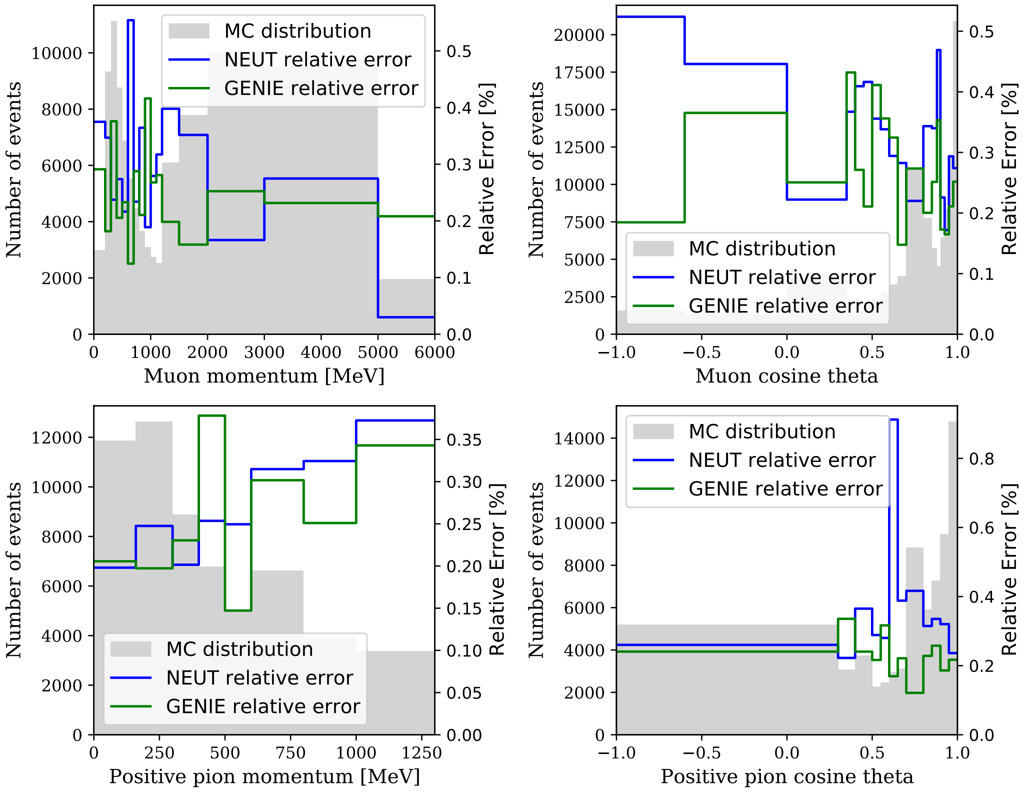

(A) SIPion

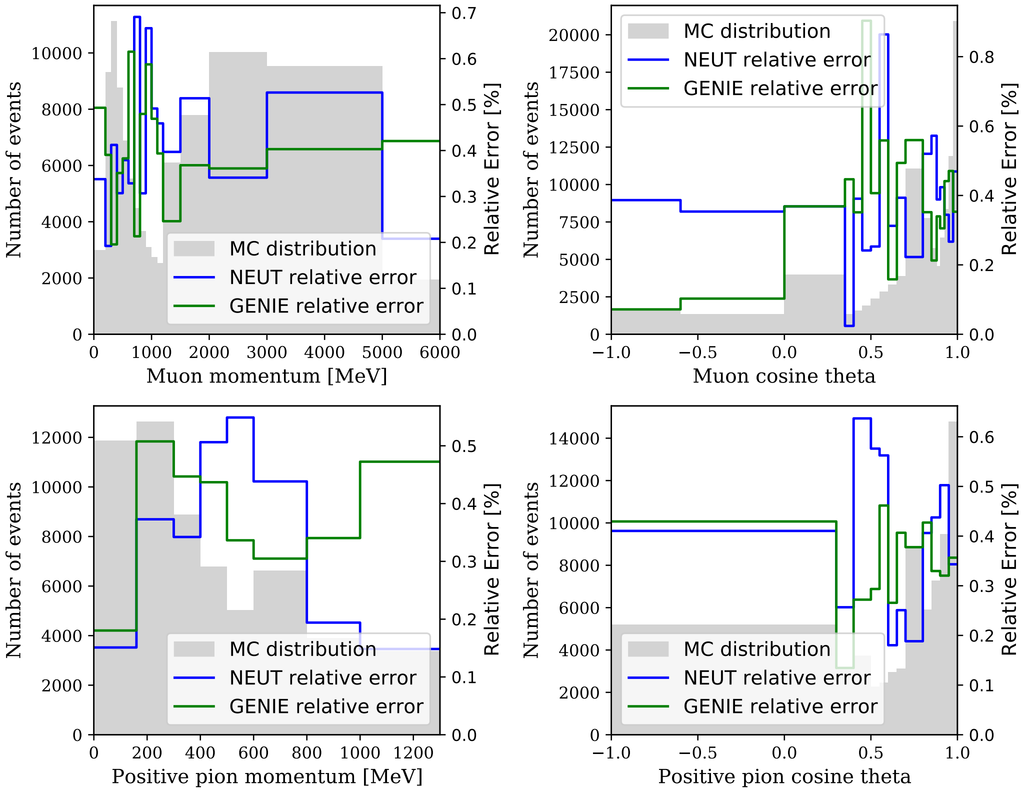

(B) SIProton

FIGURE E.14: Relative errors using NEUT (blue line), GENIE (green line) and MC distribution (gray area) as function of muon momentum (top left), muon cosine of theta (top right), positive pion momentum (bottom left) and positive pion cosine of theta (bottom right) for "SIPion" (a) and "SIProton" (b) weight systematics for the CC1π^+ sample.

Appendix F

Splines

To allow the fit to evaluate the effect of any value of any model parameter, the response functions are turned into splines by interpolating between the discrete values of the standard deviations evaluated. In this appendix can be found the different plots for all topology × reaction combinations for each model parameter.

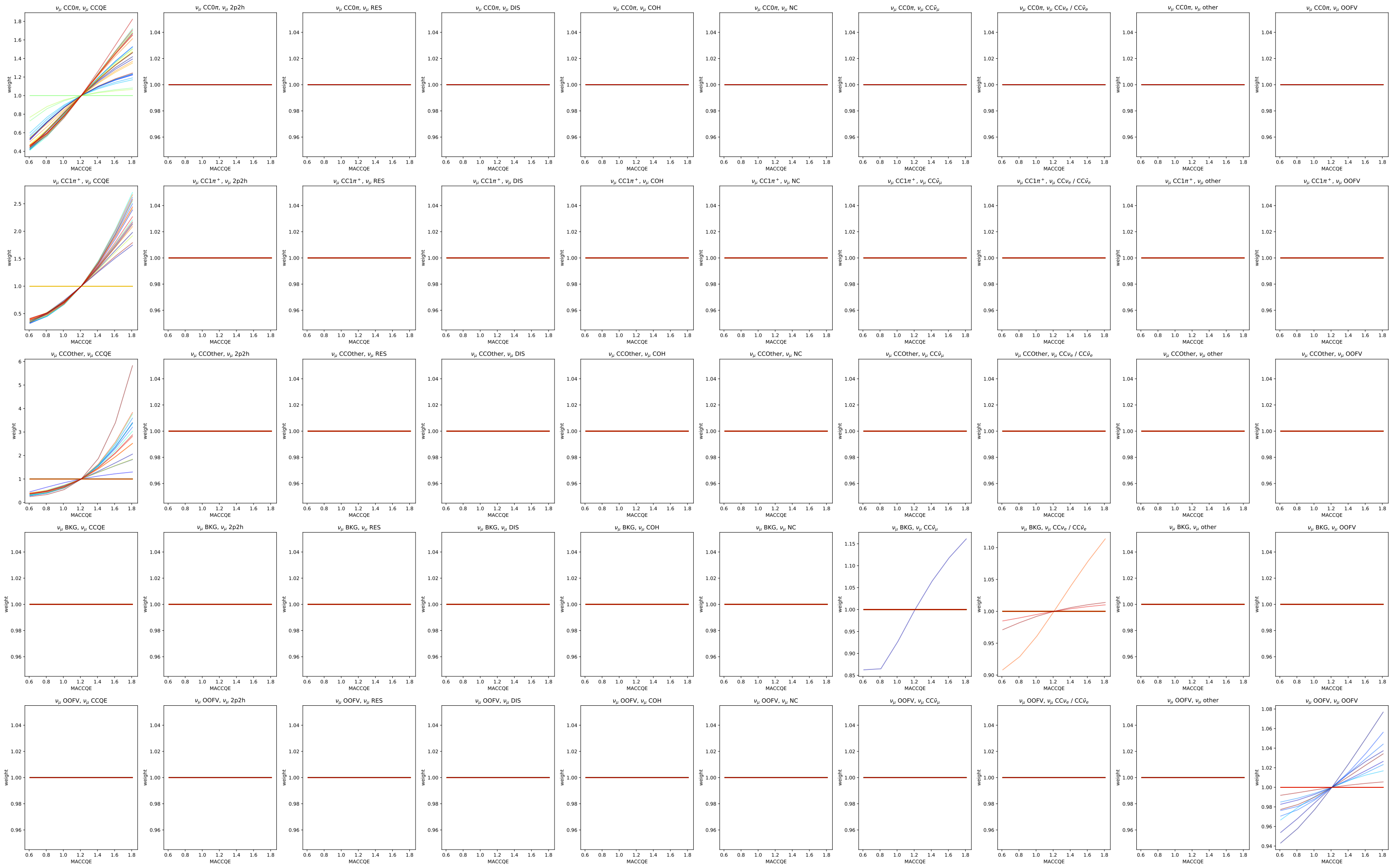

FIGURE F.1: Topology × Reactions configurations for MACCQE with 33 bins per configuration.

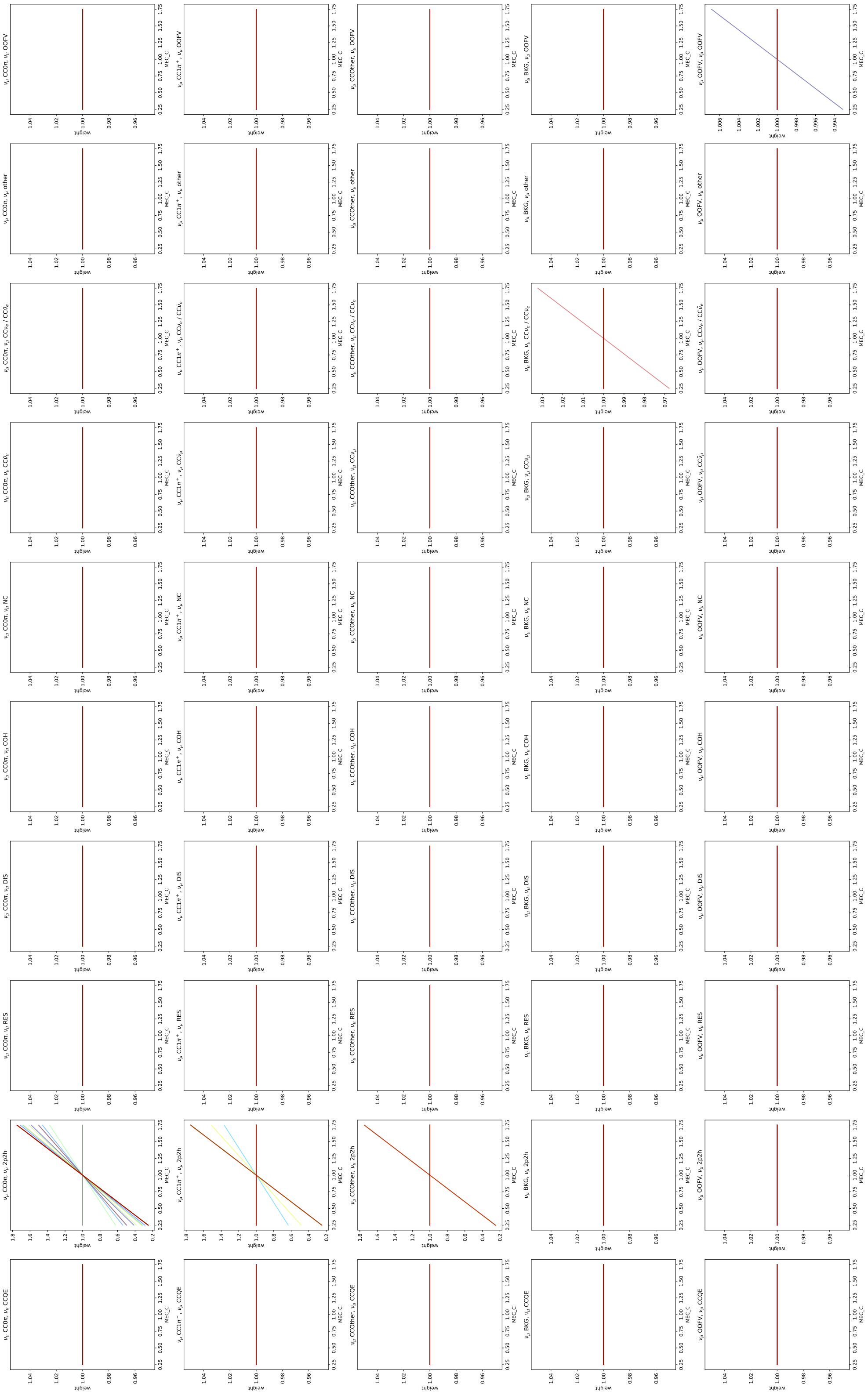

FIGURE F.2: Topology × Reactions configurations for MEC_C with 33 bins per configuration.

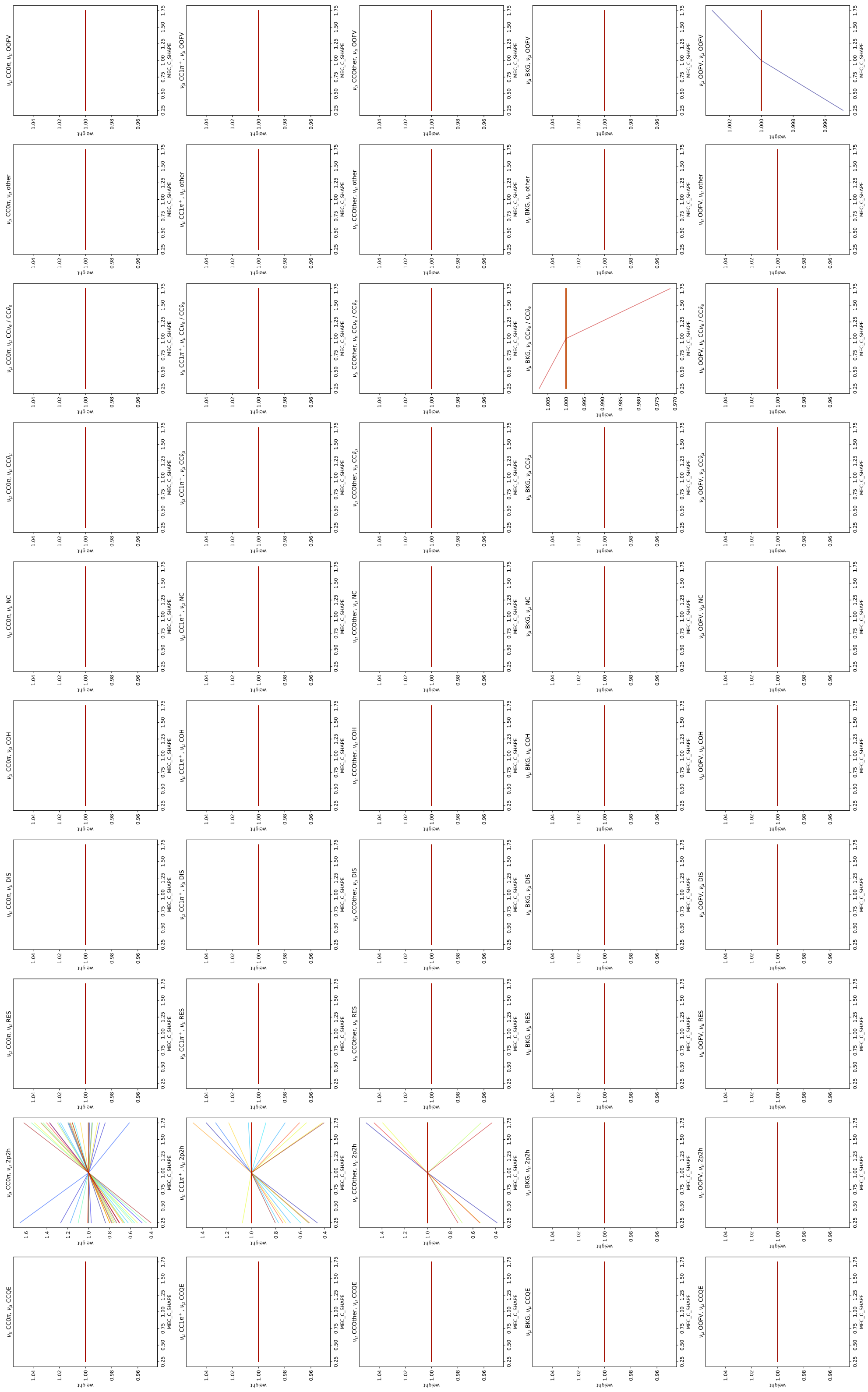

FIGURE F.3: Topology × Reactions configurations for MEC_C_SHAPE with 33 bins per configuration.

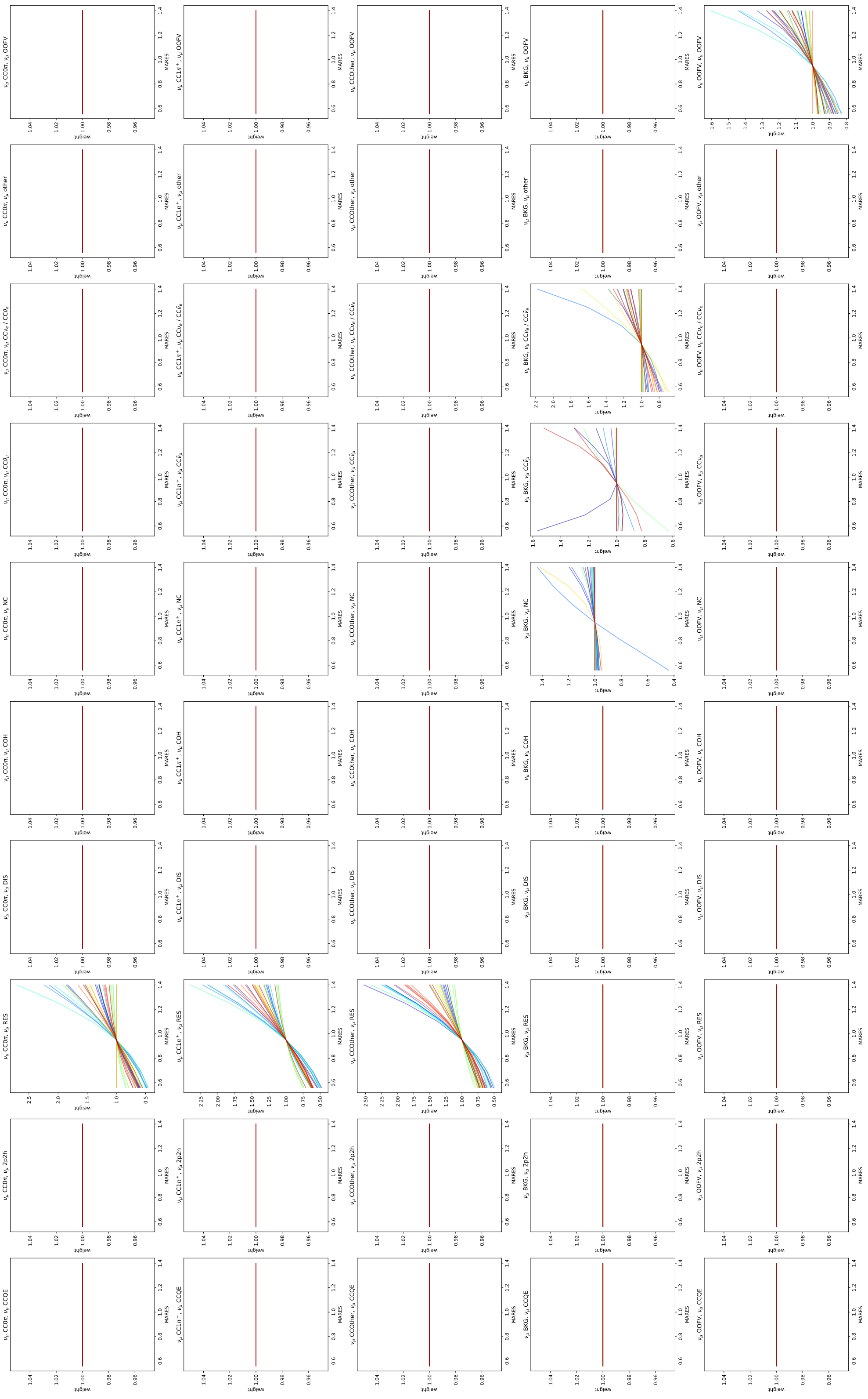

FIGURE F.4: Topology × Reactions configurations for MARES with 33 bins per configuration.

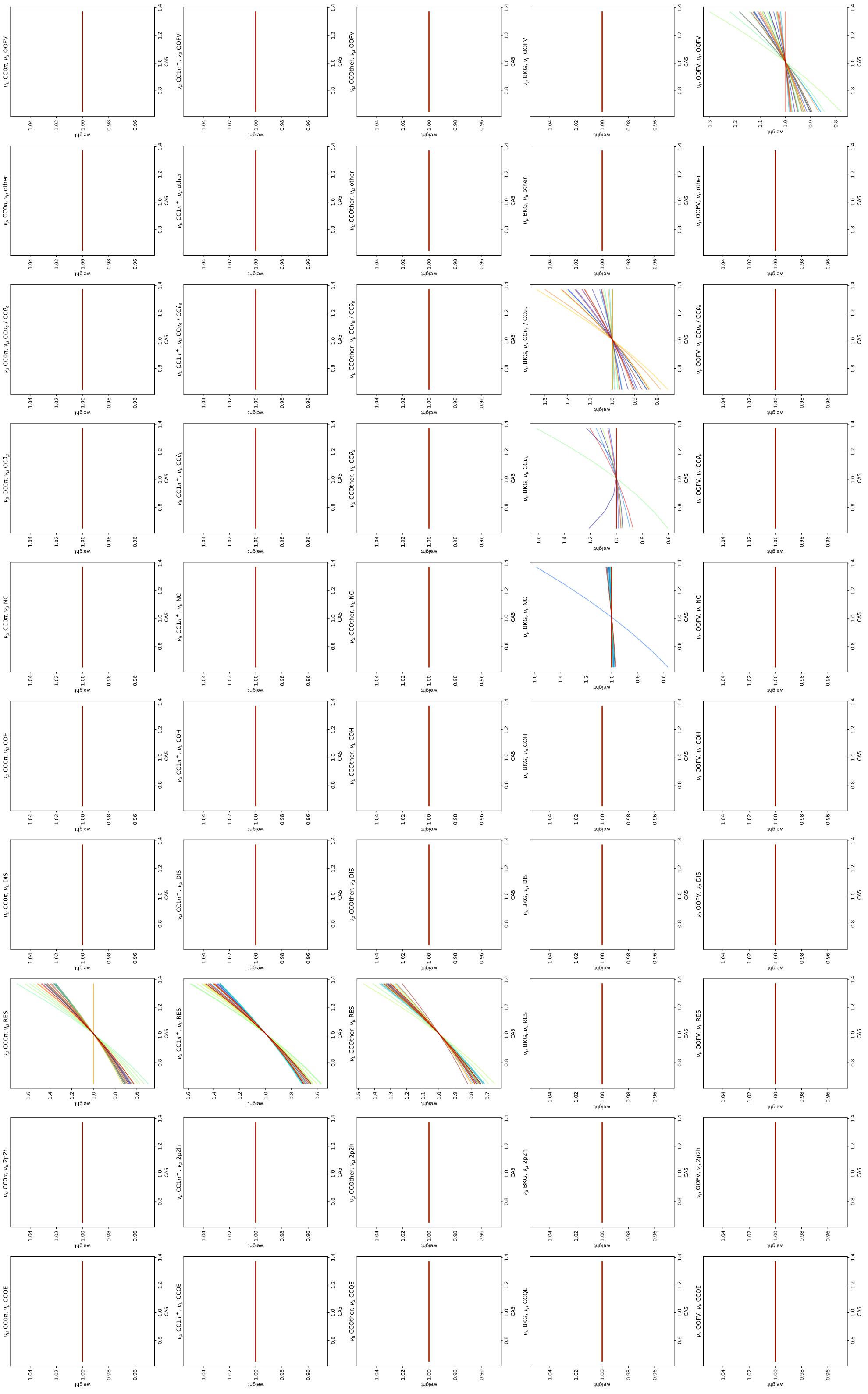

FIGURE F.5: Topology × Reactions configurations for CA5 with 33 bins per configuration.

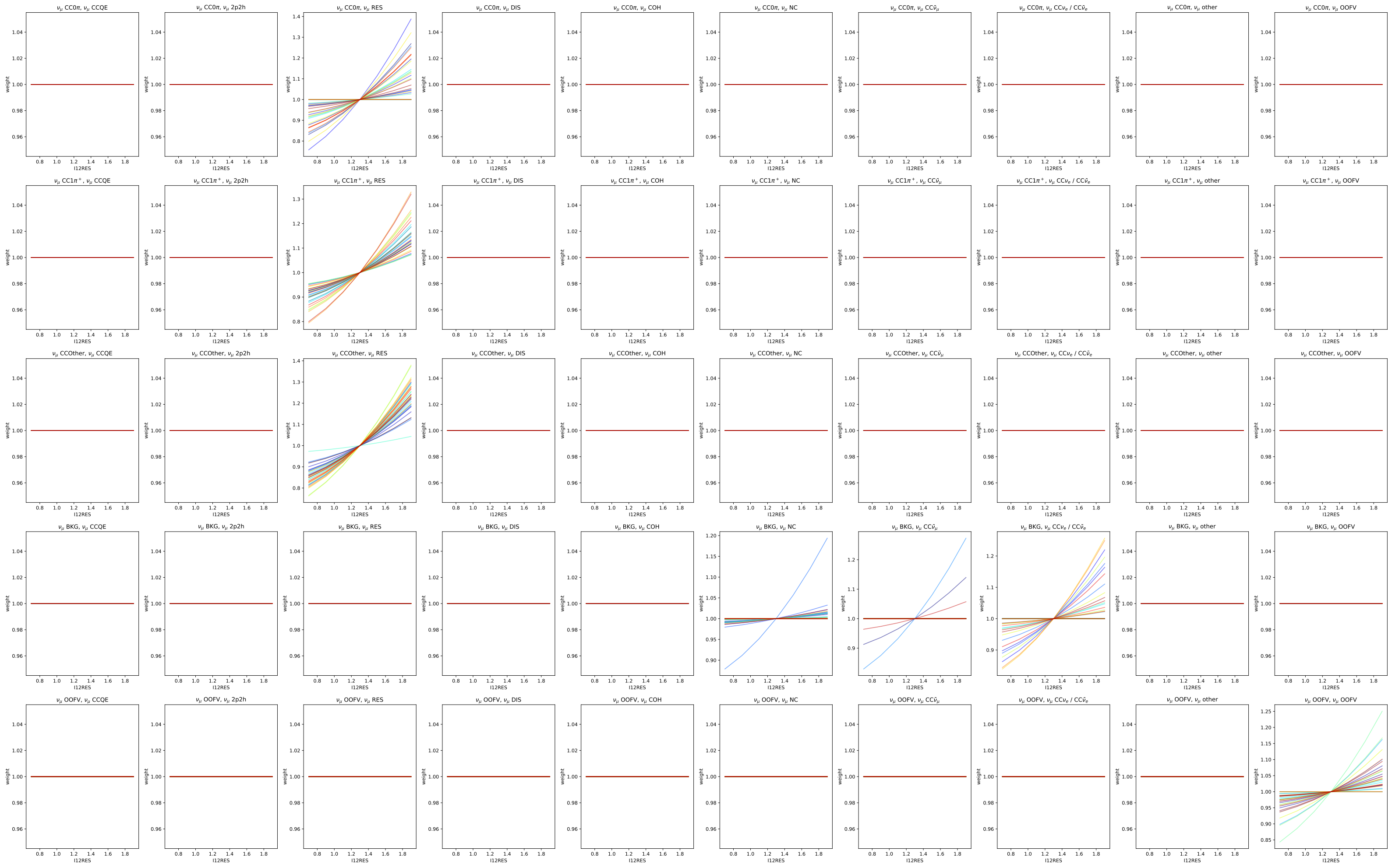

FIGURE F.6: Topology × Reactions configurations for I12RES with 33 bins per configuration.

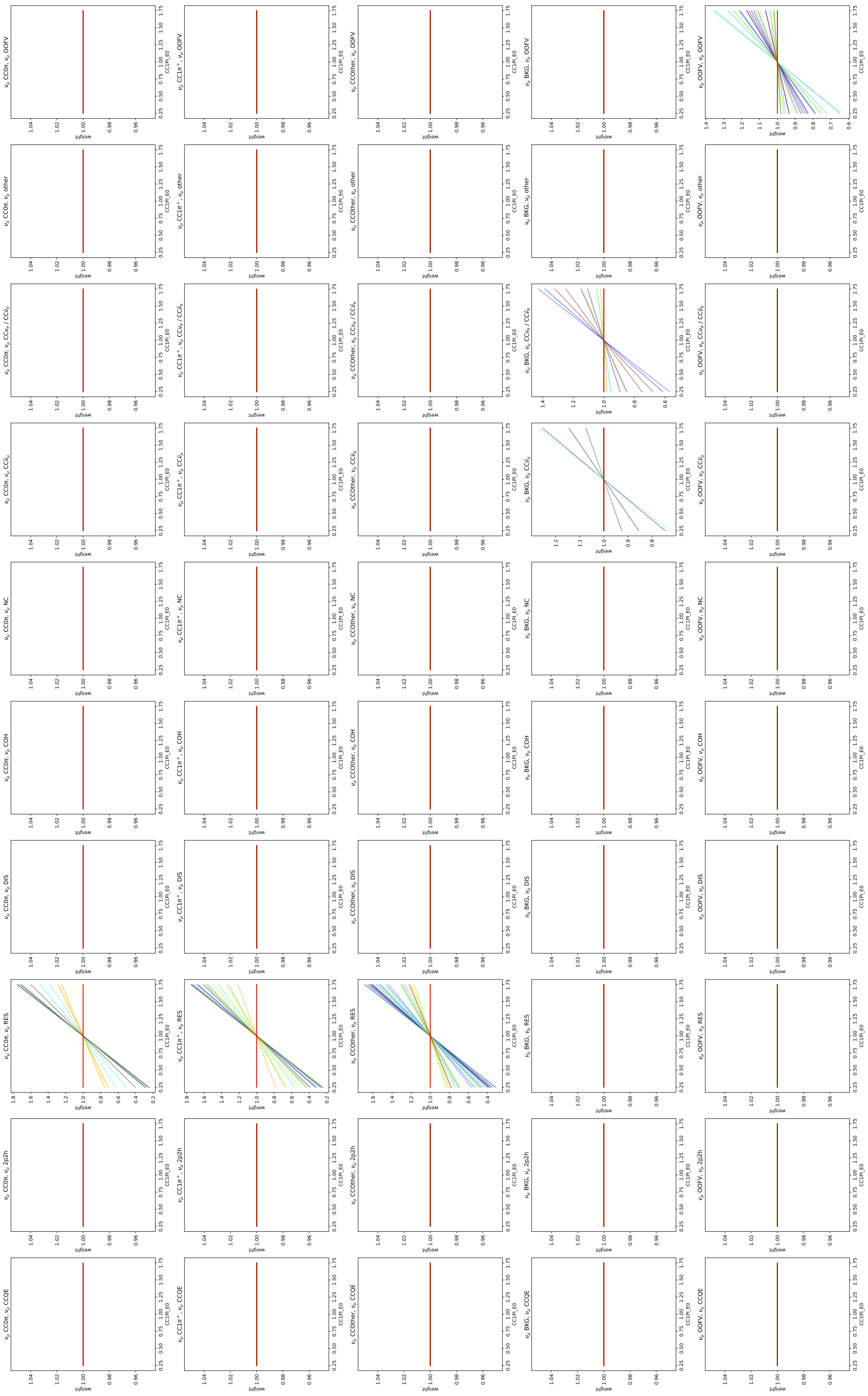

FIGURE F.7: Topology × Reactions configurations for CC1PI_E0 with 33 bins per configuration.

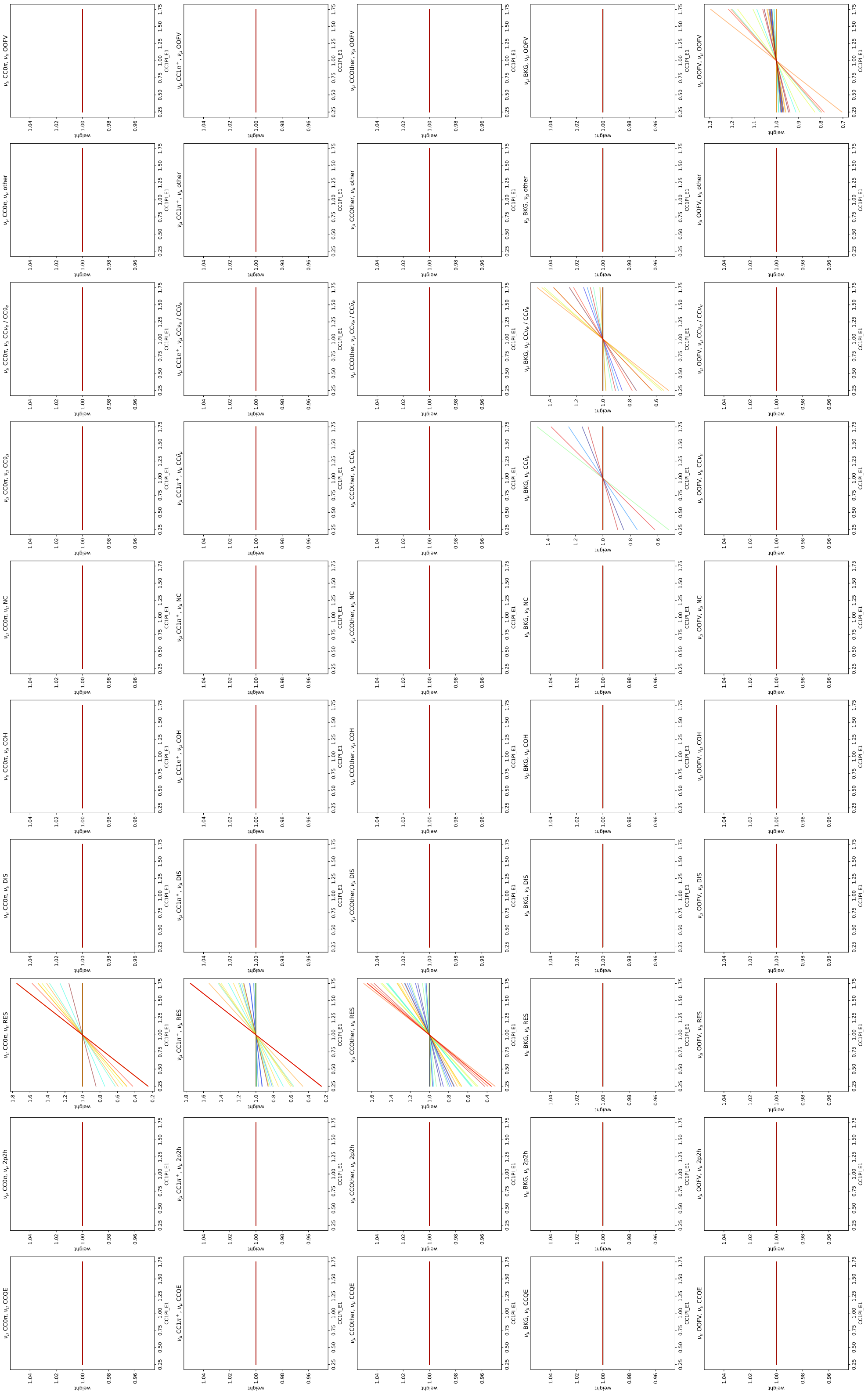

FIGURE F.8: Topology × Reactions configurations for CC1PI_E1 with 33 bins per configuration.

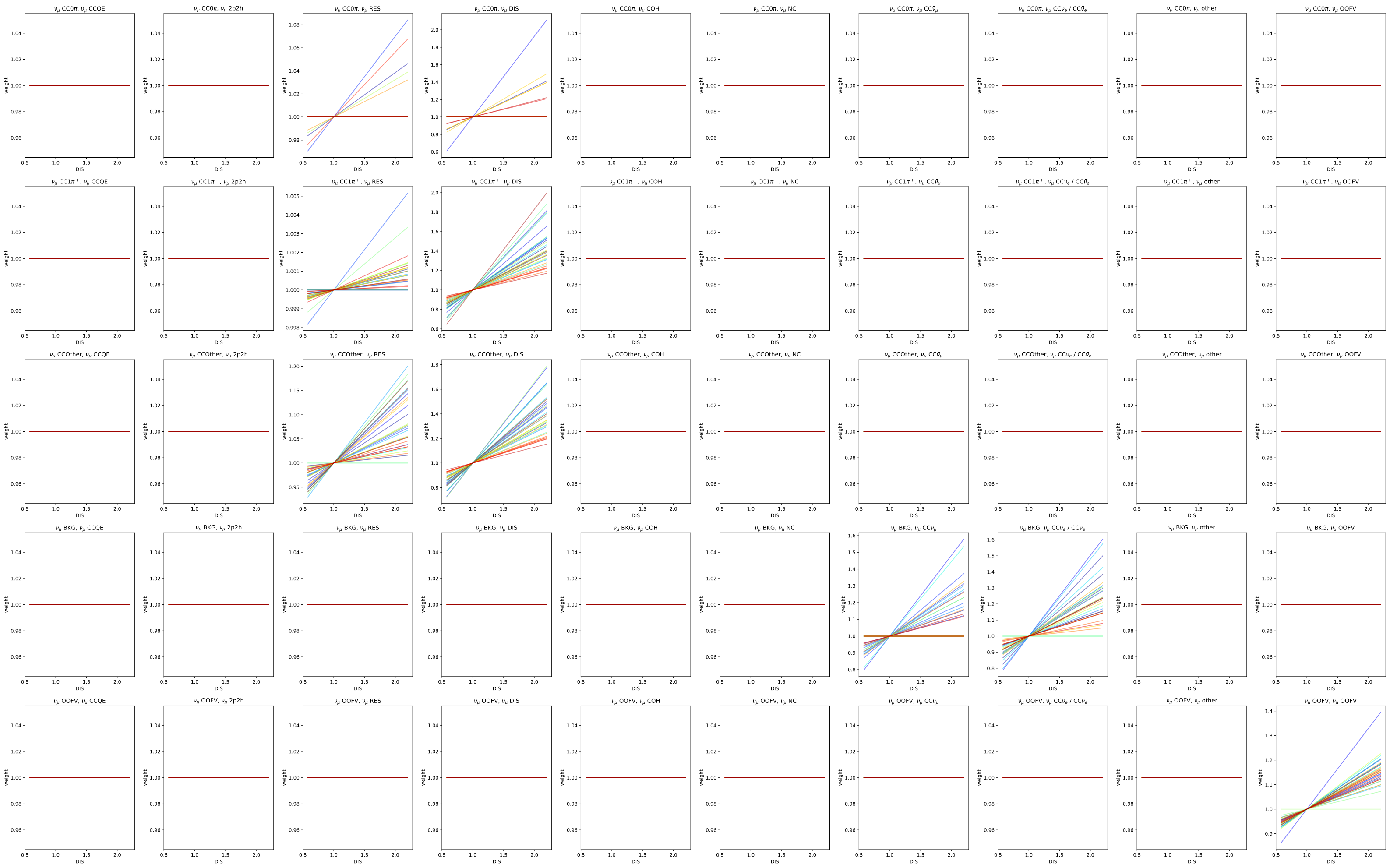

FIGURE F.9: Topology × Reactions configurations for DIS with 33 bins per configuration.

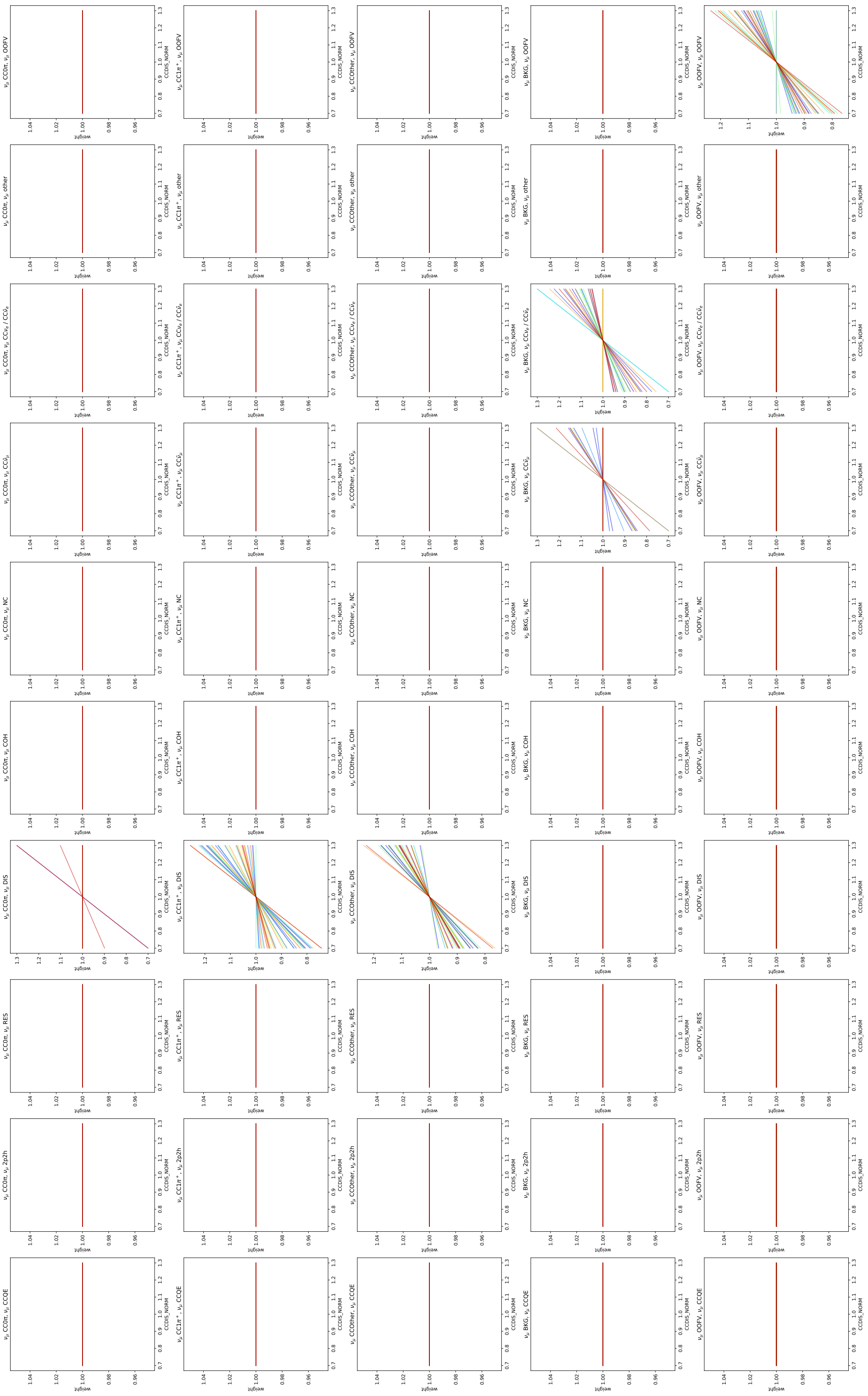

FIGURE F.10: Topology × Reactions configurations for CCDIS_NORM with 33 bins per configuration.

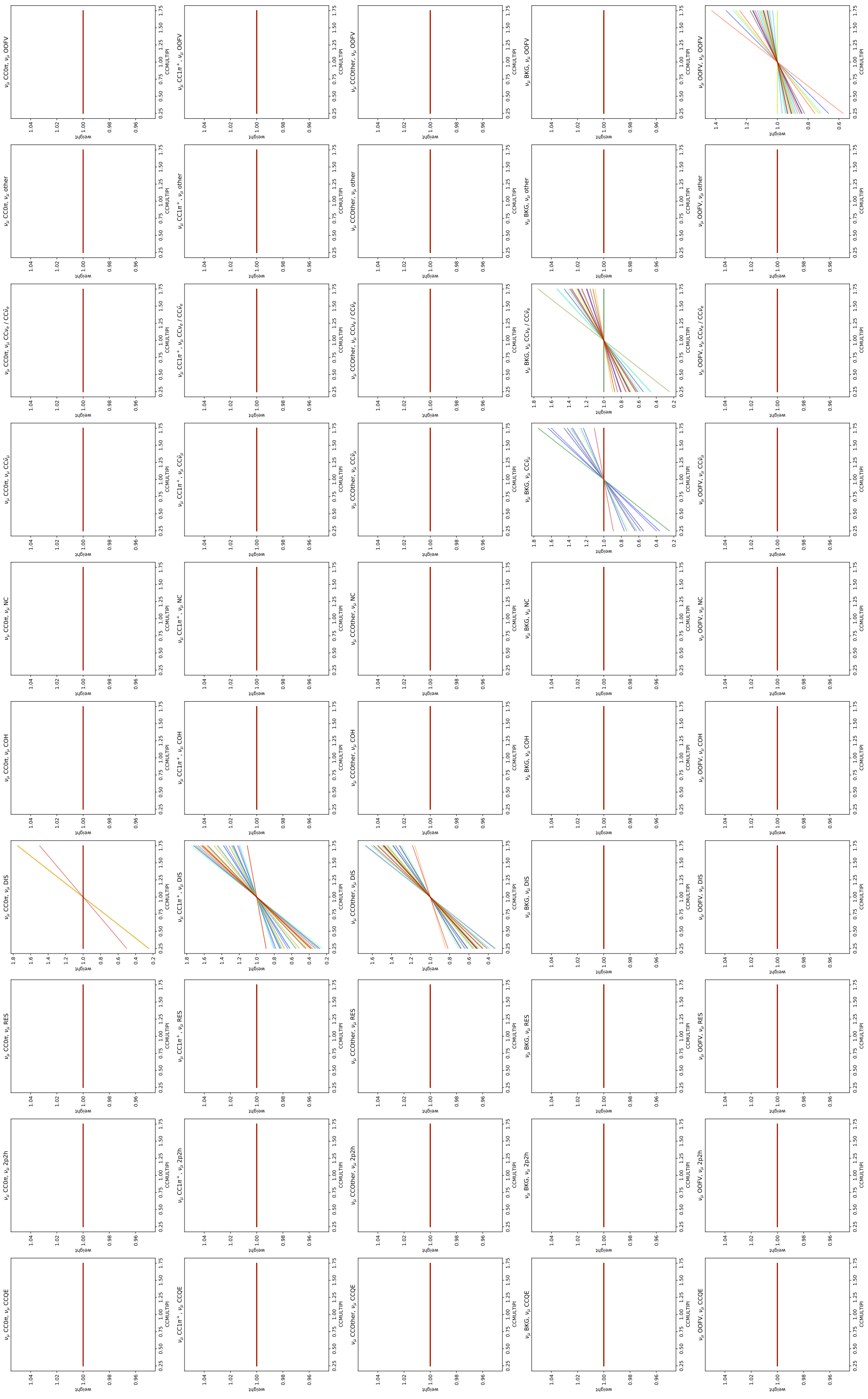

FIGURE F.11: Topology × Reactions configurations for CCMULTIPI with 33 bins per configuration.

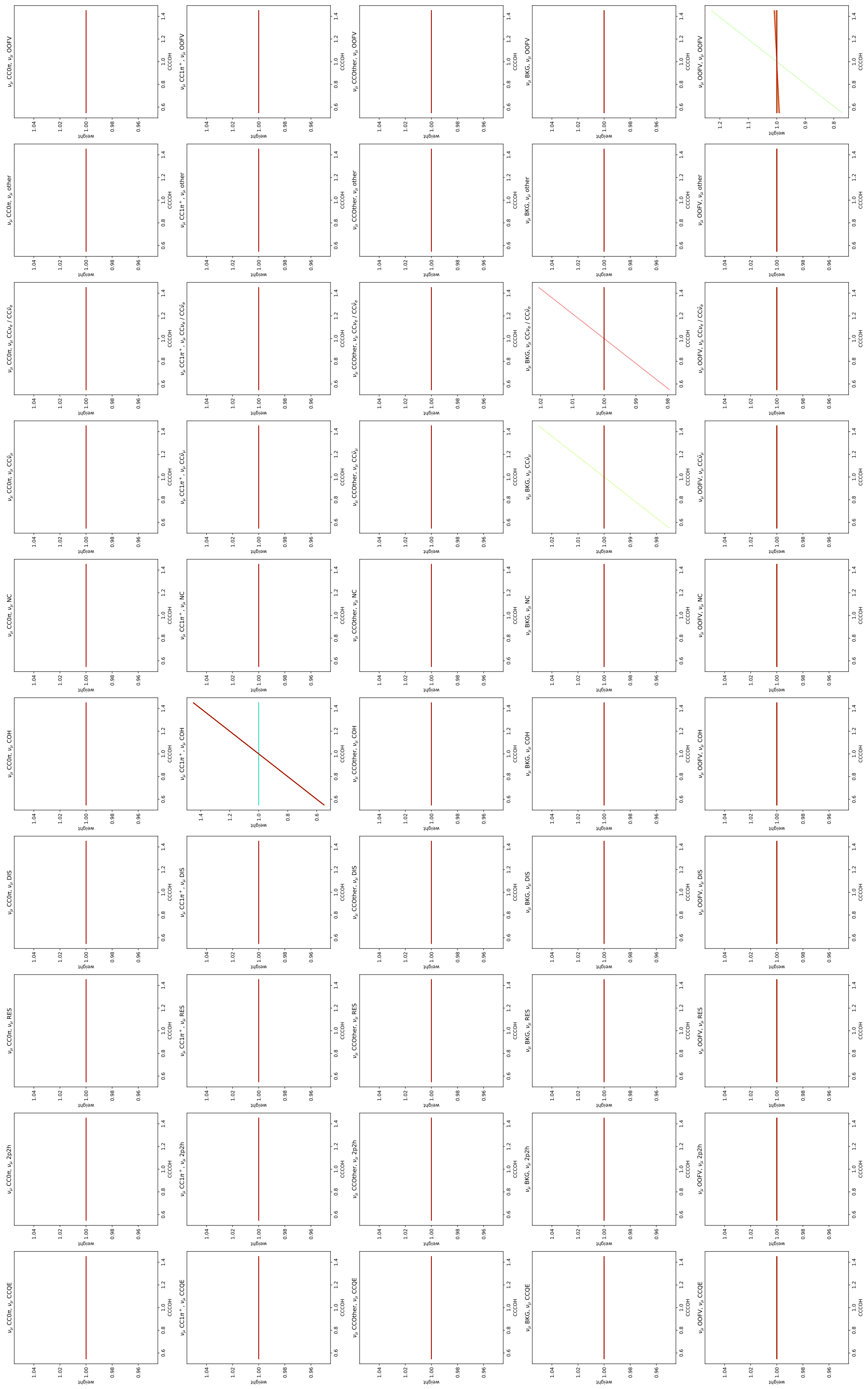

FIGURE F.12: Topology × Reactions configurations for CCCOH with 33 bins per configuration.

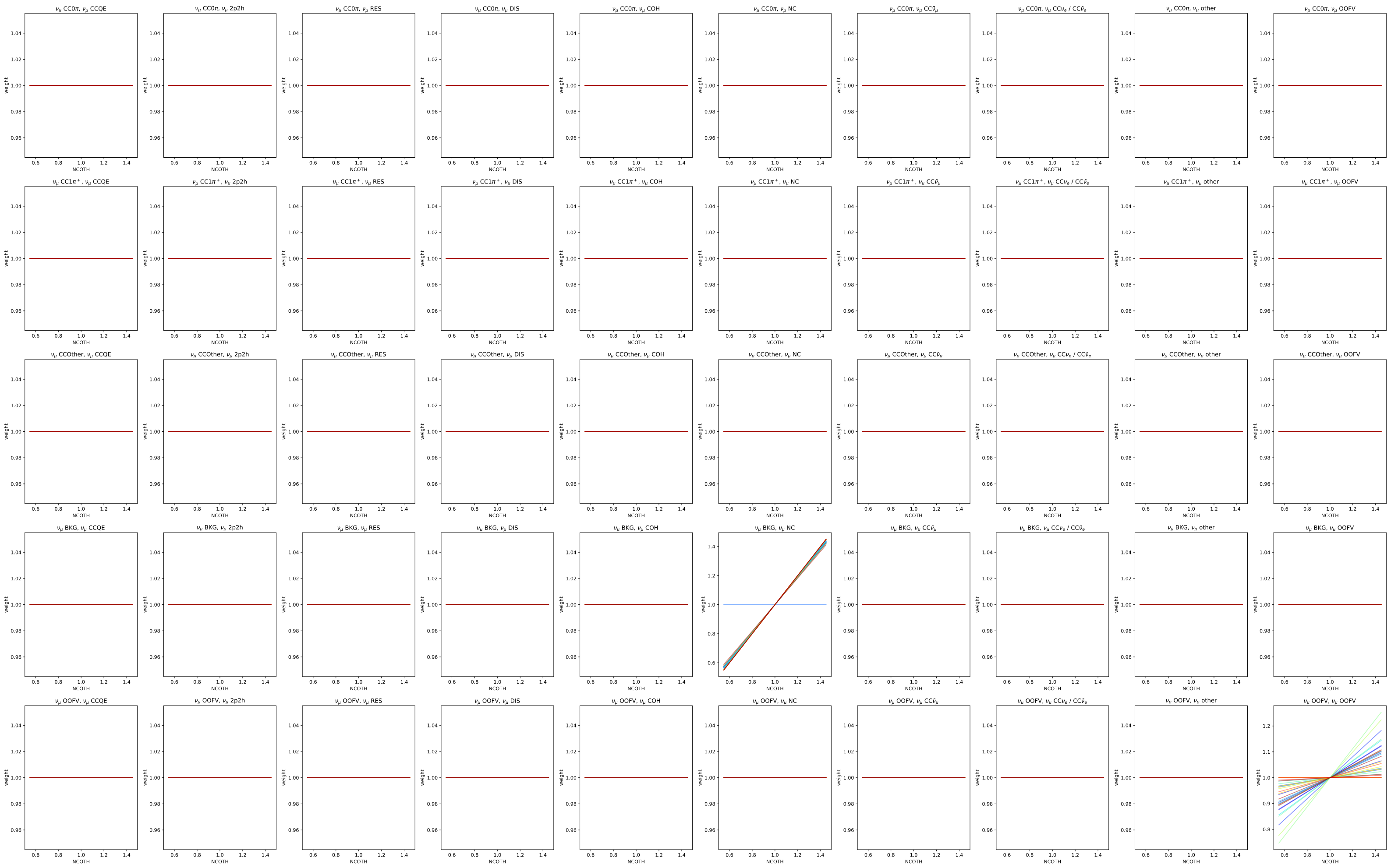

FIGURE F.13: Topology × Reactions configurations for NCOTH with 33 bins per configuration.

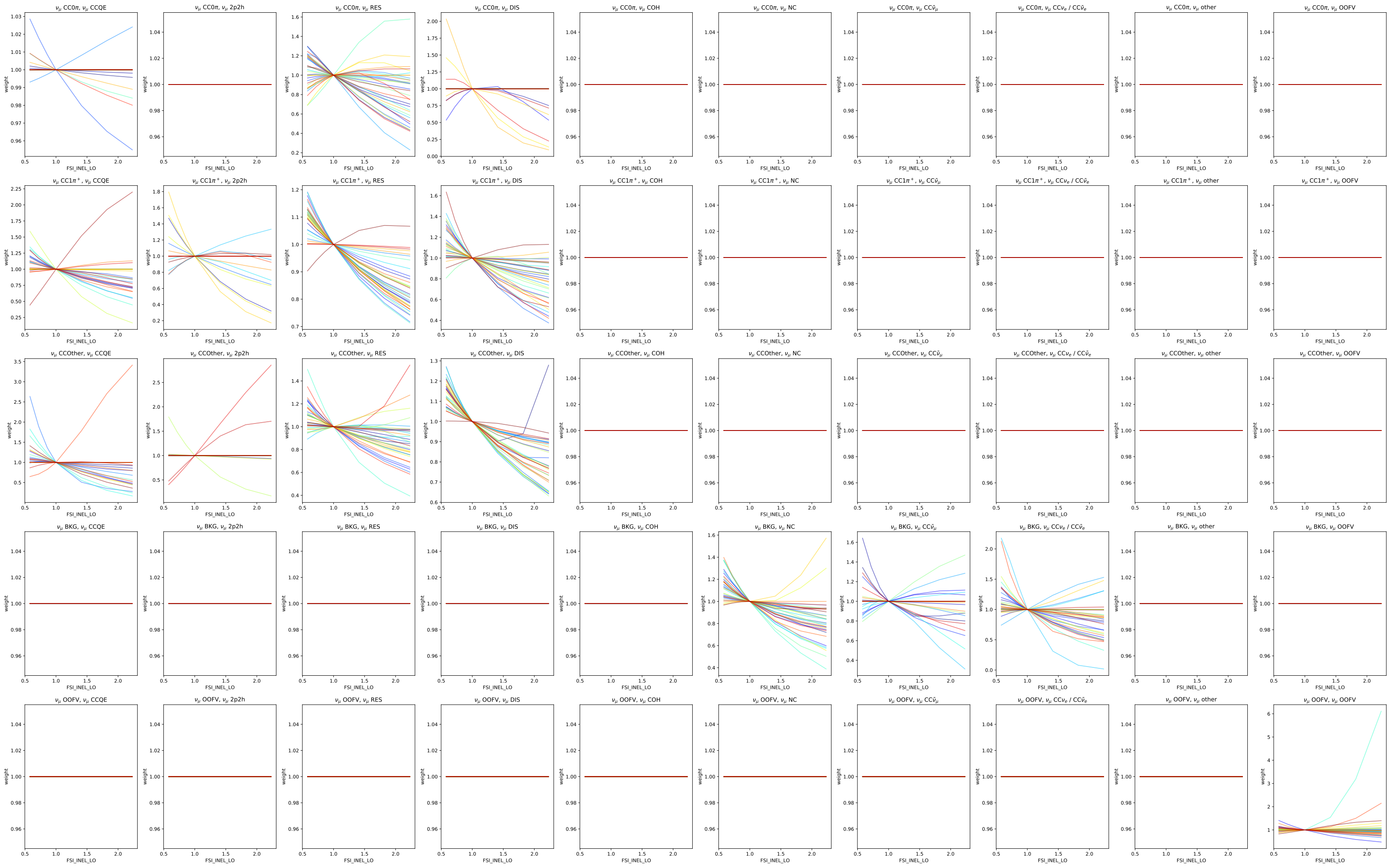

FIGURE F.14: Topology × Reactions configurations for FSI_INEL_LO with 33 bins per configuration.

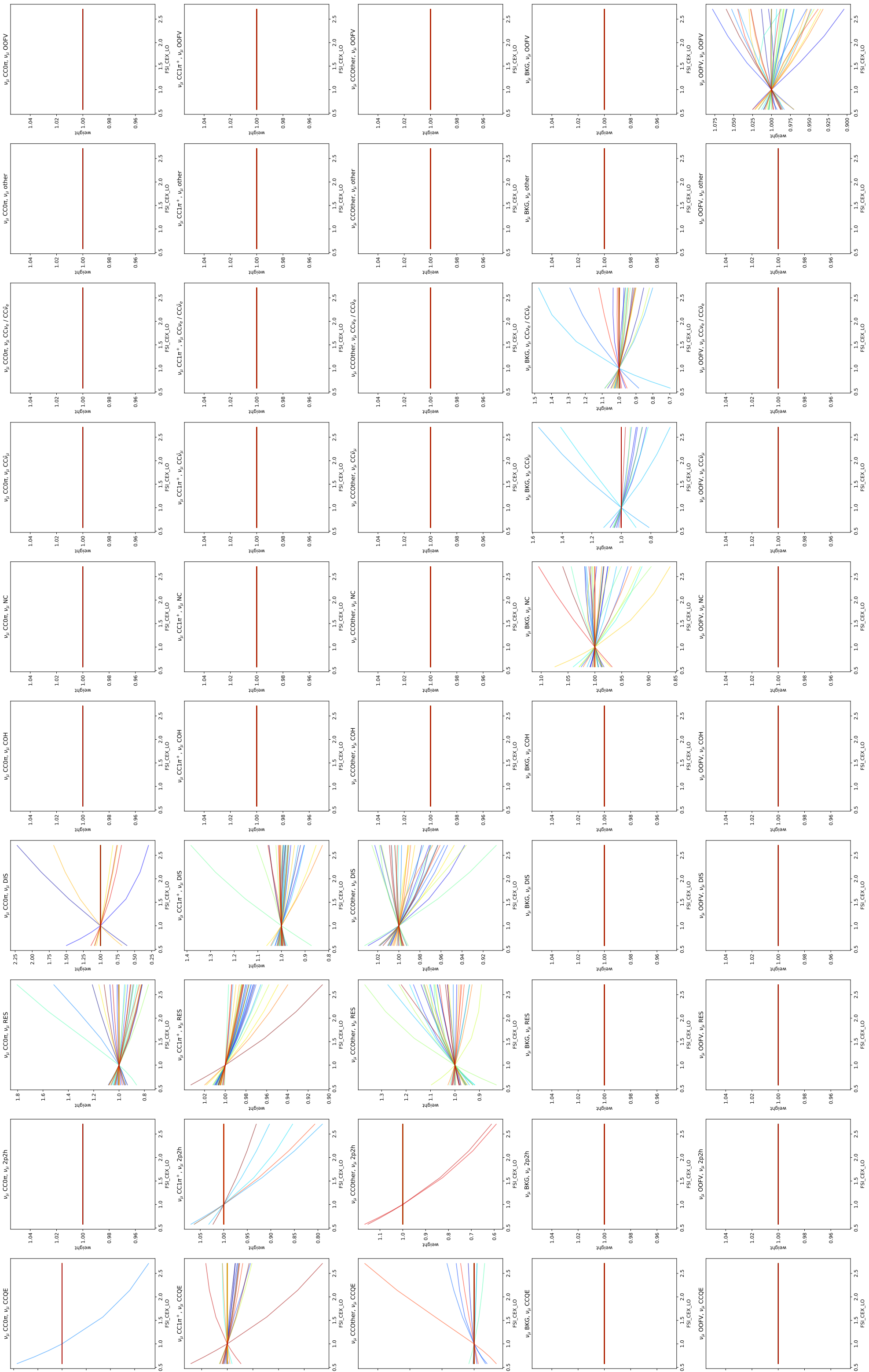

FIGURE F.15: Topology × Reactions configurations for FSI_CEX_LO with 33 bins per configuration.

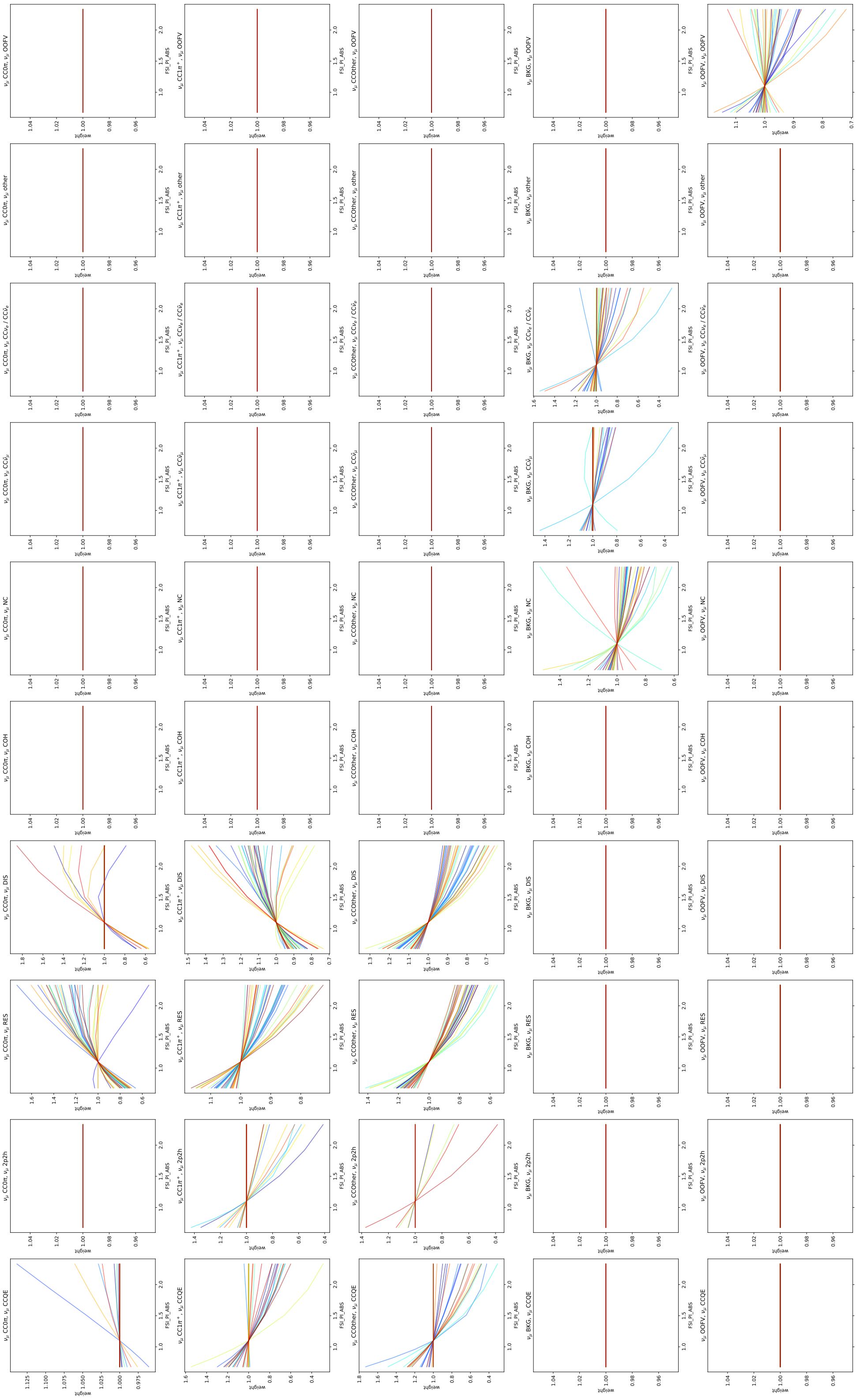

FIGURE F.16: Topology × Reactions configurations for FSI_PI_ABS with 33 bins per configuration.

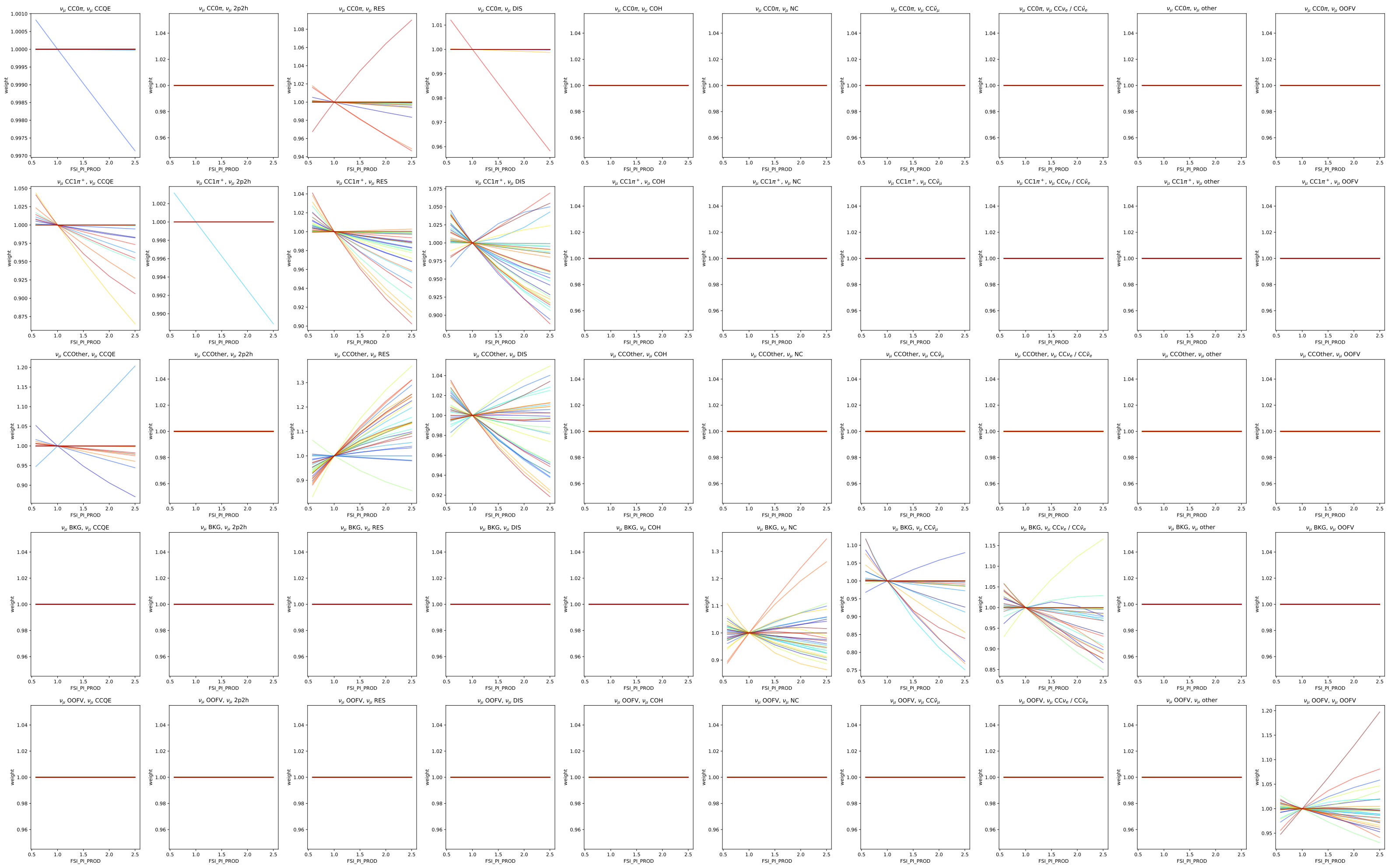

FIGURE F.17: Topology × Reactions configurations for FSI_PI_PROD with 33 bins per configuration.

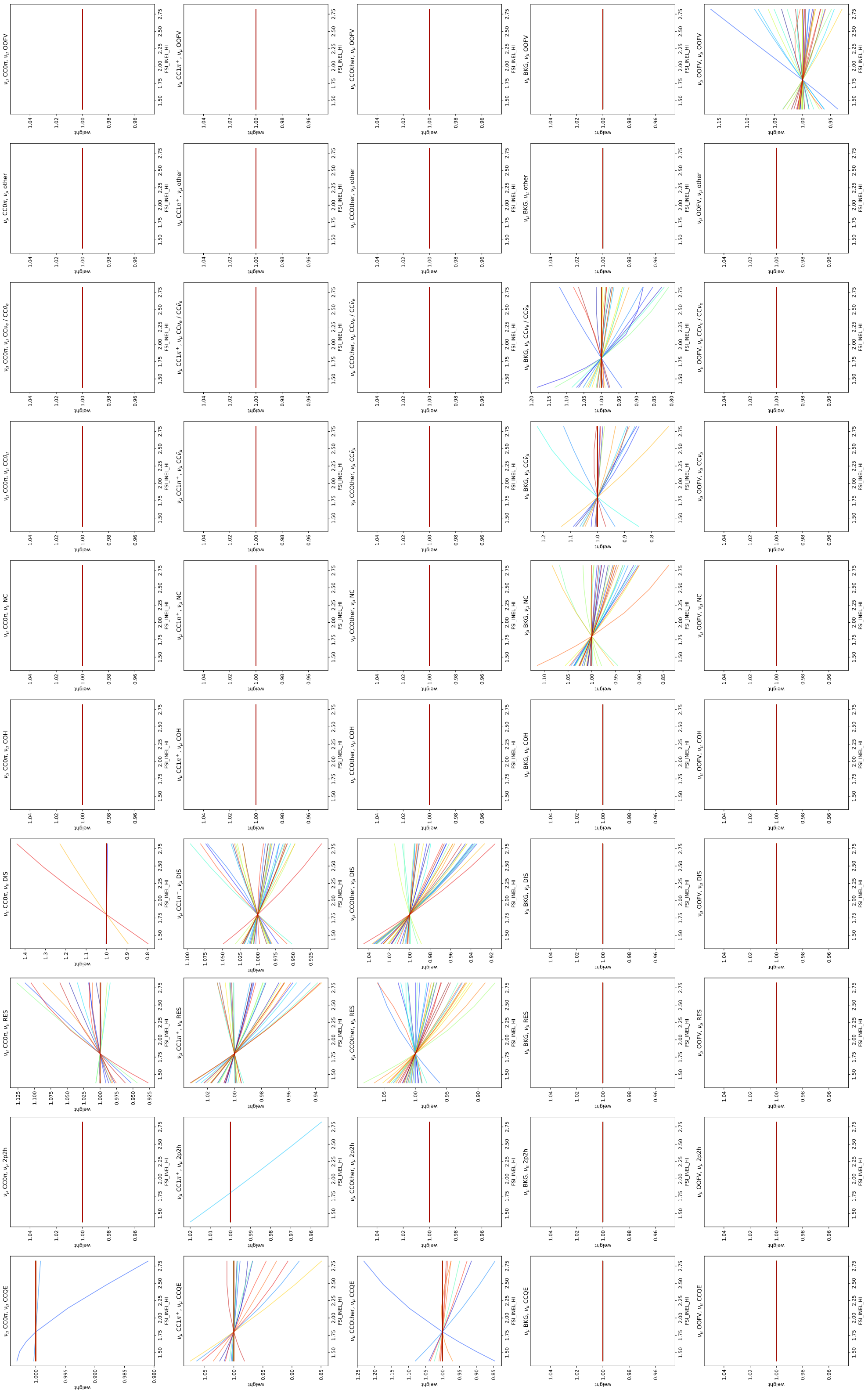

FIGURE F.18: Topology × Reactions configurations for FSI_INEL_HI with 33 bins per configuration.

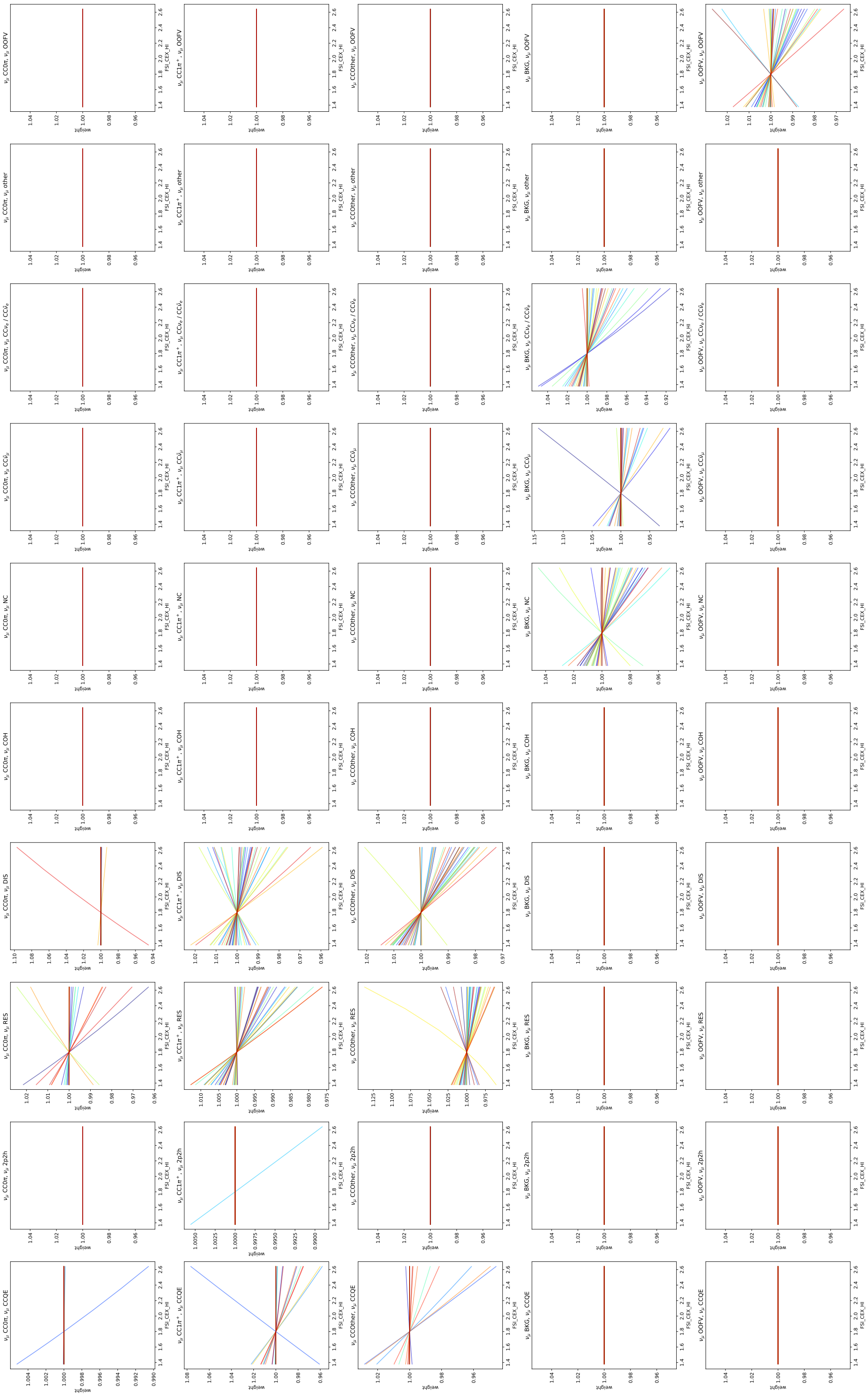

FIGURE F.19: Topology × Reactions configurations for FSI_CEX_HI with 33 bins per configuration.

Bibliography

[1] Tech. rep. T2K-TN-384. 2017.

[2] https://en.wikipedia.org/wiki/Standard_Model. 2021.

[3] https://pdg.lbl.gov/2021/listings/contents_listings.html. 2021.

[4] https://en.wikipedia.org/wiki/Neutrino_mass_hierarchy. 2021.

[5] https://neutrinos.fnal.gov/sources/reactor-neutrinos/. 2021.

[6] http://www.genie-mc.org. 2021.

[7] https://gibuu.hepforge.org/trac/wiki. 2021.

[8] http://nu.ift.uni.wroc.pl/nuwro/. 2021.

[9] https://www.t2k.org/. 2021.

[10] https://j-parc.jp/. 2021.

[11] http://www-sk.icrr.u-tokyo.ac.jp/sk/. 2021.

[12] K. Abe, and et al. "Constraint on the matter–antimatter symmetry-violating phase in neutrino oscillations". In: *Nature* (2020). DOI: `10.1038/s41586-020-2177-0`. URL: `https://doi.org/10.1038/s41586-020-2177-0`.

[13] K. Abe, and et al. "Measurement of the muon neutrino charged-current single π^+ production on hydrocarbon using the T2K off-axis near detector ND280". In: *Physical Review D* 101.1 (2020). URL: `http://dx.doi.org/10.1103/PhysRevD.101.012007`.

[14] K. Abe, and et al. "The T2K Experiment". In: *Nuclear Instruments and Methods in Physics* (2011).

[15] A.A. Aguilar-Arevalo, and et al. In: *Phys. Rev. D* 81.092005 (2010).

[16] Q. R. Ahmad, and et al. "Measurement of the Charged Current Interactions Produced by B-8 Solar Neutrinos at the Sudbury Neutrino Observatory". In: *Phys. Rev. Lett* 87.071301 (2001).

[17] M. Ahn and et al. In: *Phys.Rev.* D74.072003 (2006).

[18] M. H. Ahn, and et al. "Indications of Neutrino Oscillation in a 250-km Long-Baseline Experiment". In: *Phys. Rev. Lett* 90.041801 (2003).

[19] K. Abe et al. *T2K ND280 Upgrade – Technical Design Report*. 2020. arXiv: `1901.03750 [physics.ins-det]`.

[20] Radecky et al. "Study of single-pion production by weak charged currents in low-energy νd interactions". In: *Physical Review D* 25.5 (1982).

[21] D. Allasia et al. In: *Nucl. Phys. B* 343.285 (1990).

[22] Robert G Arns. *Detecting the Neutrino*. 2001.

[23] Y. Ashie and et al. In: *Phys.Rev.* D71.112005 (2005).

[24] C. Athanassopoulos, and et al. "Candidate Events in a Search for Muon-Antineutrino to Electron-Antineutrino Oscillations". In: *Phys. Rev. Lett* 75.2650 (1995).

[25] N.J. Baker, and et al. In: *Phys. Rev. D* 23.2499 (1981).

[26] S.J. Barish, and et al. In: *Phys. Rev.D* 16.3103 (1977).

[27] P. Bartet and et al. *ν_μ CC event selections in the ND280 tracker using Run 2+3+4 data*. Tech. rep. T2K-TN-245. 2017.

[28] S.V. Belikov, and et al. In: *Z. Phys. A* 320.625 (1985).

[29] J. Beringer, and et al. "Review of Particle Physics". In: *Phys. Rev. D* 86.010001 (2012), pp. 1305–1326.

[30] C. Bojechko and et al. *CC-multiple-pion ν_μ event selections in the ND280 tracker using Run 1+2+3+4 data*. Tech. rep. T2K-TN-152. 2013.

[31] J. Brunner, and et al. In: *Z. Phys. C* 45.551 (1990).

[32] M. Zito C. Giganti and et al. *Particle Identification with the T2K TPC*. Tech. rep. T2K-TN-001. 2009.

[33] D. Casper. ""The nuance Neutrino Physics Simulation, and the Future"". In: *Nuclear Physics B (Proc. Suppl.)* 112 (2002), pp. 161–170.

[34] Sacha Davidson, Enrico Nardi, and Yosef Nir. "Leptogenesis". In: *Physics Reports* 466.4-5 (2008), 105–177. ISSN: 0370-1573. DOI: `10.1016/j.physrep.2008.06.002`. URL: `http://dx.doi.org/10.1016/j.physrep.2008.06.002`.

[35] D. Day, and et al. In: *Phys. Rev. D* 28.2714 (1983).

[36] M. Derrick et al. In: *Phys. Lett. B* 92.363 (1980).

[37] DoubleChooz. urlhttp://doublechooz.in2p3.fr/About/about.php. 2016.

[38] K. Eguchi, and et al. "First Results from KamLAND: Evidence for Reactor Antineutrino Disappearance". In: *Phys. Rev. Lett* 90.021802 (2003).

[39] Sánchez F. "Possibility of measuring Adler angles in charged current single pion neutrino-nucleus interactions". In: *Physical Review D* 93.093015 (2016).

[40] Joseph A. Formaggio and G. P Zeller. "From eV to EeV: Neutrino cross sections across energy scales". In: *Rev. Mod. Phys* 84.3 (2012), pp. 1307–1341.

[41] Martin Freund. "Analytic approximations for three neutrino oscillation parameters and probabilities in matter". In: *Physical Review D* 64.5 (2001). ISSN: 1089-4918. DOI: `10.1103/physrevd.64.053003`. URL: `http://dx.doi.org/10.1103/PhysRevD.64.053003`.

[42] Y. Fukuda, and et al. "Evidence for Oscillation of Atmospheric Neutrinos". In: *Phys. Rev. Lett* 81.1562 (1998).

[43] Y. Fukuda and et al. In: *Phys.Rev.Lett.* 81.1562–1567 (1998).

[44] Y. Fukuda and et al. In: *Phys.Rev.Lett.* 82.2430–2434 (1999).

[45] A. A. García Soto. "Study of the ν_μ interactions via charged current in the T2K near detector". PhD thesis. Universitat Autónoma de Barcelona, 2017.

[46] G.T. Garvey et al. "Recent advances and open questions in neutrino-induced quasi-elastic scattering and single photon production". In: *Phy. Rep* 580.4 (2015), 1–45.

[47] Carlo Giunti and W. Kim Chung. *Fundamentals of Neutrino Physics and Astrophysics*. Oxford University Press, 2007.

[48] Hayato. In: *Acta Physica Polonica B* 40.2477 (2009).

[49] Y. Hayato and et al. In: *Phys.Rev.Lett.* 83.1529–1533 (1999).

[50] J. Hosaka and et al. In: *Phys.Rev.* D74.032002 (2006).

[51] J. Kim and et al. *Michel Electron Tagging in FGD1*. Tech. rep. T2K-TN-104. 2012.

[52] T. Kitagaki, and et al. In: *Phys. Rev. D* 28.436 (1983).

[53] K. Kodama, and et al. "Observation of τ Neutrino Interactions". In: *Phys. Lett* B504.218 (2001).

[54] W. Krenz et al. In: *Nucl. Phys. B* 135.45 (1978).

[55] V. Lyubushkin, and et al. "A study of quasi-elastic muon neutrino and antineutrino scattering in the NOMAD experiment". In: *Eur. Phys. J. C* 63 (2009), 355–381.

[56] H. Nishino and et al. In: *Phys.Rev.Lett.* 102.141801 (2009).

[57] Tomas Nosek. *Effects of Matter in Neutrino Oscillations and Determination of Neutrino Mass Hierarchy at Long-baseline Experiments*. 2017. arXiv: `1612.09132 [hep-ph]`.

[58] J. Erler P. Langacker and E. Peinado. *Neutrino Physics*. 2005.

[59] W. Pauli. "Cambridge Monogr". In: *Part. Phys. Nucl. Phys. Cosmol.* 14 (2000).

[60] B. Pontecorvo. "Neutrino Experiments and the Question of Leptonic Charge Conservation". In: *Sov. Phys. JETP* 26.984 (1968).

[61] Castillo Fernández R. "Mesurement of the muon neutrino charge current interactions and the the muon neutrino single pion cross section on CH using the T2K near detector". PhD thesis. Universitat Autónoma de Barcelona, 2015.

[62] D. Rein. "Angular distribution in neutrino-induced single pion production processes". In: *Z.phys. C Particles and Fields* 35 (1987), pp. 43–64. URL: `https://doi.org/10.1007/BF01561054`.

[63] F. Reines and C. L. Cowan. "Detection of the Free Neutrino". In: *Phys. Rev* 92.830 (1953).

[64] SanOnofreSafety. urlhttps://sanonofresafety.org/. 2016.

[65] N. Schmitz. *Neutrino physik Teubner Studienbücher*. Stuttgart, 1997.

[66] Royal Swedish Academy of Sciences. *Neutrino Oscillations*. Tech. rep. Box 50005 (Lilla Fresativägen 4 A), SE-104 05 Stockholm, Sweden: The Royal Swedish Academy of Sciences, 2015.

[67] M. Shiozawa and et al. In: *Phys.Rev.Lett.* 81.3319–3323 (1998).

[68] SNO. urlhttp://www.sno.phy.queensu.ca/. 2016.

[69] Francisco R Villatoro. *Borexino observó neutrinos de la primera reacción pp en el núcleo del Sol*. urlhttp://francis.naukas.com/2014/12/27/borexino-observa-neutrinos-de-la-primera-reaccion-pp-en-el-nucleo-del-sol. Accedido 12-04-2016. 2014.

[70] Guillermo Daniel Megías Vázquez. "Charged-current neutrino interactions with nucleons and nuclei at intermediate energies". PhD thesis. Universidad de Sevilla, 2017.

[71] S. S. Wilks. "The Large-Sample Distribution of the Likelihood Ratio for Testing Composite Hypotheses". In: *Ann. Math. Statist.* 9.1.pp. 60–62 (1938). DOI: `10.1214/aoms/1177732360.`. URL: `https://doi.org/10.1214/aoms/`.